

EVOLUTION OF THE CHARGE DENSITY WAVE STATE IN THE  
RARE-EARTH TRITELLURIDES UNDER UNIAXIAL STRESS AND DISORDER

A DISSERTATION  
SUBMITTED TO THE DEPARTMENT OF APPLIED PHYSICS  
AND THE COMMITTEE ON GRADUATE STUDIES  
OF STANFORD UNIVERSITY  
IN PARTIAL FULFILLMENT OF THE REQUIREMENTS  
FOR THE DEGREE OF  
DOCTOR OF PHILOSOPHY

Joshua Alan Wolfe Straquadine

June 2020

© 2020 by Joshua Alan Wolfe Straquadine. All Rights Reserved.  
Re-distributed by Stanford University under license with the author.



This work is licensed under a Creative Commons Attribution-Noncommercial 3.0 United States License.

<http://creativecommons.org/licenses/by-nc/3.0/us/>

This dissertation is online at: <http://purl.stanford.edu/fb238bq0146>

I certify that I have read this dissertation and that, in my opinion, it is fully adequate in scope and quality as a dissertation for the degree of Doctor of Philosophy.

**Ian Fisher, Primary Adviser**

I certify that I have read this dissertation and that, in my opinion, it is fully adequate in scope and quality as a dissertation for the degree of Doctor of Philosophy.

**Harold Hwang**

I certify that I have read this dissertation and that, in my opinion, it is fully adequate in scope and quality as a dissertation for the degree of Doctor of Philosophy.

**Steven Kivelson**

Approved for the Stanford University Committee on Graduate Studies.

**Stacey F. Bent, Vice Provost for Graduate Education**

*This signature page was generated electronically upon submission of this dissertation in electronic format. An original signed hard copy of the signature page is on file in University Archives.*



# Abstract

Materials with strong electron correlations often exhibit a complex interplay between competing or coexisting ordered phases, such as charge order, magnetism, and superconductivity. Model systems which isolate just one of these components, however, can provide a practical path for navigating this complexity. The family of rare-earth tritellurides ( $R\text{Te}_3$  where  $R=\text{Y, La-Nd, Sm, Gd-Tm}$ ) are one candidate model system for the study of charge density wave (CDW) formation in quasi-two-dimensional metals with a fourfold in-plane tetragonal symmetry. Bilayers of square Te planes provide the metallic character, while the rare earth element tunes the CDW transition temperature through chemical pressure. For the lighter rare-earths (La-Gd) a single, incommensurate, unidirectional CDW transition is observed ( $T_{CDW1}$ ), while a second CDW transition at lower temperatures ( $T_{CDW2}$ ) with an orthogonal in-plane wavevector appears for heavier rare earths (Tb-Tm). The slightly orthorhombic crystal structure (in which the  $a$  and  $c$  lattice vectors lie in the Te planes) constrains the wavevector of the high-temperature transition along the  $c$ -axis. This dissertation focuses primarily on  $\text{ErTe}_3$  and  $\text{TmTe}_3$ , both of which exhibit two CDW transitions below 300 K.

This dissertation provides detailed studies of the behavior of this candidate model system under two different perturbations, namely uniaxial stress and disorder. First, however, I present the results of analytical and numerical modeling of heat flow in measurements of the AC elastocaloric effect (AC-ECE), a new experimental tool that I use to investigate the title compounds. The AC-ECE technique uses oscillating strain to examine strain-induced temperature changes in a sample under quasi-adiabatic conditions. This signal arises from strain-induced changes in the entropy, and as such relates to several other thermodynamic properties. My work demonstrates that the details of the frequency-dependent sensitivity in AC-ECE measurements are highly nontrivial, and I present both intuitive explanations of these effects as well as a quantitative match with experiment.

I apply the AC-ECE technique to explore the effects of in-plane uniaxial stress on the CDW transitions in both  $\text{ErTe}_3$  and  $\text{TmTe}_3$ . A combination of AC-ECE measurements, together with in-plane and out-of-plane elastoresistivity measurements, clearly detects changes in the critical temperatures, transport anisotropy, and thermodynamic quantities as a function of strain. I also show that modest antisymmetric strains can cause the wavevector of the primary CDW transition at  $T_{CDW1}$  to switch such that it aligns with the  $a$ -axis rather than the  $c$ -axis. Below  $T_{CDW1}$ , strain

can then drive a first order transition between these two phases. The synthesis of all of these results allows me to develop a phenomenological model identifying the minimal CDW-strain couplings which reproduce the observed phase diagram.

Finally, I describe the transport, thermodynamic, and scattering characteristics of single crystals of  $\text{Pd}_x\text{ErTe}_3$ , in which neutral Pd atoms intercalated between the Te bilayers act as a weak random potential. As the Pd concentration increases, I show that both CDW crossovers are suppressed to lower temperatures, eventually giving way to a superconducting state with maximum critical temperature around 2.5 K.

This work has established  $R\text{Te}_3$  as a model system for studying the interplay of unidirectional CDW formation, in-plane uniaxial stress, disorder, and superconductivity. Further investigation of the inter-relation of these effects could have direct bearing on a range of other material systems of current interest.

# Acknowledgments

Modern research simply cannot happen without a support network, and I have been blessed with one of the best. I would like to extend my heartfelt thanks to everyone who has lent their time and talents to make this research possible, and from whom I have learned so much over the past few years.

To my research advisor, Ian Fisher: thank you for establishing and maintaining the kind of collegial research environment in which I could thrive. The variety of opportunities both within the lab and without, including collaborations with folks around the world, travel to national labs across the country, and the chances to present my work, have allowed me to grow into the scientist that I am today. Your kind and personalized support of each of your students (and so many others who aren't your students) quickly sets everyone around you at ease, and facilitates a creative and productive community in your lab and in the entirety of GLAM.

To the post-docs and senior grad students within from whom I've learned so much: it's hard to overstate how much I learned from all of you. Among the post-docs, I owe quite a bit of my success to the support of Matthias Ikeda, Phil Walmsley, Pierre Massat, Harlyn Silverstein, and Paula Giraldo-Gallo. I would particularly like to thank Matthias, who shares my love of building things and improving instrumentation; Phil, who led me through almost all of my "firsts" in Ian's lab; and Harlyn, the image furnace wizard himself. I would also like to thank Alex Hristov, who never shrank in the face of a complex problem, and who always sought the highest level of quality in his work. Special thanks also go out to Jack DiSciaccia and Richard (Will) Turner; much of my own scientific approach is modeled on their stellar examples.

To all the other researchers within GLAM: thank you for making the department a pleasant and stimulating place to work, and for always being willing to bounce ideas around and to share your knowledge. Among many, I would especially like to thank Alan Fang, Xinyang Zhang, Erik Kountz in Aharon Kapitulnik's lab, Chris Watson and Yusuke Iguchi in Kam Moler's Lab, and Emily Lindgren in Yuri Suzuki's lab.

To the staff at the Stanford Nano Shared Facilities (SNSF): learning from and working with you has been a huge cornerstone of my graduate school experience. Sharing a building with the SNSF meant that the whole alphabet soup of supporting techniques at my fingertips—TEM, SEM, FIB,

XRD, WDS, AFM, XPS, etc.–but even more importantly it put me in close proximity to the SNSF staff. This talented and passionate group of scientists and technical staff, especially Ann Marshall, Dale Burns, Juliet Jamtgaard, Rich Chin, Arturas Vailionis, Tom Carver, Cliff Knollenberg – was always accessible and incredibly helpful and always willing to lend a hand and offer advice. Outside of my own research, I am especially grateful to Ann Marshall for bringing me into the SNSF family as a student TEM trainer. The experience made it possible for me to learn about a wide range of techniques and research even outside of condensed matter physics, and to become comfortable with all the TEM instrument had to offer.

To the staff at the Stanford Physics Machine Shop, specifically Mehmet Solyalı, Karlheinz Merkle, and Matthew Chuck: thank you for your time and skill, and for the scientific autonomy it afforded me in my research. One of my favorite parts of experimental physics has always been the development of new tools and instruments to make all of the measurements happen. The machine shop staff not only shares my enthusiasm for making stuff, but were always willing to share their techniques, tricks, and tools with new folks like me. The hours I spent at the lathes and mills in the Varian basement were always both productive and enjoyable, regardless of how my research or classes was going that week. I can't thank the machine shop staff enough for their help and support.

To all those who work so hard behind the scenes to keep the GLAM community running at full capacity: I have a profound appreciation for your efforts, and I'm entirely convinced that the department and all of its research would collapse without your support. I interacted most closely with Clora Yeung, Sybille Katz, Margo Holley, Mark Gibson, and Larry Candido, and they always knew how to get things done.

To those who supported my foray into thin-film cuprates and the world of molecular beam epitaxy, including Carolina Adamo at Stanford and the group of Ivan Božović at Brookhaven National Lab: thank you for bringing me into your world and sharing your experience. A special thanks goes out to Anthony Bollinger at BNL; there's no better partner for performing photolithography in a 98°F cleanroom at 1:00 AM.

To the infallible faculty and staff at The National High Magnetic Field Laboratory (NHMFL), including both the DC Field and Pulsed Field facilities in Tallahassee and Los Alamos: thank you for your consistent, impressive efforts to adapt and synthesize high-field techniques, and to share those advances with the users like me. Traveling to the MagLab was always a positive experience—I could always count on excellent equipment and even better technical advice and assistance through all stages of the project. In particular, I would like to thank Franziska Weickert, Marcelo Jaime, Ross McDonald, Fedor Balakirev, Mun K. Chan, Scott Hannahs.

To the x-ray experts working at or collaborating through the Advanced Photon Source at Argonne National Lab: thank you for inviting me into your world, even though I knew very little when I started. In particular, many thanks to Stephan Rosenkranz, Frank Weber, Ayman Said, Ray Osborn, and Matt Krogstad.

To the various collaborators in and around the Stanford Synchrotron Radiation Laboratory: thank you for helping me expand my own understanding of diffraction, ultrafast optics, and ARPES techniques. Specifically I would like to thank David Reis, Jerry Hastings, Yijing Huang, Gilberto de la Peña, Makoto Hashimoto, Donghui Lu, Sudi Chen, Heike Pfau at Stanford, and Nuh Gedik, Alfred Zong, and Anshul Kogar of MIT.

And finally, to my family for supporting me throughout this whole grad school process: thank you for being there for me, even though you definitely thought I was nuts. And to Kristen McKibben: words can't describe how much I appreciate the support you've given me, even as we both went through our ups and downs. I know I can always rely on you for a healthy dose of truth at exactly the right time. I'm not sure where I would be without your love and support.



# Contents

<b>Abstract</b>	<b>v</b>
<b>Acknowledgments</b>	<b>vii</b>
<b>1 Introduction and background</b>	<b>1</b>
1.1 Motivation . . . . .	1
1.1.1 Prevalence of charge order in strongly correlated materials . . . . .	1
1.1.2 Model systems . . . . .	2
1.1.3 Layout of this dissertation . . . . .	3
1.2 Charge Density Waves in Metals . . . . .	4
1.2.1 Microscopies . . . . .	4
1.2.1.1 The Peierls instability . . . . .	4
1.2.1.2 Assumptions, approximations, and caveats . . . . .	7
1.2.2 Effects of quenched disorder on CDWs . . . . .	10
1.2.2.1 Vestigial nematic phases . . . . .	11
1.2.2.2 The Bragg glass phase . . . . .	12
1.2.3 CDWs and superconductivity . . . . .	12
1.2.4 Landau theory of CDWs . . . . .	14
1.3 Rare-Earth Tritellurides . . . . .	16
1.3.1 Crystal and electronic structure . . . . .	16
1.3.2 CDW ground states . . . . .	19
1.3.3 Signatures of the CDW transition . . . . .	21
1.3.4 The second CDW transition . . . . .	24
1.3.5 Disorder in $R\text{Te}_3$ by Pd-intercalation . . . . .	24
1.4 Summary . . . . .	25
<b>2 Experimental methods</b>	<b>27</b>
2.1 Working with $R\text{Te}_3$ . . . . .	27
2.1.1 Synthesis of single-crystal $R\text{Te}_3$ and $\text{Pd}_x\text{ErTe}_3$ . . . . .	27

2.1.2	Crystal characterization and alignment . . . . .	28
2.1.3	Transport measurements . . . . .	28
2.1.4	Electron diffraction . . . . .	30
2.2	Measurements under uniaxial stress . . . . .	31
2.2.1	Generating stress and strain . . . . .	31
2.2.2	Elastoresistivity . . . . .	34
2.2.3	Elastocaloric effect measurements . . . . .	38
2.2.4	Sample mounting . . . . .	42
2.2.5	Strain detection and calibration . . . . .	42
<b>3</b>	<b>Frequency-dependent sensitivity of AC elastocaloric effect measurements explored through analytical and numerical models</b>	<b>45</b>
3.1	Introduction . . . . .	45
3.2	Statement of the problem . . . . .	49
3.3	Exactly soluble models for $\Gamma_b(\omega)$ . . . . .	51
3.3.1	Continuum model . . . . .	51
3.3.2	Discretized model . . . . .	54
3.4	FEM Implementation . . . . .	57
3.5	Results of FEM simulations . . . . .	58
3.5.1	Sample-bath coupling . . . . .	58
3.5.2	Sample-thermometer coupling . . . . .	61
3.6	Results of full simulations . . . . .	64
3.6.1	Material property dependence . . . . .	64
3.6.2	Comparisons to experiment . . . . .	67
3.7	Conclusions . . . . .	71
<b>4</b>	<b>Evidence for realignment of the charge density wave state in <math>\text{ErTe}_3</math> and <math>\text{TmTe}_3</math> under uniaxial stress via elastocaloric and elastoresistivity measurements</b>	<b>73</b>
4.1	Introduction . . . . .	73
4.2	Unidirectional CDWs in a quasi-tetragonal system . . . . .	75
4.3	Experimental Methods . . . . .	78
4.4	Results . . . . .	81
4.4.1	Elastocaloric effect measurements . . . . .	81
4.4.2	Resistivity . . . . .	83
4.4.3	Elastoresistivity . . . . .	87
4.5	Discussion . . . . .	90
4.5.1	Elastocaloric effect . . . . .	90
4.5.2	Resistivity . . . . .	92

4.5.3	Elastoresistivity . . . . .	93
4.6	Conclusions . . . . .	95
4.A	AC capacitance measurements . . . . .	95
4.B	Frequency dependence of ECE measurements . . . . .	97
<b>5</b>	<b>Disorder suppression of CDW order in Pd-intercalated ErTe<sub>3</sub></b>	<b>101</b>
5.1	Introduction . . . . .	101
5.2	Experimental Methods . . . . .	105
5.3	Results and Discussion . . . . .	106
5.4	Conclusions . . . . .	116
<b>6</b>	<b>Concluding Remarks</b>	<b>117</b>
6.1	Current status of uniaxial stress techniques . . . . .	117
6.2	Future outlook for research in the tritellurides . . . . .	118
6.2.1	X-ray diffraction under stress . . . . .	118
6.2.2	Uniaxial stress combined with disorder . . . . .	119
6.2.3	Phonon and electron spectroscopies under stress . . . . .	120
6.2.4	CDW depinning under strain . . . . .	120
6.3	Final remarks . . . . .	121
<b>A</b>	<b>AC Capacitance Measurements</b>	<b>123</b>
A.1	Introduction . . . . .	123
A.2	Autobalancing bridge circuit for capacitance measurements . . . . .	124
A.3	Theory of operation for modulated capacitance . . . . .	126
A.4	Calibration . . . . .	128
<b>B</b>	<b>Details of the RTe<sub>3</sub> Landau Expansion</b>	<b>133</b>
B.1	Setup and definitions . . . . .	133
B.1.1	Terms allowed in the Landau expansion . . . . .	135
B.1.2	Legendre transform to Gibbs ensemble . . . . .	138
B.2	Assembling a model . . . . .	140
B.3	Higher order terms: reintroducing the second CDW . . . . .	144
B.4	Quantifying the tritellurides . . . . .	146



# List of Tables

3.1	Baseline thermal parameters used for the calculations of the AC-ECE. . . . .	57
4.1	Rate of change of critical temperature $T_{CDW1}$ and $T_{CDW2}$ with strain in the strain-induced $\mathbf{q}_a$ state. . . . .	94



# List of Figures

1.1	Schematic diagrams indicating the expected behavior in the standard weak-coupling theory of charge density waves. . . . .	8
1.2	Summary of evidence for CDW-SC competition in the cuprate superconductors. . . .	13
1.3	Crystal and electronic structure of the rare-earth tritellurides . . . . .	17
1.4	Calculation of the real and imaginary parts of the Lindhard response function for $R\text{Te}_3$	20
1.5	Measurements of the phonon energies of $R\text{Te}_3$ through inelastic x-ray scattering . .	22
2.1	Schematic diagrams illustrating the crystal growth process for $R\text{Te}_3$ and $\text{Pd}_x\text{ErTe}_3$ .	29
2.2	Schematic and photograph of the <i>Razorbill</i> CS-100 uniaxial stress cell and the cryostat probe head . . . . .	32
2.3	Schematic of the experimental setup for the AC elastoresistivity technique . . . . .	37
2.4	Expectations in the elastocaloric effect in the vicinity of a second order phase transition.	41
2.5	Schematic of the sample mounting process in the CS-100 uniaxial stress cell. . . . .	43
3.1	Frequency dependent magnitude of the temperature dependent oscillation signal observed in the AC-ECE. . . . .	47
3.2	Low frequency component $\Gamma_b(\omega)$ of the AC-ECE sensitivity in the 1D continuum model.	52
3.3	Discretized model of heat flow in the AC-ECE. . . . .	55
3.4	Geometry of the experimental setup, seen in top (a) and side (b) view. . . . .	56
3.5	Results of FEM simulations of the effects of mounting plates and sample geometry on the AC-ECE sensitivity function . . . . .	59
3.6	High-frequency contributions to the AC-ECE sensitivity function arising from the geometry and material properties of the thermocouple. . . . .	61
3.7	Dependence of the full AC-ECE sensitivity function on frequency and materials parameters . . . . .	65
3.8	Demonstration of the independence of the AC-ECE sensitivity from the ratio of in-plane to out-of-plane thermal conductivity tensor components $k_{xx}$ and $k_{zz}$ . . . . .	66
3.9	Comparison between experimental results of the AC-ECE technique on $\text{Ba}(\text{Fe}_{1-x}\text{Co}_x)_2\text{As}_2$ and the results of full FEM simulation . . . . .	68

3.10	Graphical depiction of an empirical method for estimating the peak sensitivity of the AC-ECE technique based on the shape of the frequency dependence . . . . .	70
4.1	Crystal structure and possible phenomenological phase diagrams for $R\text{Te}_3$ under uniaxial stress. . . . .	76
4.2	Description of the experimental setup for experiments on $R\text{Te}_3$ under uniaxial stress. . . . .	79
4.3	Elastocaloric effect measurements of $\text{ErTe}_3$ under uniaxial stress. . . . .	82
4.4	Elastocaloric effect measurements in $\text{TmTe}_3$ with stress parallel to the $a$ -axis. . . . .	84
4.5	Out of plane resistivity component $\rho_{bb}$ in $\text{ErTe}_3$ as a function of $a$ -axis stress. . . . .	85
4.6	In-plane resistivity components of $\text{ErTe}_3$ as a function of temperature and strain. . . . .	86
4.7	Ratiometric change in $\rho_{aa}$ of $\text{ErTe}_3$ through stress cycles performed at a few representative temperatures. . . . .	88
4.8	Longitudinal elastoresistivity components of $\text{ErTe}_3$ under three different stress orientations, as functions of temperature and PZT voltage. . . . .	89
4.9	Longitudinal $a$ -axis elastoresistivity in $\text{TmTe}_3$ . . . . .	91
4.10	Construction and calibration of the auto-balancing capacitance bridge . . . . .	96
4.11	Frequency dependence of AC-elastocaloric measurements on $\text{ErTe}_3$ under $a$ -axis stress. . . . .	98
5.1	Crystal structure and lattice parameters of $\text{Pd}_x\text{ErTe}_3$ . . . . .	103
5.2	Electron microprobe measurements confirming chemical composition of $\text{Pd}_x\text{ErTe}_3$ . . . . .	107
5.3	In-plane resistivity components of the resistivity of $\text{Pd}_x\text{ErTe}_3$ as a function of $x$ . . . . .	108
5.4	Representative AC magnetic susceptibility of $\text{Pd}_x\text{ErTe}_3$ in and around the superconducting state . . . . .	109
5.5	Complete disorder-temperature phase diagram of single crystal $\text{Pd}_x\text{ErTe}_3$ . . . . .	111
5.6	Electron diffraction patterns of $\text{Pd}_x\text{ErTe}_3$ as a function of disorder and temperature . . . . .	112
5.7	Temperature dependence of the elastic superlattice peak intensity and FWHM for $\text{Pd}_x\text{ErTe}_3$ , $x = 0.023$ . . . . .	115
A.1	Schematic of the capacitance bridge used for detecting oscillating displacements of a capacitance sensor . . . . .	125
A.2	Photograph of the AC-capacitance bridge circuit . . . . .	125
A.3	Characteristic curves for the expected signal from the capacitance bridge. . . . .	128
A.4	Calibration of the AC capacitance bridge for quasi-static capacitors . . . . .	129
A.5	Dependence of AC capacitance bridge signals on the frequency of modulation. . . . .	130
A.6	Temperature dependence of the capacitance modulation of the CS-100 displacement sensor . . . . .	131

# Chapter 1

## Introduction and background

### 1.1 Motivation

#### 1.1.1 Prevalence of charge order in strongly correlated materials

At the risk of oversimplifying a complex and multifaceted field of study, research in condensed matter physics can be characterized as the study of emergent properties. When a large number ( $\approx 10^{23}$ ) of subunits are allowed to interact with each other, the total system can behave in ways which are qualitatively different from the isolated subunit. The properties of the bulk, in this case, becomes more than the just the sum of its parts.[1]

This dissertation focuses on one particular class of emergent phases that can occur when a sea of mobile charge carriers, in concert with the underlying crystal lattice, spontaneously adopts a spatially inhomogeneous configuration which breaks the translational symmetry of the lattice. In particular I will specialize the study to the case of a charge density wave, where the ordered state consists of a consistent modulation of the local charge density with well-defined wavevector. Experimental evidence for the presence of charge density wave order appears in several different forms—periodic lattice modulation, metal-insulator transition, complete softening of a phonon mode—each of which will be discussed at length in Section 1.2. However, not all CDW states exhibit all of these signatures, which points to the fact that there likely is not a single underlying mechanism which can describe all such states.

One example of emergent charge order which is the subject of intense study is found in the high- $T_c$  cuprate superconductors. Less than a decade after the discovery of the high- $T_c$  superconducting state in the cuprates,[2], evidence for short-range charge and spin density wave order was observed in neutron scattering experiments[3]. In particular, the underdoped cuprates exhibit a “stripe” state in which the doped holes organize loosely into conductive chains within the  $\text{CuO}_2$  planes, separated by bands of antiferromagnetic correlations.[3, 4, 5] Short range deviations in the charge order have

since been observed in numerous other probes, including scanning tunneling microscopy[6, 7], nuclear magnetic resonance[8], x-ray scattering[9, 10, 11], and possible evidence a Fermi surface reconstruction has been observed in quantum oscillations[12, 13]. More recently, long-range and three-dimensionally coherent charge density wave order has been observed in several cuprates at high magnetic fields as well as under strain.[14, 15, 16, 17, 18] The ubiquity of charge order in the cuprates is clear, as is the competition between charge order and superconductivity. However, the question of the relevance of broken translational symmetry to the formation of high- $T_c$  superconductor, pseudogap, and the strange metal regions of the phase diagram remains unresolved.

However, besides various types of long- and short-range charge order, the cuprate phase diagram is host to a wide range of competing or coexisting ordered states including magnetic order, superconductivity, and a number of other phenomena including the enigmatic pseudogap. Proposals for other possible phases abound, including intra-unit cell orbital order[19], electronic nematic order of several different flavors[20, 21, 22], topological states[23], and the list goes on. Due to the inevitable interactions between these states, and with the quenched disorder that is implicit as a consequence of chemical substitution, attributing any given experimental result to one of these microscopic mechanisms is challenging.

### 1.1.2 Model systems

Putting aside for a moment issues resulting from the coexistence with other ordered phases[24], the structure of charge order in the cuprates raises some questions of its own. First, short-range charge order in the hole-doped cuprates only occupies a region of the phase diagram characterized by finite doping. As a consequence, charge order in the cuprates always appears in the presence of strong chemical disorder which limits the length scale over which a charge modulation can be coherent. Secondly, the appearance of short-range domains of a unidirectional stripe phase[25] indicates that the charge order also spontaneously and locally breaks the four-fold rotational symmetry of the crystal, at least within a single  $\text{CuO}_2$  plane. Understanding the underlying mechanisms of this sort of charge order, as well as the consequences they have on material properties, is crucial to understanding the interplay between charge order and other degrees of freedom.

One fruitful approach to this problem is to divide and conquer. Specifically, one can study simple “model” materials in which one type of order dominates the phase diagram, existing in isolation or near just one or two other phases. Comparing the characteristics of a given experimental signature in both a strongly correlated material and a simpler, better understood analogue can help to identify—or rule out—the operative degrees of freedom which dictate the appearance and properties of a given ordered state in the more complex material. We wish to find a model material that specifically targets the interaction between unidirectional density wave order on a square lattice and disorder arising from chemical substitution.

Regarding the specific study of charge density wave order, several different families of materials

have been investigated and have, with certain caveats, been described as “model” systems in a variety of circumstances. These include the quasi-1D organic compounds TTF-TCNQ and  $\text{K}_2\text{Pt}(\text{CN})_4\text{Br}_{0.30} \cdot x\text{H}_2\text{O}$ , as well as inorganic chain compounds such as  $\text{NbSe}_3$ [26], and the molybdenum bronzes[27, 28]. Additionally, quite a few members of the family of transition metal dichalcogenides[29, 30] serve as quasi-2D examples of CDW materials, where the CDW wavevectors form parallel to the plane. However, neither of these classes of material can claim to have the same 4-fold symmetry that characterizes the cuprates.

This thesis focuses on one other particular candidate model system—the family of quasi-2D rare-earth tritellurides ( $R\text{Te}_3$ ) for which a unidirectional charge density wave forms on an (almost) square lattice. The objective of this research was to determine the extent to which the rare-earth tritellurides ( $R\text{Te}_3$ ) represent a model system for the study of uniaxial, incommensurate CDW states on a tetragonal or quasi-tetragonal lattice. In particular, I demonstrate evolution of  $R\text{Te}_3$  under the influence of two practical tuning parameters which are relevant to the study of charge order in the cuprates, namely symmetry-breaking uniaxial stress and chemical disorder.

### 1.1.3 Layout of this dissertation

The remaining sections of this chapter review the history and state-of-the-art understanding of charge density wave states in metals from theoretical and experimental perspectives, and then discusses the specific case of the  $R\text{Te}_3$  family. Chapter 2 provides an introduction to and summary of the experimental methods which will be used throughout this work. One particular technique, the AC-elastocaloric effect, is developed in more detail in Chapter 3. Specifically, the frequency-dependent sensitivity of this technique is modeled through analytical and numerical heat flow calculations, providing a basis upon which to evaluate the results of the measurement on a quantitative level. In Chapter 4, the AC-elastocaloric effect and elastoresistivity measurements are performed on  $\text{ErTe}_3$  and  $\text{TmTe}_3$ , together establishing the presence of a strain-induced transition under which the CDW wavevector abruptly rotates  $90^\circ$  within the plane. The evolution of single crystals of  $\text{ErTe}_3$  upon the intercalation of Pd atoms between the layers is described in Chapter 5, and it is shown that Pd acts as a controllable source of chemical disorder and which can completely suppress both of the CDW crossovers in favor of a superconducting ground state. Chapter 6 summarizes the new insights provided by these studies and presents a perspective on future research into the rare-earth tritellurides. The dissertation closes with the inclusion of two appendices: Appendix A describes the design and implementation of a system for measuring fast sinusoidal modulations of a capacitive displacement sensor, and Appendix B contains the fine details of a Landau free energy expansion describing the CDW transitions in  $R\text{Te}_3$ .

## 1.2 Charge Density Waves in Metals

### 1.2.1 Microscopics

The historical development of the theory of charge density wave (CDW) states in metals began as a passing comment in a 1955 textbook by Peierls[31] while evaluating the cohesive energy of a one dimensional metal. Experimental anomalies in the electrical resistivity, magnetic susceptibility, and heat capacity only began to be attributed to CDWs in the mid-1970s[32, 29, 26] In the almost half-century since these discoveries, charge density waves and other variations of charge order have cropped up in a wide variety of materials, many of which do *not* satisfy the assumptions set forth by Peierls. Further study has revealed that not all CDW states arise from the same mechanisms, although much of the early terminology persists in the modern literature. This section begins with a brief summary of ideas on which humanity's understanding of the CDW phase was founded, but which seem to hold only for precious few experimental cases. The discussion then turns to a modern understanding of the physics of CDW phases, in which several of the founding assumptions are challenged.

#### 1.2.1.1 The Peierls instability

Consider a gas of electrons which are free to move along one dimension.[33] Breaking the translational symmetry by introducing a sinusoidal potential with an arbitrarily small amplitude  $V$  and period  $2a$  generates discontinuities in the electron dispersion for at wavevectors  $k = \pm\pi/a$ , creating bands of allowed electron energies separated by gaps of forbidden energies. This basic observation is a common starting point for the understanding of electronic band theory. Peierls noticed in 1955, however, that one need not always impose the sinusoidal potential externally in order to cause the formation of gaps; under certain circumstances, a periodic distortion may form spontaneously, generating an electronic bandgap in the process. In particular, he described the case of a half-filled metal in one dimension. In this case, the Fermi surface (FS) consists of two points in  $k$ -space which we label as  $\pm k_F$ . Peierls noted that a periodic distortion of the density of the electron gas with wavevector  $2k_F$  would open gaps at both  $\pm k_F$  and decrease the total electronic energy; electrons in states near  $k_F$  are pushed down in energy to form the valence band of a new band insulator. At the same time, the rearrangement of the electrons into this new state will exert a force on the underlying atomic lattice of the 1D metal. Assuming the lattice began in stable equilibrium, the displacement will to leading order cost an amount of energy quadratic in the amplitude of the distortion. However, by integrating the total energy gain of the electrons, it can be shown that a one dimensional metal can never be stable: any small distortion at wavevector  $2k_F$  produces an insulator with lower total energy.

We can place this argument on a firmer theoretical footing through a simple mean-field model. Roughly following the terminology defined in Ref. [34], we consider a jellium model in which the lattice is described by a uniform positive charge background upon which a gas of electrons with equal

and opposite charge is free to move. Working in reciprocal space, an external potential  $\phi_e(\mathbf{q})$  will induce deviations in the uniform charge density  $\rho(\mathbf{q})$  given by

$$\rho_i(\mathbf{q}) = \chi(\mathbf{q})(\phi_e(\mathbf{q}) + \phi_i(\mathbf{q})) \quad (1.1)$$

where  $\chi(\mathbf{q})$  is the electronic susceptibility, and  $\phi_i(\mathbf{q})$  is the potential induced by  $\rho_i(\mathbf{q})$ , and the two are assumed to be related by

$$\phi_i(\mathbf{q}) = -g\rho_i(\mathbf{q}) \quad (1.2)$$

where  $g$  is a coupling constant. Solving Eqs. (1.1) and (1.2) self-consistently for  $\rho_i(\mathbf{q})$  results in

$$\rho_i(\mathbf{q}) = \left( \frac{\chi(\mathbf{q})}{1 + g\chi(\mathbf{q})} \right) \phi_e(\mathbf{q}). \quad (1.3)$$

From this we can see that the induced charge density  $\rho_i(\mathbf{q})$  will become unstable if  $g < 0$  such that

$$1 + g\chi(\mathbf{q}) = 0. \quad (1.4)$$

Further progress requires an explicit formula for  $\chi(\mathbf{q})$ . The susceptibility for electronic bands with dispersion  $\epsilon_{\mathbf{k}}$  can be described in  $d$  dimensions by the Lindhard response function[35]

$$\chi(\mathbf{q}) = \int \frac{d\mathbf{k}^d}{(2\pi)^d} \frac{f_{\mathbf{k}} - f_{\mathbf{k}+\mathbf{q}}}{\epsilon_{\mathbf{k}} - \epsilon_{\mathbf{k}+\mathbf{q}}} \quad (1.5)$$

where  $f_{\mathbf{k}}$  is the Fermi distribution  $f_{\mathbf{k}} = (1 + \exp[(\epsilon_{\mathbf{k}} - \epsilon_F)/k_B T])^{-1}$  and where  $\epsilon_F$  is the Fermi energy,  $k_B$  is Boltzmann's constant. In  $d = 1$  and taking  $q = 2k_F$  in reference to Peierls's original arguments, Eq. (1.5) evaluates

$$\chi(2k_F, T) = -e^2 n(\epsilon_F) \log\left(\frac{1.14\epsilon_0}{k_B T}\right) \quad (1.6)$$

where  $e$  is the elementary charge,  $n(\epsilon_F)$  is the density of states at the Fermi energy, and  $\epsilon_0$  is an arbitrary cutoff energy usually taken as  $\epsilon_F$ . The salient feature of the susceptibility is a logarithmic divergence toward  $T = 0$ . Inserting Eq. (1.6) into Eq. (1.4) we can establish a mean field transition temperature  $T_{MF}$  at which the state with uniform charge density becomes unstable

$$k_B T_{MF} = 1.14\epsilon_0 \exp\left(\frac{-1}{gn(\epsilon_F)}\right) \quad (1.7)$$

Continuing in a mean-field approximation, we can also calculate the electron-phonon coupling (EPC) constant  $g$  from a fixed-ion approximation. In second quantized notation, we can describe the

instantaneous lattice displacement  $u(x)$  as

$$u(x) = \sum_q \sqrt{\frac{\hbar}{2NM\omega_q}} (b_q + b_{-q}^\dagger) e^{iqx} \quad (1.8)$$

where  $N$  is the number of lattice sites per unit length,  $M$  is the ionic mass,  $\omega_q$  is the phonon dispersion, and  $b_q$  and  $b_q^\dagger$  are the phonon annihilation and creation operators, respectively. The interaction term between electrons and phonons then depends on the ionic potential  $V(r)$  as

$$H_{EPC} = \sum_{k,k',l} \langle k|V(r-l-u(x))|k'\rangle a_k^\dagger a_{k'} \quad (1.9)$$

where  $l$  represents the coordinates of the idealized atomic lattice sites. Assuming that the lattice displacements are small, the EPC term can be rewritten as

$$H_{EPC} = \sum_{k,q} g_q (b_{-q}^\dagger + b_q) a_{k+q}^\dagger a_k \quad (1.10)$$

where

$$g_q = i \sqrt{\frac{\hbar}{2M\omega_q}} |q| V_q \quad (1.11)$$

and  $V_q$  is defined as the Fourier transform of  $V(r)$

While we have thus far focused on the effect of the phonons on the electronic degrees of freedom, the electrons also exert a back-reaction on the phonon spectrum. On very general grounds, W. Kohn demonstrated in 1959[36] that the presence of both a Fermi surface of any shape and any finite electron-phonon coupling matrix element implies that the abrupt change in electronic screening will always lead to a sharp feature in the phonon dispersion at  $2k_F$ , even in the absence of nesting or incipient CDW order. This ‘‘image’’ of the Fermi surface in the phonon spectrum arises due to the abrupt change in the ability of the electron gas to screen oscillations with  $k > 2k_F$ . As one approaches a CDW phase transition, however, this effect is amplified the renormalization becomes increasingly extreme until a phonon mode at the ordering wavevector softens completely to zero.

To see how this Kohn anomaly develops, consider the charge density response to an ionic potential in the same spirit as Eq. (1.1)

$$\rho_q = \chi(q) g \sqrt{\frac{2M\omega_Q}{\hbar}} Q_q \quad (1.12)$$

where  $Q$  is a generalized phonon coordinate and it has been assumed that  $g_q = g$  is momentum independent. This density fluctuation becomes an effective potential in the equations of motion for  $Q_q$ , and one can show that the interaction leads to a renormalized phonon frequency  $\omega_{\text{ren},q}$  given by

$$\omega_{\text{ren},q}^2 = \omega_q^2 + \frac{2g^2\omega_q}{\hbar} \chi(q) \quad (1.13)$$

It can therefore easily be seen that if  $\chi(q)$  diverges, the renormalized phonon frequency will eventually vanish. The point at which the phonon frequency reaches zero defines a phase transition to a CDW state in which the lattice adopts a fixed distortion at that characteristic wavevector. Using the 1D Lindhard susceptibility Eq. (1.6) for  $\chi(q)$ , this produces the same condition as Eq. (1.7)

$$k_B T_{MF} = 1.14 \epsilon_0 e^{-1/\lambda} \quad (1.14)$$

where the dimensionless electron-phonon coupling constant  $\lambda$  is defined as

$$\lambda = \frac{g^2 n(\epsilon_F)}{\hbar \omega_{2k_F}} \quad (1.15)$$

### 1.2.1.2 Assumptions, approximations, and caveats

Having established this formalism, it is prudent to step back and address some of the assumptions and approximations which have been implemented, in order to predict which realistic cases might be explained using this model. We begin with a discussion of the Lindhard susceptibility. The first and most limiting assumption made in the development of this theory is the choice of  $d = 1$ . A comparison of Eq. (1.5) for  $d = 1, 2$ , and  $3$  is shown in Fig. 1.1(d) for the case of a circular or spherical Fermi surface (FS). The idealized  $d = 1$  case exhibits a logarithmic divergence, but neither  $d = 2$  nor  $d = 3$  exhibits even a local maximum near  $2k_F$ . This is a consequence of the sharply reduced area over which any given wavevector nests the FS. In principle, a FS which does exhibit finite regions which are well nested could show an enhancement of  $\chi(\mathbf{q})$  at the nesting wavevector, but unless the nesting covers the entire FS, the divergence will always be rounded and peak at a finite value. Already, we anticipate problems in applying this simple theory to strongly correlated materials which exhibit quasi-2D layered structures.

The *strictly* one-dimensional Peierls transition, as it was originally described, is an entirely academic affair for two reasons. In practice, no material is ever truly one-dimensional, but rather consists of a bundle of 1D chains. Secondly, even if such a 1D material could be engineered, the reduction of phase space will cause fluctuations to overwhelm any incipient ordered state at any finite temperature. However, each one of these “problems” turns out to be the solution to the other, and together they lend some practical credence to the Peierls transition. True long-range order requires some finite coupling in at least two spatial dimensions—that is, interchain or interplane interactions—in order to become stable. Consider a set of loosely-coupled quasi-1D metallic chains with interchain CDW coupling  $t_\perp$ . For  $k_B T \gg t_\perp$ , the chains will all behave independently—as the temperature decreases, the correlation length within a given chain will grow, but never diverge to form long-range order. At some crossover temperature  $k_B T_{3D} \sim t_\perp$ , however, the interchain correlations become relevant and the correlation lengths both parallel and perpendicular to the chains diverge as the system enters a long-range CDW state.

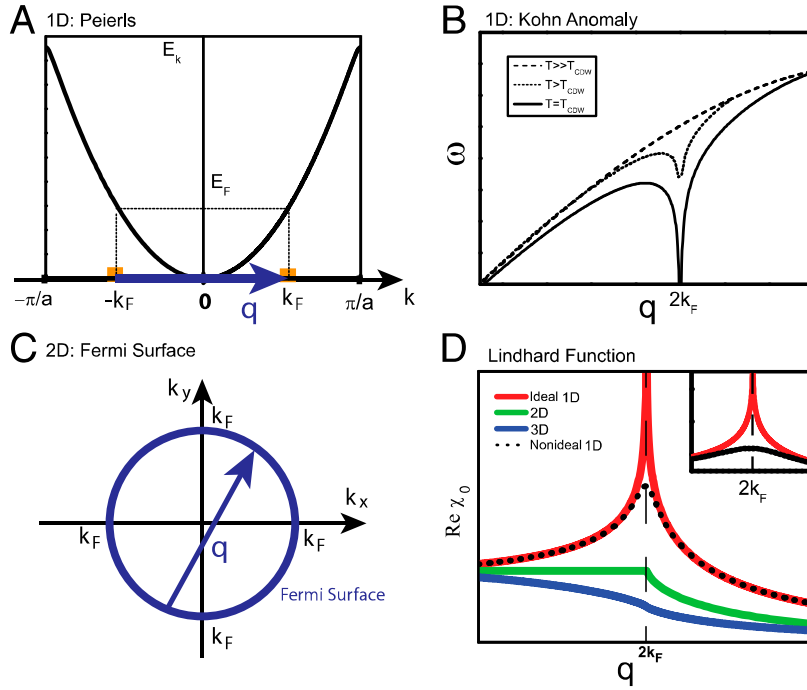


Figure 1.1: Schematic diagrams indicating the expected behavior in the standard weak-coupling theory of charge density waves. (a) Dispersion relation for nearly free electrons. The Fermi surface consists only of two points,  $\pm k_F$  which are perfectly nested by the wavevector  $q$ . (b) Dispersion relation of an acoustic phonon in a charge density wave material. As the temperature decreases toward  $T_{\text{CDW}}$ , the phonon spectrum is sharply renormalized to lower frequencies (“softened”) at the nesting wavevector. (c) Fermi surface for nearly free electrons in two dimensions. In this circular Fermi surface, the wavevector  $q$  only nests diametrically opposed points rather than the entire FS. (d) Calculation of the Lindhard response function for nearly free electrons for different dimensionality. The logarithmic divergence at the nesting vector drives the CDW transition in the ideal 1D case, while no such divergence exists for 2D or 3D. In practice, even in quasi-1D materials, the divergence is always rounded. Figure reproduced from Zhu et al, “Classification of charge density waves based on their nature”. *Proc. Natl. Acad. Sci. U. S. A.* **112**, 2367–71 (2015)

Even if a region of the Fermi surface can be described by a quasi-1D band which is convincingly well-nested, however, there are further limitations to the applicability of the Lindhard susceptibility. The original formulation of the Lindhard susceptibility arose from a self-consistent field approach, which provides the same results of the more modern random phase approximation (RPA) of the interacting electron gas in many-body theory.[37] Both of these approximations rely on the assumption of a high density electron gas such that the kinetic energy is dominant and that the electron-electron Coulomb interaction is heavily screened. Again, we can anticipate this to cause problems in applying the formulae presented above to charge order strongly correlated materials—for example, the “normal” state of the cuprates out of which both high- $T_c$  superconductivity as well as the stripe-ordered states emerge, is most succinctly represented as a doped antiferromagnetic Mott insulator. The localized Cu  $3d$  orbitals cost an enormous ( $\approx 2$  eV) on-site Hubbard  $U$  in order for two electrons to occupy the same lattice site. Even the eternal optimist would be hard-pressed to describe the electron-electron interaction in such a material as “well-screened”.

Additionally, the simple mean-field treatment assumed from the start that the Lindhard response function is a strictly real quantity. This is justified by the observation that a divergence in the real part of the Lindhard susceptibility is indeed a sufficient condition for a CDW instability. In reality, however, the degree to which the FS is well nested at a particular  $q$  is directly reflected in the  $\omega \rightarrow 0$  limit of the *imaginary* part of  $\chi(q)$ [38] and contributes to the real part only indirectly. DFT calculations[39, 40] for NbSe<sub>2</sub>, CeTe<sub>3</sub>, and even an idealized 1D chain of sodium atoms, however, show quite clearly that while partial nesting does create maxima in  $\Im[\chi(q)]$ , this does not at all imply the existence of a maximum anywhere near the nesting wavevector in  $\Re[\chi(q)]$ . As a consequence, it is apparent that the Lindhard response function, which takes only the electronic structure as its input, misses some important piece of physics for the formation of a CDW state.

By now it is clear that while the Peierls picture of CDW formation provides attractive intuition, experimental results show that real CDW states are not so simple. In some cases, the theory predicts experimental signatures which are not observed. For instance, several CDW materials (including NbSe<sub>3</sub>, TTF-TCNQ, BaVS<sub>3</sub>[41]) exhibit either only a partial phonon softening or no evidence of a Kohn anomaly at all, despite exhibiting clear periodic modulations of the charge density below a certain temperature. Similarly, the Peierls standard formally corresponds to a metal-insulator transition—while the opening of a CDW tends to increase the resistivity just below the CDW transition, many materials continue to display metallic behavior down to low temperatures.

On the other hand, the conventional weak-coupling theory also predicts the *absence* of signatures which are, in fact, detected. The susceptibility  $\chi(q)$  for an imperfectly nested FS in two or three dimensions, for instance, should not diverge strongly enough to trigger an electronic instability. The most prominent counterexamples are the quasi-2D transition metal dichalcogenides which present a variety CDW arrangements, and the hole-doped cuprates, where the closest approximation to nesting exists between antinodal regions of a nearly circular hole-like FS. It can also be shown that

the mean field theory presented above shares many mathematical features with the BCS theory of superconductivity[34], and that the magnitude of the CDW gap  $\Delta$  and the critical temperature  $T_{\text{CDW}}$  ought to be related by

$$2\Delta \approx 3.52k_B T_{\text{CDW}} \quad (1.16)$$

and a similar relation between  $T_{\text{CDW}}$  and the size of the jump in heat capacity  $\Delta C$  is given by [42]

$$\Delta C \approx 10.2k_B^2 T_{\text{CDW}} N(0) \quad (1.17)$$

where  $N(0)$  is the density of states. In quite a few materials, however, both the gap and the specific heat anomaly are far too large, by factors of 5-15.[43, 44] This may suggest that  $T_{\text{CDW}}$  is significantly suppressed below the mean-field value by fluctuations, but several strongly coupled theories have also been proposed. [43, 42]

Furthermore, experimental signatures such as phonon softening, when a Kohn anomaly is present, occasionally also display qualitatively different behavior from the weak-coupling limit. For example, it has recently been observed in NbSe<sub>2</sub>[45] and TbTe<sub>3</sub>[46] that the phonon dispersion collapses to zero energy over a finite range of  $k$ -space, rather than simply at a single point at  $q_{\text{CDW}}$ . The larger the region of reciprocal space over which phonons are able to contribute to the condensate by forming electron-hole pairs, the shorter the real space correlation length must be. [43, 42] Comparisons of the phonon lifetimes near this extended Kohn anomaly suggest that the electron phonon coupling constant  $\lambda$  is in fact strong as well as strongly momentum dependent, a feature which is neglected in the mean-field treatment above.

### 1.2.2 Effects of quenched disorder on CDWs

Within an incommensurate CDW state in a pristine system, all positions of peaks and troughs of charge density relative to the crystal lattice are equally likely. The phase of the complex CDW order parameter can take any value, and therefore a gapless Goldstone boson known as a ‘‘phason’’ arises from the  $U(1)$  character of the broken translational symmetry. The presence of a single point defect, however, lifts the degeneracy and opens a gap in the phason dispersion. Additional point defects, unless they differ in position by some integer multiple of the incommensurate wavevector  $\mathbf{q}$ , will generically frustrate the CDW by preventing true long-range phase coherence.

In a conventional uniform metal, a point defect will always nucleate Friedel oscillations in the charge density as a consequence of imperfect screening of potential components at and above the Fermi wavevector. If this metal also displays a CDW instability at low temperatures, then the lattice itself will also tend to respond with oscillations at the CDW wavevector.[47]. The qualitative structure of a disordered CDW depends, however, on the strength and sharpness of the disorder potential. These define how well the local CDW phase is ‘‘pinned’’ to the defect location. In the limit of strong pinning, the CDW phase is such that the maximum or minimum of the charge density (depending

on the sign of the potential) is centered on the defect, and the density wave distorts elastically to accommodate the positions of all of the defects. In the opposite limit of weak pinning, none of the defects alone can dictate the phase individually. Rather, long-wavelength distortions of the phase arise from the collective effect of multiple randomly-positioned defects.[48, 49]

Looking at the disordered CDW on a larger scale, however, there are several subtly different types of phases into which a CDW could reorganize in response to disorder.

### 1.2.2.1 Vestigial nematic phases

One aspect of uniaxial density wave states which has attracted significant recent attention is the composite nature of the order parameter.[50, 51, 52] Consider a simple example of a two-dimensional material with tetragonal symmetry. In order for an incommensurate, uniaxial density wave state to form in this material, two symmetries must be broken. The first is translational symmetry, which is related to local phase of the density wave. Since we're considering only incommensurate density waves, states with any possible local phase referenced to the lattice are degenerate, so this component is considered to have  $U(1)$  character. The second symmetry is rotational symmetry, which is lowered from a fourfold rotation to a twofold rotation upon entering the density wave state. Given the two possible in-plane orientations of the ordering wavevector, this component has  $Z_2$  (Ising) character.

In principle the two symmetries are not *required* to break simultaneously, although this can be the case. Starting from a long-range-ordered uniaxial CDW ground state and increasing the temperature, these different components can melt at different temperatures. The intervening phases between pristine CDW and the uniform,  $C_4$  symmetric metal are known as “vestigial” phases, and an extensive theoretical framework has been developed to study their properties.

In the restricted case of incommensurate charge density waves in a tetragonal material, each orientation of the density wave can be described by a complex scalar order parameter. The  $U(1)$  translational order component belongs to the same universality class as the XY model of local moments constrained to a plane but with full rotational symmetry in this plane. This model has lower critical dimension  $d_c = 2$ — true long-range order can only occur in  $d \geq 3$ . However, this only applies for the ideal case with no disorder; the addition of arbitrarily weak disorder formally disrupts long-range order for continuous order parameters in *any* dimension less than 4.[53]

This theorem does not apply to the case of order parameters which break discrete symmetries, such as the  $Z_2$  rotational component. Consider for example a transition in the same universality class as the Ising model. The critical exponent for the correlation length  $\xi \propto |T - T_c|^{-\nu}$  takes the value  $\nu \approx 0.63$  in  $d = 3$ [54]. Violation of the Harris criterion[55] ( $d\nu < 2$ ) indicates that the critical behavior will be renormalized by weak disorder, but in this case a sharp thermodynamic phase transition is still allowed to occur up to a finite disorder strength.[56]

This qualitative discrepancy in the responses of the translational and rotational components of the incommensurate CDW order parameter to disorder sets the stage for the exploration and control

of vestigial phases as a function of disorder. In this particular case, a phase which breaks rotational symmetry but preserves translational symmetry is known as a "vestigial nematic" phase. It should be remembered, however, that the absence of long-range translational order does not imply that the vestigial nematic state *locally* preserves translational symmetry; short-range CDW correlations still dominate the microscopic structure, but the strength of the correlation falls exponentially with distance. Despite the loss of CDW order, however, the vestigial nematic state will still be bounded by a thermodynamically sharp phase transition and all the accompanying experimental signatures.

### 1.2.2.2 The Bragg glass phase

Another subtle variation on the theme of "melting" stripe order is the possibility of a so-called "Bragg glass" phase. This was first conjectured in the context of the arrangement and motion of vortices in the intermediate state of type II superconductors in the presence of weak disorder[57], but which is expected to hold in general for any complex scalar order parameter.

If weak disorder is introduced into a complex scalar order parameter field  $\Delta(x) = |\Delta(x)|e^{i\phi(x)}$ , Imry and Ma[53] have already shown that true long-range phase order ( $\langle\phi(0)\phi(\mathbf{x})\rangle \sim \text{const}$  as  $|\mathbf{x}| \rightarrow \infty$ ) cannot exist. However, if the disorder is weak enough and only generates vortex-antivortex pairs rather than unpaired vortices, then a quasi-long-range phase-ordered phase ( $\langle\phi(0)\phi(\mathbf{x})\rangle \sim |\mathbf{x}|^a$  as  $|\mathbf{x}| \rightarrow \infty$ ) may still persist. Similar to the vestigial nematic phase, this phase should also be bounded by sharp transitions. However, the glassy behavior will also lead to a strong slowing-down of the critical fluctuations and loss of equilibrium as one approaches the glass transition.[24]

### 1.2.3 CDWs and superconductivity

As mentioned briefly in Section 1.2.1.2, the weak coupling theory presented in Section 1.2.1.1 is mathematically equivalent to the BCS theory of superconductivity.[58] In this sense, a CDW phase can be considered as a condensation of electron-hole pairs with finite momentum, rather than a  $\mathbf{q} = 0$  pair of two electrons, as is observed in superconductors. In both cases, however, both the CDW and SC ground states rely on having sufficient density of states at the Fermi level and a sufficiently strong electron-phonon interaction. As a consequence, many materials which exhibit CDW order have also been found to host superconducting ground states either natively or under an external perturbation such as pressure or disorder.

One particularly clear example of superconductivity arising as charge order is suppressed occurs in the isoelectronic alloy system  $2\text{H-TaSe}_{2-x}\text{S}_x$  for which  $x$  can be continuously tuned between the  $\text{TaSe}_2$  and  $\text{TaS}_2$  end members.[59]. As one moves away from either end point and the disorder increases, the superconducting critical temperature  $T_c$  increases sharply to approximately 3 K. Simultaneously, signatures of the CDW phase transition weaken. Isoelectronic substitutional disorder exerts strong scattering forces on the CDW order, limiting the correlation length. However, as the disorder does not break time-reversal symmetry, Anderson's theorem[60] dictates that  $T_c$  will be largely unaffected.

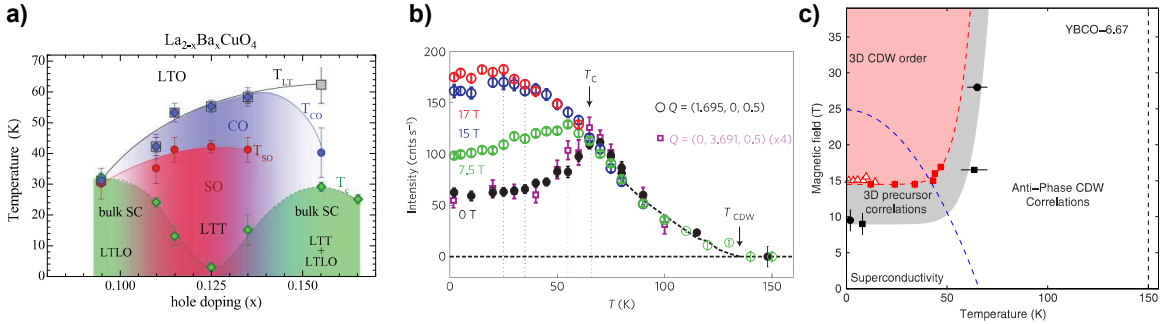


Figure 1.2: Summary of experimental evidence for CDW-SC competition in the cuprate superconductors. (a) Phase diagram of  $\text{La}_{2-x}\text{Ba}_x\text{CuO}_4$  in proximity to the phase diagram. The deep suppression of the superconducting critical temperature corresponds to the region where charge order becomes most stable, which seems to indicate competition between the two phases. Reproduced from Hücker et al *Phys. Rev. B* **83**, 104506 (2011), used with permission of the American Physical Society. (b) X-ray scattering intensity at the superlattice peak corresponding to charge order in  $\text{YBa}_2\text{Cu}_3\text{O}_{6.67}$  (YBCO). Upon entering the superconducting state below  $T_c$ , charge order is suppressed. Conversely, suppressing superconductivity with magnetic field allows the CDW correlations to strengthen once more. Reprinted by permission from Springer Nature Customer Service Centre GmbH: Springer Nature, Chang et al, *Nat. Phys.* **8**, 871–876 (2012). (c) Temperature-magnetic field phase diagram of YBCO. Not only does suppressing superconductivity with field enhance charge order, but it in fact uncovers a qualitatively different 3D CDW phase. Reproduced from Chang et al, *Nat. Commun.* **7**, 11494 (2016) under the terms of the Creative Commons Attribution 4.0 International License, <https://creativecommons.org/licenses/by/4.0/>

Disorder, therefore, simply paves the way for the superconducting state by preventing formation of a CDW gap, preserving significant density of states at the Fermi level for the formation of a superconducting condensate.

Similar results have also been observed in  $\text{Cu}_x\text{TiSe}_2$ [61] in which the introduction of copper intercalation between the planes of the quasi-2D structure suppresses charge order in favor of a dome of superconductivity. In this system, the  $x = 0$  parent compound hosts a commensurate CDW, but for  $x \gtrsim 0.04$  the wavevector has been shown to become incommensurate.[62] The onset of an incommensurate structure coincides with the onset of a superconducting ground state, indicating a possible relation between the two. The dome-like phase diagram also raises the question of whether quantum critical CDW fluctuations might even contribute to the pairing interaction in this system, though that is currently contentious.

However, the most heavily studied case of SC-CDW competition in recent years has been the superconducting cuprates. The competition between these two ordered states is most striking in the phase diagram of  $\text{La}_{2-x}\text{Ba}_x\text{CuO}_4$ . In this material, the superconducting dome is nearly split in two. The minimum in  $T_c$  appears for roughly the same carrier concentration as where the charge order is most stable. Additionally, x-ray scattering measurements of  $\text{YBa}_2\text{Cu}_3\text{O}_{6.67}$  have shown that upon entering the superconducting state, charge order is significantly suppressed. Suppressing

superconductivity with a large magnetic field, however, allows the CDW to return to its original amplitude.

One recent proposal for the outcome of the CDW-SC competition is the appearance of spatially inhomogeneous “fragile” order.[63] Disorder- or field-induced spatial inhomogeneities in one order parameter can therefore become host to small regions of the other ordered phase, provided the correlation lengths and condensation energies of both phases conspire to make such an arrangement energetically favorable. For example, the nucleation of small bubbles of charge order in the vortex cores of the superconducting state in the  $\text{Bi}_2\text{Sr}_2\text{CaCu}_2\text{O}_{8+\delta}$  has been observed in scanning tunneling microscopy (STM)[6, 7]. The opposite case, in which superconductivity can arise within a disorder-induced dislocation of the CDW, is also possible in principle.

When superconducting vortices are sparse, the CDW correlations within the core are effectively isolated from those of the nearest vortex. As the vortex density grows, however, so does the coupling between the CDW bubbles—at a some critical value of the density, long-range interactions between CDW pockets can give rise to an ordered phase. Here again, as in the case of any incommensurate CDW in the presence of arbitrarily weak disorder, a fully phase-coherent CDW state is forbidden on general grounds, but a nematic component may still be allowed to exist. This variation has been called a “fragile nematic” [63] due to the relatively weak long-range interactions between individual CDW pockets. The dual phase of a “fragile superconductor” can also appear in approaching the crossover from the opposite limit, where a small bubble of superconductivity can nucleate at a dislocation of the CDW, and a Josephson coupling between nearby bubbles mediates an ordering transition. The high-field phase diagram of the cuprates is flush with examples of CDW order emerging as superconductivity is suppressed with magnetic field[14, 64, 15, 17], many of which appear to demonstrate a temperature-field phase diagram consistent with this picture.

#### 1.2.4 Landau theory of CDWs

As with many other symmetry-breaking phase transitions, much of the basic structure of the phase diagram can be understood from a free energy expansion near the critical point. In this approach, one regards the order parameter phenomenologically, ignoring the microscopic mechanisms which may or may not instigate the phase transition, and explores the importance of various symmetry-allowed combinations and powers of this order parameter. Such approaches are valid in the vicinity of the transition only, but often contain valuable information regarding the behavior of a particular system. Free energy expansions for CDW phases have been studied in great detail. This section follows the definitions proposed by McMillan[65].

The order parameter for a uniaxial charge density wave is taken to be a complex quantity

$$\psi_1(\mathbf{r}) = |\psi_1(\mathbf{r})|e^{i\phi_1\mathbf{r}} \quad (1.18)$$

which corresponds to the physically observable charge density  $\rho(\mathbf{r})$  given by

$$\rho(\mathbf{r}) = \rho_0 (1 + \alpha(\mathbf{r})) \quad (1.19)$$

where  $\alpha = \Re[\psi_1(\mathbf{r})]$ .

Treating the phase  $\phi_1(\mathbf{x})$  as a spatially varying parameter requires the expansion of a nonuniform free energy *density*  $f(\mathbf{r})$  rather than a single macroscopic free energy. Effects of spatially varying coefficients (which must have the periodicity of the underlying crystal lattice) must also be considered, and the total free energy to be minimized is the integral of  $f(\mathbf{r})$  over all space.

The simplest allowed terms in the expansion for this free energy density are of the form

$$f_1(\mathbf{r}) = a_i(\mathbf{r})\alpha^i(\mathbf{r}) \quad (1.20)$$

where  $i$  in principle runs from 1 to infinity. The term for  $i = 1$  must vanish; retaining this term means that the charge density can consistently lower its energy by adopting charge density waves at the periodicity of the lattice and with ever-increasing amplitudes. All other terms for  $i \neq 1$  are allowed, although including only  $i = 2, 3, 4$  suffices for most calculations.

In long-range ordered CDW state, variations in the charge density propagate in space with a wavevector  $\mathbf{q}$ , the direction and magnitude of which stems from microscopic details of the electronic structure and electron-phonon interaction, as described above. The wavevector can be included as a phenomenological parameter through the introduction of gradient terms of the form

$$f_2(\mathbf{r}) = c(\mathbf{r}) |(\mathbf{q} \cdot \nabla - iq^2)\psi_1|^2 + d(\mathbf{r}) |\mathbf{q} \times \nabla\psi|^2 \quad (1.21)$$

where  $q = |\mathbf{q}|$ . These terms together describe the energetic cost of states in which the wavevector differs in either magnitude or direction from the ideal value.

The discussion above assumed the simple case of a single CDW wavevector. In real materials such as the transition metal dichalcogenides there are up to three independent wavevectors, usually pointing along symmetry-equivalent directions. Aside from the trivial terms which copy the single-wavevector case but alter the direction or magnitude of the wavevector, non-orthogonal CDW wavevectors can also give rise to quartic interaction and phasing terms of the form  $|\psi_i\psi_j|^2$ . If the two wavevectors  $\mathbf{q}_i$  and  $\mathbf{q}_j$  are not orthogonal, these terms define the locations of the maxima and minima in the charge density relative to the underlying lattice. The magnitude of the biquadratic terms can also control whether the system condenses into a state with a single CDW or with multiple CDWs.

The simplest case arises when  $\mathbf{q}$  is incommensurate with the lattice and the lattice is free of disorder. In this case, the integral of the free energy density over all space causes all but the constant component of the coefficients  $a_i(\mathbf{r})$  to vanish. Furthermore, any odd powers of the order parameter

must also average to zero, and the gradient terms will favor a state exhibiting a homogeneous value of the wavevector  $\mathbf{q}$ . The total free energy therefore collapses to a single scalar in the same way as a spatially uniform order parameter such as a ferromagnet is often described. The phase transition between the normal metal and the incommensurate CDW occurs when the quadratic coefficient  $a_2$  changes from positive to negative.

In the case of a nearly commensurate wavevector, however, the situation becomes more complicated. In particular, it may become favorable for the wavevector to deviate slightly in the direction or magnitude of  $\mathbf{q}$  (costing energy related to the gradient terms of Eq. (1.21)) in order to gain energy arising from one of the  $a_i$  terms for odd  $i$ . For example, if  $|\mathbf{q}| \approx |\mathbf{G}|/3$  for some reciprocal lattice vector  $\mathbf{G}$ , then the cubic  $a_3$  term no longer vanishes when integrated over space. This condition can lead to a “lock-in” transition from an incommensurate to a commensurate CDW.

The effects of disorder can be included with the introduction of a spatially inhomogeneous potential term  $U(\mathbf{r})$ , which can be described differently depending on the strength of the CDW-impurity pinning forces. In the limit of strong pinning, one can consider a delta function potential corresponding to an isolated point defect. McMillan[65] showed that at the level of the Landau expansion, a single impurity will nucleate a region of CDW correlations even in the normal state above  $T_{CDW1}$ . However, the problem of more general types of disorder usually require recourse to more involved techniques from many-body theory[48, 47, 50] which will not be discussed here.

## 1.3 Rare-Earth Tritellurides

### 1.3.1 Crystal and electronic structure

The rare-earth tritelluride crystal structure consists of an alternating pattern of 2D layers. The active, metallic component consists of a Te bilayer, consisting of a pair of nearly square Te nets, which alternates with an insulating, buckled, rock-salt monolayer of  $R\text{Te}$ . [72] The latter is often referred to as the “slab” layer. The  $R\text{Te}_3$  structure is slightly orthorhombic. [73] This symmetry does not arise from the layers themselves: the homologous structure  $R\text{Te}_2$ , which includes a monolayer of Te rather than a bilayer but otherwise shares the same structural components, exhibits true tetragonal symmetry. However, the second Te net prevents two  $R$  Te slabs from aligning perfectly. Instead, one must be shifted by half of a unit cell along either of the in-plane axes. Empirically, the preferred stacking is for all of the offsets to align with the same axis, producing a glide plane and breaking the degeneracy. Crystallographic convention defines the out-of-plane axis as the  $b$  axis in this space group, with  $a$  and  $c$  in the plane. The glide operation runs parallel to the  $c$ -axis, which is the longer of the two ( $c = 1.001a$ ).

The rare-earth tritellurides can be viewed as a member a much larger class of crystal structures. Quite a few chalcogenide materials contain a structural motif which is derived from square monolayer nets, including the prototypical structures of  $\text{NdTe}_3$ ,  $\text{GdPS}$ ,  $\text{ZrSiS}$ ,  $\text{NbSe}_3$ ,  $\text{K}_{0.33}\text{Ba}_{0.67}\text{AgTe}_2$ , and

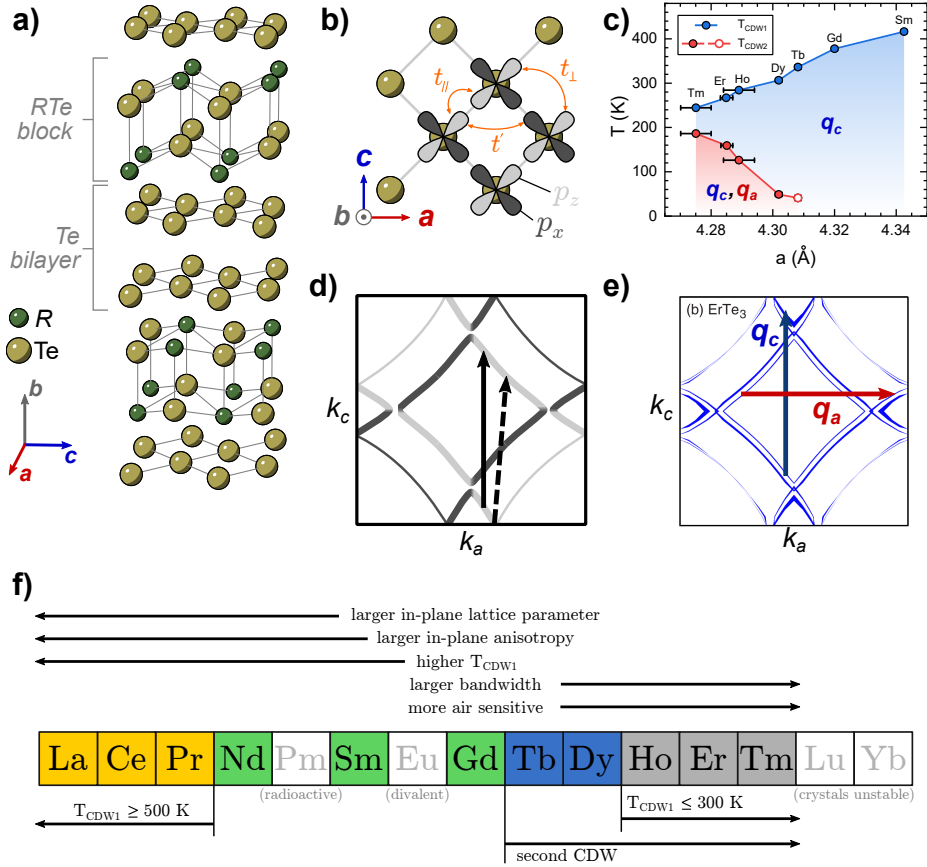


Figure 1.3: Crystal and electronic structure of the rare-earth tritelluride ( $R\text{Te}_3$ ) family. (a) The alternating layered structure. Note that the  $b$ -axis is defined as perpendicular to the basal plane. (b) Top view of one of the  $\text{Te}$  net layers, showing the in-plane  $p_x$  and  $p_z$  orbitals which lie at the Fermi level. The hopping parameters  $t_{\parallel}$ ,  $t_{\perp}$ , and  $t'$  are approximately 2.0 eV, 0.35 eV, and 0.16 eV, respectively.[66, 67, 68] (c) Chemical pressure phase diagram showing the CDW transition temperatures as a function of in-plane lattice parameter  $a$ . Lanthanide contraction for heavier rare-earths suppresses  $T_{CDW1}$  and a second, perpendicular CDW appears at  $T_{CDW2}$  for  $R=\text{Tb-Tm}$ . Filled symbols taken from ref. [69], hollow symbol for  $\text{TbTe}_3$  taken from ref. [70]. (d) Schematic Fermi surface for the estimated hopping parameters in a tight binding model. Different shades of gray indicate the  $p_x$  and  $p_z$  orbital character, and thin lines indicate bands folded into the smaller 3D Brillouin zone. The arrows indicate two possible nesting vectors: the dashed arrow nests one of the two bands very well, while the solid arrow nests both bands, but to a lesser degree. (e) Full Fermi surface of  $\text{ErTe}_3$  from DFT calculations. The presence of a second  $\text{Te}$  plane generates a small bilayer splitting which is most noticeable around the central square pocket. The width of the lines indicates total band dispersion along the out-of-plane  $b$ -axis; the Fermi surface is highly two-dimensional. (f) Summary of trends of  $R\text{Te}_3$  across the lanthanide series.  $\text{YTe}_3$  also forms in this structure and exhibits  $T_{CDW1}=334\text{ K}$ [71]. Panels (c) and (e) adapted from Ru et al. "Effect of chemical pressure on the charge density wave transition in rare-earth tritellurides  $R\text{Te}_3$ ." *Phys. Rev. B* **77**, 035114 (2008), used with permission of the American Physical Society.

many others. The wide range of electronic properties of such materials, however, arise from the extent to which the square net has been distorted away from its maximum symmetry. In the case of  $\text{K}_{0.33}\text{Ba}_{0.67}\text{AgTe}_2$ , for instance, the perfect tetragonal symmetry is broken by the presence of an incommensurate orthorhombic superstructure along one of the in-plane axes, which converts what would otherwise be a metal into a semiconductor.[74] A less obvious example is the quasi-1D family  $\text{NbSe}_3$ ; here the planes buckle and dimerize along one axis, creating a lattice of loosely-coupled conductive chains along the orthogonal axis. Several other variants of the  $\text{ZrSiS}$  structure rearrange the atoms into diagonal zig-zag chains ( $\text{GdPS}$ ) or *cis-trans* chains running parallel to the original bond direction ( $\text{CeAsS}$ )[75] The loss of symmetry accompanied by partial or complete loss of metallic behavior, as might be expected by the basic arguments underlying the Jahn-Teller effect [76], appears to be a general feature of crystal structures derived from stacked square nets, and in very few of these cases can a transition to the high symmetry “parent” state be observed at temperatures below the melting point.

By analogy to these related structures, one should then expect that the crystal structure will be unstable to some form of distortion. Indeed, examinations of the high-symmetry structure show that average Te-Te bond length in the undistorted  $R\text{Te}_3$  structure is approximately 3.1 Å, significantly longer than the Te-Te bond of 2.83 Å.[77, 78]. As will be described in detail in Section 1.3.2, a distortion (which is precisely the CDW to be studied) does indeed occur. The rare-earth tritellurides provide a unique case in which the primary distortive transition of the square chalcogenide net occurs within an experimentally accessible temperature range.

As mentioned above, the metallic character of  $R\text{Te}_3$  arises from the square Te bilayers. The valence  $5p^4$  electrons on neutral Te are split in energy due to crystal electric fields of the  $R\text{Te}$  bilayers, and the out-of-plane  $p_y$  orbitals are suppressed below the FS and always filled. The remaining in-plane orbitals ( $p_x$  and  $p_z$ ) produce two orthogonal quasi-one-dimensional bands in a Brillouin zone (BZ) defined by a single Te layer[66]. The quasi-1D hopping term for each band is  $t_{\parallel}$ . These bands warp inward slightly due to finite coupling in the perpendicular direction,  $t_{\perp}$ . Experimentally,  $t_{\parallel} \approx 1.8$  eV and  $t_{\perp} \approx 0.35$  eV.[67, 68] The large  $\sigma$  overlap between collinear  $p$  orbitals gives rise to a wide band ( $\approx 5$  eV) which makes  $R\text{Te}_3$  a very good metal in the plane.[79]

The model described thus far has considered only a single square Te net of appropriate filling. The full crystalline unit cell of  $R\text{Te}_3$ , as a consequence of the  $R\text{Te}$  slab layer, is doubled and rotated by  $45^\circ$  relative to the unit cell of a single Te net. Moving into the resulting “3D” Brillouin zone folds parts of the quasi-1D bands. The two bands interact weakly, opening small gaps at the corner crossing points and generating a large diamond-shaped hole pocket centered on the  $\Gamma$  point and a smaller electron pocket near the  $X$  and  $Y$  points. Finally, the presence of a second, identical Te layer produces a small bilayer splitting which doubles all of the bands.

Electron transfer from the  $R\text{Te}$  slab layers dictates the electron filling of the  $p_x$  and  $p_z$  bands. Each unit of  $R^{3+}\text{Te}^{2-}$  donates one electron, which is shared between eight different states within the

bilayers: two layers, two orbitals per layer ( $p_x$  and  $p_z$ ) and two spin states per orbital. The resulting filling is  $5/8$ , which matches well with the FS shape and volume observed by positron annihilation[80] and angle-resolved photoemission spectroscopy (ARPES).[67, 81]

The layered structure implies very little dispersion of these bands in the cross-plane direction. As a consequence, the FS sheets are very 2D, as observed by nearly perfect  $\sec(\theta)$  angular dependence of de Haas-van Alphen oscillations.[82] Additionally, the resistivity tensor is highly anisotropic; the cross-plane resistivity  $\rho_{bb}$  is approximately 100 times larger than either in-plane component.[73, 83]

$R\text{Te}_3$  can be formed using almost all of the lanthanide elements. The  $R\text{Te}_3$  structure requires a trivalent ion in the  $R$  site, which precludes Eu due to its tendency to favor divalent oxidation states.  $\text{PmTe}_3$  would likely form from a chemical perspective, but the radioactivity of Pm makes this both unstable and impractical. Trivalent yttrium (Y), with an ionic radius approximately equal to that of Ho, can also be used. It is worth noting, however, that the structure is not stable in air for any  $R$ . When not stored under an inert atmosphere, the surface of the crystals progresses from the original orange, copper-like luster to a dull gray over the course of a few hours. The stability decreases in moving toward increasingly heavy atoms, such that  $\text{TmTe}_3$  crystals will darken significantly in roughly 30 minutes. Crystals of compounds involving the two heaviest rare-earths,  $\text{YbTe}_3$  and  $\text{LuTe}_3$ , have not been observed.

The local moments of the rare-earth ions do order magnetically at low temperatures through sometimes as many as three different transitions[84, 85, 86, 87]. The highest magnetic transition temperature appears in  $\text{GdTe}_3$  at approximately 13 K, which is approximately an order of magnitude smaller than the critical temperatures of the CDW phases. This relatively small energy scale, compared to the critical temperatures of the CDW transition, implies that magnetism is a small perturbation at all but the lowest temperatures.

### 1.3.2 CDW ground states

At first glance, the CDW wavevector in  $R\text{Te}_3$  appears consistent with the simple Peierls picture of a pair of well-nested, quasi-1D bands. Finite curvature of the Fermi surface sheets, a consequence of  $t_{\perp} \neq 0$ , produces two different choices for the nesting vector, shown in Fig. 1.3. The dashed wavevector most optimally nests just one of the quasi-1D bands, but does a poor job of nesting the other. In contrast, the solid arrow provides but decent nesting of both bands simultaneously. Calculations of the Lindhard susceptibility assuming a momentum-independent electron-phonon coupling  $\lambda$  support the formation of stripe rather corresponding to the latter rather than checkerboard order for a realistic set of parameters[88]. In practice, the nesting is not perfect, which results in a CDW gap which is not exactly centered at the Fermi level and which is inhomogeneous in  $k$ -space [89, 67] However, ARPES studies do show that significant portions of the Fermi surface are indeed gapped in the CDW state. Additionally, studies of the homologous structure  $R\text{Te}_2$  doped with Sb showed that the wavevector could be tuned over a large range and appeared to track with  $2k_F$ [90],

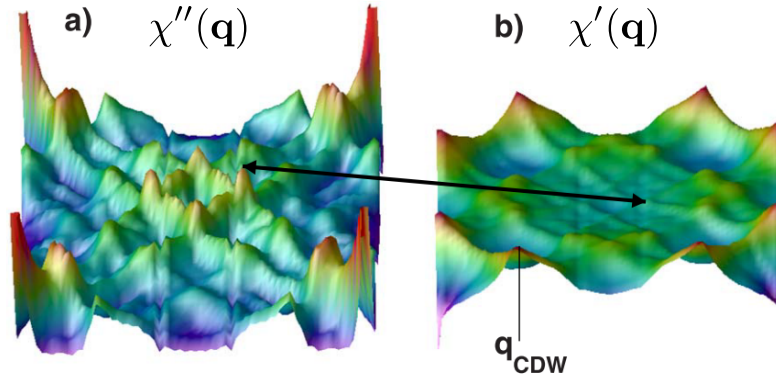


Figure 1.4: (a) Imaginary and (b) real parts of the Lindhard susceptibility calculated for  $\text{CeTe}_3$ . The  $\Gamma$  point lies in the bottom left corner of both panels. The black arrow connects the two positions which correspond to the nesting wavevector, where a peak is observed in  $\chi''$ , but where  $\chi'$  is nearly featureless. The true wavevector  $\mathbf{q}_c$  corresponds to a weak maximum in  $\chi'$ . Reproduced from Johannes and Mazin, “Fermi surface nesting and the origin of charge density waves in metals”. *Phys. Rev. B* **77**, 165135 (2008) used with permission of the American Physical Society.

further implicating Fermi surface nesting for driving the creation of the CDW transition.

Further studies of the nesting condition, however, have found the Peierls picture in  $R\text{Te}_3$  to be lacking in rigor and predictive power, as mentioned in Section 1.2.1.2. In particular, the true CDW wavevector ( $\mathbf{q}_c = 0.298c^*$  for  $\text{DyTe}_3$ ) quantitatively disagrees with the nesting wavevector ( $\mathbf{q}_{\text{nest}} = 0.25c^*$ ). [46] A detailed calculation of the Lindhard susceptibility (Fig. 1.4) shows that while the  $\chi''(\mathbf{q})$  does exhibit peaks at the nesting vector, no corresponding peak is observed in the real part,  $\chi'(\mathbf{q})$ . Instead, a gentle peak is observed at the experimentally validated wavevector  $\mathbf{q}_c$ , as well as a peak with nearly the same amplitude at  $\mathbf{q}_a$ . While this maximum in  $\chi'(\mathbf{q})$  does undoubtedly increase the tendency toward CDW formation in  $R\text{Te}_3$ , the modest values make this qualitatively insufficient to drive a CDW instability by itself.

However, the CDW itself is, in many ways, exemplary of the basic properties one would expect of a unidirectional incommensurate density wave. An incommensurate modulation is perhaps most clearly distinguished from a high-order commensurate modulation by the presence of a smooth variation of wavevector with temperature or some other tuning parameter. A commensurate state would remain precisely locked with some fraction of the reciprocal lattice spacing. For  $R\text{Te}_3$ , scattering experiments have shown that the superlattice spacing does indeed vary smoothly as a function of temperature [70], chemical pressure [91, 92, 67], and hydrostatic pressure [93]. Electron and x-ray diffraction experiments at low temperatures clearly show resolution-limited superlattice peaks [91, 78, 69] corresponding to the incommensurate wavevector  $\mathbf{q}_c$  and indicating that the correlation lengths are very long compared to the lattice. [71] Peaks at the second harmonic  $2\mathbf{q}_c$  are also present, indicating that the modulation does contain some anharmonic terms. For the heavier rare earths, superlattice peaks are

also observed along the orthogonal direction with an incommensurate wavevector  $\mathbf{q}_a$  with magnitude slightly smaller than  $\mathbf{q}_c$ .

The wide, weakly correlated band structure of  $R\text{Te}_3$  makes it an ideal system for angle resolved photoemission spectroscopy studies (ARPES). At high temperatures, the FS matches quantitatively with the DFT results presented in Fig. 1.3(e). Well below  $T_{CDW1}$  in the lighter rare-earth compounds, a gap opens at the corners of the square near  $\mathbf{q}_c$ [89, 94] which varies approximately parabolically in magnitude as one moves away from  $\mathbf{q}_c$  along the FS.[67] For the heavier rare earths a similar trend is observed, but with the addition of a smaller gap at  $\mathbf{q}_a$ . At low temperature in  $\text{ErTe}_3$ , for example, the central square sheet of the FS is almost entirely reconstructed due to gaps at all four corners; all that remains is a small pocket of metallic quasiparticles in between the two gaps.[81]

Scanning tunneling microscopy (STM) studies of the surface of  $R\text{Te}_3$  also provide clear evidence of relatively large CDW modulations.[95, 96, 97, 44] As a real-space probe of the CDW structure, STM topography and spectroscopy studies together show that the fundamental wavevector of  $\text{TbTe}_3$  at low temperatures is  $q = 0.71c^*$ , whereas scattering techniques are unable to distinguish between this and  $0.29c^*$ .[95]

Optical spectroscopy studies of the CDW gap show that the both the magnitude and extent in  $k$ -space of the CDW gap decrease under hydrostatic pressure.[98, 99] For sufficient pressure, the CDW gap disappears completely. [93] At very low temperatures ( $\lesssim 4$  K) and hydrostatic pressure above 2.3 GPa,  $R\text{Te}_3$  develops a superconducting ground state.[100, 101] Pristine, free-standing  $R\text{Te}_3$  is not known to superconduct above approximately 100 mK.

### 1.3.3 Signatures of the CDW transition

Up to this point, only the characteristics of the  $R\text{Te}_3$  CDW states themselves have been discussed; we now turn our attention to the phase transitions which separate the CDW states from the uniform metal and each other. We focus primarily on the behavior of the more commonly studied transition at  $T_{CDW1}$  which appears in all  $R\text{Te}_3$  compounds, and reserve comments on the behavior at  $T_{CDW2}$  for the Section 1.3.4

Synchrotron x-ray diffraction measurements of the superlattice peaks at  $\mathbf{q}_c$  and  $\mathbf{q}_a$  as a function of temperature show that the transitions at both  $T_{CDW1}$  and  $T_{CDW2}$  are continuous.[69, 93, 70, 102]. The increase of the order parameter closely follows a BCS-like temperature dependence on cooling, with the exception of a slight rounding of the transition presumably arising from critical fluctuations.[69]

Inelastic x-ray scattering (IXS) shows a clear phonon softening at  $\mathbf{q}_c$  upon cooling through  $T_{CDW1}$ . [102] Interestingly, a similar phonon softening is also observed at the orthogonal wavevector  $\mathbf{q}_a$  at the same temperature. The phonon at  $\mathbf{q}_a$  never *completely* softens to zero energy, but the existence of a near-softening indicates that the energy differences between the two in-plane CDW components are small, of order 2 mV. Additionally, the phonon dispersion seems to vanish for a finite region of  $k$ -space centered at  $\mathbf{q}_c$ . First principles calculations of the lattice dynamics and electron-phonon

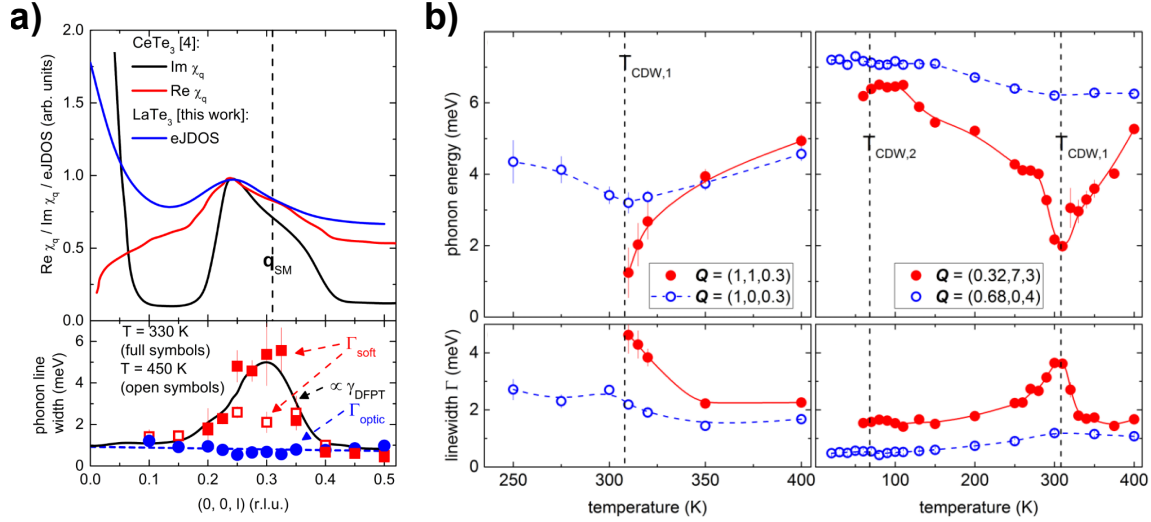


Figure 1.5: Inelastic x-ray results on  $R\text{Te}_3$ . (a) Top: calculations of the Lindhard susceptibility and the electron joint density of states for  $R\text{Te}_3$ . Bottom: measurements of the soft phonon mode linewidth in  $\text{TbTe}_3$  compared to results from density functional perturbation theory. This shows that  $\chi(q)$  alone does not properly describe the CDW: the full lattice response is required in order to achieve agreement. Reproduced from Maschek, et al, “Wave-vector-dependent electron-phonon coupling and the charge-density-wave transition in  $\text{TbTe}_3$ ” *Phys. Rev. B* **91**, 235146 (2015), used with permission of the American Physical Society. (b) Measurements of the phonon energy and linewidth at reciprocal space positions corresponding to  $\mathbf{q}_a$  (left panel) and  $\mathbf{q}_c$  (right panel). While the phonon begins to soften at both  $\mathbf{q}_c$  and  $\mathbf{q}_a$  as one approaches  $T_{CDW,1}$ , the phonon at  $\mathbf{q}_c$  softens completely while the  $\mathbf{q}_a$  mode stiffens again. No significant softening is observed in either direction on approach to  $T_{CDW,2}$ . Reproduced from Maschek, et al “Competing soft phonon modes at the charge-density-wave transitions in  $\text{DyTe}_3$ ” *Phys. Rev. B* **98**, 094304 (2018), used with permission of the American Physical Society.

coupling demonstrates that the electron phonon coupling is strongly momentum dependent.[46] These calculations are able to quantitatively reproduce the phonon dispersion as well as phonon linewidths.

The Debye temperature of  $R\text{Te}_3$  varies between 140-180 K depending on  $R$ . [83, 70]. As a consequence, the phonon contribution to the specific heat at  $T_{CDW1}$  (which at its minimum is  $\approx 245$  K in  $\text{TmTe}_3$ ) is quite large and approaches the value expected by the Dulong-Petit law. This large background tends to completely overwhelm the electronic contribution to the heat capacity anomaly at  $T_{CDW1}$ , and few researchers have succeeded in detecting the anomaly at all. [103, 104]

While the most clear evidence of a CDW phase is the presence of superlattice peaks at finite wavevector, the  $\mathbf{q} = 0$  behavior of the lattice is also a sensitive thermodynamic witness for changes in the electronic structure. On cooling through  $T_{CDW1}$  and entering the  $\mathbf{q}_c$  CDW phase, opening of a highly anisotropic gap on the Fermi surface also causes a sharp change in the thermal expansion coefficients.[69]. As the temperature decreases, the growing order parameter reinforces the orthorhombic distortion, causing the  $a$  lattice parameter to contract more quickly while slowing the contraction of  $c$ . Ultrasound attenuation experiments have also shown that the sound velocity and elastic constants both exhibit small, but sharp, anomalies at  $T_{CDW1}$ . [103, 104, 105]

Measurements of the electrical resistivity directly probe the behavior of the electrons near the Fermi level; the same electrons which participate most strongly in the CDW transition. In the particular case of  $R\text{Te}_3$ , the phase transitions are observed most clearly in the out-of-plane resistivity,  $\rho_{bb}$ . The small dispersion of the FS along the  $b$ -axis depends very little on the azimuthal angle within the plane, such that gaps along both  $c$  and  $a$  axes affect  $\rho_{bb}$  in similar ways. Cooling through  $T_{CDW1}$  resistivity  $\rho_{bb}$  shows a sharp upturn as the opening of the CDW gap causes a loss of density of states. With continued cooling, the resistivity eventually reaches a maximum, then decreases again

Within the plane, the resistivity signal becomes slightly more subtle. The same general arguments applied to  $\rho_{bb}$  at the CDW transition hold for both  $\rho_{aa}$  and  $\rho_{cc}$ ; opening a gap lowers the carrier density, causing an increase in the resistivity. However, the contribution of any given section of the FS to the electronic conduction along a given axis is weighted by the projection of the Fermi velocity  $\mathbf{v}_F$  at that point onto the electric field axis. The curvature of the  $R\text{Te}_3$  FS is such that  $\mathbf{v}_F$  for  $\mathbf{k} \approx \mathbf{q}_c$  has a larger projection on the  $a$  axis than on the  $c$  axis. As a consequence, opening a gap near  $\mathbf{q}_c$  creates a much larger increase in  $\rho_{aa}$  rather than  $\rho_{cc}$ , and vice versa. [106, 107]

For all of the components of the resistivity tensor, the CDW transition appears as a sharp minimum in the temperature derivative  $d\rho_{ii}/dT$ . As will be discussed in detail in the following section, general considerations [108] lead to a proportionality between this derivative and the critical contribution to the specific heat. The shape of the resistivity indicates increased scattering due to critical fluctuations in a region approximately 20 K above  $T_{CDW1}$ , and the cusp-like shape of the  $d\rho_{ii}/dT$  makes clear that the phase transition is not well described by a mean-field description.

### 1.3.4 The second CDW transition

The vast majority of studies on the  $R\text{Te}_3$  family performed to date have focused on the much more clear-cut physics of the CDW transition at  $T_{CDW1}$ . The second, lower temperature CDW phase, however, is somewhat more enigmatic. In general, even for the pristine compounds, the slight bump in the resistivity upon passing through  $T_{CDW2}$ , while clearly visible in the resistivity derivative, is never as sharp as the transition at  $T_{CDW1}$ . Similarly the temperature dependence of the superlattice intensity at  $\mathbf{q}_a$  turns on near  $T_{CDW2}$  with a much more rounded transition than the  $\mathbf{q}_c$  peak shows at  $T_{CDW1}$ .<sup>[102]</sup> Also, unlike the case above  $T_{CDW1}$ , where phonons at both  $\mathbf{q}_c$  and  $\mathbf{q}_a$  decrease in energy approaching the transition, no phonon softening is observed at either wavevector, raising questions regarding the nature of the second CDW.

Recent Hall effect measurements in the vicinity of the second CDW phase have also cast doubt on the second order character of the transition at  $T_{CDW2}$ . Specifically, the Hall number in  $\text{HoTe}_3$  and  $\text{ErTe}_3$  appears to differ significantly if measured while cooling or while warming the sample. <sup>[109]</sup>  $R\text{Te}_3$  contains both hole and electron pockets, so interpreting the Hall number is not trivial—however the observation of hysteresis in the temperature response, especially in the vicinity of a known phase transition, indicates that the transition at  $T_{CDW2}$  may either be first order or may exhibit more of a glassy character, such that the CDW fluctuations slow down and fall out of equilibrium as the transition is approached. The latter would reconcile the smoothed transition observed in resistivity and scattering probes.

Systematic studies of quasiparticle effective mass as a function of chemical pressure<sup>[110]</sup> also finds no evidence of a mass enhancement near the putative quantum critical endpoint where  $T_{CDW2}$  is suppressed to zero temperature, which while not conclusive on its own, could arise due to the transition either being or becoming first order.

### 1.3.5 Disorder in $R\text{Te}_3$ by Pd-intercalation

Samples of  $R\text{Te}_3$  are generally quite clean and free of defects or disorder. Perhaps no other probe makes this as clear as the near-perfect topographical maps which can be acquired by scanning tunneling microscopy.<sup>[95]</sup> One commonly used technique for introducing disorder into quasi-2D materials is to intercalate impurities (usually metal ions, but occasionally even small molecules) into the space between the layers.<sup>[111, 112, 61]</sup> <sup>1</sup> Prior to the start of this work, He et al<sup>[113]</sup> reported studies of  $R\text{Te}_3$  with Pd atoms inserted in between the layers. Their results showed that for samples across the lanthanide series, the introduction of Pd tends to suppress signatures of charge order and cause the material to superconduct beyond a critical Pd concentration.

---

<sup>1</sup>The term “intercalation” is used inconsistently throughout the literature—sometimes it is used to denote a reversible process where one can alter the intercalant density at will, and which occurs after the sample has been synthesized. Other times it refers simply to altering a material by inserting impurities between the planes where they will remain, which usually occurs during the synthesis process. For the purposes of this dissertation, I will adopt the latter definition, as it is the effect of disorder on the CDW state which is important, not how the disorder got there.

While this work demonstrated that Pd ions could be inserted into the  $R\text{Te}_3$  crystal structure as a source of disorder, it was performed primarily on polycrystalline samples, with the exception of a single ARPES study.[114]. Developing a well-characterized series of single crystal samples is crucial in order to enable many of the experimental studies which could elucidate the evolution of the CDW in the presence of disorder. Chapter 5 seeks to bridge the gap by establishing a detailed map of the physical properties of single-crystal samples of  $\text{Pd}_x\text{ErTe}_3$ .

## 1.4 Summary

Despite the simple beginnings of the theory of charge density waves in metals, reality has turned out to be much more intricate. The study of charge order and charge density waves has become a rich and complex field in its own right. The coexistence of charge order with other nontrivial states of matter such as high temperature superconductivity only further muddies the waters. As such, the study of simple model systems where one aspect of the emergent behavior can be studied in isolation provides an avenue for progress. In comparison to the cuprates, the rare-earth tritellurides have several of the similar ingredients required for a model system—both are quasi-2D, based on a square lattice, and both exhibit some form of stripe charge order. If one were able to tune  $R\text{Te}_3$  with disorder, use symmetry-breaking strains to observe degeneracy between the orthogonal in-plane stripe states, and one could also elicit a superconducting ground state in free-standing crystals, then it would be accurate to call  $R\text{Te}_3$  a model system to study aspects of charge order that might be relevant to the cuprates.

Of course, the tritellurides do not account for *all* aspects of the cuprates. For instance, the  $R\text{Te}_3$  completely neglects the strong magnetic interactions which dominate regions of the cuprate phase diagram, and therefore also neglects states in which charge and spin degrees of freedom are intimately connected. This may have the consequence that the character of the charge order in  $R\text{Te}_3$  differs significantly from that of the cuprates. However, this is exactly the purpose of developing a model system; we do not seek to reproduce all aspects of the more complex material, but rather to select a few. In this case, the purpose is to select unidirectional CDW order. So while it is unlikely that unidirectional CDW order is crucial for all of the emergent behavior observed in the cuprates, the study of a model system like  $R\text{Te}_3$  does allow for a new perspective into a specialized region of phase space inside of a complex problem. The purpose and scope of this thesis is therefore to demonstrate that  $R\text{Te}_3$  does indeed admit controlled (but large) alterations to its properties under both uniaxial stress and disorder, and to provide a detailed roadmap such that future studies may isolate and identify some general, shared features between  $R\text{Te}_3$  and more complex systems.



## Chapter 2

# Experimental methods

### 2.1 Working with $R\text{Te}_3$

#### 2.1.1 Synthesis of single-crystal $R\text{Te}_3$ and $\text{Pd}_x\text{ErTe}_3$

Well-controlled material synthesis is required for reproducible experiments. More importantly, measurements of the most interesting properties of  $R\text{Te}_3$ , those stemming from the structural and electronic anisotropy, require single crystals rather than polycrystalline samples. Single crystals of rare-earth tritellurides can be synthesized from a binary melt following the method first used by N. Ru[83, 71] and described in great detail in [115]. The synthesis process, illustrated in Fig. 2.1, begins by mixing solid Te lumps with small quantities of the desired rare-earth, in a molar ratio of approximately 97:3, in a 2 mL alumina crucible. The total mass of the starting materials is approximately 4 g.  $R\text{Te}_3$  is the most Te-rich compound on the  $R$ -Te binary phase diagram, so any  $R$ :Te ratio around 5% produces the correct phase, although crystal size and degree of intergrowth both depend on this ratio. The crystals in this work were grown using approximately 1.3-3.0 atomic percent Er. A second alumina crucible is filled with loosely-packed quartz wool, and placed upside down on top of the first.

This pair of crucibles is placed inside of a quartz tube, padded on the top and bottom with more quartz wool, this time used both as padding as well as to push the two crucibles together. The quartz tube is then purged with argon and evacuated several times in order to minimize contaminant oxygen or moisture, and then the tube is sealed with a hydrogen/oxygen torch. A final argon pressure of 60 mTorr or lower was used for the growths in this work. The ampoules were heated to a maximum temperature  $T_{soak}$  over the course of 8 hours, held at that temperature for 8 hours, and then cooled to a final temperature  $T_{spin}$  over 72-100 hours. For  $\text{ErTe}_3$  and  $\text{Pd}_x\text{ErTe}_3$  for  $x \lesssim 2\%$ ,  $T_{soak}$  of  $700^\circ\text{C}$  works well, and the decant was performed final temperature is  $515^\circ\text{C}$ . The ampoule is then allowed to cool before it is broken open and the crystals extracted by hand.

Crystals of  $R\text{Te}_3$  (for any  $R$ ) are air-sensitive and will degrade in ambient atmosphere. Over time, crystal surfaces gradually darken from a copper color to a dark gray. The stability decreases as the atomic number of the rare earth element increases; the timescale is on the order of a few hours for  $\text{LaTe}_3$ , but decreases to about half an hour for  $\text{TmTe}_3$ . If left out for even longer periods, the degradation will work its way through the entire crystal, causing the edges to swell and wrinkle not unlike a water-damaged book. The resulting material has not been studied in detail, but experience shows that it is both amorphous and electrically insulating.

To combat this, care must be taken to store samples of  $R\text{Te}_3$  under an inert environment. We used a nitrogen glovebox with  $< 1$  ppm oxygen to store samples—surface darkening occurs in this environment over the course of years rather than hours. However, working with samples in a glovebox is impractical for most stages of sample preparation. Crystal alignment is generally performed first, followed by shaping the crystal as needed by cutting it with a scalpel. Any degraded surfaces are then cleaved off as late in the process as possible, revealing fresh copper-colored surfaces.

### 2.1.2 Crystal characterization and alignment

The  $a$  and  $c$ -axes are identified using single-crystal x-ray diffraction. The orthorhombic space  $Cmcm$  space group presents anisotropic rules for allowed diffraction peaks. Specifically, peaks of index  $(0, k, l)$  are present in the diffraction pattern for even  $k$ , while peaks of index  $(h, k, 0)$  are present only if both  $h$  and  $k$  are even. For the samples used throughout this dissertation, the intensities at the allowed  $(0, 6, 1)$  and the forbidden  $(1, 6, 0)$  peak are compared. The forbidden peak is undetectable in all the samples used here, implying that the samples are free from in-plane twin domains.

In principle, a planar stacking fault could produce domains beneath the surface, and the  $\text{Cu K}\alpha$  radiation used is only sensitive to a depth of approximately  $2\ \mu\text{m}$ . However, since the weak van der Waals interlayer bonding allows for exfoliation with adhesive tape, one can perform successive scans of the  $(0, 6, 1)$  and  $(1, 6, 0)$  peaks, removing a few microns of material from the sample each time without removing the sample from the diffractometer. This provides an effective method of depth-profiling within the crystal structure, although it does destroy the sample in the process. No change in the relative intensities of the two peaks was observed in any of these exfoliation series experiments. This evidence implies that stacking faults are rare within the material.

### 2.1.3 Transport measurements

Electrical contacts are formed first by sputtering gold onto a freshly cleaved surface. The gold layer acts as an inert buffer between  $R\text{Te}_3$  and the silver paint used to contact wires onto the crystal, as silver will react with the  $R\text{Te}_3$ . This passivating gold layer greatly extends the life of electrical contacts, but experience has shown that even when stored in a vacuum at room temperature the contact resistance degrades substantially over the course of several days.

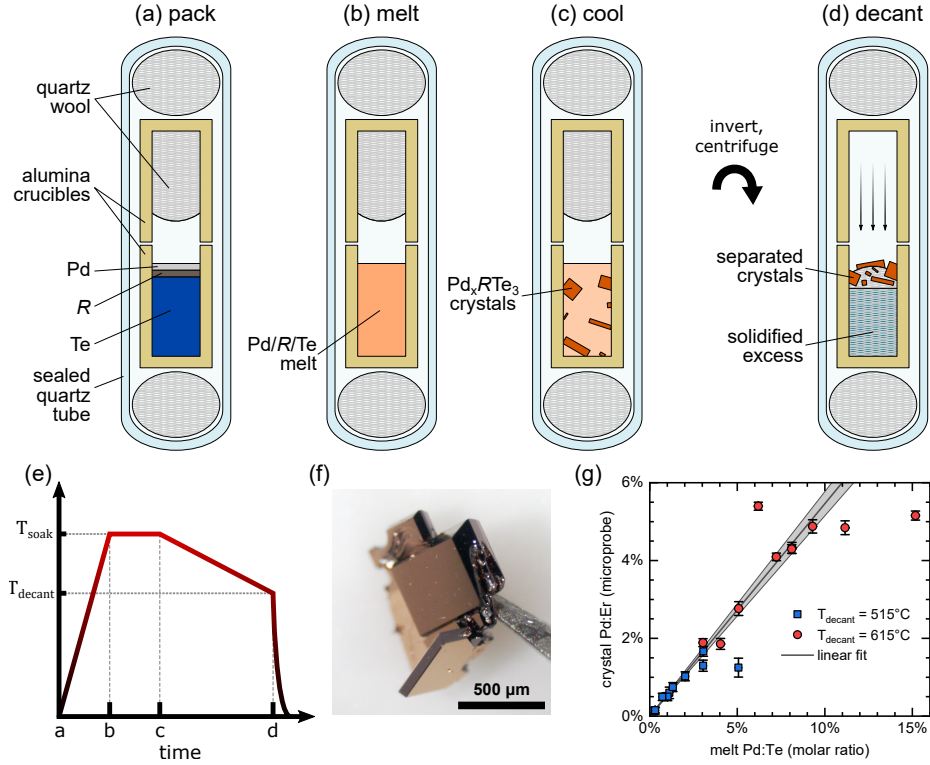


Figure 2.1: Schematic diagrams illustrating the crystal growth process for  $RTE_3$  and  $Pd_xErTe_3$ . (a) solid pieces of the three constituent elements are added in the desired ratio into a 2 mL alumina crucible. A second crucible is filled partially with quartz wool, and the two are sealed together inside of a quartz tube under a rarified Ar atmosphere, cushioned on either side by more quartz wool. (b) The entire ampoule is placed inside a box furnace, held vertically as drawn, and the temperature is increased to where the raw material melts together into a homogeneous liquid. (c) The ampoule is then cooled slowly over the course of several days. During this period, crystals nucleate and grow within the melt. (d) The ampoule is then quickly removed from the furnace, flipped over, and then centrifuged to push any remaining liquid down into the porous quartz wool. The larger crystals remain on top of the quartz wool, effectively separating them from the rest of the material. (e) Schematic of the temperature profile through the flux growth process. For  $ErTe_3$ ,  $T_{soak} = 700^\circ\text{C}$  and  $T_{decant} = 515^\circ\text{C}$ . The first two time steps  $t_{ab}$  and  $t_{bc}$  are between 4-8 hours each, and  $t_{cd}$  is between 72-100 hours. (f) Microscope image of a few representative crystal after the synthesis process. The shiny square surfaces are the basal  $ac$  planes. This cluster consists of several separate crystals which grew into each other, and which can be separated with a scalpel. (g) For  $Pd_xErTe_3$ , the resultant Pd concentration  $x$  tracks most closely with the starting Pd:Te ratio. The slope of the linear fit relating these two ratios is  $0.546 \pm 0.031$ . Increasing the decant temperature is necessary for  $x \gtrsim 2\%$  in order to prevent preferential growth of  $PdTe_2$ , but does not significantly affect the resulting  $x$ .

In order to isolate various components of the resistivity tensor, I have used three different contact geometries throughout this dissertation. The most straightforward of these is the standard in-plane four-point longitudinal measurement, in which current is passed through a crystal parallel to one of the lattice vectors, and a voltage difference between two points along the same axis is detected. This technique isolates a single in-plane component, either  $\rho_{aa}$  or  $\rho_{cc}$ . Sputtered gold and silver paint is applied to both the top as well as some of the edges of the crystal to ensure that this technique probes the entire bulk rather than just the top surface layer.

The crystal morphology is not, however, conducive to performing simple longitudinal measurements along the out-of-plane direction, corresponding to  $\rho_{bb}$ . Measurements of  $\rho_{bb}$  are performed using six contacts, with three on the top surface and three on the bottom. The outer two contacts on the top face are shorted together and used as a current source, while the outer two on the bottom act as the current sink.<sup>1</sup> The voltage difference between the two center contacts is then measured to extract  $\rho_{bb}$ . The high resistivity anisotropy ( $\rho_{bb} \approx 100\rho_{cc}$ ) of  $R\text{Te}_3$  makes this technique very insensitive to contact misalignment between the top and bottom surfaces.

Direct measurements of the in-plane resistivity *anisotropy*,  $\rho_{cc} - \rho_{aa}$ , were performed using a transverse resistivity technique.[107] In this case, a bar-shaped crystal is cut with its long axis running at 45° degree angle to the  $a$  and  $c$  axes. A set of four longitudinal contacts, similar to the first case presented above, provide a measurement of  $\rho_{aa} + \rho_{cc}$ . Measurement of a voltage difference perpendicular to the direction of the current flow, is sensitive to the difference  $\rho_{cc} - \rho_{aa}$ . The contact geometry is similar to that used in standard Hall effect measurements, except that in this case the transverse signal arises from a broken mirror symmetry (where the mirror plane contains the current axis) rather than a magnetic-field-induced breaking of time reversal symmetry. The individual components  $\rho_{aa}$  and  $\rho_{cc}$  can then be calculated through linear combinations of the two signals. This technique has the benefit of detecting both in-plane resistivity components on the same sample under the same conditions.

#### 2.1.4 Electron diffraction

Special preparation is required for preparing samples for electron diffraction in a transmission electron microscope (TEM). Electron transmission requires regions of samples are less than 100 nm thick, and at least tens of microns across. I tested a variety of different methods, including focused ion beam micromilling and plasma polishing, but the most reliable technique is a simple exfoliation. Crystals are glued across the  $\approx 1$  mm wide hole in a TEM slot grid, and then the surface is exfoliated with adhesive tape. The process is continued until the exfoliation opens a hole near the center of the sample. This method produces regions suitable for electron diffraction around some of the remaining

---

<sup>1</sup>The *ideal* case would be to use a ring-shaped current contact on both the top and bottom, rather than a pair of separate contacts. However, the requirement of a bar-shaped sample for the uniaxial stress measurements discussed in Section 2.2 and Chapter 4 limits the area available for a ring contact, and the use of a split current contact is the next best option.

edges.

Selected Area Electron Diffraction Patterns (SADPs) were performed using an FEI Tecnai G2 F20 X-TWIN transmission electron microscope at a beam energy of 200 keV. Patterns were taken using an aperture corresponding to approximately 200  $\mu\text{m}$  in diameter at the sample. The sample was aligned such that the electron beam passes parallel to the [010] zone axis. Patterns were taken at temperatures between 95 K and room temperature using a Gatan 636 double-tilt liquid nitrogen cooling holder. The sample position and alignment were continuously monitored to correct for thermal contraction of the holder.

## 2.2 Measurements under uniaxial stress

Uniaxial stress measurements are quite simple in principle: one can use the same electrical contacts or thermocouples as for freestanding measurements, and simply stretch or squeeze the sample along a given axis. The practice, however, is complicated by several practical factors which require careful consideration.

### 2.2.1 Generating stress and strain

One simple method for generating strain within a sample is to adhere the sample directly to the side of a piezoelectric actuator. These are made of stacks of prepolarized lead zirconate titanate (PZT) layers interleaved with planar electrodes. Positive voltages on the electrodes cause the stacks to elongate along the poling axis, and negative voltages cause contraction.

While some of the preliminary data for this thesis was collected using this technique, it was found that the epoxy, whether encapsulating the entire sample or simply bonding the bottom surface of the sample, tended to cause mechanical damage to the sample and its contacts. The soft, micaceous nature of the sample made it difficult to obtain reproducible results, leading to the adoption of a uniaxial stress cell for studies of  $R\text{Te}_3$  under strain.

The uniaxial stress cell used here was the CS-100 from *Razorbill Instruments*.<sup>[116, 117]</sup> The operative component for tuning the uniaxial stress *in situ* in the Razorbill stress cell is a trio of PZT stacks aligned parallel to each other. The outer two affect the relative spacing between the main cell body and a metal bracket, and the third controls the spacing between this bracket and a movable island. This island, which is stabilized and constrained to linear motion by a pair of flexures, holds one end of a bar-shaped sample, and the other end is attached to the main body. In the opposing configuration, the maximum tensile (compressive) stress on the sample can be achieved by expanding (contracting) the outer two stacks and contracting (expanding) the inner stack. The outer stack electrodes are attached in parallel, so the three stacks are controlled by two separate voltages. We denote the two control voltages as  $V_{\text{outer}}$  and  $V_{\text{inner}}$ .

Because samples of  $R\text{Te}_3$  are so soft, strain studies on  $R\text{Te}_3$  have been performed primarily

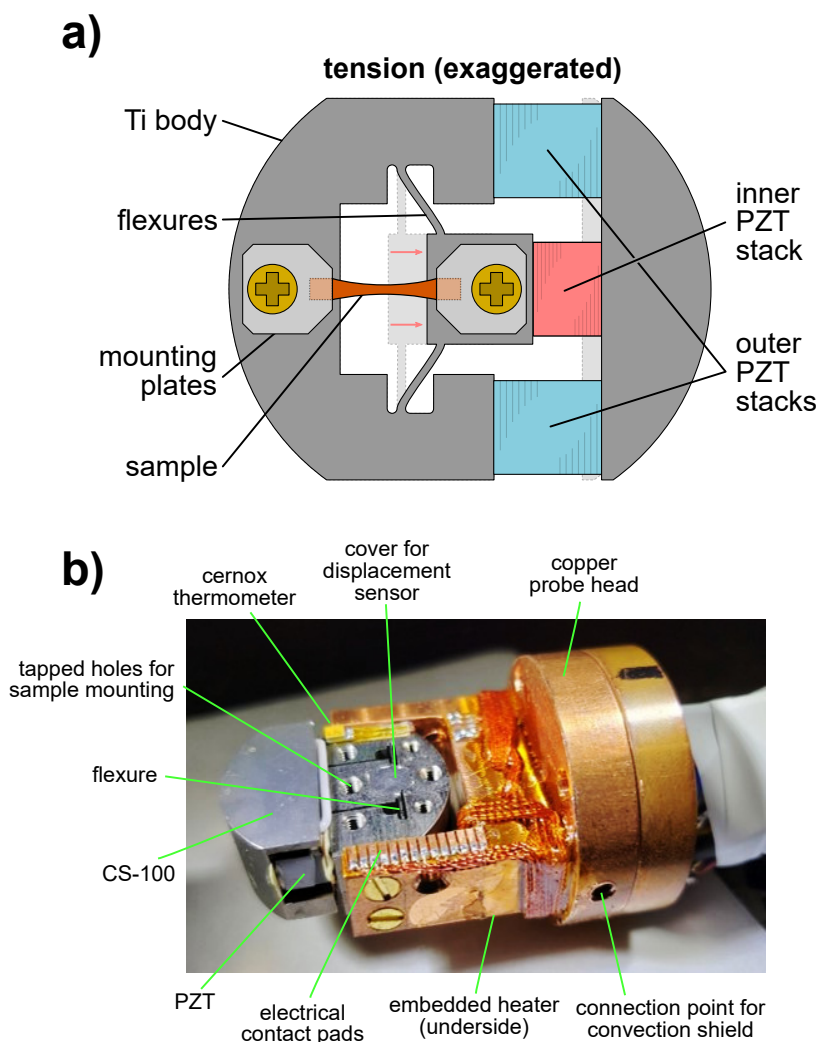


Figure 2.2: Components and operating principle of the *Razorbill* CS-100 uniaxial stress cell. (a) Schematic of the cell showing the case of tensile stress. The inner PZT stack is contracted and the outer two are expanded for maximum stress. A pair of flexures machined directly into the cell body serve to stabilize the moving jaw. (b) Photograph of the cell mounted on the end of a custom-built cryostat probe used for a liquid helium flow cryostat. Neither the sample nor the mounting plates have been attached in this image. A Cernox thermometer is connected to the cell body with GE varnish, and a constantan wire heater is embedded into the underside of the copper body to provide temperature control. Electrical contacts for the sample or thermocouple are made through a row of polyimide-backed copper pads which connect to twisted pairs running up the length of the probe. High voltage wires and coaxial cables for the PZTs and displacement sensor, respectively, connect to the underside of the probe head and are not visible here. While an experiment is in progress, a hollow copper convection shield surrounds the entire cell and probe head, held in place by a pair of set screws.

in tension (positive  $V_{\text{outer}}$ ) to avoid buckling or delaminating the samples in compression. We superimpose a small sinusoidal oscillation in order to measure both the AC elastoresistivity and the elastocaloric effects. The oscillating and quasi-static components are generated by the reference output and an auxiliary output of a *Stanford Research* 830 lock-in amplifier. The two are combined using a custom-built non-inverting summing amplifier circuit, and the output is amplified by a factor of 50 by a Tegam 2350 high-voltage amplifier. In between measurements and before the sample is mounted, all of the PZT stacks are held at +100 V for at least an hour in order to minimize any voltage-history-induced thermal expansion mismatch between the inner and outer stacks.

Piezoelectric stacks exhibit a negative thermal expansion coefficient: they tend to extend along their poling axis as one reduces the temperature due to a stabilization of the ferroelectric order parameter. In principle, the thermal expansion of the opposing inner and outer PZT stacks in the *Razorbill* stress cell will cancel each other, resulting in a consistent jaw displacement seen by the sample. In practice, two separate effects will still alter the jaw spacing as the temperature changes. First, the expansion of the lead zirconate titanate (PZT) piezoelectric actuators are highly dependent on their both the temperature and voltage history. Before mounting each sample, all of the actuators are held at +100 V at room temperature for approximately an hour to allow the stacks to relax into similar states. However, the different voltages applied to the inner and outer stacks during the experiment unavoidably upset the balanced expansion.

Second, the titanium cell body itself also contracts at decreasing temperatures. At room temperature, for instance, the thermal expansion of Ti is approximately 9 ppm  $\text{K}^{-1}$ [118], while the thermal expansion of  $R\text{Te}_3$  is approximately 45 ppm  $\text{K}^{-1}$ [69]. This means that even if the expansion of the inner and outer stacks is perfectly balanced the sample will contract more than the cell and produce tensile stress and strain on the sample. In theory, one could incorporate this expansion into one's definition of the sample strain and correct for the mismatch. In practice, however, the thermal expansion of  $R\text{Te}_3$  has not been characterized at all temperatures, and even if it were, imperfect strain transmission will still introduce significant uncertainty. Throughout this work we have taken the approach that by sweeping a large enough range of stresses, we will still recover the correct topology of the phase diagram, even though measurements at low temperature will always underestimate the tensile stress. The reported strain values are all referenced to a sample with the same thermal expansion as titanium, and assuming 100% strain transmission—this minimizes the need for ancillary measurements or extrapolations from other measured data.

In early runs, it was observed that despite the application of tensile stresses samples would still appear buckled after thermal cycling. Based on the behavior of the elastoresistive response, it was determined that the thermal contraction mismatch between  $R\text{Te}_3$  and the titanium in the stress cell caused a significant deformation of the sample mounting epoxy during the first cooldown; the sample contracted beyond the yield strength of the epoxy. As the sample warmed and expanded, the sample itself buckled rather than generating enough compressive stress to push the epoxy back into place.

To avoid this effect, a quasi-static positive voltage was applied to the inner stack, increasing linearly as the temperature decreases. The elongation of this inner stack minimizes the extreme forces and prevents the epoxy creep which forced sample buckling.

## 2.2.2 Elastoresistivity

The linear elastoresistivity tensor  $m_{ijkl}$  is defined as the derivative of the normalized change in resistivity  $\rho_{ij}$  with respect to strain  $\varepsilon_{kl}$ :

$$m_{ijkl} = \left( \frac{d(\rho_{ij}(\varepsilon)/\rho_0)}{d\varepsilon_{kl}} \right) \Big|_{\varepsilon=0} \quad (2.1)$$

where  $\rho_0$  is an appropriately chosen normalizing resistivity and  $m_{ijkl}$  is conventionally defined for small deformations centered at the neutral position  $\varepsilon = 0$ . The choice of  $\rho_0$  is a subtle issue. Consider a sample material with orthorhombic symmetry and with principal axes aligned with the coordinate frame ( $\rho_{ij} = 0$  for  $i \neq j$ ). The proper definition of  $\rho_0$  for an elastoresistivity measurement in which  $i = j$  is simply  $\rho_{ii}(\varepsilon = 0)$ . In measurements of  $m_{ijkl}$  for  $i \neq j$ , the most rigorously well-defined value for normalizing is the geometric mean  $\rho_0 = (\rho_{ii}(\varepsilon = 0)\rho_{jj}(\varepsilon = 0))^{1/2}$ . [119] This definition ensures that the ratiometric change in resistivity  $(\Delta\rho/\rho)_{ij} = (\rho_{ij}(\varepsilon)/\rho_0)$  itself remains a second rank tensor regardless of orientation.

Elastoresistivity (or often its counterpart piezoelectricity, in which the derivative is taken with respect to stress) has been applied to several different classes of materials. The most well-developed application lies in the field of microelectronics, where it has been noticed that the carrier mobilities in doped silicon are highly sensitive to strain.[120] Strain engineering—in which a patterned semiconductor is locally deformed to alter conductivities in a way which improves device performance—is now a standard technique in the design and fabrication of cutting edge nanoelectronic devices.

Within the context of fundamental condensed matter research, however, the use of elastoresistivity has been primarily focused on strongly correlated metals. The most well studied case is in the iron-pnictide superconductors, which have been shown to undergo an electronically-driven nematic phase transition, in which the structure becomes orthorhombic.[121, 122, 123, 124, 125] As a transport technique, elastoresistivity is sensitive to the behavior of the electrons at the Fermi level. In the example of an electronic nematic transition, where the in-plane resistivity anisotropy can be taken as a proxy of the order parameter, the elastoresistivity component relating the resistivity anisotropy to the proper symmetry-breaking strain is in fact proportional to the nematic susceptibility  $\chi_N$ . [119] In the case of most iron-pnictide superconductors, the relevant component is  $m_{xyxy}$ . This component has also been given the equivalent labels  $m_{66}$  (in Voigt notation) or  $m_{B_{2g}}^{B_{2g}}$  in reference to the irreducible representations of the point group to which the resistivity and strain components belong.[126] In general, this latter symmetry-motivated basis of irreducible representations of a given point group provides a powerful and intuitive framework for discussing the physical nature of and

interactions between various tensors. Due to its nature as a tensor of fourth rank, measurements of the elastoresistivity in a material have the ability to distinguish different forms of broken symmetries to which lower rank tensors, such as the resistivity itself, are insensitive.

In practice, the most intuitive technique for extracting the elastoresistivity is to step the sample strain up and down quasi-statically while measuring both the sample resistance and strain. The elastoresistivity is the slope of the resistance response versus strain, which is extracted with a linear regression. While this technique is effective and provides the most direct insight into the strain dependence, the data can take a prohibitively long time to acquire. Each stress cycle at a given temperature takes several minutes, and hysteretic behavior in the strain-generating apparatus requires that more than one cycle must be performed for a consistent measurement. Additionally, the temperature must be stable during each cycle, and the temperature stabilization process is often slower than the measurement itself. Altogether, acquiring a full dataset for the temperature dependence of a single sample can take several days of continuous measurement. However, this technique still has the benefit of being sensitive to nonlinear effects as well as accessing the largest possible strains.

Despite the success of this quasi-static (DC) technique for measuring the elastoresistivity, there are also several benefits of a sinusoidally-varying strain.[127] First, oscillating strains greatly speed data acquisition. In fact, data can be acquired continuously as the temperature is changed, shrinking the total experiment time from days to hours. The resulting dataset is also much denser in temperature, allowing for careful studies of the singular behavior near phase transitions[128].

Second, oscillating strains enable the use of phase-sensitive detection, which can improve the sensitivity [127] and allow for the use of smaller strain amplitudes. This is important for the measurement of brittle materials or materials which are easily cleaved under stress, where large quasi-static stress cycles will tend to fatigue and crack the sample.

Finite frequency techniques also make it possible in principle to explore the dynamical response of the sample. For example, the strain-induced motion of domain walls appears as a frequency-dependent signal which is most clear in the phase angle of the measured elastoresistivity.[129] Finally, the introduction of frequency as a tuning parameter makes it possible to study the elastoresistivity in challenging environments such as 65 T pulsed magnetic fields[130], where the entire measurement must be performed within approximately 6 milliseconds.

To understand the operating principles behind the AC elastoresistivity technique, consider a four-contact resistivity measurement using standard phase sensitive detection. An excitation current  $I(t)$  described by

$$I(t) = I_0 \cos(\omega_c t) \quad (2.2)$$

passing through a sample generates a voltage  $V(t)$

$$V(t) \propto \rho_{ij} I(t) \quad (2.3)$$

where which component of  $\rho_{ij}$  is used depends on details of the sample and current orientation. If the sample strain  $\varepsilon_{kl}(t)$  is simultaneously modulated at a different frequency  $\omega_s$ , such that

$$\varepsilon_{kl}(t) = \varepsilon_{kl}^0 \cos(\omega_s t) \quad (2.4)$$

then the existence of a finite elastoresistivity  $m_{ijkl}$  will result in a modulation of the sample resistivity:

$$\rho_{ij}(t) = \rho_{ij}^0 (1 + m_{ijkl} \cos(\omega_s t)) \quad (2.5)$$

where the superscript 0 denotes the resistivity for  $\varepsilon_{kl} = 0$ . The detected voltage is then described by an amplitude-modulated sine wave

$$V(t) \propto \rho_{ij}^0 I_0 (1 + m_{ijkl} \cos(\omega_s t)) \cos(\omega_c t) \quad (2.6)$$

$$\propto \rho_{ij}^0 I_0 \cos(\omega_c t) + \rho_{ij}^0 I_0 m_{ijkl} [\cos((\omega_c + \omega_s)t) + \cos((\omega_c - \omega_s)t)]. \quad (2.7)$$

The frequency spectrum of this signal consists of on large peak centered on the “carrier” frequency  $\omega_c$  which is flanked by two “sideband” peaks at  $\omega_c \pm \omega_s$ .<sup>2</sup> While it should again be emphasized that the relevant components of the resistivity, strain, and elastoresistivity tensors, as well as the constant of proportionality in Eq. (2.6) depend on the orientation of the current, voltage contacts, crystal axes, and externally applied stresses, the elastoresistivity component  $m_{ijkl}$  can be calculated as the ratio of the amplitudes of the sideband and carrier peaks divided by the amplitude of the strain oscillation.

One possible practical implementation for actually extracting these peak amplitudes the elastoresistivity using this technique is shown in Fig. 2.3. A sinusoidal voltage is applied to a piezoelectric actuator at  $\omega_s$ , which tunes the strain in the sample, and the current excitation at  $\omega_c$  is passed into the sample. The resulting signal is fed into a lock-in amplifier to perform the signal demodulation. The mixer at the heart of a lock-in amplifier shifts the carrier down to DC ( $\omega = 0$ ), bringing the sidebands to  $\omega_s$ . A copy of the carrier signal is also generated at  $2\omega_c$  with sidebands at  $2\omega_c \pm \omega_s$ , which is attenuated by the low-pass filter. The resulting signal consists of a DC offset voltage proportional to the amplitude of the carrier signal with a superimposed oscillation at the strain frequency. The DC component can be measured as the time-averaged signal of the lock-in amplifier, and the oscillating component can be measured by a second lock-in amplifier referenced to the strain frequency.

When using a lock-in amplifier for electrical demodulation, the characteristics of the low-pass filter on the output are crucial. The cutoff frequency should be at least a decade lower than any harmonics of the carrier frequency, but a decade higher than the strain frequency—otherwise the modulation signal will be attenuated as well. When these conditions cannot be met, some attenuation

---

<sup>2</sup>The terminology used here derives from the theory of amplitude modulation (AM) radio, which operates on the same basic principles. In case of AC elastoresistivity, the sample itself acts like the mixer at the heart of an AM transmitter, although at significantly lower frequencies.

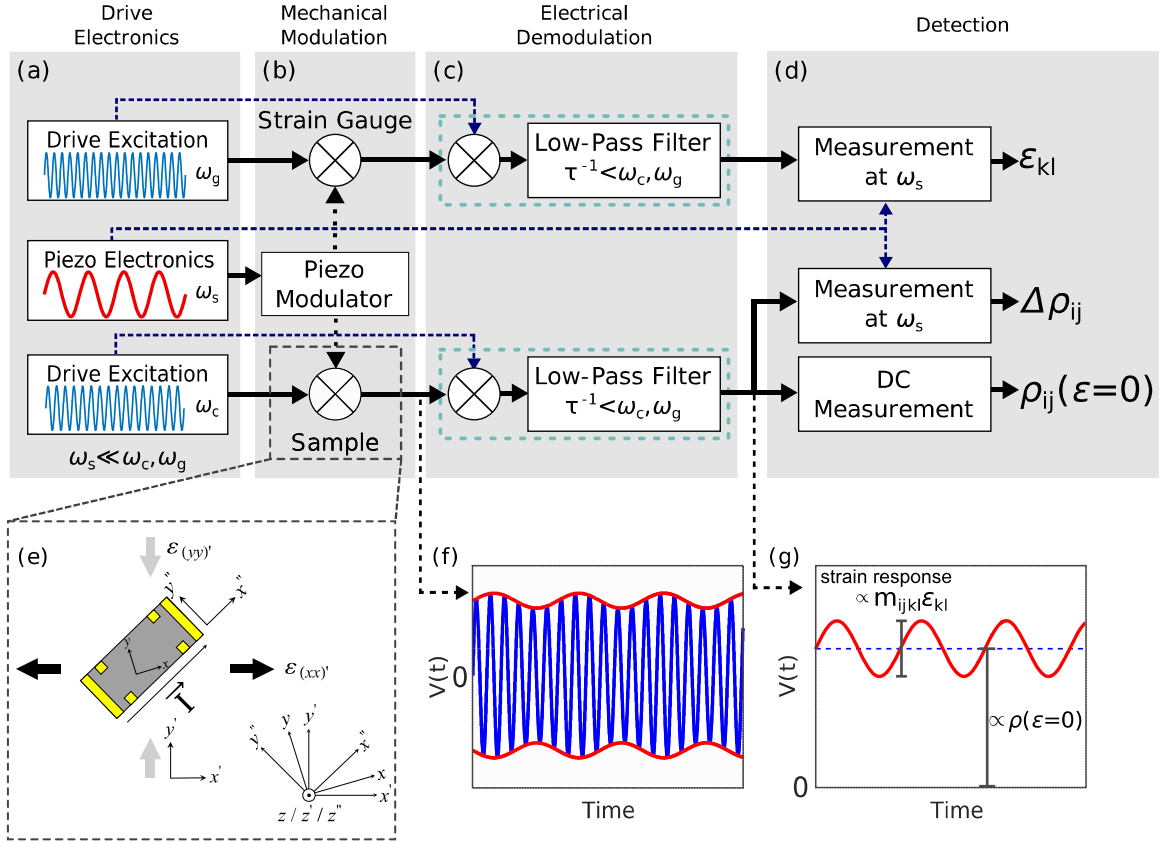


Figure 2.3: Schematic of the experimental setup for the AC elastoresistivity technique. (a) A current at carrier frequency  $\omega_c$  is passed through a sample while the sample is strained by a piezoelectric actuator at a frequency of  $\omega_s$ . (b) The elastoresistivities of both the sample and a resistive strain gauge cause act like an analog mixer, multiplying the waveforms generated in panel (a) of the current excitation with the strain-modulated resistivity and resulting in amplitude modulated waveforms like that seen in (f). (c) The action of a lock-in amplifier performs a demodulation stage and measures the DC offset while isolating the modulated component (g). Faithful extraction of the modulation requires careful attention to behavior of the low pass filter intrinsic to the lock-in amplifier. (d) A second lock-in amplifier quantifies the oscillation at  $\omega_s$ . (e) schematic of the sample being measured—the relative alignment between the crystal axes, the piezoelectric stress, and the current flow direction dictates which components of  $m_{ijkl}$  contribute to the signal. Reproduced from Hristov et al “Measurement of elastoresistivity at finite frequency by amplitude demodulation.” *Rev. Sci. Instrum.* **89**, 103901 (2018), with the permission of AIP Publishing.

of the sideband signal is to be expected. As long as the filter transfer function is well-characterized, one can correct for this attenuation, although at the cost of a lower signal-to-noise ratio.

In this implementation, the strain is measured using a resistive strain gauge, which is simply a patterned metallic foil with a well-known elasto-resistive gauge factor, usually approximately 2. In this case, duplicating the same signal processing pipeline for the strain gauge as is used for the sample provides a measurement of the AC and DC strain components. Other implementations, such as optical measurements of the strain with a fiber Bragg grating[131, 130] or capacitive measurements of displacement[132] are also possible. In principle, the same signal processing steps for both the strain and sample measurements could also be performed entirely in software, provided the voltage signal can be digitized at a fast enough rate.[130]

The elasto-resistivity measurements on  $\text{ErTe}_3$  and  $\text{TmTe}_3$  presented in Chapter 4 were performed using a carrier frequency of approximately 1.2 kHz and strain frequencies in the range of 20-80 Hz. The strain was detected using the same cascaded lock-in amplifier setup as in Fig. 2.3, but using a capacitive sensor rather than a resistive one. A custom-built auto-balancing bridge, which is described in detail in Appendix A, was used to convert the changing capacitance into an amplitude modulated signal.

### 2.2.3 Elastocaloric effect measurements

The elasto-resistivity tensor contains a wealth of symmetry-motivated information about electrons in a metal, but is only directly sensitive to the behavior of quasiparticles within  $\pm k_B T$  of the Fermi level. Strain-induced changes in other degrees of freedom only contribute to the elasto-resistivity signal through the interaction with the itinerant charge carriers. The elastocaloric effect (ECE), which relates changes in entropy to changes in strain, is a complementary thermodynamic probe which is sensitive to any degrees of freedom which are affected by strain. There two equivalent definitions of the ECE in common usage. The first considers the magnitude of a change in entropy induced by an isothermal change in strain, and the second considers the change in temperature induced by an adiabatic change in strain. For the purposes of this work, I will consider only the latter definition.

Applying stress to a material always requires thermal contact, which makes truly adiabatic conditions impossible. The most common workaround for measuring the temperature change under strain is simply to strain a material quickly, and measure the time evolution of the temperature in reaction to the shock. This technique has been applied most commonly to study the first-order martensitic transition in metals known as shape-memory alloys (SMAs). This transition is of practical interest for use in elastocaloric cooling technologies, a promising form of solid state refrigeration, on account of the large strain susceptibility of the martensitic state as well as the large latent heat involved with switching from one orientation to the other. Within the context of strongly correlated materials, however, such large strains are often destructive (especially for brittle or layered samples which cleave easily) and are difficult to generate *in situ* at cryogenic temperatures where many of the

interesting ordered states occur. An alternative technique is to employ small, sinusoidally oscillating strains in the same way as the AC-elastoresistivity technique presented above. If the strain frequency can be set high enough, the elastocaloric temperature change oscillates faster than the thermal relaxation rate, providing quasi-adiabatic behavior within the sample.

It should be noted that the elastocaloric effect is distinct from changes in internal energy due to mechanical work being done on the sample. The elastocaloric effect changes sign as the strain changes sign—if a material cools under tension, it will heat under compression, and vice versa. Both tension and compression, when starting from the neutral state of a freestanding crystal, do positive work, such that the temperature change arising from the work oscillates at twice the frequency of the strain. If the strain oscillation is superimposed on a constant offset, however, then the mechanical work component can produce a background signal at the measurement frequency.

Working in the adiabatic limit ( $dS = 0$ ) the magnitude of the elastocaloric effect is directly related to several other thermodynamic quantities through a generalized Ehrenfest relation:

$$\left( \frac{dT}{d\varepsilon_{ij}} \right)_S = -\frac{T/C_\sigma}{\alpha_{ij}} C_{ijkl} \quad (2.8)$$

where  $C_\sigma$  is the specific heat at constant stress,  $\alpha_{ij}$  is the thermal expansion coefficient, and  $C_{ijkl}$  is the elastic stiffness tensor.[133, 134]

Near a strain-tuned continuous phase transition, however, critical fluctuations can also significantly alter the elastocaloric response. Consider an isothermal change in strain at temperature  $T$ ; if the strain alters the critical temperature  $T_c$ , then the reduced temperature  $t = (T - T_c)/T_c$  will shift in the opposite direction. The critical exponent scaling which controls the correlation length ( $\xi \sim |t|^{-\nu}$ ) then implies that the contribution of critical fluctuations to the entropy at  $T$ . An immediate corollary of this is that an adiabatic change in strain near a continuous phase transition will induce a change in temperature in order to maintain the total entropy. To linear order this effect can be quantified as

$$\left( \frac{dT}{d\varepsilon_{ij}} \right)_S = \frac{C_\sigma^{(c)}}{C_\sigma} \frac{dT_c}{d\varepsilon_{ij}} \quad (2.9)$$

where the superscript  $(c)$  denotes the contribution to the specific heat of the critical fluctuations.

This relation is just one piece of a more general correspondence between various thermodynamic and transport properties in the presence of critical fluctuations. It was first established by Fisher and Langer in 1968[108] for the case of a magnetic phase transition that the singular behavior of the resistivity  $\rho$  (or more precisely, the temperature derivative of the resistivity  $d\rho/dT$ ) depends on the spin-spin correlation function. The same correlation function also dictates the shape of the anomaly in the specific heat  $C_p$ , such that

$$C_p^{(c)}(t) \propto \left( \frac{d\rho^{(c)}}{dT} \right)(t) \quad (2.10)$$

where  $t = (T - T_c)/T_c$  is the reduced temperature. This correspondence in fact holds for continuous phase transitions of any nature, not just magnetic critical points; critical fluctuations of any sort contribute to the heat capacity and resistivity in the same way, although the constant of proportionality in Eq. (2.10) may differ. In the case where an external parameter such as strain alters the critical temperature  $T_c$ , this relation can be generalized further to read[128]

$$C_p^{(c)}(t) \propto \left( \frac{d\rho^{(c)}(t)}{dT} \right)_\varepsilon \propto \left( \frac{dU^{(c)}(t)}{d\varepsilon_{ij}} \right)_T \propto \left( \frac{d\rho^{(c)}(t)}{d\varepsilon_{ij}} \right)_T \quad (2.11)$$

Physically, where the first two terms correspond to the response of thermodynamic and transport properties to changing sample temperature  $T$ , the latter two describe the response to changing *reduced* temperature  $t$  as  $T_c$  shifts under strain. As all of these responses stem from the same critical fluctuations, all of them must carry the same singular behavior at the phase transition, up to a factor of proportionality.

Perhaps the biggest advantage of using the elastocaloric effect to probe a material’s thermodynamic properties comes from the low background signal. Unlike the specific heat, for example, where every phonon mode, electron state, and local magnetic moment contributes, ECE measurements are sensitive only to those degrees of freedom which change with strain. For most materials, this means that the ECE signal primarily arises from the symmetry-breaking ordered phases and related fluctuations, while “trivial” changes such as strain-induced modifications to the sound velocity hardly contribute at all. This strain-selectivity makes the ECE a highly sensitive probe of thermodynamic effects of strain, as well as a promising technique for detecting thermodynamic anomalies at high temperatures where specific heat techniques are challenging.

For the experiments presented in Chapter 4, elastocaloric temperature oscillations of a sample under AC strain was detected using type E thermocouples (constantan-chromel)[135]. The thermocouple (TC) junction is formed using a home-built spot-welder to connect 12.5  $\mu\text{m}$  diameter wires, where the smallest possible wire diameter is used in order to minimize the heat capacity and thermal leakage of the sensor. The junction is then connected to the surface of the sample with epoxy. The reference junction is formed at a pair of copper pads which are thermally (but not electrically) connected to the CS-100 cell body. The total resistivity of the thermocouple including the junction and the thin wires is approximately 60  $\Omega$ . A low-noise signal transformer (SR554, operated in passive mode) amplifies the signal by a factor of 100, followed by a preamplifier (SR560) which provides further amplification by a factor of 20. The amplified signal is then detected with an SR830 or SR860 lock-in amplifier. Prior to an AC-ECE measurement, the frequency dependence of the transformer and preamplifier gain is measured by placing an AC current source in parallel with the thermocouple and passing a small current through the thermocouple, while simultaneously measuring the amplitude and phase at both the input to the transformer and the output of the preamplifier.

The conditions for “quasi-adiabatic” temperature oscillation require a careful selection of the

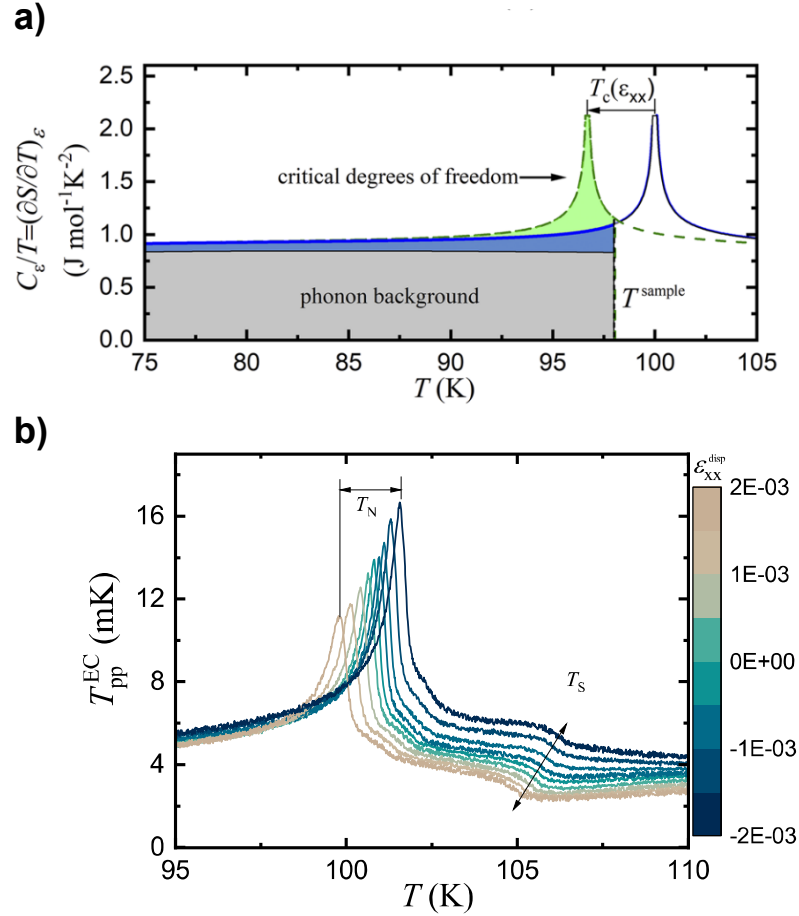


Figure 2.4: Expectations in the elastocaloric effect in the vicinity of a second order phase transition. (a) Schematic diagram of the heat capacity divided by temperature  $C_\epsilon/T$  as a function of temperature. The area under this curve, integrated from  $T = 0$  to the sample temperature, corresponds to the total entropy. If a strain  $\epsilon_{xx}$  suppresses the critical temperature  $T_c$ , the heat capacity peak also decreases in temperature (blue solid line to green dashed line). The new state has significantly more entropy due to the addition of the green shaded region; an isentropic change in strain would require  $T_{\text{sample}}$  to decrease in order to preserve the area under this curve. (b) AC-ECE measurements on  $\text{Ba}(\text{Fe}_{1-x}\text{Co}_x)_2\text{As}_2$  near the antiferromagnetic and electronic nematic transitions as a function of temperature and offset strain (line color). The peaks correspond to exactly the scenario presented in panel (a). Figures reproduced from Ikeda et al “AC elastocaloric effect as a probe for thermodynamic signatures of continuous phase transitions”. *Rev. Sci. Instrum.* **90**, 083902 (2019), with the permission of AIP Publishing. Data taken by M. Ikeda.

strain frequency  $f$ ; if  $f$  is too low the sample will thermalize with the bath through the connection to the mounting plates, and if  $f$  is too high the thermocouple will no longer faithfully follow the temperature oscillation within the sample. The reader is referred to Chapter 3 for a more in-depth discussion of optimizing AC-ECE measurements and the frequency dependent sensitivity inherent to this technique.

### 2.2.4 Sample mounting

The quality of the mechanical coupling between the sample and the uniaxial stress cell is a major contributor to the quality of a given experiment. The process used in preparing samples of  $R\text{Te}_3$  for uniaxial stress measurements is as follows. First, the bottom mounting plates are epoxied in place along the edges. Adhesion between the glue and mounting plates is maximized by roughening the mounting surfaces which will hold the sample. The sample is electrically isolated from the lower mounting plate by a thin piece of tissue paper which is impregnated in epoxy. The sample is held in place by two more beads of epoxy, and both a spacer washer and a top mounting plate is applied on top, held in place by a mounting screw. The spacer serves to ensure the sample is not crushed during the clamping process, and also produces a reliable thickness of epoxy between the plates.

Two different epoxies are used in the mounting process. The bottom mounting plates are held in place with a quick-drying “5-Minute” epoxy from DuPont. This connection is most important during the mounting process itself to ensure that the bottom plates do not rotate once the sample is in place, causing the sample to bend or tear. During the measurement itself, however, the plates are also held in place by the mounting screws. A stronger material, DuPont “Two-Ton” epoxy, is used for the sample itself in order to minimize the risk of the glue delaminating from the sample or mounting plates. Two-Ton epoxy requires several hours to fully cure, even at elevated temperatures. To ensure high strength connections while preserving the air-sensitive  $R\text{Te}_3$  sample, the epoxy was allowed to cure on a hot plate inside an inert atmosphere glovebox at  $60^\circ\text{C}$  for 8-12 hours. This is made both possible and practical by a detachable probe head; the copper piece on which the stress cell was mounted could be disconnected from the probe without disturbing the sample, and all necessary wiring for the sample, stress cell, and thermometry was equipped with easily detachable connectors.

### 2.2.5 Strain detection and calibration

In an ideal strain-tuning apparatus, every component would be infinitely stiff compared to the sample. In reality of course this is not the case, and the softest component is the epoxy which holds the sample in place. Finite element simulations of the stress and strain distribution in the sample mounting scheme[136] suggest that for realistic parameters (in the case of an iron-pnictide superconductor sample) the real stress in the sample is approximately 70% of the ideal value, and is fairly constant for a wide range of elastic stiffness parameters in the epoxy. The strain is, however, fairly uniform within the freestanding regions of the sample itself, and relaxes exponentially within

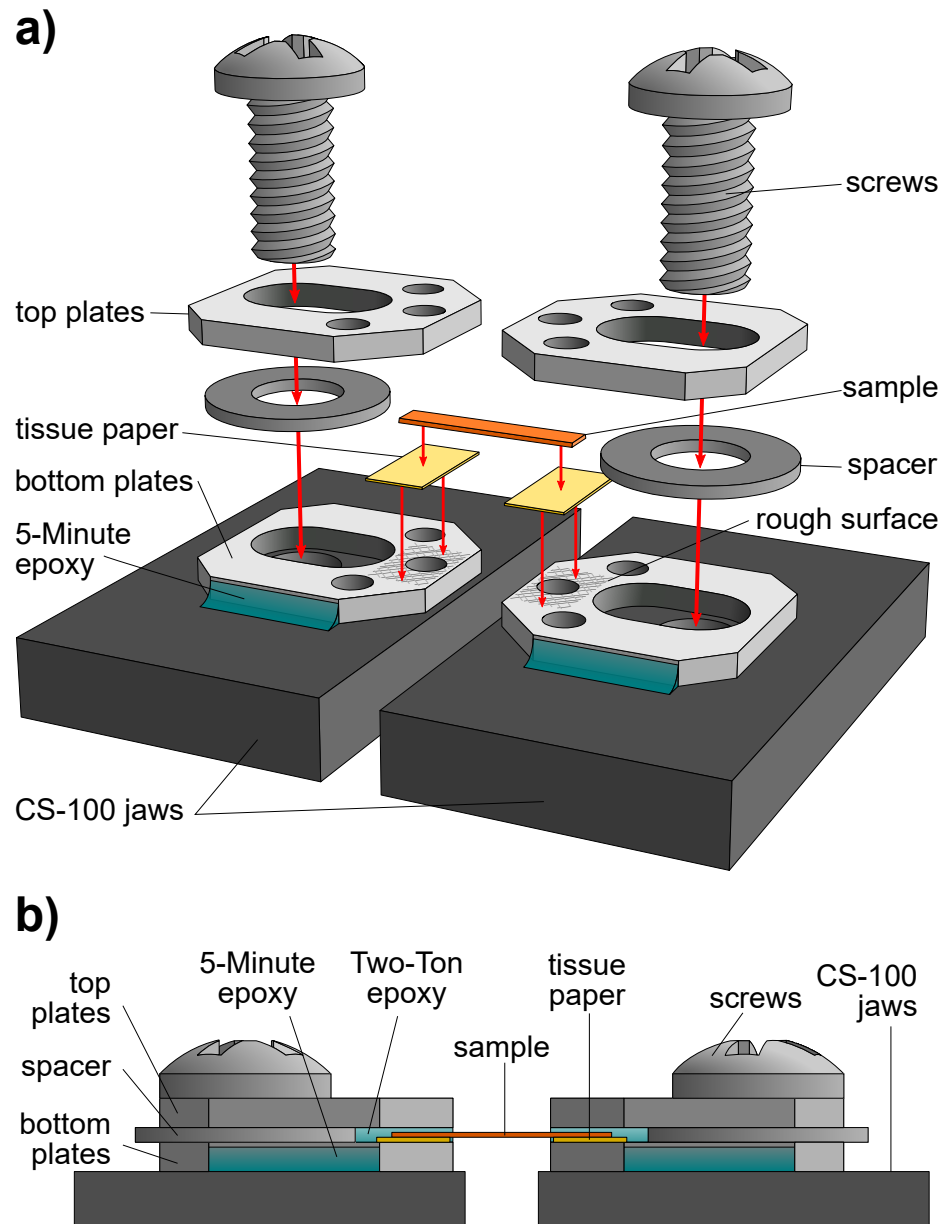


Figure 2.5: Schematic of the sample mounting process for the CS-100 uniaxial stress cell. Panel (a) shows the components in an exploded view. The bottom mounting plates are first screwed in place alone, and small amounts of epoxy are applied to the edges to keep the plates in place. The screws are then removed, and a thin layer of tissue paper is epoxied to the roughened surfaces of the mounting plates. Once this has dried, the sample, spacers, and mounting plates are assembled, epoxied, and the screws are inserted again to hold everything together. The top mounting plates are then screwed in place and any Panel (b) shows a side view of the completed sample mounting assembly. The spacer between the top and bottom mounting plates ensures that the samples is not crushed between the mounting plates.

the glued regions, as discussed in Chapter 3 and [136]. From the point of view of the elastocaloric effect, the inhomogeneity of strain within the clamped region of the sample has very little effect on the result. Resistivity and elastoresistivity are more sensitive to strain inhomogeneities and any resulting deviations in the current path within the sample. To minimize the issue here, all of the electrical contacts for resistivity and elastoresistivity under stress are placed on the freestanding region, rather than within the glued and clamped sections.

For a sample of length  $L$  and a relative jaw displacement of  $\Delta L$ , the linear strain  $\varepsilon$  in the sample is given by  $\varepsilon = \Delta L/L$ . (The relationship of this  $\varepsilon$  to specific components of the strain tensor depends on the crystallographic orientation of the sample.) The sample length  $L$  can be measured optically with a calibrated microscope. The *in situ* displacement, however, requires a sensor embedded in the cell. *Razorbill* CS-100 cells incorporate a capacitive displacement sensor for this purpose, with one plate attached to either jaw.

The displacement between the jaws generates a capacitance  $C$  of

$$C = \frac{\epsilon_0 A}{d_0 + \Delta L} + C_p \quad (2.12)$$

where  $\epsilon_0$  is the permittivity of free space,  $A$  is the plate area,  $d_0$  is the neutral plate spacing,  $\Delta L$  is the displacement, and  $C_p$  is an extra parasitic capacitance from fringing fields or coupling to sensor housing. All of the parameters except  $\Delta L$  are known or calibrated by the manufacturer. The total capacitance is on the order of 1 pF.

Constant or slowly varying capacitance values can be measured *in situ* with phenomenal precision using commercial bridges such as the *Andeen Hagerling* AH2700A.[137] However, the uncommon problem of quantifying small, fast, periodic changes in capacitance—like those generated by the use of AC strains for elastoresistivity and elastocaloric effect measurements—does not have a simple off-the-shelf solution. In order to solve this problem, a custom-built capacitance bridge was designed and built to convert the capacitance signal into an amplitude modulated voltage, which could then be detected using the same demodulation setup as the AC elastoresistivity technique. The instrument was capable of resolving sub-femtofarad changes in capacitance at strain frequencies up to 1 kHz. The resolution of this system is two orders of magnitude worse than that of the AH2700A for quasi-static capacitances, but several orders of magnitude better than the AH2700A at frequencies greater than approximately 10 Hz. A more in-depth discussion of the detection of modulated capacitance values is available in Appendix A.

## Chapter 3

# Frequency-dependent sensitivity of AC elastocaloric effect measurements explored through analytical and numerical models

*In this chapter, a comprehensive study of the frequency-dependent sensitivity for measurements of the AC elastocaloric effect based on both exactly soluble models and numerical methods to the oscillating heat flow problem is presented. These models reproduce the finer details of the thermal transfer functions observed in experiments. Conducting this study allows one to propose a set of practical guidelines for experimentalists using this technique. This chapter also establishes a baseline against which the frequency response of the AC elastocaloric technique can be compared and provides intuitive explanations of the detailed structure observed in experiments. This chapter is taken nearly verbatim from [138]. This work was supported by the U. S. Department of Energy (DOE) Office of Basic Energy Science, Division of Materials Science and Engineering at Stanford under contract No. DE-AC02-76SF00515.*

### 3.1 Introduction

The elastocaloric effect (ECE) describes the dependence of a material's entropy on externally imposed strain. This can be quantified either by measuring the change in entropy  $S$  resulting from isothermal changes in strain  $\varepsilon_{ij}$ , or by measuring the change in temperature resulting from adiabatic changes in strain. For the purposes of this work, we adopt the latter definition. The

simplest and most common technique for measuring the ECE is simply to measure the temperature during a single rapid application of compressive or tensile strain. This technique has been applied extensively in studying materials such as shape-memory alloys, which show significant promise for solid-state elastocaloric refrigeration due to the high latent heat of strain-induced martensitic transitions.[139, 140, 141, 142, 143] The ECE is, however, a much more general feature of the solid state; any change of entropy induced by strain, regardless of the microscopic details, is necessarily reflected in an elastocaloric temperature change under adiabatic conditions. While few materials are expected to have as dramatic an ECE response as shape-memory alloys, uniaxial stress and the accompanying symmetry-breaking strains have emerged in recent years as versatile tuning parameters for the phases and phase transitions in several families of strongly correlated materials.[123, 144, 18, 145, 146] Consequently, ECE measurements have the potential to directly probe changes in the entropy of these strain-sensitive materials. However, the large deformations required for conventional ECE measurements are not well-suited to these materials, which are often brittle, highly anisotropic, or cleave easily under stress. With this in mind, Ikeda et al [134] developed the use of small oscillating (AC) strains to measure the elastocaloric effect. In an AC-ECE measurement, a bar-shaped sample is glued or clamped between a pair of mounting plates, which then apply a small oscillating stress to the sample, as shown in Fig. 3.1(a). The resulting temperature oscillations are detected with a small thermometer (usually a thermocouple) attached to the center of the freestanding section.

The development of the AC-ECE technique presents several benefits for fundamental research. Firstly, AC-ECE enables the use of phase-sensitive detection, enabling long averaging times and high resolving power. Furthermore, the ability to detect small signals makes it possible to use much smaller strains than conventional techniques, preventing sample fatigue effects and operating in a regime of linear response to changes in both strain and temperature. Modern piezoelectric technology easily facilitates the *in situ* application of small oscillating stresses at temperatures spanning from above room temperature to below 1 K, such that a single apparatus can access large regimes of phase space.[116] Finally, by introducing frequency as a new tuning parameter, the AC-ECE creates the possibility of exploring dynamical effects intrinsic to the sample material, such as the motion of domain walls[129].

At the most basic level, the elastocaloric effect can be modeled as a series of discrete thermal elements, as illustrated in Fig. 3.1(a). A sample with heat capacity  $C_s$  is coupled with thermal conductance  $K_b$  to a thermal reservoir at temperature  $T_0$  and with thermal conductance  $K_t$  to a thermometer of heat capacity  $C_t$ . We define thermal relaxation times of the sample and thermometer as  $\tau_s = C_s/K_b$  and  $\tau_t = C_t/K_t$ , respectively, and assume that  $\tau_t < \tau_s$ . The sample is then exposed to endogenous heating and cooling within the strained section which oscillates sinusoidally at frequency  $f$ .

This simple model describes the asymptotic behavior of the AC-ECE. In the limit  $f \ll \tau_s^{-1}$ , the

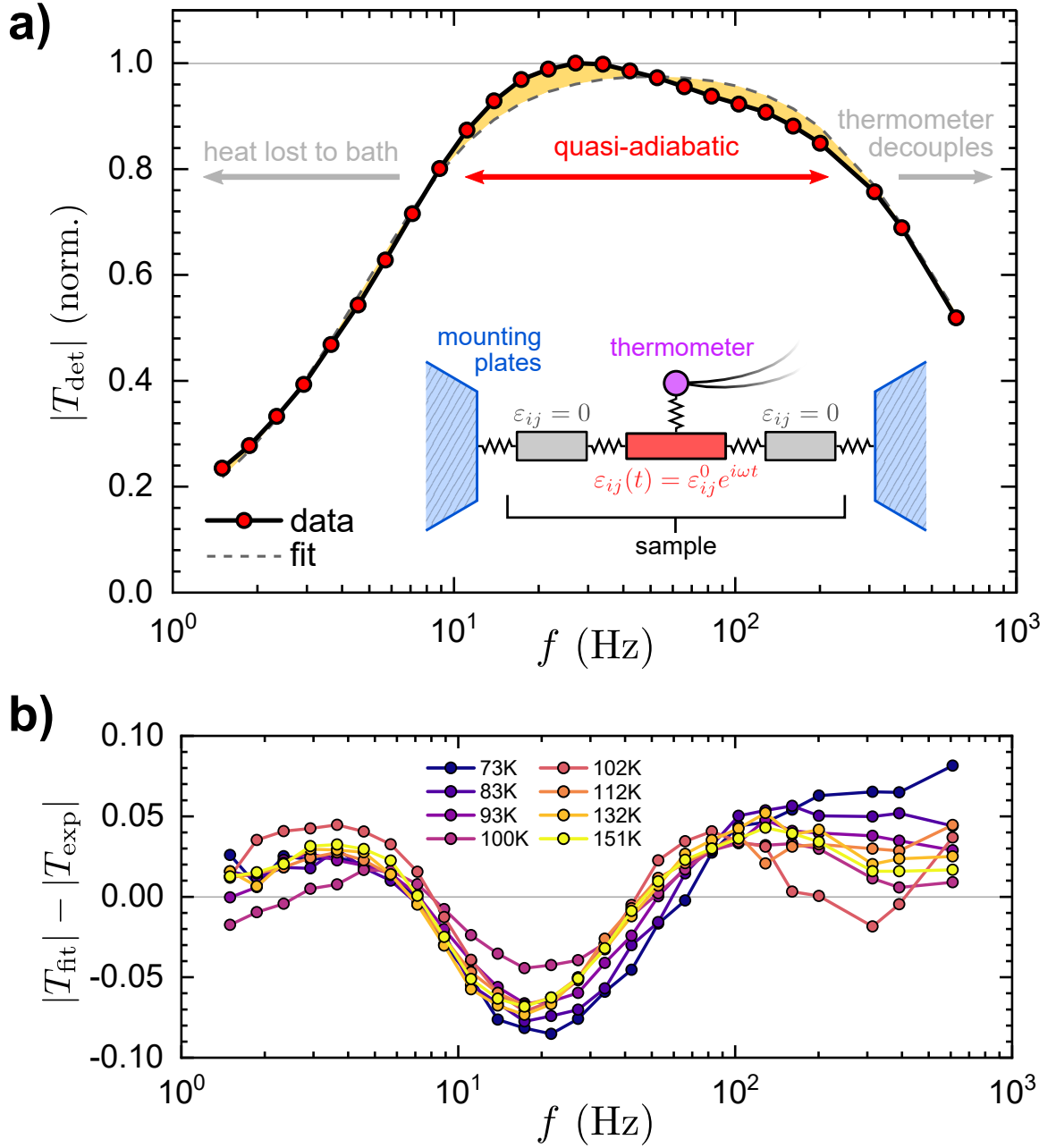


Figure 3.1: The frequency-dependent magnitude of the temperature oscillation signal observed in the AC-ECE. (a) Magnitude of the observed temperature oscillation  $T_{det}$  as a function of frequency for an AC-ECE measurement of a sample of  $\text{Ba}(\text{Fe}_{1-x}\text{Co}_x)_2\text{As}_2$  at 100 K. Shaded regions highlight the deviations of the data from the best fit prediction for the simplest discrete model. A schematic of this model is shown in the inset. (b) Residuals of fits like the one shown in panel (a) for a series temperatures. The primary goal of this paper is to provide an understanding of the consistent deviations in experimental data from the fits.

temperature of the thermometer  $T_t$  and the sample  $T_s$  only experience small oscillations about the bath temperature  $T_0$ . In the limit of  $f \gg \tau_t^{-1}$ , the sample temperature oscillates around  $T_0$  with amplitude  $T_\infty = QC_s^{-1}$ , where  $Q$  represents the effective heat generated by the elastocaloric effect. The thermometer temperature, however, again performs vanishingly small oscillations around  $T_0$  due to the finite thermal relaxation time of the thermometer. The magnitude of the thermometer temperature oscillation reaches a maximum at intermediate frequencies, and the transfer function has a flat plateau in the range  $\tau_s^{-1} < f < \tau_t^{-1}$  with no dependence on frequency.

As a concrete example, we consider the case of a prototypical iron-based superconductor material,  $\text{Ba}(\text{Fe}_{1-x}\text{Co}_x)_2\text{As}_2$ . These materials exhibit a coupled electronic nematic/orthorhombic phase transition as well an antiferromagnetic transition, both of which have been shown to be highly sensitive to strain.[136]. The frequency-dependent AC-ECE signal is presented in Fig. 3.1(a) for a sample of this material for  $x = 0.021$  measured at 100 K.

The best fit of the simple discrete model to the experimental result is plotted on the same axis, and it can easily be seen that the experimental results deviate in several nontrivial ways. First, the corner between the low and intermediate frequency ranges always appears significantly sharper than this model would predict. Secondly, the predicted flat plateau is replaced by a sloping shoulder. Incorporating a frequency dependence to the ratio of the thermometer and sample heat capacities (a consequence of a finite thermal length  $\xi \equiv (D/f)^{-1/2}$ , where  $D = k_s/C_s$  is the thermal diffusivity of the sample[147, 134]) does slightly suppress the high frequency response, but improvement in fit quality is minor.

The consistent behavior of the residuals of the fit (Fig. 3.1(b)) indicates that this simple model overlooks some nontrivial details in the frequency-dependent sensitivity of the AC-ECE technique. Without a quantitative theoretical understanding of the frequency-dependent behavior of the AC-ECE, the overall signal magnitude cannot be ascertained with confidence. Also, the present understanding of the details of heat transfer during a measurement is also insufficient to identify or rule out experimental artifacts which could contribute to these deviations. Finally, frequency-dependent dynamical behavior intrinsic to the sample will also be at least partially masked by the experimental sensitivity. A thorough understanding of the practical frequency dependence effects is critical to interpreting the empirical results and in benchmarking the quality of a given measurement. This work seeks to establish both a detailed description and an intuitive interpretation of the frequency-dependent sensitivity inherent in thermocouple-based AC-ECE measurements.

We begin in Section 3.2 by establishing a formal definition of the frequency-dependent AC-ECE sensitivity function  $\Gamma(\omega)$ . In Section 3.3, we present a pair of exactly soluble models for the low-frequency component of  $\Gamma(\omega)$  which exhibit and provide an intuitive basis for understanding the low frequency behavior. We then describe the setup and implementation for our finite element calculations in Section 3.4, and then use this model to describe the contributions to  $\Gamma(\omega)$  arising from practical effects such as sample mounting and thermometer characteristics in Section 3.5. Finally

in Section 3.6 we solve for the full sensitivity function with the finite element method, revisit the comparison of these results to experimental results, and provide an empirical method for estimating the peak sensitivity in a given measurement.

## 3.2 Statement of the problem

Consider a bar-shaped sample composed of a material with volumetric heat capacity  $c(\mathbf{r})$  and thermal conductivity  $k(\mathbf{r})$ . We define the elastocaloric tensor  $\eta_{ij}$  of the sample material as

$$\eta_{ij} \equiv \left( \frac{dT}{d\varepsilon_{ij}} \right)_S \quad (3.1)$$

and we assume for now that the sample experiences a spatially homogeneous time-varying strain  $\varepsilon_{ij} = \varepsilon_{ij}^0 e^{i\omega t}$ . In general,  $\eta_{ij}$  may carry a frequency dependence and may take on complex values  $\eta_{ij} = \eta'_{ij}(\omega) + i\eta''_{ij}(\omega)$  reflecting the dynamical behavior of the material. However, for the purposes of this work we enforce  $\eta''_{ij}(\omega) = 0$  and  $d\eta_{ij}/d\omega = 0$ . The sample temperature oscillation in the adiabatic limit  $T_\infty$  will therefore be given by

$$T_\infty(\mathbf{r}, t) = \eta_{ij} \varepsilon_{ij}^0(\mathbf{r}) e^{i\omega t}. \quad (3.2)$$

The goal of the AC-ECE technique is to use this oscillating temperature signal to accurately quantify  $\eta_{ij}$ .

Deviations from the ideal adiabatic limit due to practical constraints can be described by a complex-valued sensitivity function  $\Gamma(\omega)$  such that the temperature oscillation  $T_{\text{det}}(t)$  detected by a thermometer at position  $\mathbf{r}_0$  is given by

$$T_{\text{det}}(t) = \Gamma(\omega) T_\infty(t) = \Gamma(\omega) \eta_{ij} \varepsilon_{ij}^0 e^{i\omega t} \quad (3.3)$$

We can separate the impacts of different practical limitations by writing the sensitivity as a product  $\Gamma(\omega) = \Gamma_b(\omega) \Gamma_t(\omega)$ . Here  $\Gamma_b(\omega)$  describes the loss of heat due to coupling to the bath, which is the dominant deleterious effect at low frequencies.  $\Gamma_t(\omega)$  describes sensitivity losses due to poor coupling of the thermometer to the sample, which dominates at high frequencies.

The sound velocity in most solids is typically several thousand meters per second; for a millimeter-scale sample, a sound wave traverses the entire sample in  $\lesssim 1 \mu\text{s}$ . Current technology imposes an upper bound on the range of accessible strain frequencies at approximately 10 kHz.<sup>1</sup> The minimum applicable strain oscillation period is then two orders of magnitude greater than both the

---

<sup>1</sup>Piezoelectric actuators can, and often are, operated at strain frequencies well into the ultrasound range. However, incorporating piezoelectric actuators into a uniaxial stress cell assembly[116] lowers resonance frequencies and creates a risk of vibrational fatigue within epoxies and the piezoelectric actuators themselves. Careful design of future devices may raise this practical upper bound.

shock propagation time as well as the estimated thermoelastic relaxation times for most solids.[148] Additionally, the amplitude of both the strain and temperature oscillations are assumed to be small, which justifies the use of constant values of  $c(\mathbf{r})$  and  $k(\mathbf{r})$ . (The position dependence of these parameters reflects only the possibility of regions of different materials, such as the sample and the mounting plates—the heat capacity and thermal conductivity are assumed to be homogeneous throughout a given material.) As a consequence, the simplest Fourier heat flow model can be expected to capture the observable phenomena without requiring recourse to a full set of hyperbolic thermoelastic partial differential equations.[149, 150, 151] Similarly, second sound effects are not included in this work.

Linear response (small strain oscillations and small temperature oscillations) justifies the use of the standard heat equation in describing heat transfer in AC-ECE measurements:

$$c(\mathbf{r})\frac{dT(\mathbf{r}, t)}{dt} = k(\mathbf{r})\nabla^2 T(\mathbf{r}, t) + Q(\mathbf{r}, t) \quad (3.4)$$

where  $T(\mathbf{r}, t)$  is the temperature profile within the sample, and the source term  $Q(\mathbf{r}, t)$  simulates the elastocaloric effect. This source term does not represent conductive, radiative, or convective heat transfer between the sample and another body, but rather the redistribution of entropy between various microscopic subsystems within the sample. One example would be entropy due to fluctuations in electronic degrees of freedom near a continuous phase transition—if a change in the sample strain alters the total entropy in these fluctuations, isentropic conditions dictate that the sum of all other degrees of freedom in the sample (phonons, magnetic moments, etc.) must experience an equal and opposite change in entropy, which is reflected in a change in temperature. Away from the adiabatic limit heat may flow into or out of the sample, and this will suppress the observed temperature oscillation. However, this effect is described solely by the Fourier heat conduction term proportional to  $k(\mathbf{r})$ , not the elastocaloric heat generation term  $Q(\mathbf{r})$ .<sup>2</sup>

With these physical definitions, Eq. (3.4) holds regardless of the functional form of  $Q(\mathbf{r}, t)$ . However, we specialize to the case of sinusoidal strains, taking as an ansatz  $Q(\mathbf{r}, t) = Q_0 e^{i\omega t}$ . We define the magnitude and phase  $Q_0$  of the heat term in the adiabatic limit  $\omega \rightarrow \infty$ , or, equivalently,  $k \rightarrow 0$ . In this limit, Eqs. (3.3) and (3.4) show that

$$Q_0(\mathbf{r}) = i\omega\eta_{ij}c\varepsilon_{ij}^0(\mathbf{r}). \quad (3.5)$$

Equivalently, the source term in Eq. (3.3) is linear in the ECE tensor, the volumetric heat capacity,

---

<sup>2</sup>Changes of strain imply that work is being done on the sample, changing the internal elastic energy even in the adiabatic limit. This would also result in a change in the sample temperature; but since both compressive and tensile deformations of a solid at equilibrium requires positive work, an oscillation at frequency  $f$  about the strain-neutral condition generates temperature oscillations at frequency  $2f$ , which will not affect phase sensitive measurements. If the oscillation is superimposed on a constant strain offset, there *will* be a contribution to the signal at  $f$  arising from the work done on the sample. Both the conventional elastocaloric effect and the elastic energy away from the strain-neutral point, however, can be lumped together into our definition of  $Q(\mathbf{r}, t)$ .

and the rate of change of strain. Throughout this work, we assume that the magnitude of the strain oscillation is known—this must be measured independently of the temperature oscillation. Techniques for quantifying oscillating strain are beyond the scope of this paper, and the reader is referred to refs. [127, 130, 132] for three different options.

All that remains is to define a suitable geometry and boundary conditions under which to solve Eq. (3.4) for  $T_{\text{det}}(t) = T(\mathbf{r}_0, t)$ , which, given  $\eta_{ij}$  and  $\varepsilon_{ij}^0$ , allows the characterization of  $\Gamma(\omega)$ . We begin by examining two models which can be solved exactly and which isolate  $\Gamma_b(\omega)$ . We then explore both  $\Gamma_t(\omega)$  and the full  $\Gamma(\omega)$  numerically through the finite element method.

### 3.3 Exactly soluble models for $\Gamma_b(\omega)$

#### 3.3.1 Continuum model

We begin with a simple one-dimensional continuum model for heat flow within the sample. We discard the geometry of the thermometer and mounting plates, and consider the sample as a one-dimensional object for  $x \in [-s, s]$ , as shown in Fig. 3.2(a). Neglecting the thermometer allows us to set  $\Gamma_t(\omega) = 1$ . We denote by  $c$ ,  $k$  and  $T(x, t)$  the heat capacity per unit length, the thermal conductance, and the temperature distribution within the sample. At either end of the sample, we dictate that  $T(x = \pm s, t) = T_0$ . We assume that the region  $x \in [-h, h]$  is subjected to homogeneous strain  $\varepsilon = \varepsilon_0 e^{i\omega t}$ , resulting in

$$Q(x, t) = Q_0 [\Theta(x + h) - \Theta(x - h)] e^{i\omega t} \quad (3.6)$$

where  $\Theta(x)$  is the Heaviside step function,  $Q_0 = i\omega\eta c\varepsilon_0$ , and where we have dropped the tensor indices on  $\eta$  and  $\varepsilon$  for brevity.

The solution for  $T(x, t)$  can be determined through a straightforward eigenfunction expansion

$$T(x, t) = \sum_{n=0}^{\infty} A_n(t) B_n(x) \quad (3.7)$$

where the  $n^{\text{th}}$  spatial mode is described by  $B_n(x) = \cos(\xi_n^{-1}x)$  and where

$$\xi_n = \frac{2s}{\pi(2n + 1)} \quad (3.8)$$

is the characteristic thermal length of the  $n^{\text{th}}$  mode. The steady-state amplitude of the  $n^{\text{th}}$  mode can be evaluated to be

$$A_n(t) = \frac{4\eta\varepsilon_0}{\pi(2n + 1)} \sin(\xi_n^{-1}h) \left( \frac{\omega}{\omega - i\gamma_n} \right) e^{i\omega t} \quad (3.9)$$

where  $\gamma_n = \xi_n^{-2}D$  is the characteristic thermal relaxation and  $D = k/c$  is the thermal diffusivity.

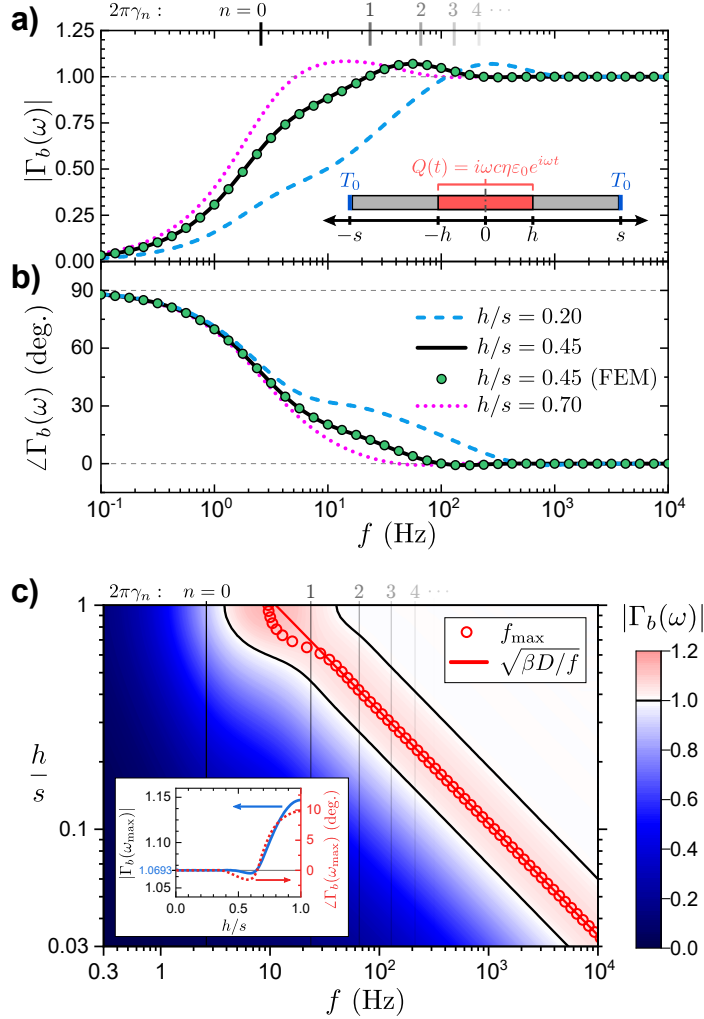


Figure 3.2: Low frequency component  $\Gamma_b(\omega)$  of the AC-ECE sensitivity calculated using the 1D continuum model. Magnitude (a) and phase (b) of the sensitivity function as a function of frequency for several different ratios of sample length  $s$  to the length of the thermally excited region  $h$ . Lines correspond to the result of evaluating Eq. (3.11), and filled circles denote FEM solutions for a three-dimensional bar-shaped sample with the same geometry and boundary conditions along one axis. All calculations use the same values of the sample specific heat and thermal conductivity, as described in Section 3.6. A schematic of the geometry and boundary conditions is shown in the inset of panel (a). The  $h/s$  ratio alters the location of the maximum in  $|\Gamma_b(\omega)|$ , and affects the slope of the curve for slightly lower frequencies, but otherwise preserves the general structure. Smaller values of  $h/s$  retain a finite phase lag out to higher frequencies. Magnitude values are plotted for a larger parameter space in panel (c), which allows the structure and geometry dependence to be seen more clearly. Dark lines enclose the region of  $|\Gamma_b(\omega)| > 1$ , which exists for any geometry, but which moves to higher  $f$  for smaller  $h/s$ . Vertical lines indicate the characteristic relaxation rates of the thermal modes. Inset: magnitude and phase of  $\Gamma_b(\omega)$  at the peak frequency as a function of  $h/s$ .

Now suppose an ideal thermometer ( $\Gamma_t(\omega) = 1$ ) is placed at  $x = 0$ . The detected temperature  $T_{\text{det}}(t) = T(x = 0, t)$  is given by

$$T_{\text{det}}(t) = \sum_n A_n(t) = \Gamma_b(\omega)\eta\varepsilon_0 e^{i\omega t} \quad (3.10)$$

resulting in

$$\Gamma_b(\omega) = \frac{4}{\pi} \sum_n \left[ \frac{\sin(\xi_n^{-1}h)}{(2n+1)} \left( \frac{\omega}{\omega - i\gamma_n} \right) \right] \quad (3.11)$$

The magnitude and phase of  $\Gamma_b(\omega)$  for realistic values of  $k$ ,  $c$ ,  $h$ , and  $s$  is shown in Fig. 3.2. As expected,  $|\Gamma_b(\omega)|$  approaches zero as  $\omega \rightarrow 0$  and approaches unity as  $\omega \rightarrow \infty$ . At an intermediate frequency which we label as  $f_{\text{max}} = 2\pi\omega_{\text{max}}$ , however, we observe a global maximum in  $|\Gamma_b(\omega)|$  where the sensitivity function reaches values greater than unity. Figure 3.2(c) shows  $|\Gamma_b(\omega)|$  for a range of values of  $h/s$ , demonstrating that the presence of such a peak is not an artifact of the geometry. Holding the thermal parameters constant, decreasing the proportion of the sample which is heated pushes the maximum out to higher frequencies. For  $h/s \lesssim 0.6$ , when  $f_{\text{max}} \gtrsim 2\pi\gamma_1$ , the peak frequency is closely approximated by  $f_{\text{max}} \approx (h/s)^2(\beta D)^{-1}$ , where  $\beta$  is a constant with value  $\approx 1.687$  and  $D$  is the thermal diffusivity. The peak magnitude is largest for  $h/s = 1$ , at which  $|\Gamma_b(\omega_{\text{max}})| = 1.147$ , and for  $h/s \lesssim 0.5$  the amplitude approaches a constant value of 1.0693. Put another way, this peak always occurs as the characteristic diffusion length becomes smaller than the length of the excited region. These calculations suggest that this peak is a robust feature of the AC-ECE sensitivity function. Physically, the temperature gradient arising from the spatial variation of the phase of temperature oscillations generates a retarded flow of heat (and therefore entropy) within the sample. The phase delay between the elastocaloric heating and the conductive heat flow can boost the total rate of change of the temperature at and near the center of the sample. The results presented in Fig. 3.2 show that decreasing the thermal conductivity does not remove this peak, but rather pushes the peak to higher frequencies. We also refer the reader to Section 3.3.2 for an equivalent understanding of this peak motivated from the principle of superposition.

Additionally, the thermal parameters  $k$  and  $c$  only enter Eq. (3.11) in the form of the diffusivity ratio  $D = k/c$  within the definition of  $\gamma_n$ ; scaling  $D$  by a multiplicative factor simply rescales the frequency axes in Fig. 3.2 by the same factor.

As a verification of these results as well as a benchmark for the numerical methods used in Section 3.5 used here, we have also performed finite element simulations for similar conditions. We used a three-dimensional rectangular prism of length  $2s$ , width  $w$ , and thickness  $d$ , with specific heat  $c_{3D} = (wd)^{-1}c$  and thermal conductivity  $k_{3D} = (wd)^{-1}k$ , with the same heating and boundary conditions. The results obtained through both numerical and analytical methods match quantitatively.

In practice, the sample mounting plates generate more complicated boundary conditions; the epoxy holding the sample in place will allow for finite heat flow for  $h < x < s$ . However, as the

freestanding region  $-h < x < h$  is still thermally isolated on all other surfaces, this nonideality will only result in a smaller effective value of  $s$ . This will tend to increase  $h/s$ , resulting in a lower peak frequency for the same  $h$ ,  $k$ , and  $c$ . This acts in the experimentalist's favor by increasing the frequency range over which  $|\Gamma(\omega)| \sim 1$ . This effect is quantified in FEM calculations presented in Section 3.5.1.

### 3.3.2 Discretized model

The results of the previous section, are not limited to continuous thermal models. We now examine a minimal lumped-element thermal model which reproduces the same behavior and provides further intuition for the physical meaning of  $|\Gamma_b(\omega)| > 1$ . We begin by separating the 1D sample of the previous section into a linear chain of  $2N$  discrete elements ( $N \geq 2$ ), each with heat capacity  $C$  and coupled to its nearest neighbors with thermal conductance  $K$ . We maintain the same thermal behavior by defining  $C = c(s/N)$  and  $K = k(s/N)$ . The first and last elements are also coupled to a heat bath at temperature  $T_0$  with thermal conductance  $K$ . By merit of the symmetry of the chain, we safely neglect one half and only consider the first  $N$  elements as shown in Fig. 3.3(a).

We denote the temperature of the  $i^{\text{th}}$  element by  $T_i(t)$ , and collect these terms into a vector  $\mathbf{T} = (T_1 \ T_2 \ \dots \ T_N)^T$ . The  $M$  elements closest to the center of the sample ( $M \leq N$ ) are subjected to an oscillating heat term

$$Q_i(t) = \begin{cases} Q_0 e^{i\omega t} & \text{where } (N - M) < i \leq N \\ 0 & \text{otherwise} \end{cases} \quad (3.12)$$

The equations for heat flow between elements, taking as our ansatz  $T_i = T_0 + T_i^0 e^{i\omega t}$ , can be collected into matrix form  $\mathbf{Q} = A\mathbf{T}$  where  $A$  is a tridiagonal matrix given by

$$A = \begin{pmatrix} g & K & & & \\ K & g & K & & \\ & K & \ddots & \ddots & \\ & & \ddots & g & K \\ & & & K & (g + K) \end{pmatrix} \quad (3.13)$$

where  $g = i\omega C - 2K$ , and all omitted elements vanish. The extra unit of  $K$  in element  $A_{NN}$  reflects the fact that no heat flows across the mirror plane in the sample. The temperature profile can be computed immediately as  $\mathbf{T} = A^{-1}\mathbf{Q}$ . We finally extract the low-frequency sensitivity function  $\Gamma_b$  by setting the elastocaloric tensor  $\eta$  and strain magnitude  $\varepsilon_0$  to unity, which by Eq. (3.3) equates the

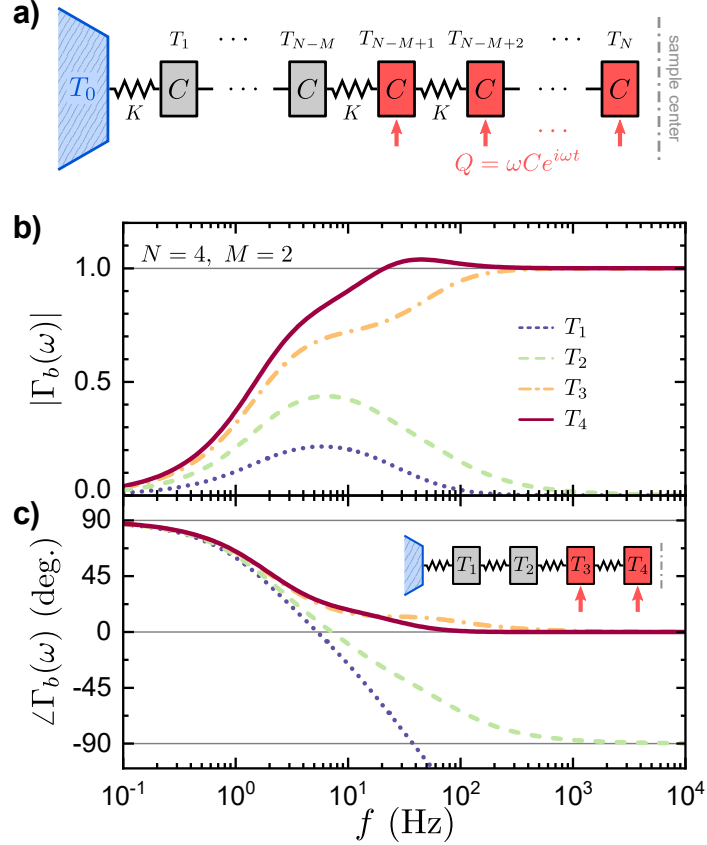


Figure 3.3: Discretized model of heat flow in the AC-ECE. (a) Schematic of the model, in which a 1D sample is collected into  $2N$  identical discrete elements. Only one half needs to be considered due to symmetry about the sample center. The  $M$  units closest to the middle are subjected to an oscillating heat term. (b) Magnitude and (c) phase of the low frequency sensitivity function  $\Gamma_b(\omega)$  for  $N = 4$  and  $M = 2$ . We have set both  $\eta$  and  $\varepsilon$  to unity such that the observed temperature oscillation  $T_n$  is identical to the sensitivity function for a thermometer placed on the  $n^{\text{th}}$  element. Similar to Fig. 3.2, a peak greater than unity is observed in  $T_4$  at intermediate frequencies.

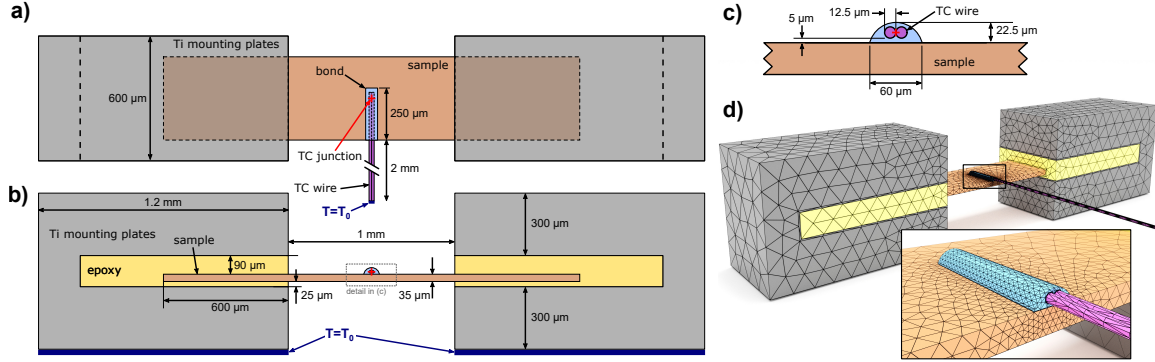


Figure 3.4: Geometry of the experimental setup, seen in top (a) and side (b) view. (c) Detailed side view of the thermocouple bond bead and thermocouple wire. (d) Rendered image of the full mesh and the thermocouple bond. Characteristic element sizes near the center of the sample are  $10\ \mu\text{m}$ , expanding to  $75\ \mu\text{m}$  at the edge of the mounting plates. As several variations of this standard mesh are used throughout this work, differences from this geometry are described in the text.

magnitude and phase of  $T_i$  with that of  $\Gamma_b$  for an ideal thermometer placed on the  $i^{\text{th}}$  element. For all cases for which of  $N \geq M \geq 2$ , the elements  $i$  for which  $N - M + 2 \leq i$  exhibit a peak temperature oscillation magnitude greater than unity.

The principle of superposition, afforded by the linearity of Eq. (3.4), provides an intuitive explanation for the appearance of this peak. Consider first a case where  $N = 2$  and  $M = 1$ ; this model is related to the model first applied to interpreting AC-ECE measurements, but with the assumption of an ideal thermometer placed at  $i = 2$ . In this case,  $|\Gamma_b(\omega)|$  will increase monotonically with frequency and will not generate a peak. In contrast, consider a case in which  $N = 2$  but heat is applied only to the  $i = 1$  element, not the  $i = 2$  element, which is reminiscent of the model used in AC heat capacity measurements.[152, 153]. Here  $|\Gamma_b(\omega)|$  (still as measured at  $i = 2$ ) will vanish at either frequency limit, but will have a finite peak below unity at some intermediate frequency.

The case of  $N = M = 2$ , the simplest case in which  $|\Gamma_b(\omega)| > 1$ , can be considered the superposition of these two cases. If the peak in the second case occurs at or above the frequency at which the oscillation amplitude in the first case approaches unity, then the total response can result in a peak amplitude greater than unity. This is always the case for the model considered here due to the equal heat capacity of and thermal conductances between the elements. In summary, the peak in  $|\Gamma_b(\omega)|$  is a robust feature which contributes to the thermal transfer function of all AC-ECE measurements. It is possible, however, that the peak itself is masked by the high-frequency component of the sensitivity function,  $\Gamma_t(\omega)$ , which will be discussed in later sections.

Table 3.1: Baseline thermal parameters used for the calculations in this paper. We emulate an AC-ECE measurement on a sample of  $\text{Ba}(\text{Fe}_{1-x}\text{Co}_x)_2\text{As}_2$  at a temperature of 100 K. The thermocouple is assumed to be Type E (chromel-constantan[135]).

	k ( $\text{Wm}^{-1}\text{K}^{-1}$ )	C ( $\text{J cm}^{-3}\text{K}^{-1}$ )	Refs.
sample	$k_{xx} = 10.6$ $k_{zz} = 3.2$	1.31	[[157, 121, 158]]
titanium	9.6	1.36	[[159, 160]]
thermocouple	15.6	2.11	[[161]]
sample/TC epoxy	0.19	0.497	[[162]]

### 3.4 FEM Implementation

We now turn our attention to nontrivial effects of the 3D geometry of the sample, mounting plates, and thermometer. We apply the finite element method (FEM) to solve Eq. (3.4) on a 3D mesh in which regions representing different materials are assigned appropriate thermal conductivities and heat capacities. We use a Python implementation of the open-source FEniCS Project[154, 155] as our FEM solver. Generation and optimization of the mesh was performed using Gmsh.[156]

The complete finite element mesh, slightly simplified from practical experiments, is shown in Fig. 3.4. Each pair of mounting plates, as well as the screws which hold the assembly together, are represented by a single C-shaped block. The regions between the mounting plates are completely filled with epoxy, into which either end of the sample is then embedded. The thermometer used to detect the temperature oscillation is taken to be a thermocouple (TC) and is represented by two cylinders approximately 2 mm in length. One end is “adhered” to the sample with a bead of some bonding material. In practice such material could be an epoxy, an electrically conductive paint, or a small quantity of solder. For simplicity, the TC wires are taken to lie parallel and adjacent to each other and the TC “junction” is defined as the point directly between the wires and above the center of the sample. We describe the glue bead as a section of a cylinder 60  $\mu\text{m}$  in diameter and 250  $\mu\text{m}$  in length, which spans from one edge of the sample to slightly beyond the end of the TC wire. Several studies in Section 3.5 employ meshes which remove either the mounting plates or the TC in order to isolate the  $\Gamma_b(\omega)$  and  $\Gamma_t(\omega)$  components independently.

Characteristic dimensions of the tetrahedral mesh elements within the sample vary from less than 10  $\mu\text{m}$  near the center and within the TC to approximately 75  $\mu\text{m}$  where the sample meets the mounting plates. Elements composing the mounting epoxy and the mounting plates increase from 75  $\mu\text{m}$  to 125  $\mu\text{m}$  at the outside edge. As will be shown in later sections, the temperature variation in these regions is negligibly small for realistic parameters, which makes additional refinement of the mesh in and around the mounting plates unnecessary.

The section of the sample which is suspended between the plates experiences a fairly homogeneous strain environment. However, finite but inhomogeneous strain persists within the glued ends of the

sample. This strain will still contribute to the overall elastocaloric response of the sample. Using the strain profile reported in ref. [136] for a similar setup, we find that the strain within the glued sections can be approximated by

$$\varepsilon_{xx}(x) = 0.0286 \exp\left(\frac{-(x + 597)}{168}\right) \quad (3.14)$$

where  $x$  is the depth (in microns) within the glue, with the end of the freestanding sample at  $x = 0$ .

We take as our initial conditions that the entire mesh is at a constant temperature  $T_0$ . The linearity of the heat equation allows us to set this temperature as  $T_0 = 0$  without loss of generality, interpreting the reported temperature as the deviation from this reference. We employ Dirichlet boundary conditions enforcing  $T = T_0$  on three surfaces; the bottom faces of both of the titanium mounting blocks, and the far end of the thermocouple wires, 2 mm away from the center of the sample. All other surfaces are assumed to be thermally insulated.

We employ an implicit Crank-Nicholson trapezoidal scheme to advance the heat equation in time. We calculate the temperature distribution at the  $(n + 1)^{\text{th}}$  timestep by solving

$$c(\mathbf{x}) \frac{T_{n+1} - T_n}{\Delta t} = \frac{\partial}{\partial x_i} \left[ k_{ij}(\mathbf{x}) \frac{\partial}{\partial x_j} \left( \frac{T_{n+1} + T_n}{2} \right) \right] + \frac{Q_{n+1} + Q_n}{2} \quad (3.15)$$

which is then converted into the weak variational form through standard techniques.[163] We use a space of linear basis functions defined on scalar elements.

In order to extract the magnitude and phase of the thermal transfer function from the temperature profile, we must first run the simulation through a finite number of cycles. For all simulations shown here, the time step  $\Delta t$  was chosen such that  $\Delta t = 1/(100f)$ , where  $f$  is the strain frequency. At each frequency, we allow the system to run through ten full cycles, or 1000 timesteps, extracting the temperature from various relevant locations within the sample and thermometer at each step. To minimize the effect of transient fluctuations in the finite number of cycles, we discard the results of the first five cycles, and perform a sinusoidal fit to the final five cycles.

## 3.5 Results of FEM simulations

### 3.5.1 Sample-bath coupling

We begin by studying the details of the thermal connection between the sample and the reservoir. To again isolate only the  $\Gamma_b(\omega)$  component, we remove the thermocouple and bonding material from the geometry shown in Fig. 3.4. We then generate several instances of the mesh with varying sample length and thickness. For all of the calculations in this section we maintain the same dimensions of the mounting plate blocks, the width of the sample, and the length of the glued regions of the sample.

The sample itself can be expected to behave in a similar fashion to what was presented in Section

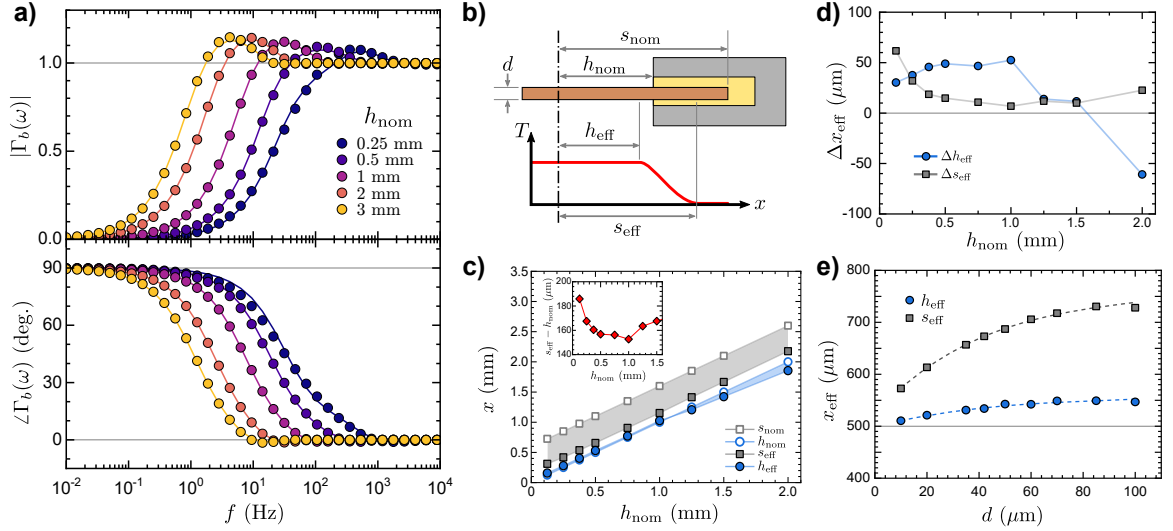


Figure 3.5: Results of FEM simulations of the effects of mounting plates and sample geometry on the AC-ECE sensitivity function. (a) Magnitude and phase of ECE temperature oscillations within the sample for different values of plate spacing  $h_{\text{nom}}$ . Filled symbols correspond to numerical results, and solid lines represent fits of the continuum model of Eq. (3.11) using the lengths  $s_{\text{eff}}$  and  $h_{\text{eff}}$  as free parameters. (b) Schematic defining the nominal and effective sample dimensions. (c) Dependence of the effective sample dimensions on the sample length. Open symbols show the nominal values, and shaded regions highlight the observed deviations. Inset to (c) shows the relatively weak dependence of the thermalization length of the sample, defined as  $s_{\text{eff}} - h_{\text{nom}}$  as a function of sample length. (d) Differences in effective dimensions with and without including the inhomogeneous strain within the glued sections of the sample, showing the relatively small role the details of strain relaxation within the sample ends plays in the overall response. (e) Effective dimensions as a function of sample thickness. Dashed lines indicate exponential fits to the data as described in the text.

3.3.1, although the boundary conditions differ slightly near the ends. We define the nominal total sample length (including the glued regions) as  $2s_{\text{nom}}$ , and the spacing between the mounting plates as  $2h_{\text{nom}}$ . To account for the differences in boundary conditions, we also define effective dimensions  $s_{\text{eff}}$  and  $h_{\text{eff}}$ , for which Eq. (3.11) reproduces the behavior most faithfully. These parameters are defined schematically in Fig. 3.5(b). These two effective dimensions are the only free parameters in a least-squares fit of Eq. (3.11) to the FEM results.

The results of FEM calculations for several different mounting plate spacings are shown in Fig. 3.5(a), superimposed over fits to the continuum model.

Good fits are achieved for all sample lengths, with the shortest samples displaying the largest deviations. The frequency of the crossover peak scales with the inverse square of the sample length, as would be expected from the diffusion equation. The initial rise of the magnitude also varies in steepness, becoming more gradual as the sample decreases in length. This change in shape is also observed in Fig. 3.2(a), as a consequence of changing the  $h/s$  ratio.

The nominal and effective lengths extracted from fits to the FEM results are presented in Fig. 3.5(c). As  $h_{\text{nom}}$  increases, the effective dimensions grow approximately linearly as well. The sample thermalization length, defined as the difference between the edge of the mounting plates  $h_{\text{nom}}$  and the total effective half-length of the sample  $s_{\text{eff}}$ , is plotted in the inset to Fig. 3.5(c). The thermalization length exhibits only a weak dependence on the plate spacing, adopting values near  $150\ \mu\text{m}$  to  $180\ \mu\text{m}$  for all spacings studied.

As mentioned in Section 3.4, we have also included the finite strain within the glued regions of the sample in our definition of the heat term  $Q$ . We have performed FEM calculations both with and without these exponential tails, and the difference in the effective dimensions are presented in Fig. 3.5(d). We find relatively little effect on the resulting effective dimensions, amounting to just a few microns of difference. The characteristic strain relaxation length is approximately the same as the sample thermalization length. The effective dimensions are most sensitive to strain relaxation effects for small plate spacings, but the total effect is negligible compared to practical uncertainty in the epoxy dimensions and strain transmission. As a consequence, the details of strain relaxation within the sample ends are unlikely to have a significant effect on the frequency dependence.

The operative parameter for controlling the difference between the nominal and effective dimensions is the thickness of the sample. As shown in Fig. 3.5(e), increasing the sample thickness causes an increase in  $s_{\text{eff}}$  and  $h_{\text{eff}}$  following an exponential curve with characteristic length of approximately  $42\ \mu\text{m}$ . The growing thermalization length is a consequence of the increasing total thermal conductance, as might be expected for a static thermalization problem[164].

The effects of the thermal conductivity and heat capacity of the sample mounting epoxy has also been explored. We find that varying the diffusivity over three orders of magnitude has very little effect on the resulting effective dimensions.

The practical consequence of this relatively short thermalization length for the frequency-dependent

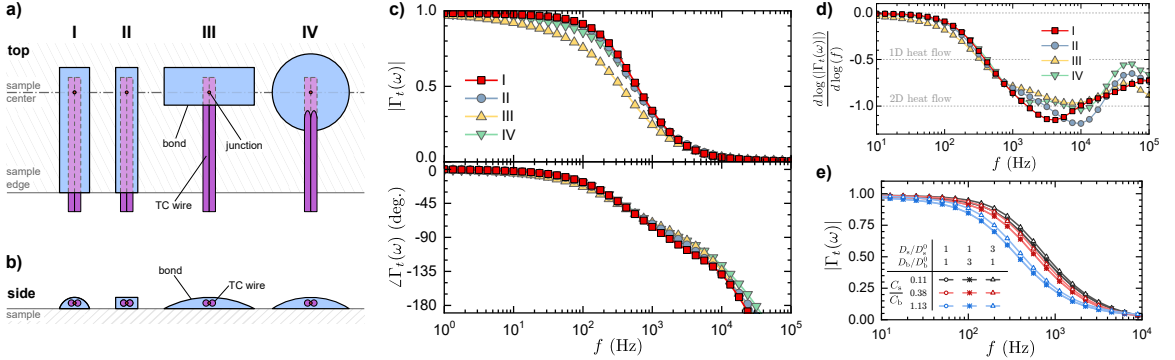


Figure 3.6: High-frequency contributions to the AC-ECE sensitivity function arising from the geometry and material properties of the thermocouple. Four different geometries of the TC bond, each containing the same total volume of the bond material, are shown in panels (a) and (b). Panel (c) shows the magnitude and phase response of  $\Gamma_t(\omega)$  for each variant. We find that bond I (red squares) maintains the largest magnitudes out to the highest frequencies, indicating that a long and thin bond bead with a center of mass as close as possible to the sample surface is the best choice for a given bond volume. Panel (d) extracts the effective power law  $\alpha = d \log |\Gamma_t(\omega)| / d \log(f)$  describing the frequency dependence of the magnitude. For heat flow of dimension  $d$ , one expects  $\alpha = -d_\theta/2$ . All four thermocouple bond variants initially exhibit a trend in  $\alpha$  toward the 2D limit interrupted by a rebound back to  $\alpha > -0.5$  over roughly one decade in frequency. Panel (e) shows the expected behavior of  $|\Gamma_t(\omega)|$  for bond I for various material conditions. Increasing the sample diffusivity increases the cutoff frequency most strongly, while the bond diffusivity dominates for  $f \gtrsim 10$  kHz. Changing the ratio between the sample and bond specific heat (holding the diffusivity constant) causes very little effect.

sensitivity function is that  $h_{\text{eff}}/s_{\text{eff}} \approx 0.9$  largely independent of the sample dimensions when the sample is of order 1 mm or longer. This condition places the response squarely in the regime where the greater-than-unity peak in the transfer function reaches the largest values (cf. inset to Fig. 3.2(b)).

### 3.5.2 Sample-thermometer coupling

We now apply the finite element technique to quantify the high-frequency contribution  $\Gamma_t(\omega)$  to the sensitivity function. As the sample changes in temperature due to the elastocaloric effect, the thermocouple and bonding material must absorb or release heat in order to change the temperature of the junction. This heat flow will suppress the temperature oscillation within the sample, and the magnitude of the suppression is related to the ratio between the heat capacity of the TC  $C_{\text{TC}}$  and the heat capacity of the sample  $C_s$ . Considering the TC as a point particle, the relevant sample volume for calculating  $C_s$  is the region of the sample within one thermal diffusion length  $L_{\text{th}} = (D/f)^{1/2}$  of the TC. As the frequency  $f$  rises and  $L_{\text{th}}$  shrinks below the length, width, and eventually thickness of the sample, the ratio  $C_{\text{TC}}/C_s$  will vary as  $f^{-d_\theta/2}$  where  $d_\theta$  is the effective dimensionality of the thermal volume, and  $d_\theta$  will increase from 0 to 3.

In principle, the ideal case would be to directly embed, deposit, or weld the thermocouple to the

surface of the sample, minimizing extra thermal mass such as epoxy while creating solid thermal contact. A thermocouple which is directly embedded into a sample can react within approximately 10  $\mu\text{s}$ , [165] while using the sample surface itself (assuming it is conductive) as one leg of an intrinsic thermocouple can produce response times of 3  $\mu\text{s}$  [166]. However, use of such techniques will be highly material-dependent and may damage the sample; using a small bead of a bonding material such as an epoxy is a more generally applicable solution. Additionally, thermocouples are often adhered to samples by hand. This certainly allows for decent measurements to be made, although some variance in the quality of the thermal contact is to be expected. In principle, micro-manipulators and small syringes could be employed in order to improve reproducibility.

In practice, the dimensions of the thermocouple and bonding material may be of similar orders of magnitude to the dimensions of the sample itself. In order to test the influence of bond geometry in a controlled way, we have developed a set of four different geometries for the TC bonding material, labeled by Roman numerals I through IV, each of which includes the same volume of material and therefore the same total  $C_{TC}$ . The size, shape and orientation of the thermocouple wires are held fixed, as is the total height of the bonding material above the top surface of the sample. The different shapes are shown schematically in Fig. 3.6(a) and (b). Bonds I and II are long and thin volumes running along the thermocouple wire but with cross sections of a circular segment and a rectangle, respectively. Bond III is wide and short, near the TC junction only, and also has a circular segment cross section. Bond IV consists of a spherical cap with its axis of revolution passing through the TC junction.

We isolate the high frequency contributions  $\Gamma_t(\omega)$  of the TC bond by removing the components of the mesh corresponding to the mounting plates and epoxy. The entire sample is considered to be strained uniformly at a given frequency and the entire mesh is thermally isolated except for the far end of the TC wires. FEM calculations are otherwise identical to those in the previous section.

Results of FEM calculations for these four meshes are presented in Fig. 3.6(c). As expected, the magnitude of  $\Gamma_t(\omega)$  approaches unity at low frequencies.<sup>3</sup>

As the frequency increases, the magnitude drops over approximately one decade of frequency. It is observed that for strain frequencies above  $\approx 100$  Hz, the sensitivity function is largest for the long, thin, cylindrical bond I, while the short and wide bond III performs most poorly. The phase of the signal decreases linearly between 100 Hz and 10 kHz, then decreases more quickly at larger frequencies.

We find that a long thin bead of a bonding material running from the tip of the thermocouple along the wires to the edge of the sample provides better thermal coupling than a shorter, but wider, bead of identical volume and thermal parameters. This geometry is a compromise between the optimal case of minimum bond volume and the reality of working with liquid adhesives. For example,

---

<sup>3</sup>The true value is slightly depressed below one, due to the finite heat capacity of the thermocouple and bond. Additionally, the boundary conditions at the far end of the wire will implement  $\Gamma_b(\omega)$  effects, but at very low frequencies due to the low total conductance.

a low-viscosity epoxy would wick along the surface of the thermocouple wire by capillary action.

In order to evaluate the effective dimensionality  $d_\theta$  of the thermal diffusion volume of the sample, we extract the instantaneous power law dependence of  $|\Gamma_t(\omega)| = f^\alpha$  as a logarithmic derivative in Fig. 3.6(d). Beginning in the low-frequency limit,  $\alpha \approx 0$ , indicating that the thermal diffusion volume is larger than the sample. As the frequency increases and the thermal length decreases, the magnitude begins to decline rapidly. The onset of the decline corresponds to  $L_{th} \approx 250 \mu\text{m}$ , the length of the bond region. Increasing the frequency further,  $\alpha$  reaches a minimum just beyond  $\alpha = -1$ , which corresponds to 2D heat flow. This minimum corresponds to the crossover between different thermal bottlenecks: for frequencies below this minimum heat flow is dominated by the changing thermal volume of the sample, while heat flow at higher frequencies is limited by diffusion through the bonding material. At this point, the diffusion length within the sample becomes smaller than the short axis of the interfacial area between the sample and the bond. For extreme frequencies  $\gtrsim 10 \text{ kHz}$ ,  $\alpha$  indicates an approach to 1D behavior, and the thermal contact between the sample and thermocouple is dominated by flow perpendicular to this interface.

Finally, we compare the results for different thermal parameters in both the sample and bond material in Fig. 3.6(e). We consider changes in the diffusivity of the sample ( $D_s$ ) and the thermocouple bond  $D_b$  relative to the default values  $D_s^0$  and  $D_b^0$ , as well as the ratio between the sample and bond heat capacities  $C_s/C_b$ . Of these parameters, we find that the the heat capacity ratio exerts the largest effect on the cutoff frequency  $\omega_t$ , although an order of magnitude change of  $C_s/C_b$  causes  $\omega$  to vary by less than a factor of three. Changes in the diffusivity of the TC bond material has no noticeable effect, consistent with the interpretation that the behavior is limited by  $L_{th}$  within the sample. Increasing  $D_s$  by a factor of three does increase the cutoff frequency, but only slightly.

A consequence of the results presented in Fig. 3.6(e) is that *both* the high and low frequency cutoff frequencies (which we will denote by  $\omega_t$  and  $\omega_b$ , respectively) are primarily determined by the geometry and diffusivity of the sample, parameters which cannot generally be controlled by the experimentalist. In the context of experiments making use of round-wire thermocouples, then, there are relatively few parameters which can be optimized. Further improvements would require a significant paradigm shift, such as the implementation of thin-film thermometers which can be deposited onto the sample surface and the thermal coupling will be very close to ideal for all strain frequencies. However, it should be noted that in such a case, strain transmission between the sample and thermometer material will also be nearly perfect, so care must be taken to ensure the thermometer's response is insensitive to strain.

To widen the quasi-adiabatic region by minimizing  $\omega_b$ , one can use the longest sample possible. Increasing the length by a factor of  $\lambda$  will decrease the cutoff frequency by  $\lambda^{-2}$ . Simultaneously, however, the sample strain for a given stress will decrease by  $\lambda^{-1}$  and the critical compressive buckling stress will decrease by  $\lambda^{-2}$  as well. Increasing the sample thickness by a factor of  $\gamma$  can counteract the buckling condition somewhat (increasing the buckling force by  $\gamma^3$  due to changes in the bending

moment of the sample) at the further cost of strain ( $\gamma^{-1}$ ). While the practical limits will depend on the material under test, increasing the length, thickness, and driving stress generally provides the best conditions for quasi-adiabatic behavior at the lowest frequencies possible.

To improve the response on the high-frequency side by maximizing  $\omega_t$ , the choice of bond material (with the optimum corresponding to minimizing  $C_b$ , while  $D_b$  appears irrelevant) has the largest effect, although even this effect is somewhat muted. The shape of the bond bead can alter the cutoff frequency by approximately a factor of two. The optimal geometry consists of a thin, low-volume bead which connects a significant portion of the thermocouple wire to the sample surface, and which has a low center of mass relative to the sample surface to maximize thermal coupling. Additionally, samples which are thinner than the bond bead is wide, for instance, tend to reduce the cutoff frequency due to a reduction of heat capacity per unit area of the sample. However, the cutoff frequency saturates when the sample thickness is increased beyond the width of the bond bead, making sample thickness a poor tuning parameter for increasing the cutoff frequency.

## 3.6 Results of full simulations

Finally, we combine the low- and high-frequency effects and study the complete sensitivity function  $\Gamma(\omega)$  for realistic parameters.

### 3.6.1 Material property dependence

Figure 3.7 shows a map of  $\Gamma(\omega)$  as a function of the heat capacity and thermal conductivity of the sample, sample mounting epoxy, thermocouple, and thermocouple bond material. All parameters except the one being varied are set to the values in Table 3.1. Despite the variability of the response across the range of parameters, the shape of the response takes on only two qualitatively different forms. In the low sensitivity case,  $\Gamma(\omega)$  consists of a single sharp peak. For larger values of the sensitivity, the response splits into a peak on the low frequency side and a shoulder on the high frequency side.

Within the field of fundamental condensed matter physics research, many of the most actively studied materials families exhibit significantly anisotropic crystal structures. The flat sample morphology presented here is particularly well-suited to layered materials which can be cleaved easily; however, the layered structure usually also implies an anisotropic thermal conductivity as well. Thermalization between the sample and thermocouple, as well as between the sample and mounting plates, primarily occurs through heat flow which runs perpendicular to the plane of the sample, whereas thermalization within the sample occurs primarily within the plane. As such, anisotropy in the thermal conductivity may have a substantial effect on the sensitivity function  $\Gamma(\omega)$ .

We consider a sample material which exhibits a three-, four- or six-fold symmetry axis normal to

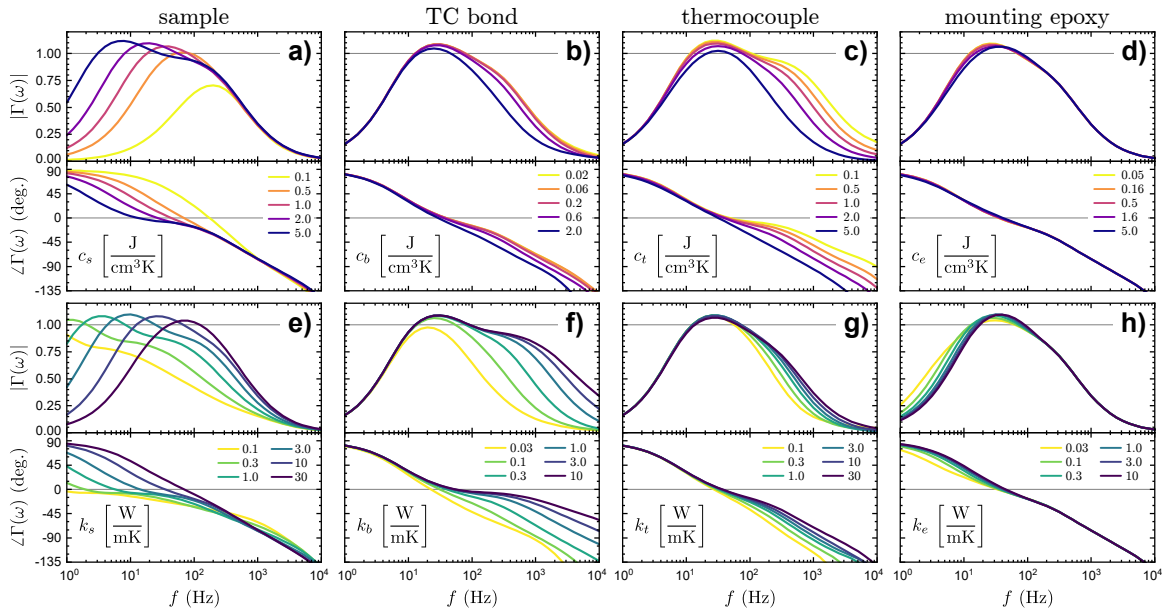


Figure 3.7: Dependence of the full AC-ECE sensitivity function  $\Gamma(\omega)$  on strain frequency and materials parameters. Panels (a)-(d) illustrate the effects of the volumetric heat capacity of the sample, the thermocouple bond, the thermocouple itself, the sample mounting epoxy respectively. Panels (e)-(h) show the effect of the thermal conductivity of the same materials. Only one parameter is varied at a time; all the rest are held at the values in Table 3.1. In panel (e) the sample thermal conductivity anisotropy ratio  $k_{xx}/k_{yy}$  is held constant, and the legend corresponds to values of  $k_{xx}$ .

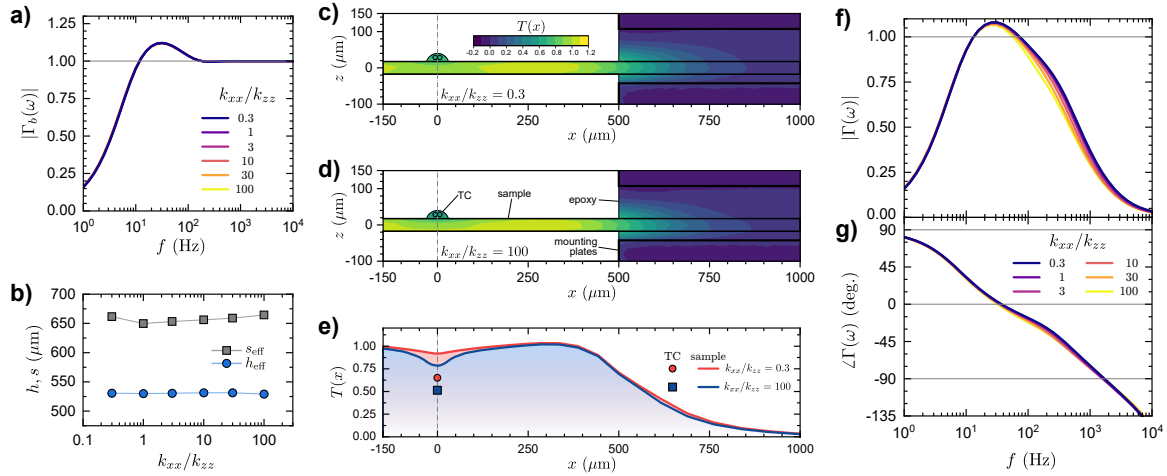


Figure 3.8: Demonstration of the independence of the AC-ECE sensitivity from the ratio of in-plane to out-of-plane thermal conductivity tensor components  $k_{xx}$  and  $k_{zz}$ . (a) Magnitude of the bath coupling sensitivity component  $\Gamma_b(\omega)$  for a range of anisotropy ratios, holding  $k_{xx}$  fixed. More than two orders of magnitude of change in  $k_{zz}$  causes no noticeable change in  $|\Gamma_b(\omega)|$  and all curves collapse onto each other. (b) Effective sample dimensions extracted from fits to the continuum model. The thermalization lengths are nearly constant. (c) Temperature profile for a cross-section of the mesh for  $k_{xx}/k_{zz} = 0.3$  and (d)  $k_{xx}/k_{zz} = 100$ . Both profiles are taken at  $f = 316.2$  Hz and  $t = 9.25/f$ . (e) Temperature extracted running along the top surface of the sample ( $z = d/2$ ) extracted from panels (c) and (d). The sample surface temperature is slightly suppressed for the  $k_{xx}/k_{zz} = 100$  case. The instantaneous temperature of the TC junction is shown by the symbols at  $x = 0$ : the measured temperature is suppressed by roughly 0.15 in normalized units for the highly anisotropic case. (f) Magnitude and (g) phase of  $\Gamma(\omega)$  for FEM simulations of the full assembly. While higher anisotropy ratios tend to suppress the high frequency response, the effect is slight.

the plane (parallel to the  $\hat{z}$ -axis), such that the thermal conductivity tensor  $k_{ij}$  takes on the form

$$k_{ij} = \begin{pmatrix} k_{xx} & 0 & 0 \\ 0 & k_{xx} & 0 \\ 0 & & k_{zz} \end{pmatrix}. \quad (3.16)$$

We neglect any strain-induced anisotropy within the plane. A series of FEM calculations varying the out-of-plane component  $k_{zz}$  while holding  $k_{xx}$  fixed is presented in Fig. 3.8. Focusing first on the behavior of the bath coupling component  $\Gamma_b(\omega)$ , we see that increasing  $k_{zz}$  has almost no change in the magnitude. Fits of this data to the continuum model of Eq. (3.11) show that neither of the effective lengths depend on the out-of-plane thermal conductivity, further indicating that  $z$ -axis heat flow normal to the the sample-epoxy interface is significantly less important than the  $x$ -axis heat flow between the strained and unstrained sections of the sample.

The temperature measured at the thermocouple junction, however, does depend modestly on  $k_{zz}$ . Temperature profiles in the cross-section of the sample shown in Fig. 3.8(c)-(e) show that the actual temperature within the sample hardly varies only slightly. The behavior is most different on the top surface of the sample, where it is suppressed slightly in the highly anisotropic case. The thermocouple temperature is similarly affected. The resulting impact of this effect on the sensitivity function is a slight decrease in the magnitude on the high frequency side of the peak, but the difference is minor. In the case of an extremely thermally anisotropic material, If shaping a sample such that the largest thermal conductivity points normal to the plane is not possible, then the frequency range can be improved slightly by adhering the thermocouple to the side of the sample rather than the top.

### 3.6.2 Comparisons to experiment

We now revisit the experimental results for AC-ECE measurements on Co-doped  $\text{BaFe}_2\text{As}_2$  and compare the phenomenology to FEM results for the full mesh presented in Fig. 3.4. A comparison between experimental results at three different temperatures are compared to three values of the thermal conductivity of the TC bonding material. Unlike the simplified model presented in Fig. 3.1, the FEM results accurately predict the shape of the signal.

Two parameters were required to bring the experimental and simulated curves into quantitative agreement. One is the vertical scale factor between the measured elastocaloric effect and  $|\Gamma(\omega)|$ , which is the quantity we are trying to measure. The other parameter is the thermal conductivity of the bonding material. Depending on the type of bond used, the thermal properties or the shape of the bond may be unknown or poorly defined. Allowing one of the thermal properties of this material to vary, however, is sufficient to capture all of these effects. Most importantly, the elastocaloric scale factor and the thermal properties of the bond affect the sensitivity function in orthogonal ways—the scale factor only affects the height of the curve while the thermal parameters affect the width of the

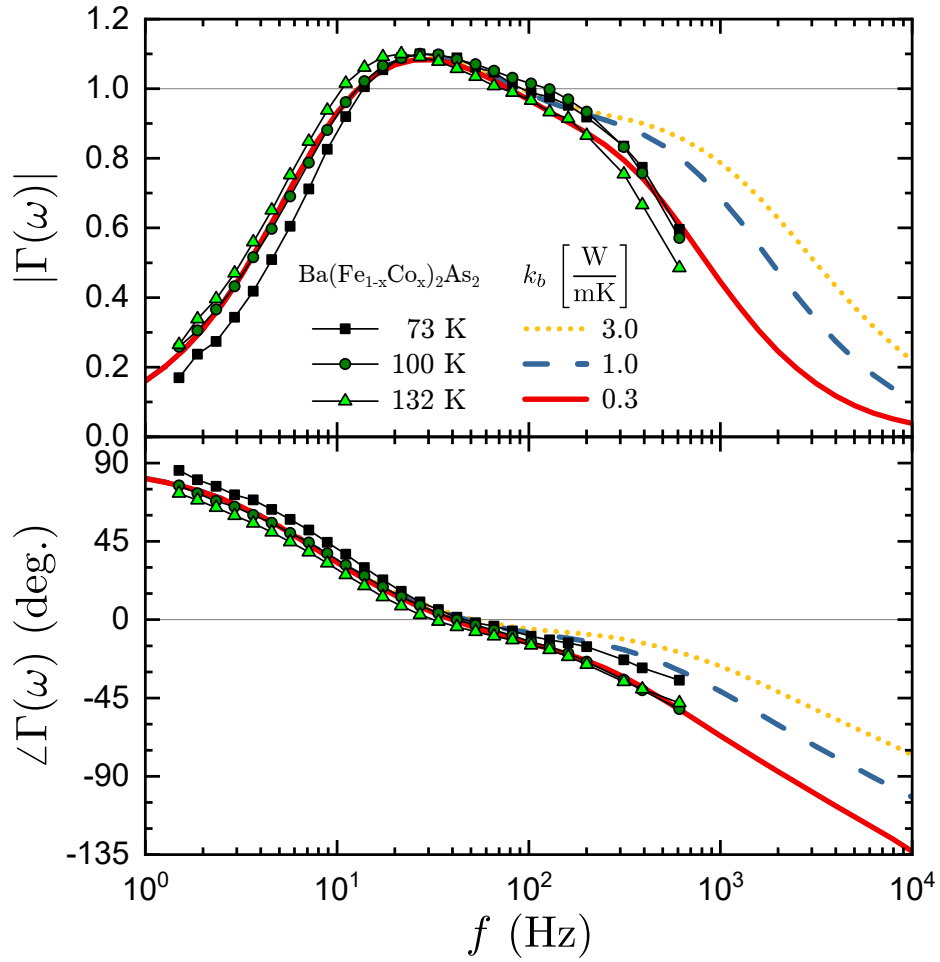


Figure 3.9: Comparison between experimental results of the AC-ECE technique on  $\text{Ba}(\text{Fe}_{1-x}\text{Co}_x)_2\text{As}_2$  and the results of full FEM simulation. Two free parameters are needed to acquire quantitative agreement—the thermal conductivity of the TC bonding material  $k_b$ , and the peak magnitude of the elastocaloric effect. All other parameters are set to the independently verified values in Table 3.1. The experimental data has been scaled using the quantification technique presented in this section, and the quantitative match between the simulation and experiment indicates that this measurement faithfully reproduced the intrinsic elastocaloric tensor  $\eta_{ij}$ .

response in frequency space.

In practice, when  $\eta_{ij}$  is not known *a priori*, the frequency dependence of the signal can be used to determine the quality of the thermal coupling for a given sample and material. Unlike specific heat measurements in which an external heater is used[153], a flat plateau is almost never to be expected in an AC-ECE measurement implemented using round wires. Instead, we propose an empirical prescription for evaluating the quality of a given measurement and the peak magnitude of  $\Gamma(\omega)$  without requiring recourse to one's own finite element calculations. The prescription is shown graphically in Fig. 3.10.

Consider a single measurement of the frequency-dependent AC-ECE signal, consisting of oscillations in temperature  $T'(\omega)$  and strain  $\varepsilon'_{ij}(\omega)$ , where both are complex quantities. In what follows, we denote measured quantities with primes, while unprimed variables denote the true value corrected for frequency-dependence of the sensitivity. Calculate the raw elastocaloric response  $\eta'_{ij}(\omega) = T'(\omega)/\varepsilon'_{ij}(\omega)$  calculate the normalized magnitude  $H(f)$  defined as

$$H(f) = \frac{|\eta'_{ij}(\omega)|}{|\eta'_{ij}(\omega_{\max})|}. \quad (3.17)$$

where  $\omega = 2\pi f$ . Define a concavity function  $J(\omega)$  which is the second derivative of  $H(f)$  with respect to  $\log(f)$

$$J(f) = \frac{d^2 H(f)}{d(\log(f))^2} \quad (3.18)$$

In “optimal” cases, where the experimental setup permits  $|\Gamma(\omega_{\max})| \approx 1.1$ ,  $J(f)$  will exhibit a local maximum at  $f_1$ . By calculating  $J(f)$  for all of the simulated traces in Fig. 3.7 and comparing its behavior to the simulated  $\Gamma(\omega)$ , we have found consistent relationships between the two despite the variability in terms of frequency dependence. By comparing the value of  $J$  at this local maximum to the true peak in the sensitivity function  $|\Gamma(\omega_{\max})|$ , we have found the two to be related linearly by the equation

$$|\Gamma(\omega_{\max})| = 1.085(2) + 0.20(3) \cdot J(f_1). \quad (3.19)$$

In cases where no such local maximum is observed, extract the local minimum of  $J$  at  $f_2$ , which lies on the low frequency side of the peak in  $H$ . in this case, the peak sensitivity can be estimated with the relation

$$|\Gamma(\omega_{\max})| = 1.39(10) + 1.16(30)J(f_2). \quad (3.20)$$

Regardless of which case is used, the peak sensitivity  $|\Gamma(\omega_{\max})|$  sets the scale factor for calculating the bare elastocaloric tensor.

$$\eta_{ij} = \frac{\eta'_{ij}(\omega_{\max})}{|\Gamma(\omega_{\max})|} \quad (3.21)$$

This procedure assumes that the bare elastocaloric tensor is frequency independent.

The results of this study clearly demonstrate both the possibility of and protocol for measuring

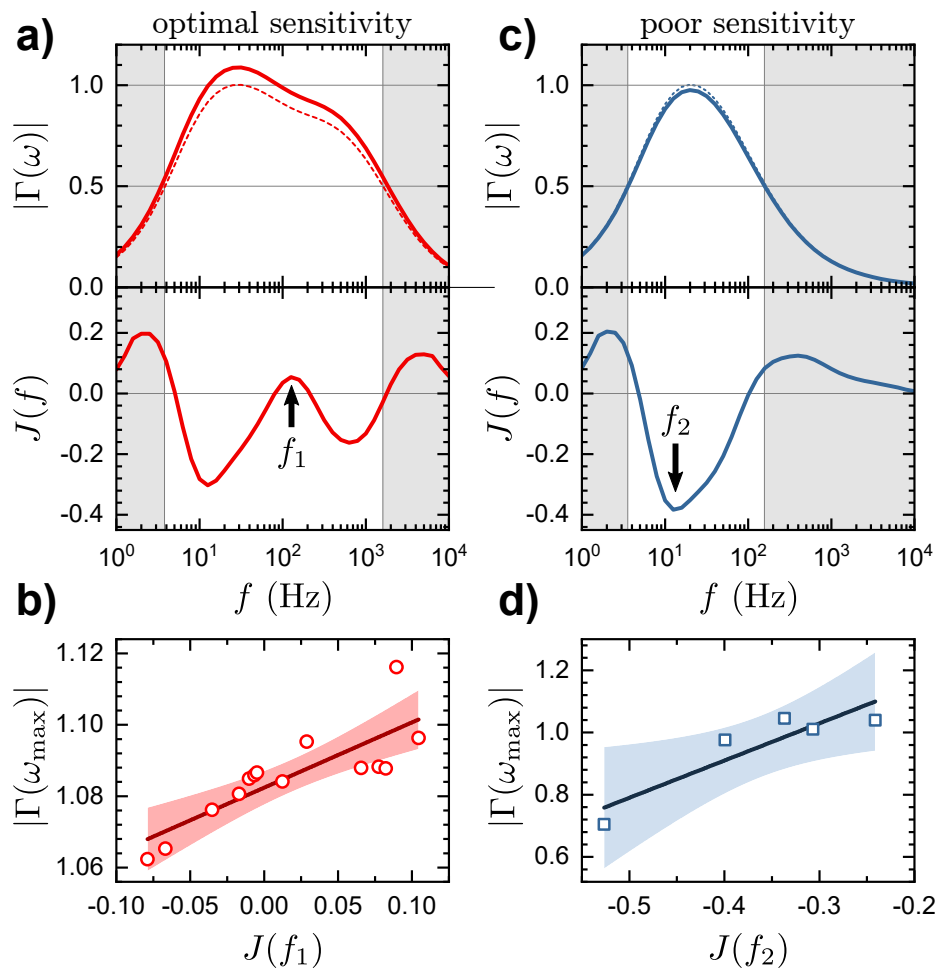


Figure 3.10: Graphical depiction of an empirical method for estimating the peak sensitivity of the AC-ECE technique based on the shape of the frequency dependence. Panels (a) and (b) show a representative simulation for which the sensitivity is high, and (c) and (d) show the case of poor sensitivity. Considering only data within the full-width at half-maximum of the normalized sensitivity, calculate  $J(f)$ , the second derivative with respect to  $\log(f)$  as described in the text. If  $J(f)$  exhibits a local maximum at  $f_1$  as in (a), the approximate peak magnitude can be read from panel (b) or calculated using Eq. (3.19). If no such peak exists, the peak sensitivity can be estimated based on the minimum at  $f_2$  using panel (d) or Eq. (3.20). Shaded regions in (b) and (d) indicate 95% confidence intervals of a linear fit to values extracted from the curves in Fig. 3.7.

the AC-ECE in absolute units. However, even once the experiment has been optimized it should be remembered that  $\Gamma(\omega)$  will vary with temperature as the thermal parameters shift. The sloping “pseudo-plateau” region of Fig. 3.10(a), for example, spans approximately 25% of the maximum sensitivity. Quantitative measurements of  $\eta_{ij}$  as a function of temperature therefore require that the frequency dependence be measured for a range of temperatures of interest in order to correct for these effects.

### 3.7 Conclusions

Numerical and analytical heat flow studies have been applied to the frequency-dependent AC elastocaloric sensitivity function  $\Gamma(\omega) = \Gamma_b(\omega)\Gamma_t(\omega)$ . We have shown through analytical models that coupling between the sample and the bath always give rise to a small peak where  $|\Gamma_b(\omega)| > 1$ , which arises as a consequence of the finite spatial extent of the elastocalorically excited region. By comparison to finite element simulation, we have also quantified the effects of sample dimensions and strain relaxation. Examination of the decoupling behavior of the thermocouple at high frequencies indicates that the optimal thermocouple bond geometry is a long, thin bead with a center of mass closest to the sample surface. We have demonstrated the effects of the heat capacity and thermal conductivity of the various materials involved in this measurement, including anisotropy in the sample thermal conductivity tensor. By combining both the high and low frequency components we have shown good agreement with data acquired on a sample of  $\text{Ba}(\text{Fe}_{1-x}\text{Co}_x)_2\text{As}_2$ . Finally, we have provided an empirical technique for estimating the absolute magnitude of the elastocaloric tensor through measurements of the frequency dependence. This work provides an intuitive baseline for the detailed interpretation of the frequency dependence of AC elastocaloric effect measurements.



## Chapter 4

# Evidence for realignment of the charge density wave state in $\text{ErTe}_3$ and $\text{TmTe}_3$ under uniaxial stress via elastocaloric and elastoresistivity measurements

*In this chapter, the behavior of  $\text{ErTe}_3$  and  $\text{TmTe}_3$  under uniaxial stress is studied. Measurements of the elastocaloric effect, resistivity, and elastoresistivity allow one to demonstrate the importance of in-plane antisymmetric strain on the CDW and to establish a phase diagram. We show that modest tensile stress parallel to the in-plane  $a$ -axis can reversibly switch the direction of the ordering wavevector between the two in-plane directions. This chapter establishes  $\text{RTe}_3$  as a promising model system for the study of strain-CDW interactions in a quasi-2D square lattice. This chapter is taken nearly verbatim from [132]. Part of this work was performed at the Stanford Nano Shared Facilities (SNSF) supported by the National Science Foundation under award ECCS-1542152. This work was supported by the U. S. Department of Energy (DOE) Office of Basic Energy Science, Division of Materials Science and Engineering at Stanford under contract No. DE-AC02-76SF00515.*

### 4.1 Introduction

Electronic correlations, especially in low-dimensional materials, give rise to a wide variety of charge ordered states, often in close proximity to other competing phases. Perhaps the most prominent

example is the recent evidence for charge density wave (CDW) order in the cuprate superconductors [167, 168, 14, 15, 169]; the interplay between the CDW and superconducting states in these materials is currently a subject of debate. However, the interpretation of measurements of the charge order in materials such as the cuprates is made more complicated by the neighboring phases.

While the mechanisms driving CDW formation can be material-dependent [170, 171, 172, 173, 102], there is an overarching consensus that strong coupling between the electronic and lattice degrees of freedom is crucial. [40] As such, modifying the lattice with hydrostatic pressure, chemical pressure, or uniaxial stress can produce substantial changes in the CDW state. [100, 174, 175, 101, 79] The response of the CDW to such perturbations contains a wealth of information about the host material, ordered state, and the phase transition.

Of particular contemporary interest are layered materials which host in-plane unidirectional CDW states—such states break not just translational but also rotational symmetries. The component of the electronic order parameter that breaks rotational symmetry can then couple strongly to induced strains which break the same symmetry. In the presence of disorder, vestiges of the broken rotational symmetry may still persist despite a lack of true long-range phase coherence of the CDW correlations. This kind of “vestigial nematicity” has been proposed as an important component in the phase diagrams of a variety of strongly correlated materials [50, 176, 51, 52]. However, such materials can also exhibit a wide range of competing or cooperating phases, which complicates the interpretation of experimental results. By identifying and studying model systems—that is, relatively simple materials in which the uniaxial CDW phase appears in isolation or next to only a small number of other phases—one can gain a deeper understanding of CDW formation and the roles played by CDW fluctuations. Such studies can provide powerful guiding principles for further research into more complicated systems.

Uniaxial stress has emerged in recent years as a versatile tuning parameter for strongly correlated materials. Certain orientations of stress result in symmetry-breaking strains which can couple strongly to ordered phases which break similar symmetries. One can probe both the thermodynamic and transport behavior under strain using elastocaloric and elastoresistivity techniques, respectively. The elastocaloric effect—that is, the change in temperature under adiabatic changes in strain—provides insight into the effects of strain on the entropy landscape. Elastocaloric effect (ECE) measurements display similar singular behavior at phase transitions as other thermodynamic quantities such as the heat capacity. However, ECE measurements are selectively sensitive only to degrees of freedom which change due to strain, resulting in a much smaller background relative to the size of an anomaly at a phase transition. [128] Elastoresistivity, on the other hand, is defined as the normalized change in resistivity as a function of strain. As a transport technique, elastoresistivity (ER) probes strain-induced changes in the Fermi surface topology, density of states at the Fermi surface, and scattering processes such as critical fluctuations. The tensor describing the ER coefficients is fourth-rank, which is useful in discriminating a material’s response to strains belonging to different superimposed

orthogonal symmetry channels.

The rare-earth tritelluride family of quasi-2D metals ( $R\text{Te}_3$ ,  $R=\text{La-Nd, Sm, Gd-Tm, Y}$ ) consist of bilayers of square Te nets separated by a buckled rock-salt layer of  $R\text{Te}$ , shown in Fig. 4.1(a). The crystal structure  $R\text{Te}_3$  belongs to the orthorhombic space group  $Cmcm$ . (The standard crystallographic setting for this group defines the  $a$  and  $c$  axes as spanning the basal plane, with  $b$  normal to the plane.) The orthorhombicity arises due to a glide plane along the in-plane  $c$ -axis, which dictates the stacking of the  $R\text{Te}$  slab layers and generates a slight difference in the two in-plane lattice parameters:  $a \approx 0.999c$ . For all  $R$ , the material undergoes a transition to a unidirectional, incommensurate CDW phase with the wavevector  $q_c \approx (0, 0, 2c^*/7)$ . Chemical pressure tunes the transition temperature from above 500 K in  $\text{LaTe}_3$  to 250 K in  $\text{TmTe}_3$ . A second incommensurate CDW perpendicular to the first, with wavevector  $q_a \approx (5a^*/7, 0, 0)$ , appears for  $R=\text{Tb, Dy, Ho, Er, Tm}$  at temperatures ranging from 41 K in  $\text{TbTe}_3$ [70] to 180 K in  $\text{TmTe}_3$ . Throughout this work, we denote the higher transition temperature as  $T_{CDW1}$  and the lower transition as  $T_{CDW2}$ .

In this paper, we report investigations of the effect of in-plane uniaxial stress on unidirectional CDW states in this material. Measurements of the resistivity, elastoresistivity, and elastocaloric effect of two representative members,  $\text{ErTe}_3$  and  $\text{TmTe}_3$ , as a function of temperature and stress all suggest an abrupt  $90^\circ$  in-plane realignment of the CDW wavevector under modest and practically accessible stresses, illustrated schematically in Fig. 4.1(f). Through this comprehensive study of the various phases and phase transitions, we establish  $R\text{Te}_3$  as a promising model system for the study of strain-CDW interactions in a quasi-2D square lattice.

## 4.2 Unidirectional CDWs in a quasi-tetragonal system

Before describing our results in this specific model system, it is instructive to consider the general expectations based on a phenomenological free energy expansion. Consider a two-dimensional system with tetragonal symmetry which supports incommensurate unidirectional CDW order along both the  $a$ - and  $c$ -axes, where we keep the notation of  $a$  and  $c$  as in-plane lattice parameters for immediate comparison to  $R\text{Te}_3$ .

Following the seminal work of McMillan[65], but using the crystallographic coordinates of  $R\text{Te}_3$ , we take as our order parameters

$$\psi_i(\mathbf{r}) = \psi_{i0}(\mathbf{r})e^{i\mathbf{q}_i \cdot \mathbf{r}} \quad (4.1)$$

where  $i = a, c$ , and the subscript 0 is used to indicate the absence of applied stress. Knowledge of the  $R\text{Te}_3$  family allows us to make several simplifying assumptions. First, the Fourier expansion coefficients should in principle be treated as periodic functions of space with the periodicity of the lattice. However, the smooth variation of  $\mathbf{q}_c$  and  $\mathbf{q}_a$  with temperature[92, 69, 70] suggests an absence of commensurability effects. Crystals of  $R\text{Te}_3$  are also relatively free of disorder which can locally pin

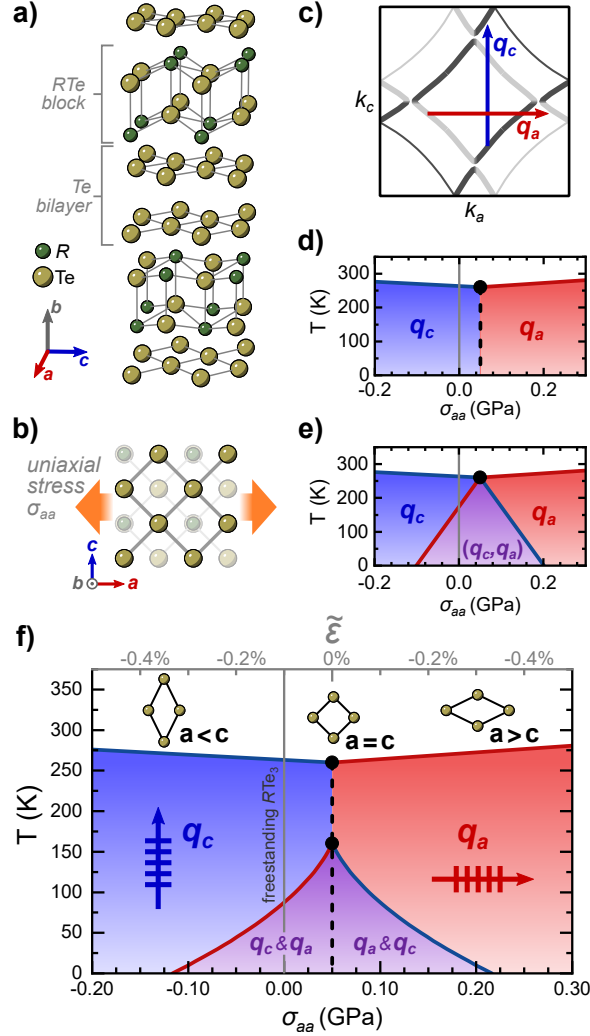


Figure 4.1: (a) Crystal structure of  $R\text{Te}_3$ . The stacking of the  $R\text{Te}$  block layers produces a glide plane which breaks  $C_4$  symmetry. (b) Crystal structure viewed along the out-of-plane  $b$ -axis. The  $c$ -axis is 0.1% longer than the  $a$ -axis, and uniaxial tensile stress along  $a$  can invert the orthorhombic distortion. (c) Schematic of the Fermi surface of  $R\text{Te}_3$ , showing the two orthogonal CDW ordering vectors. This is the result of a tight-binding model for a single plane, neglecting the effects of  $b$ -axis dispersion and bilayer splitting, both of which are small. The CDW vectors approximately nest large regions of the Fermi surface. (d) Temperature-uniaxial stress phase diagram described by Eq. (4.2) for  $g > 0$ . Solid lines indicate continuous phase transitions, and dashed lines indicate first order transitions. The stress axis is defined relative to a free-standing orthorhombic  $R\text{Te}_3$  crystal. (e) Phase diagram of Eq. (4.2) for  $g < 0$ . A region of coexisting CDW order with both wavevectors opens at low temperatures, and all transitions are continuous. (f) Phase diagram of Eq. (4.6) incorporating higher order terms, which captures the phenomenology observed in thermodynamic and transport under uniaxial stress. Both the first order transition and the coexistence region are preserved. Coefficients appropriate for  $\text{ErTe}_3$  are used in calculating (d)-(f).

the CDW phase, as observed in x-ray diffraction[69, 70], STM[95, 97, 96], electrical transport[83, 106] and quantum oscillations[82, 177, 79]. This allows us to treat the wavevectors  $\mathbf{q}_a$  and  $\mathbf{q}_c$  as fixed, spatially uniform parameters. Finally, the orthogonality of the two wavevectors ensures that in the absence of pinning potentials and higher order non-linear effects the phases of the order parameters  $\psi_a(\mathbf{r})$  and  $\psi_c(\mathbf{r})$  are mutually independent. These assumptions together allow us to consider only the CDW gap magnitudes and suppress any gradient terms in our free energy expansion. For brevity, from this point forward we use the notation  $\psi_a = |\psi_a|$ ,  $\psi_c = |\psi_c|$ .

As we introduce stress and strain terms into our free energy, we must also make a distinction between this idealized tetragonal model and the realistic orthorhombic structure of  $R\text{Te}_3$ . We define the strain  $\varepsilon_{ij}$  and stress  $\sigma_{ij}$  tensors relative to the  $R\text{Te}_3$  crystal;  $\varepsilon_{ij} = 0$  and  $\sigma_{ij} = 0$  for a freestanding sample. We add a tilde ( $\tilde{\varepsilon}_{ij}$ ,  $\tilde{\sigma}_{ij}$ ) to denote strain and stress defined such that  $\tilde{\varepsilon}_{ij} = 0$  and  $\tilde{\sigma}_{ij} = 0$  corresponds to the ideal tetragonal case. The orthorhombicity of  $R\text{Te}_3$  can be accounted for by a weakly temperature-dependent offset:  $\varepsilon_{ij} + \varepsilon_{ij}^0 = \tilde{\varepsilon}_{ij}$ ,  $\sigma_{ij} + \sigma_{ij}^0 = \tilde{\sigma}_{ij}$ .

Furthermore, we choose a basis for the stress, strain, and elastic constant tensors motivated by tetragonal symmetry, using the subscripts  $A$  and  $S$  for antisymmetric and symmetric in-plane components, respectively:  $\tilde{\varepsilon}_A = (\tilde{\varepsilon}_{cc} - \tilde{\varepsilon}_{aa})/2$ ,  $\tilde{\varepsilon}_S = (\tilde{\varepsilon}_{cc} + \tilde{\varepsilon}_{aa})/2$ , and similar for the stresses  $\tilde{\sigma}_A$  and  $\tilde{\sigma}_S$ . Analogous stress and strain terms can be defined in the orthorhombic reference frame as well (e.g.  $\varepsilon_A = (\varepsilon_{cc} - \varepsilon_{aa})/2$ ), however it should be noted that the subscripts  $A$  and  $S$  do not formally correspond to antisymmetric and symmetric strains; in the absence of tetragonal symmetry, these are no longer independent basis functions for different irreducible representations of the point group. The elastic constants of both the tetragonal model and orthorhombic  $R\text{Te}_3$  are assumed to be equivalent. In this basis, neglecting contributions from out of the plane, the symmetrized and antisymmetrized elastic constants are defined as  $\tilde{C}_S \approx C_S = 2(C_{aaaa} + C_{aacc})$  and  $\tilde{C}_A \approx C_A = 2(C_{aaaa} - C_{aacc})$ , where the factor of two is added for convenience, simplifying terms in the associated free energy after performing the necessary Legendre transformation.

Taking the tetragonal case as a reference, consider an expansion to fourth order in  $\psi_a$  and  $\psi_c$  of the Gibbs free energy (constant stress, constant temperature) given by:

$$G_4 = G_\psi + G_\varepsilon + G_c \quad (4.2)$$

$$G_\psi = \frac{a_0 t}{2}(\psi_a^2 + \psi_c^2) + \frac{b}{4}(\psi_a^2 + \psi_c^2)^2 + \frac{g}{2}\psi_a^2\psi_c^2 \quad (4.3)$$

$$G_\varepsilon = \frac{\tilde{C}_A}{2}\tilde{\varepsilon}_A^2 + \frac{\tilde{C}_S}{2}\tilde{\varepsilon}_S^2 - 2(\tilde{\sigma}_A\tilde{\varepsilon}_A + \tilde{\sigma}_S\tilde{\varepsilon}_S) \quad (4.4)$$

$$G_c = \lambda\tilde{\varepsilon}_A(\psi_c^2 - \psi_a^2) + \eta\tilde{\varepsilon}_S(\psi_c^2 + \psi_a^2) \quad (4.5)$$

where  $t = (T - T_c^0)/T_c^0$  is the reduced temperature and  $T_c^0$  is the critical temperature in a freestanding crystal. Translational symmetry prevents the existence of bilinear terms involving the order parameters; the  $\lambda$  and  $\eta$  terms are the lowest order couplings allowed. The coefficients  $a_0$ ,  $b$  as well

as the elastic constants  $C_S$  and  $C_A$  must be positive. Empirically, we note that the upper transition  $T_{CDW1}$  corresponds to the formation of a CDW state with a wavevector parallel to the longer  $c$ -axis. Therefore the coupling constant  $\lambda$  between the antisymmetric strain and the order parameters must be negative. This is also supported by measurements of the thermal expansion below  $T_{CDW1}$ [69]. Hydrostatic pressure experiments[100, 101, 79] suggest that the symmetric coupling coefficient  $\eta$  must also be negative. The phase diagram produced by this model for a few sets of coefficients are shown in panels (d) and (e) in Fig. 4.1.

The orthorhombic crystal structure (specifically the  $ab$  and  $bc$  mirror planes which contain the CDW wavevectors) precludes such an elastic coupling between the order parameters and in-plane shear strain. The lowest order coupling terms between the order parameters and shear terms  $\varepsilon_{ab}$ ,  $\varepsilon_{bc}$ , and  $\varepsilon_{ac}$  are biquadratic and are neglected here.

Previous work has explored the  $R\text{Te}_3$  phase diagram with the assumption of  $C_4$  symmetry without strain coupling[88], equivalent to the case  $\lambda = \eta = 0$ . In this case,  $g$  must be positive in order for a unidirectional CDW to form rather than a checkerboard state. Reintroducing the stress coupling, we then see that antisymmetric stress can be expected to train the CDW wavevector between the  $\mathbf{q}_c$  and  $\mathbf{q}_a$  states, which are separated by a first order transition as shown in Fig. 4.1(d). In such a model, no second CDW transition is observed at lower temperatures. This would appropriately describe the phase diagram of  $R\text{Te}_3$  for  $R=\text{La, Ce, Pr, Nd, Sm, and Gd}$ .

The case for  $g < 0$ , considered in Fig. 4.1(e), exhibits similar wavevector switching behavior but produces a finite region of coexistence of both the  $\mathbf{q}_c$  and  $\mathbf{q}_a$  states, bounded by a pair of second order transitions. At first glance, a vertical cut of this phase diagram for finite  $\tilde{\sigma}_A$  appears to reproduce the cascade of phase transitions observed in  $R\text{Te}_3$  for  $R=\text{Tb, Dy, Ho, Er, and Tm}$ . However, later sections of this work will demonstrate that the character of the observed phase transitions is incompatible with  $g < 0$ : we find that the strain-induced transition between  $\mathbf{q}_c$  and  $\mathbf{q}_a$  is indeed first order, as indicated in Fig. 4.1(d).

Reproducing the proper topology of the phase diagram for the heavy rare-earth compounds requires the inclusion of higher order terms. One such model has been explored to 8th order for the case of  $R\text{Te}_3$  in the presence of disorder[44]. In the pristine case, we have found that adding the two possible sixth order terms Eq. (4.2) suffices to capture the basic phenomenology of our observations:

$$G = G_4 + r(\psi_c^2 + \psi_a^2)^3 + \gamma(\psi_c^4\psi_a^2 + \psi_c^2\psi_a^4) \quad (4.6)$$

where  $g > 0$ ,  $r > 0$ , and  $\gamma \approx -r/2$ . This phase diagram is shown in Fig. 4.1(f).

### 4.3 Experimental Methods

Uniaxial stress was generated using a commercially available stress cell, specifically the CS-100 from *Razorbill Instruments*, in which a bar-shaped sample was attached spanning a pair of mounting

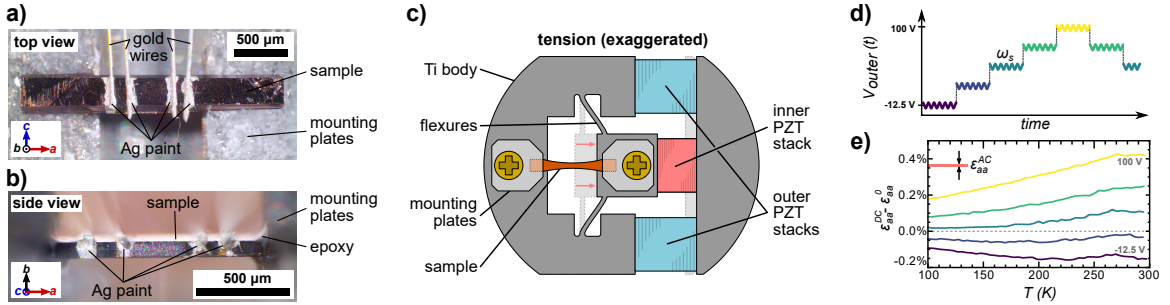


Figure 4.2: Description of the experimental setup. (a) Microscope photograph of the top and (b) side view of a representative  $\text{ErTe}_3$  sample mounted in the stress cell, and contacted for  $a$ -axis resistivity and elasto-resistivity measurements. (c) Cartoon drawing of the CS-100 stress cell from *Razorbill Instruments*. The outer two piezoelectric actuators were elongated ( $V_{\text{outer}} > 0$ ) and the inner is compressed ( $V_{\text{inner}} < 0$ ), resulting in tensile stress applied to the sample. (d) Schematic of the voltage applied to the outer stacks as a function of time. The actuator voltage was the sum of a stepwise DC offset (ca. -25-100 V) with a small sinusoidal oscillation (ca. 5  $V_{\text{rms}}$ , 30-80 Hz). Data was taken continuously while the sample temperature was ramped slowly (approx. 1 K/min), and the duration of each DC step was approximately 6.5 seconds. (e) DC component of the strain measured for a representative  $\text{ErTe}_3$  sample as a function of temperature and offset voltage  $V_{\text{outer}}$ . The temperature dependent response of the piezoelectric actuators contributes to some drift in strain for any given temperature. The height of the shaded bar in the upper left corner of (e) represents the maximum amplitude of the AC strain oscillation which was superimposed on this data.

plates, shown schematically in Fig. 4.2. The sample was then stressed by changing the spacing of the mounting plates *in situ* by applying voltages to three piezoelectric actuators (made of stacks of lead zirconate titanate, or PZT). The outer two stacks were connected in parallel to a single voltage  $V_{\text{outer}}$ , and elongation produced tensile stress. Elongation of the inner stack ( $V_{\text{inner}}$ ) generates compressive stress. This experimental design minimized effects due to thermal expansion of the PZT. The crystal changes shape due to the stress that it experiences, but we measured the resulting strain rather than the stress. Certain caveats associated with this are described below.

The measurements described in this work required the superposition of both static and oscillating stresses. We generated a waveform of  $V_{\text{outer}} = V_{\text{dc}} + V_{\text{ac}} \cos(2\pi f_s t)$  to drive the outer PZT stacks, and a separate static voltage  $V_{\text{inner}}$  was applied to the inner stack.  $V_{\text{dc}}$  varied between -25 V and 100 V,  $f_s$  varies between 20 Hz and 90 Hz, and an oscillation of 5  $V_{\text{rms}}$  was used for all measurements. Uniaxial stress was applied primarily in tension, to avoid buckling or delaminating these soft, layered samples.

In order to disentangle effects which rely on the temperature and strain history of the sample, data were collected using two different protocols. The first was to slowly sweep temperature while stepping  $V_{\text{outer}}$  up and down. On each step, the DC component was changed by  $\pm 12.5$  V. Unless otherwise noted, data presented in the figures only shows data taken for steps which were increasing in voltage although data was also taken for decreasing steps. The cases of increasing and decreasing

voltages differ by a slight hysteresis ascribed to the first order transition, but otherwise show the same qualitative behavior.

The second protocol used was to sweep temperature up and down for a fixed value of  $V_{dc}$ . It should be noted that this is not equivalent to measurement at constant strain. While the strain was monotonic in  $V_{dc}$  at any given temperature, temperature dependence of the displacement per volt in the PZT actuators caused the actual strain to drift as a function of temperature, as shown in Fig. 4.2(e).

The displacement  $\Delta L$  of the jaws was measured using the capacitive sensor built into the CS-100 cell. We used a custom-built autobalancing bridge circuit to convert the capacitance to a voltage signal, which was then interrogated with standard lock-in amplifiers. This circuit enabled accurate detection of both the constant displacement offset as well as the oscillating component (for strain frequencies up to 1 kHz), and is described in detail in appendix 4.A.

In an ideal case, where the stress cell and epoxy would be infinitely stiff compared to the sample, the sample strain is given by  $\varepsilon = \Delta L/L$ , where  $L$  is the sample length and  $\Delta L$  is the displacement detected by the capacitive sensor. This case would be equivalent to the thermodynamic condition of fixing constant strain along the long axis of the sample (temporarily defining this as the  $x$ -axis  $\varepsilon_{xx}$ ) while the other components of the strain tensor are allowed to relax. This differs slightly from the conditions described in the guiding model of the previous section, in which  $\tilde{\sigma}_{xx}$  was held constant. In a free-standing crystal, the coupling terms between the CDW and strain ( $\lambda$  and  $\eta$  in Eq. (4.5)) cause strain to behave like a secondary order parameter. A finite value of the CDW gap in either direction induces a sympathetic orthorhombic distortion. Fixing constant strain rather than stress would largely preserve the phase diagram of Fig. 4.1(f) except near the  $\mathbf{q}_a$ - $\mathbf{q}_c$  transition—the first order transition would widen to encompass a region characterized by a patchwork of orthogonal domains of  $|\tilde{\varepsilon}_A| > 0$  such that the average strain matched the externally imposed condition. In reality, however, we must mention three caveats regarding this idealized constant-strain condition.

First, the pliability of the epoxy is known to decrease the strain transmitted to the sample. Simulations for the case of iron-pnictide superconductor samples show strain transmission of approximately 70% the ideal value[136]. This effect changes quantitative estimates of critical values of the strain to induce the phase transition shown in Fig. 4.1(f), but does not affect the overall features of the phase diagram. For the present study we therefore neglect this effect since our focus is on general features of the strain-tuned phase diagram. Secondly, mismatch of the thermal expansion coefficients between the sample and titanium cell body generates a temperature-dependent stress. In the case of  $R\text{Te}_3$ , the in-plane thermal expansion is approximately five times larger than that of titanium at room temperature[69]. While the thermal expansion of  $R\text{Te}_3$  has not been measured for all temperatures, it is sensible to assume that the estimated magnitude of tensile (compressive) strain is always underestimated (overestimated). We incorporate the contraction of titanium in our estimate of the jaw spacing  $L$ , but we do not apply any correction for thermal expansion of the

sample. Finally, the process of curing the mounting epoxy can produce built-in strains even at room temperature, and this offset varies from sample to sample. In order to compare samples on the same scale, we extract the location of the critical point between the  $\mathbf{q}_c$ ,  $\mathbf{q}_a$ , and disordered states, which we define as occurring at the degeneracy strain  $\varepsilon_{aa}^0$ . The arguments provided in this paper do not require the exact knowledge of the absolute strain, but rather focus on the relative changes.

Single crystals of  $\text{ErTe}_3$  and  $\text{TmTe}_3$  are grown by a self-flux method described elsewhere.[83] The in-plane  $a$ - and  $c$ -axes are distinguished using x-ray diffraction by comparing amplitudes of the (061) peak with its forbidden counterpart (160). Samples are cleaved and cut by hand with a scalpel into rectangular bars of 1.3 mm to 2.4 mm in length, 250  $\mu\text{m}$  to 500  $\mu\text{m}$  in width, and 25  $\mu\text{m}$  to 130  $\mu\text{m}$  in thickness. The sample is then epoxied and clamped to the stress cell between a set of roughened titanium mounting plates. The sample is electrically isolated from the bottom titanium mounting plates with small pieces of thin tissue paper impregnated with epoxy. The distance between the edges of the clamps is approximately 1 mm.

We detect strain-induced oscillations in the sample temperature using a thermocouple. A Type E thermocouple is formed by spot-welding pieces of constantan and chromel thermocouple wire, both 12.5  $\mu\text{m}$  in diameter. The welded junction is then attached to the center of the top face of the sample using either two-part epoxy or silver paint. While the phenomenology is the same, we found slightly better thermal coupling between the thermocouple and sample when using silver paint. The reference junction is formed by attaching the free ends of the wires to copper pads which are thermalized to (but electrically isolated from) the body of the strain cell, as in ref. [134]. The detected signal is amplified with an SR554 transformer as well as an SR580 preamplifier, together providing a composite gain of 2000.

Electrical contacts are formed by selectively sputtering gold onto desired regions of the freshly cleaved surface, and gold wires are attached with *DuPont* 4929 silver paint. All of the contacts are placed within the suspended section of the crystal to minimize contributions from the clamped regions, which may experience significant strain inhomogeneity. The resistivity and elastoresistivity are extracted using the demodulation techniques presented in [127]. The voltage signal is amplified through an SR554 transformer from *Stanford Research Systems* with gain of 100. The transformer's frequency dependence is independently calibrated and measured signals are corrected to reflect this.

## 4.4 Results

### 4.4.1 Elastocaloric effect measurements

The elastocaloric effect (ECE) reflects the strain-dependence of the entropy of a material. The ECE can refer either to the change in entropy resulting from isothermal changes in strain  $(dS/d\varepsilon)_T$  or to the change in temperature resulting from an adiabatic change in strain:  $(dT/d\varepsilon)_S$ . We use the latter definition throughout this work. The ECE relates both to critical fluctuations near a strain-tuned

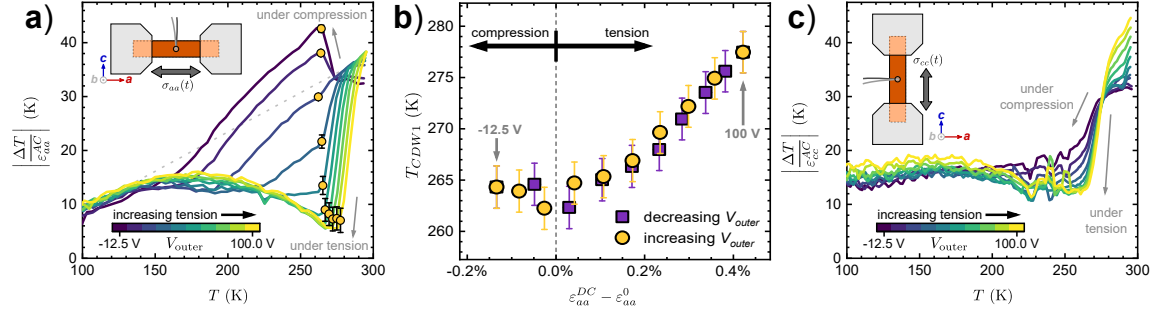


Figure 4.3: Elastocaloric effect results for a sample of  $\text{ErTe}_3$  with uniaxial stress (a) Magnitude of the elastocaloric response with stress parallel to the  $a$ -axis as a function of temperature and offset voltage. The critical temperature  $T_{CDW1}$  (circles) is extracted from an extremum in the second derivative. Inset: schematic of the experimental setup. The dotted line is a guide to the eye for a linear background independent of the strain. The anomaly at  $T_{CDW1}$  rises above this background for compressive stresses, but changes sign for large enough tensile strain. (b) Critical temperatures  $T_{CDW1}$  extracted from (a) as a function of DC offset strain, shown for both increasing and decreasing PZT voltage steps. The critical temperature rises as one departs from  $\varepsilon_{aa}^0$  toward either compressive or tensile strain. (c) Elastocaloric effect with stress parallel to the  $c$ -axis. Tension increases the magnitude of the critical anomaly, but no switching behavior is observed.

transition, as well as equilibrium thermodynamic quantities such as the heat capacity and thermal expansion, as will be described in detail in Section 4.5. The elastocaloric effect (ECE) in  $\text{ErTe}_3$  under uniaxial stress, measured while slowly cooling and stepping the PZT control voltage up and down, is presented in Fig. 4.3. Similar data for  $\text{TmTe}_3$  are shown in Fig. 4.4. In both figures, panel (a) corresponds to stress parallel to the  $a$ -axis. In this orientation, a step-like anomaly appears at  $T_{CDW1}$ , which is approximately 265 K for  $\text{ErTe}_3$ . For slightly compressive stresses (negative  $V_{\text{outer}}$ ), the anomaly at  $T_{CDW1}$  causes the ECE to increase in magnitude upon cooling through the transition. The magnitude of the step decreases with increasing tensile strain, and eventually the step inverts and the ECE decreases in magnitude upon cooling through  $T_{CDW1}$ . Further increasing the tensile stress causes the step to grow again in magnitude until it saturates. At the largest tensile strains, the transition into the CDW state corresponds to an  $\approx 85\%$  decrease of the total ECE signal.

As a thermodynamic probe, the ECE is expected to display a cusp at the critical temperature, similar to the heat capacity.[128] We identify this feature, and therefore  $T_{CDW1}$ , as an extremum in the second derivative of the ECE with temperature, which removes bias due to the background. The extracted values are plotted in panel (b) of Fig. 4.3. We define  $\varepsilon_{aa}^0$  as the strain for which  $T_{CDW1}$  reaches a minimum, corresponding to  $\tilde{\varepsilon}_A = 0$  in Section 4.2. This point also then corresponds to where  $dT_{CDW1}/d\varepsilon$  changes sign, as well as where the step-like anomaly flips its direction.

Such switching behavior is not observed when tensile stress is applied parallel to the  $c$ -axis, as seen for  $\text{ErTe}_3$  in Fig. 4.3(c). In contrast to the elastocaloric effect for  $a$ -axis stress, even the most compressive traces correspond a decrease in ECE magnitude cooling through  $T_{CDW1}$ .

Additionally, similar to the case for the strain-induced  $\mathbf{q}_a$  stripe state, increasing tensile strain slightly increases  $T_{CDW1}$ . The resemblance between the elastocaloric effects observed for  $c$ -axis stress and the limit of high tensile  $a$ -axis stress further suggests that the CDW flop preserves the qualitative structure/characteristics of the CDW with the exception of a  $90^\circ$  rotation. For  $T \lesssim T_{CDW2}$  the ECE curves again become largely independent of both the orientation and magnitude of the stress.

ECE measurements in TmTe<sub>3</sub> for  $a$ -axis strain, shown in Fig. 4.4, follow the same trends as ErTe<sub>3</sub>. Cooling through  $T_{CDW1}$  ( $\approx 245$  K) increases the ECE under compressive stress, and decreases under tensile stress. The extracted critical temperature also exhibits a weak minimum, with a stronger increase for the largest tensile strains. The response on the compressive side is mostly flat, which we attribute to buckling of the sample. Buckling would imply poorer transmission of the measured strain into the sample, which is consistent with the smaller ECE signal observed for the most compressive case,  $V_{\text{outer}} = -12.5$  V.

The data presented in Fig. 4.4 was taken under conditions of temperature sweeps with constant PZT control voltages. This dataset, in conjunction with the ErTe<sub>3</sub> data in Fig. 4.3, demonstrate that the qualitative features do not depend on the stress and temperature history.

#### 4.4.2 Resistivity

As a direct probe of quasiparticles at the Fermi level, electrical transport is highly sensitive to the opening of CDW gaps. The resistive signatures of both CDW transitions are most clear in the out-of-plane component  $\rho_{bb}$ , which averages roughly equally over the entire quasi-2D FS. Out-of-plane resistivity measurements in ErTe<sub>3</sub> under  $a$ -axis stress are presented in Fig. 4.5.  $T_{CDW1}$  and  $T_{CDW2}$  are identified as minima in the temperature derivative.

$T_{CDW1}$  shows the same trend as evinced from elastocaloric measurements—a minimum for a small amount of tensile stress with increases on either side. The height of the resistivity bump below  $T_{CDW1}$ , which is related to changes in the density of states the Fermi level due to the opening of the CDW gap, decreases only slightly. This indicates that despite the large change in behavior of the ECE signal under stress, a gap of similar magnitude appears to open regardless of the stress. Measurements of  $\rho_{bb}$  alone, however, do not provide information on which sections of the quasi-2D Fermi surface become gapped.

As the tensile strain increases, we see that  $T_{CDW2}$  decreases significantly, dropping  $\approx 20$  K for strains of 0.1%. Simultaneously, the corresponding bump in resistivity decreases in magnitude as well. Unlike  $T_{CDW1}$ ,  $T_{CDW2}$  decreases monotonically with increasing tensile strain. We attribute this to an unmeasured strain offset arising from mismatched thermal expansion between the Ti stress cell and the sample. The contraction of the sample on cooling relative to the stress cell implies that the sample has drifted toward positive tensile stress as the temperature decreased. The monotonic decrease in  $T_{CDW2}$  suggests that the stress is, at these temperatures, beyond that required to realign the primary wavevector by  $90^\circ$ .

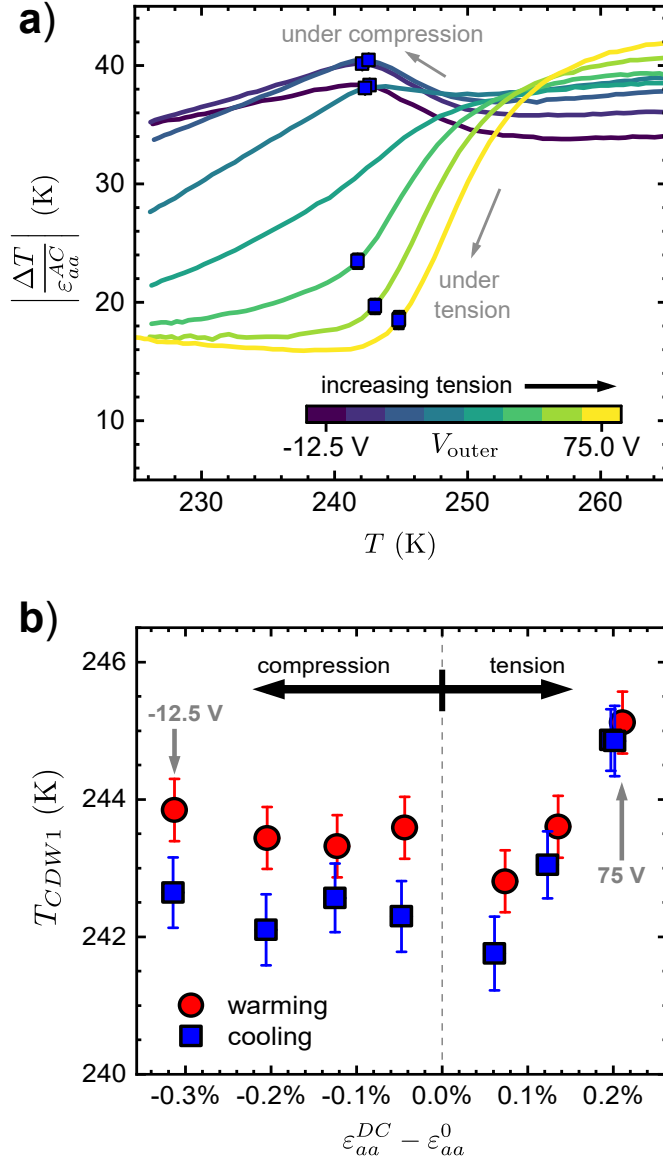


Figure 4.4: Elastocaloric effect measurements in  $\text{TmTe}_3$  with stress parallel to the  $a$ -axis. (a) Magnitude of the elastocaloric response near  $T_{CDW1}$  as a function of temperature and PZT voltage. Each trace was collected by cooling at a constant  $V_{outer}$ , and  $T_{CDW1}$  is extracted by the second derivative. Despite using different data acquisition protocols and different rare-earths, the results in Fig. 4.3 share the same behavior. (b) Extracted critical temperatures on the same sample for both warming and cooling traces. The increase of  $T_{CDW1}$  for tensile strains is clearly defined, although an increase on the compressive side is not observed. We attribute this to slight buckling of the sample, resulting in an overestimate of the compressive strain. One of the curves near the center exhibited no clear extremum in the second derivative, so  $T_{CDW1}$  could not be unequivocally identified. Tension and compression are labeled (black arrows) relative to  $\tilde{\epsilon}_A = 0$ .

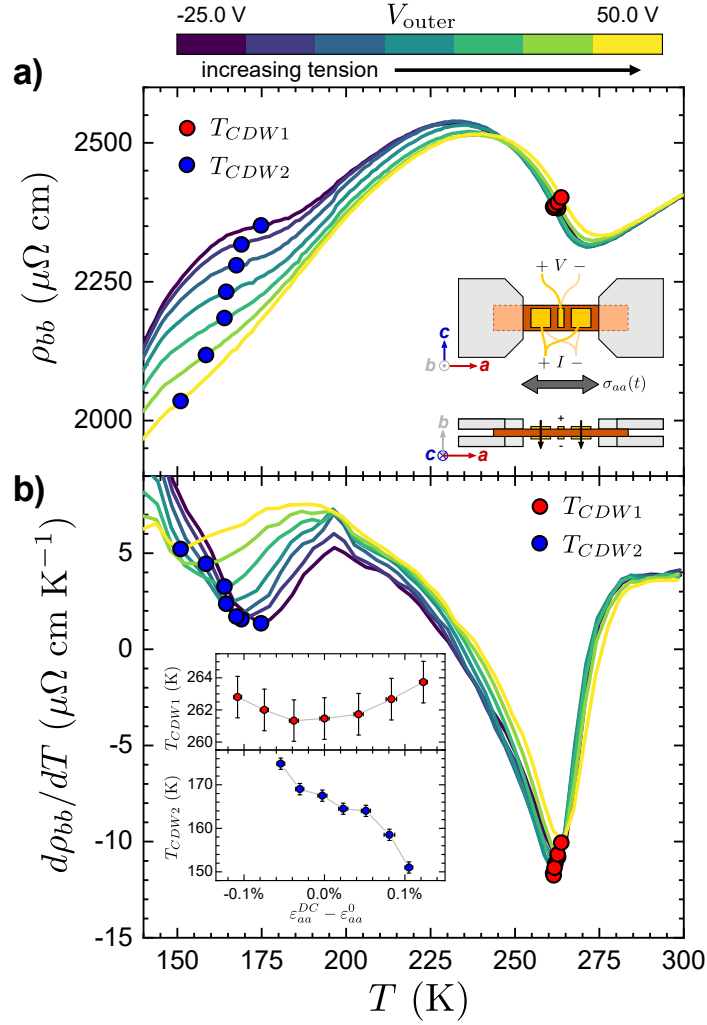


Figure 4.5: Out-of-plane resistivity  $\rho_{bb}$  in  $\text{ErTe}_3$ . Panel (a) shows the resistivity traces for a series of PZT voltages. Inset: top and side view schematics of the contact geometry used in this experiment. Current is passed into the sample through the larger, outer two contacts on both the top and bottom of the crystal, and the smaller center pads are used to detect the voltage. Temperature derivatives of the resistivity traces are shown in panel (b). The minima of the derivative traces correspond to the critical temperatures. Inset to (b):  $T_{CDW1}$  and  $T_{CDW2}$  plotted as a function of strain. The lack of a maximum in  $T_{CDW2}$  corresponding to the minimum in  $T_{CDW1}$  and the switch between the two cases is attributed to an underestimate of the tensile stress arising from mismatched thermal expansion of the sample and stress cell.

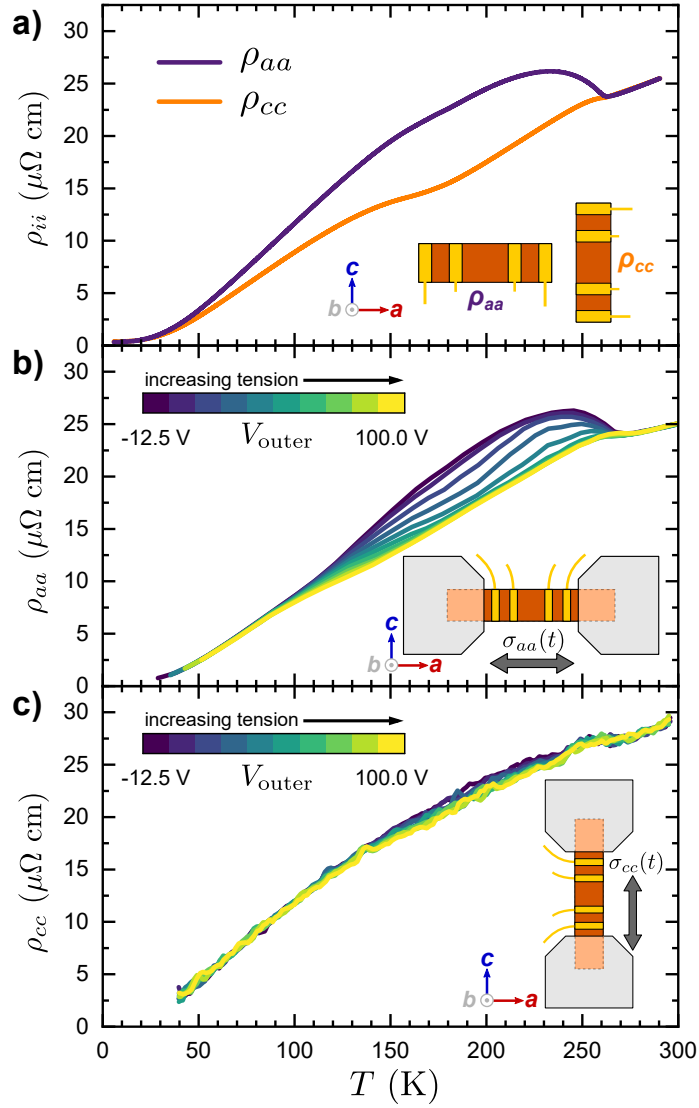


Figure 4.6: In-plane resistivity components of  $\text{ErTe}_3$  as a function of temperature and strain. (a) free-standing resistivity components of  $\text{ErTe}_3$ . Resistivity along the  $a$ -axis increases more strongly upon entering the  $\mathbf{q}_c$  state due to the curvature of the gapped region of the Fermi surface[106]. (b)  $a$ -axis resistivity of  $\text{ErTe}_3$  under  $a$ -axis stress, as a function of temperature and PZT voltage. Negative and low voltages behave similarly to the freestanding case for  $\rho_{aa}$ , but crosses over to resemble freestanding  $\rho_{cc}$  as the tension increases. (c)  $c$ -axis resistivity under  $c$ -axis stress, which does not demonstrate any switching behavior.

The in-plane resistivity components,  $\rho_{aa}$  and  $\rho_{cc}$ , are presented in Fig. 4.6 for ErTe<sub>3</sub>. These components show similar features at the CDW transitions, but also provide insight into the anisotropy of the Fermi surface in the ordered phases. In particular, it has previously been established[106, 107] that the CDW gap with wavevector  $\mathbf{q}_c$  has a larger effect on  $\rho_{aa}$  than on  $\rho_{cc}$ , and vice versa. This is also observed clearly in the top panel of Fig. 4.6 for a freestanding sample. Switching of the CDW wavevector from  $\mathbf{q}_c$  to  $\mathbf{q}_a$  would then be accompanied by a change in the relative magnitude of the anomalies at  $T_{CDW1}$  and  $T_{CDW2}$ . This is exactly what is observed.

The lower two panels in Fig. 4.6 show longitudinal measurements of both  $\rho_{aa}(\varepsilon)$  and  $\rho_{cc}(\varepsilon)$  under uniaxial stress parallel to the current flow. For slightly compressive  $a$ -axis stress,  $\rho_{aa}(\varepsilon)$  closely resembles the freestanding value,  $\rho_{aa}(\varepsilon = 0)$ . As  $\sigma_{aa}$  increases, however, the effect of  $T_{CDW1}$  decreases in magnitude, and  $\rho_{aa}(\varepsilon_{aa})$  eventually crosses over to behave like  $\rho_{cc}(\varepsilon = 0)$  instead. The switch between the two limits occurs gradually as a function of stress.

In contrast, no such switching behavior is seen in  $\rho_{cc}(\varepsilon)$ . A slight decrease of the resistivity can be observed for the largest tensile stresses, but the curves never deviate very far from  $\rho_{cc}(\varepsilon = 0)$ . On general grounds, tensile  $\sigma_{cc}$  will reinforce the intrinsic orthorhombicity of the material. Tensile  $\sigma_{aa}$  opposes this orthorhombicity, however, and will train the CDW wavevector along  $\mathbf{q}_a$  in the model presented in Section 4.2. In principle compressive  $\sigma_{cc}$  would have a similar effect, but as mentioned in Section 4.3 the soft RTe<sub>3</sub> samples are prone to buckling under compression, so this regime is not accessible here. In summary, the observed behavior of both  $\rho_{aa}(\varepsilon)$  and  $\rho_{cc}(\varepsilon)$  appears consistent with a reorientation of the CDW wavevector from  $\mathbf{q}_c$  in the freestanding crystal to  $\mathbf{q}_a$  under  $a$ -axis tensile strain.

In order to examine the character of this reorientation transition, we have performed  $\sigma_{aa}$  stress cycles on a sample of ErTe<sub>3</sub> at constant temperature while measuring the  $a$ -axis resistivity. The results of these measurements are presented in Fig. 4.7. Above  $T_{CDW1}$ , very little strain-induced change in the resistivity is observed. As the sample cools below  $T_{CDW1}$ , a clear hysteresis loop opens up and increases in area. The exact size and shape of the hysteresis loops depends on the extent of the stresses applied, which depend on the history of the PZT actuators and is not identical between samples. The inset of Fig. 4.7 shows the normalized loop area for two different ErTe<sub>3</sub> samples in the same configuration. This hysteretic behavior below  $T_{CDW1}$  demonstrates that the switching behavior seen in both the elastocaloric and resistivity data represents a first order transition.

Further decreases in temperature cause the loop to close again, then reopen traversing the loop in the counterclockwise direction instead of clockwise. This inversion occurs near  $T_{CDW2}$ , although the exact value varies sample to sample.

### 4.4.3 Elastoresistivity

More detailed information can be gleaned by examining the strain derivatives of the resistivity. These quantities can, in principle, be extracted from the resistivity traces presented in Fig. 4.6. However,

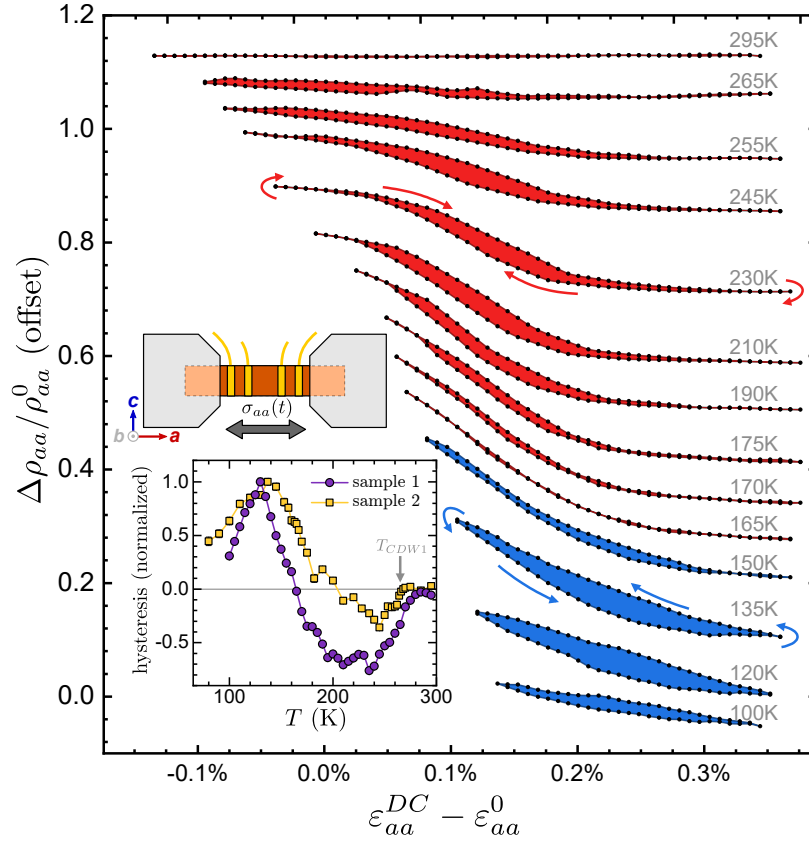


Figure 4.7: Ratiometric change in  $\rho_{aa}$  of  $\text{ErTe}_3$  through stress cycles performed at a few representative temperatures. Curves are offset vertically for clarity. Inset: Schematic of the contact and stress geometry, and plot of the integrated area contained within the hysteresis loops in (b) for two different samples of  $\text{ErTe}_3$ . In both, the hysteresis loops open as the sample cools through  $T_{CDW1}$ . The hysteresis loop changes direction (clockwise to counterclockwise) as the temperature decreases further. The extracted area is sensitive to the exact DC strain range accessed, which accounts for the differences between samples. The observed hysteresis clearly indicates the first-order nature of the phase transition where the direction of the CDW wavevector switches from  $\mathbf{q}_a$  to  $\mathbf{q}_c$ , corresponding to the schematic phase diagram shown in Fig. 4.1(f).

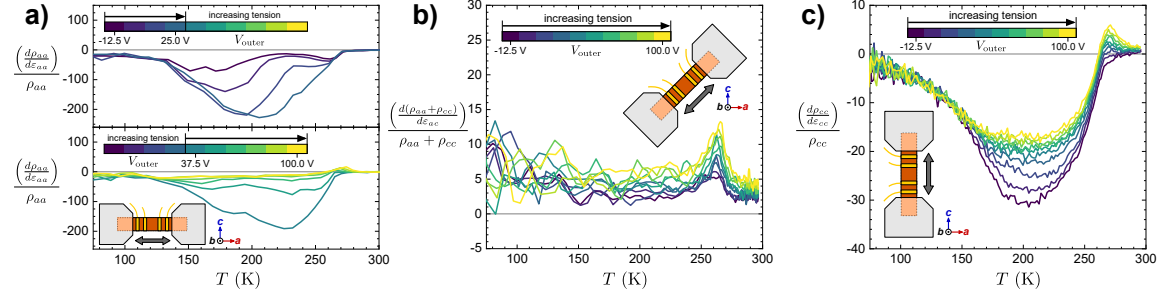


Figure 4.8: (a)-(c) Longitudinal elastoresistivity components for  $\text{ErTe}_3$  under three different stress orientations, as functions of temperature and PZT voltage. The results from the  $a$ -axis sample are split into two subpanels for clarity. Insets describe the orientation of the sample and current in each experiment. In both the  $a$ -axis case, increasing tensile strain initially causes the growth of a large negative bulge between approx. 150 K and 265 K, which then increases again for PZT voltages 37.5 V and above. The behavior in the bottom panel of (a) mimics that of (c), where tensile  $c$ -axis stress also decreases the magnitude of this negative bulge in the same temperature range. Diagonal stress, as shown in (b), does not generate any such response, indicating that the antisymmetric strain component  $\varepsilon_{aa} - \varepsilon_{cc}$  dominates the changes in resistivity. A peak localized at  $T_{CDW1}$  appears in all three sample orientations although it carries the opposite sign for compressive and small tensile  $a$ -axis stress in the top subpanel of (a). This must therefore arise from the coupling of the CDW order parameter fluctuations to the in-plane symmetric strain or out-of-plane strain.[128]

we instead used an AC elastoresistivity technique which provides a more sensitive, higher resolution probe of the strain response.[127] The tensor elastoresistivity  $m_{ijkl}$ , which relates normalized changes in the resistivity tensor  $\rho_{ij}$  to the material strain  $\varepsilon_{kl}$  is defined as

$$m_{ijkl} = d(\Delta\rho/\rho_0)_{ij}/d\varepsilon_{kl} \quad (4.7)$$

and has proven a powerful tool in the understanding of symmetry-breaking phase transitions.[123, 178, 125, 146]<sup>1</sup>

Figure 4.8 shows the in-plane, longitudinal elastoresistivity responses in three different samples of  $\text{ErTe}_3$ , each under different stress conditions. The most dramatic stress dependence arises for stress and current aligned with the  $a$ -axis. The lowest values of  $V_{\text{outer}}$ , which most closely approximate the case of a freestanding crystal, show two distinct features. The first, near  $T_{CDW1}$ , is a sharp dip toward negative elastoresistivity values. As the temperature decreases further, the elastoresistivity grows in magnitude, then shrinks again, resulting in a bulge toward negative values which is separated from the dip at  $T_{CDW1}$  by a gentle local maximum.

Increasing the tensile stress causes this larger bulge feature to increase in magnitude. The

<sup>1</sup>The normalizing resistivity  $\rho_0$  is usually taken as the geometric mean of the relevant resistivity tensor components at zero strain.[119] However, due to large ( $\approx 20\%$ ) changes in the resistivity as shown in Fig. 4.6(b), we elect instead to normalize by the simultaneously measured resistivity. This allows us to present our data without making any ancillary measurements or extrapolations.

local maximum becomes less well pronounced. Tensile stresses beyond a certain value of stress (corresponding here to  $V_{\text{outer}} \approx 25$  V) the bulge again begins to decrease in size and eventually stabilize for small ( $\approx -10$ ) elastoresistivity values for the largest stresses. Beyond this critical value of stress, the dip feature at  $T_{CDW1}$  inverts to become a small peak which grows as the tensile stress increases.

Elastoresistivity measured along the  $c$ -axis, shown in Fig. 4.8(c) produces qualitatively similar results for the large tensile stress limit of the  $a$ -axis elastoresistivity (Fig. 4.8(a), bottom panel). A small peak appears near  $T_{CDW1}$ , which also increases in magnitude for increasing stress. Simultaneously the bulge in the intermediate temperature range also decreases in size.

When stress and current are aligned in the basal plane at  $45^\circ$  to the orthorhombic axes, we observe relatively little response of the resistivity to strain. The peak at  $T_{CDW1}$  still appears, and follows a similar trend of increasing with tensile stress. However, no bulge toward negative elastoresistivity values is observed whatsoever.

Figure 4.9 shows the elastoresistivity measured in  $\text{TmTe}_3$  with stress aligned along the  $a$ -axis. The phenomenology closely matches that observed  $\text{ErTe}_3$  in Fig. 4.8(a). On the low-tension side, both a relatively sharp dip near  $T_{CDW1}$  and a negative bulge at lower temperatures is observed, and for the smallest values of  $V_{\text{outer}}$  the two are separated by a local maximum. The bulge reaches its largest magnitude at intermediate stresses, then it decreases in size again. The dip near  $T_{CDW1}$  also gives way to a positive peak upon crossing this same critical stress value. Beyond the critical stress, the bulge appears to have a sharp change in its slope; below a certain temperature, all of the traces collapse on top of each other.

The positions of the dip or peak near  $T_{CDW1}$ , the local maxima for low tension traces, and the minimum of the bulge beyond the critical stress together describe the phase diagram of  $\text{TmTe}_3$  in the  $T$ - $\sigma_{aa}$  plane. The results of previous sections allow us to identify the dip (peak) at  $T_{CDW1}$  with a transition to a CDW state with wavevector  $\mathbf{q}_c$  ( $\mathbf{q}_a$ ). The features at lower temperature correspond to a second phase transition into a bidirectional CDW state. Altogether, the phase diagram displays the same topology as that produced in Fig. 4.1(f) by the free energy expansion.

## 4.5 Discussion

The combination of thermodynamic and transport results presented here provide compelling evidence of a strain-induced wavevector realignment transition.

### 4.5.1 Elastocaloric effect

We first discuss the elastocaloric effect. The change in behavior in the ECE between freestanding  $R\text{Te}_3$  and  $R\text{Te}_3$  under  $a$ -axis tension can in principle arise from two separate physical effects. Firstly, at temperatures near a general continuous phase transition at temperature  $T_c$ , the strength of

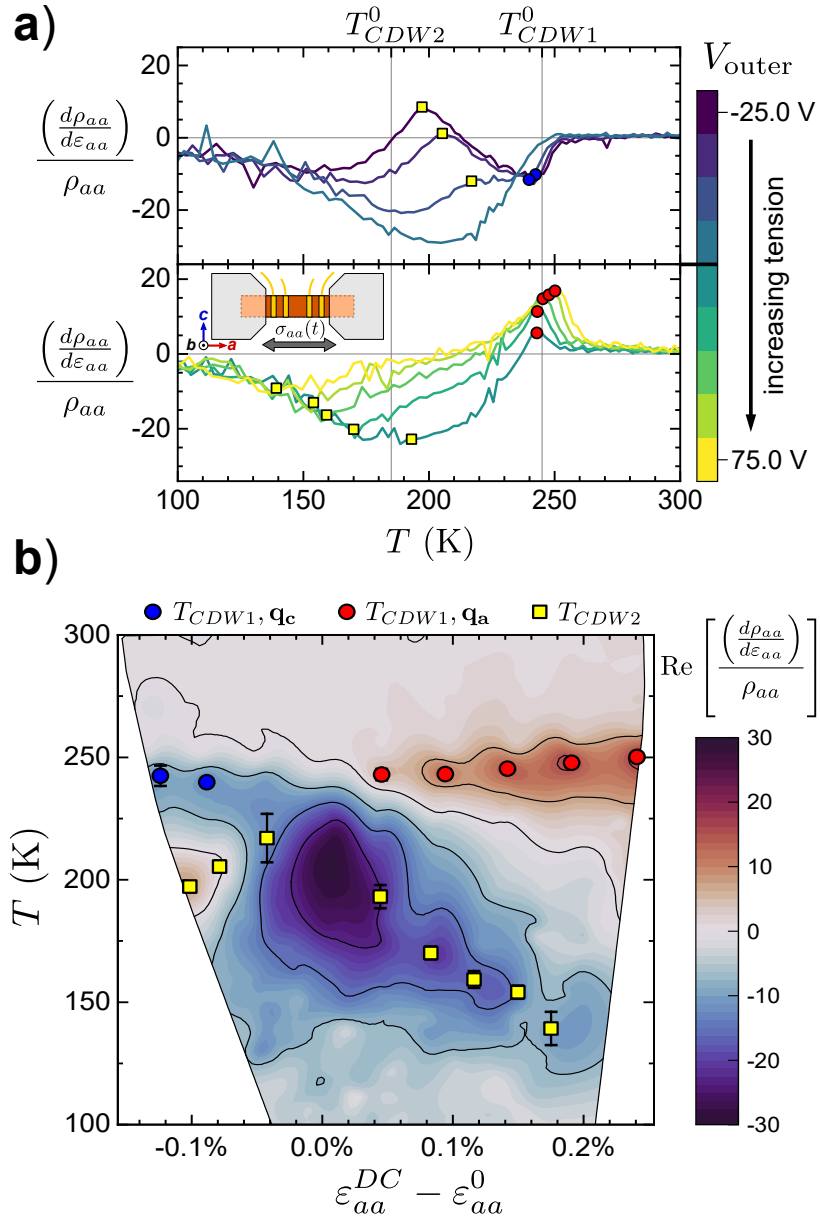


Figure 4.9: Longitudinal  $a$ -axis elastoresistivity in  $\text{TmTe}_3$ . Data presented here was taken by stepping the PZT voltage while sweeping temperature and extracted for steps of increasing tension only. (a) Elastoresistivity as a function of temperature and PZT voltage. Traces are all from the same sample, but have been separated into two panels for clarity. The top panel contains the responses for the most compressive/least tensile stress conditions, and the bottom for the largest tensile stresses. (b) The same data as in (a) presented in the strain-temperature plane. Symbols correspond to the extracted extrema in the traces in (a). The extracted phase transitions, in conjunction with the evidence for a first order transition as shown in Fig. 4.7, maps directly onto the phase diagram presented in Fig. 4.1(f).

the critical fluctuations is a function of the reduced temperature  $t = (T - T_c)/T_c$ . If  $T_c$  is tuned adiabatically by an external parameter such as strain, the sample temperature will shift such that the total entropy is conserved. The smaller  $|t|$ , the larger the change in temperature. The resulting elastocaloric effect is proportional to the critical part of the specific heat  $C_p^{(c)}$  and the rate of change of  $T_c$  with strain [134, 128]

$$\left(\frac{dT}{d\varepsilon_{ij}}\right)_S = \frac{C_p^{(c)}}{C_p} \frac{dT_c}{d\varepsilon_{ij}} + \dots \quad (4.8)$$

In  $R\text{Te}_3$ , we see that the change in sign of the ECE step occurs at the same strain as the change in sign of  $dT_{CDW1}/d\varepsilon$ , consistent with this relation.

This effect only applies in the fluctuation regime near  $T_{CDW1}$ , a region approximately 10-20 K wide in  $R\text{Te}_3$ . [179] Figure 4.3 shows that the sign changing behavior of the ECE anomaly (subtracting a linear background) spans almost 100 K. Well below the transition, the strain dependent ECE must therefore arise from a property of the CDW phase itself, rather than from critical fluctuations. Near the transition, the heat capacity anomalies have been observed to be quite small ( $\approx 1\%$  of the total  $C_p$ ) at both of the CDW transitions in  $\text{TbTe}_3$  [103] and  $\text{ErTe}_3$  [104]. The derivative of  $T_{CDW1}$  with respect to  $\varepsilon_{aa}$  is approximately 2000 K (Table 4.1), however, such that Eq. (4.8) predicts an ECE anomaly at  $T_{CDW1}$  of approximately 20 K, which is indeed what is observed in both Figs. 4.3 and 4.4.

Far from a phase transition, the elastocaloric effect relates to several thermodynamic properties

$$\left(\frac{dT}{d\varepsilon_{ij}}\right)_S = \frac{-T}{C_\sigma} C_{ijkl} \alpha_{kl} \quad (4.9)$$

where  $C_\sigma$  is the specific heat at constant stress,  $C_{ijkl}$  is the elastic constant tensor, and  $\alpha_{kl}$  is the thermal expansion tensor. Regardless of the strain in the sample, stability requires that  $C_\sigma$  and  $C_{ijkl}$  must retain the same sign, but  $\alpha_{kl}$  has no such constraint. Therefore, a strain-induced change in the thermal expansion coefficients could explain the behavior of the ECE in  $R\text{Te}_3$ .

Previous x-ray measurements [69, 93] have indicated that the antisymmetric in-plane thermal expansion component  $\alpha_A = (\alpha_{cc} - \alpha_{aa})/2$  is negative below  $T_{CDW1}$ . Ordering of the  $\mathbf{q}_c$  CDW therefore reinforces the built-in orthorhombic distortion, increasing the  $c$  lattice parameter relative to  $a$ . The observed change in sign in the elastocaloric anomaly, and therefore in the thermal expansion, suggests that the CDW wavevector has been switched from parallel to the  $c$ -axis to parallel to the  $a$ -axis.

## 4.5.2 Resistivity

As the sample traverses this transition, the cross-plane resistivity  $\rho_{bb}$  behaves qualitatively the same between  $T_{CDW1}$  and  $T_{CDW2}$ . This indicates that while the elastocaloric effect indicates a distinct change in electronic anisotropy below  $T_{CDW1}$ , a gap of similar magnitude still opens at the Fermi level regardless of the stress conditions. A slight increase is observed in the  $\rho_{aa}$  and  $\rho_{cc}$  components just

below  $T_{CDW1}$  as well, again regardless of stress. The suppression of the gap-induced increase in  $\rho_{aa}$  with increasing  $\sigma_{aa}$  further supports the inverted electronic anisotropy observed in the elastocaloric effect. These observations support the theory that while the wavevector is realigned from  $\mathbf{q}_c$  to  $\mathbf{q}_a$ , the overall structure of the new CDW phase does not change appreciably.

As mentioned above, the hysteretic response of  $\rho_{aa}$  indicates that the  $\mathbf{q}_c \leftrightarrow \mathbf{q}_a$  transition is first order, as should be expected by symmetry if there is no intervening coexistence region. Interestingly, the hysteresis loop closes again at lower temperatures. A possible explanation for this is evident in the sixth-order free energy expansion presented in Section 4.2 and Fig. 4.1(f). On either side of the first order transition, the region of metastability is bounded by a curve which starts at one of the multicritical points and ends at the other. In this model, the metastable region has the largest width along the stress axis at the temperature halfway between these points, and shrinks in width approaching either point. At the lower critical point, the transitions once again become second order in this model.

In practice, the wavevectors of the two separate CDWs are known to differ slightly in magnitude.[70, 180] This detail, which is not included in the phenomenological model presented above, would require the presence of a first order transition below the lower critical point inside the checkerboard phase. This transition would correspond to an alteration whether the CDW wavevector parallel to  $c$  or  $a$  is dominant, although both order parameters would always be nonzero. Hysteresis at low temperatures likely corresponds to such a transition.

The inverted direction of the low temperature hysteresis loop would be a simple consequence of the antisymmetric strain. For example, tensile stress  $\sigma_{aa}$  appears to stabilize the gap corresponding to  $\psi_{aa}$  and weaken the gap corresponding to  $\psi_{cc}$ . The  $c$ -axis gap affects  $\rho_{aa}$  more strongly[106], but both gaps do still cause the resistivity to increase due to loss of density of states. Below  $T_{CDW2}$  and under tensile stress, the gap at  $\mathbf{q}_a$  is well-established and less sensitive to strain, while the secondary gap at  $\mathbf{q}_c$  is small and highly sensitive. Therefore an *increase* in  $\sigma_{aa}$  will *decrease*  $\psi_c$ , leading to a *decrease* in the resistivity, which matches the observed orientation of the hysteresis loop at low temperatures.

### 4.5.3 Elastoresistivity

Orthorhombic symmetry groups, such as that found in  $R\text{Te}_3$ , impose very few constraints on the coupling between CDW phases and uniform strain  $\varepsilon_{ij}$  with wavevectors along the principle axes. Consider a generalized coupling of the form  $\varepsilon_{ij}\Lambda_{ijk}|\psi_k|^2$ , where  $k = a, c$ . The crystal structure dictates that  $\Lambda_{ijk} = 0$  for  $i = j$ , but the six remaining components may be arbitrary. In the tetragonal limit, one may take  $\Lambda_{iik} = \Lambda_{kki}$ . However, as uniaxial stress experiments generate nonzero values for several  $\varepsilon_{ii}$  components, disentangling the effects of each on the CDW is not trivial.

Despite this general complexity, the phenomenology of  $R\text{Te}_3$  under uniaxial stress is remarkably simple. Specifically, the three elastoresistivity components presented in Fig. 4.8 allow us to identify the

Table 4.1: Rate of change of the critical temperatures  $T_{CDW1}$  and  $T_{CDW2}$  with strain in the strain-induced  $\mathbf{q}_a$  state. In all of these experiments, uniaxial stress is applied long the  $a$ -axis. Not all techniques are sensitive to  $T_{CDW2}$ . The strain range of the  $\rho_{bb}$  measurements was insufficient to observe consistent linear behavior in  $T_{CDW1}$ . Sources of sample-to-sample variation are described in the text.

		$\frac{dT_{CDW1}}{d\varepsilon_{aa}}$ (K)	$\frac{dT_{CDW2}}{d\varepsilon_{aa}}$ (K)
ErTe <sub>3</sub>	ECE	4650 ± 1130	.
	$\rho_{aa}$	6840 ± 670	.
	$\rho_{bb}$	.	-13000 ± 1620
TmTe <sub>3</sub>	ECE	2210 ± 576	.
	$\rho_{aa}$	5150 ± 674	.
	ER	4370 ± 977	-22100 ± 3900

in-plane antisymmetric component of the strain,  $\varepsilon_A = (\varepsilon_{aa} - \varepsilon_{cc})/2$ , as the operative tuning parameter for the strain-induced transitions. Furthermore, the in-plane symmetric component  $\varepsilon_S = (\varepsilon_{aa} + \varepsilon_{cc})/2$  and the out-of-plane component  $\varepsilon_{bb}$  only contribute to shifts in critical temperature.

To see this, consider first the  $a$ - and  $c$ -axis elasto-resistivity measurements. Both show similar phenomenology below  $T_{CDW1}$  under large tensile stress. Except for a small anisotropy in the elastic constants, these measurements are performed under similar magnitudes of  $\varepsilon_S$ ,  $\varepsilon_{bb}$  and  $\varepsilon_A$ , although the sign of  $\varepsilon_A$  will be flipped. In contrast, applying uniaxial stress along the in-plane diagonal results in  $\varepsilon_A \approx 0$  and  $\varepsilon_{ac} \neq 0$ . The symmetric components  $\varepsilon_S$  and  $\varepsilon_{bb}$  will again be similar. Because  $\varepsilon_{ac}$  can only couple to the CDW at quadratic or higher order, this diagonal configuration effectively only probes the response to symmetric strains.

The large negative elasto-resistivity response present in the  $a$ - and  $c$ -axis configurations can then only arise from coupling to  $\varepsilon_A$ . All three experiments showed evidence of a peak (or dip) near  $T_{CDW1}$ ; this effect must then arise from coupling to the symmetric strains. By similar arguments as made above in developing Eq. (4.8), it can be shown that near a strain-tuned continuous phase transition, the elasto-resistivity will also display similar singular behavior to the heat capacity.[128] We can therefore identify the peak as arising from changes in  $T_{CDW1}$  caused by the  $\varepsilon_S$  and  $\varepsilon_{bb}$ .

Extracted values of the change in critical temperatures for the strain-induced  $\mathbf{q}_a$  state under strain are presented in Table 4.1. In general, the  $T_{CDW2}$  is seen to be approximately 3-5 times more sensitive to strain than  $T_{CDW1}$ . The relatively large scatter in the different measurement techniques likely arises from uncertainty in the strain transmission from the stress cell to the sample, as well as run-to-run variations. Possible sources of sample-to-sample differences arise from differences the thickness of the epoxy layer used for mounting and uncertainties in the spacing between the mounting plates. Additionally, near the critical point the predicted sharp cusp in  $T_{CDW1}$  is seen to be rounded somewhat, likely due to strain inhomogeneities in the sample. This curvature can also lead to an underestimate of  $dT_{CDW1}/d\varepsilon_{aa}$ . However, if we assuming a Young's

modulus  $E$  of approximately 50 GPa[181], these values are all consistent with the range of values of  $dT_{CDW1}/d\sigma_{aa} = E^{-1}(dT_{CDW1}/d\varepsilon_{aa})$  previously reported for several  $R\text{Te}_3$  compounds.[103, 104, 105]

## 4.6 Conclusions

In this work, we have shown that  $R\text{Te}_3$ , specifically  $\text{ErTe}_3$  and  $\text{TmTe}_3$ , provide a practical model system for the study of strain-CDW interactions. In particular, uniaxial stress can tune  $R\text{Te}_3$  to and beyond a quasi-tetragonal state for which the CDW wavevector realigns along the  $a$ -axis rather than the  $c$ -axis. Through thermodynamic and transport measurements, we have established a phase diagram and identified several phase transitions; a second order transition to the  $\mathbf{q}_a$ -only state upon cooling under uniaxial stress, and a first-order transition between the  $\mathbf{q}_c$  and  $\mathbf{q}_a$  states induced by uniaxial stress for temperatures below  $T_{CDW1}$ . This work motivates the application of x-ray scattering and ARPES studies of  $R\text{Te}_3$  under strain to further quantify the behavior and characteristics of the strain-induced  $\mathbf{q}_a$  state. More broadly, extension of the techniques presented here to samples with quenched disorder, such as  $\text{Pd}_xR\text{Te}_3$ [182, 114] may also provide unique insight into frustrated charge order on a tetragonal lattice under uniaxial stress. More broadly, This work provides guiding principles for the study of the general behavior of unidirectional CDW phases and lays the foundation for future, more specialized explorations.

## 4.A AC capacitance measurements

The CS-100 uniaxial stress cell from *Razorbill Instruments* incorporates a capacitive displacement sensor used to quantify the strain in the sample. Highly accurate measurements of the capacitance can be made for quasi-static cell displacements, but techniques for measuring changes in capacitance occurring at frequencies above a few Hz are not well established. To make it possible to accurately quantify the oscillating strains, and therefore of the elastoresistivity and elastocaloric effect, we have developed a custom bridge circuit (based on a commonly used impedance measurement technique[183]) which, in conjunction with a pair of lock-in amplifiers, measures both DC and AC changes in capacitance. The bridge is based on an auto-balancing bridge topology, which can effectively cancel effects of parasitic capacitances due to the cables.

A simplified circuit schematic is shown in Fig. 4.10. An AC voltage (amplitude 0.5 V, frequency around 20 kHz) is applied to the input terminal, passed through a unity-gain buffer  $Q_1$  to minimize the output impedance, and then passed to the CS-100 displacement sensor through a coaxial cable. The capacitance of the sensor is of order 1 pF and varies approximately  $\pm 250$  fF through the full range of displacements. In comparison, typical capacitances for the coaxial cables required to connect the circuit (at room temperature) to the stress cell inside the cryostat are of order 100 pF, more than two orders of magnitude larger than the changes to be observed. The low output impedance

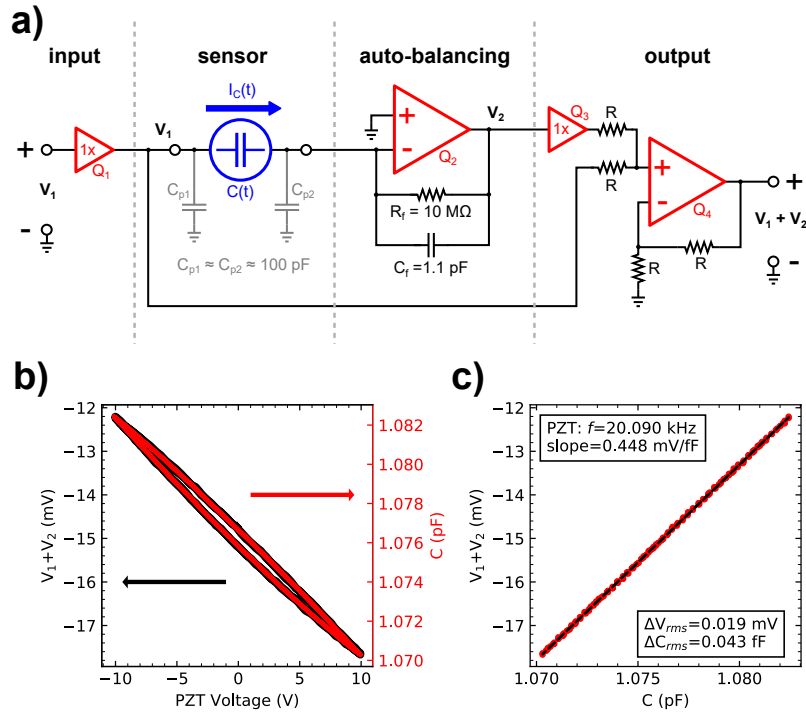


Figure 4.10: Construction and calibration of the auto-balancing capacitance bridge. (a) Diagram of the circuit employed here. A  $\approx 20$  kHz reference input sine wave ( $V_1$ ) is buffered at the input, then applied to one terminal of the displacement sensor through coaxial cables. The opposite terminal is connected to a virtual ground by the auto-balancing section, where the feedback capacitor acts as a reference. The output  $V_2$  of the auto-balancing bridge will be a sine wave with magnitude proportional to the ratio of the sensor and reference capacitances, but  $180^\circ$  out of phase with the reference. The signal at  $V_1$  and  $V_2$  are added together with a non-inverting summing amplifier, and the two will cancel if the sensor and reference capacitances are equal. (b) Output of the capacitance bridge (right axis) overlaid with independent quasistatic measurements made with a commercial capacitance bridge. (c) The output voltage plotted against the measured capacitance, demonstrating linear behavior and a sensitivity of  $448 \mu\text{V}/\text{fF}$  and a root-mean-square noise floor of  $43$  aF. This corresponds to a displacement of approximately  $2$  nm.

of the first buffer stage prevents phase lag due to charging and discharging of this parasitic cable capacitance  $C_{p1}$ .

The other terminal of the capacitive sensor is connected to a virtual ground at the inverting terminal of the auto-balancing stage. The feedback network of this stage contains capacitor which acts as the reference, as well as a resistor for stability. The output of this stage is such that the second terminal of the capacitive sensor remains at zero volts, implying that the parasitic capacitance  $C_{p2}$  at this terminal does not draw any current. The output voltage  $V_2$  required for this is proportional to the ratio of the sensor capacitance  $C(t)$  to the reference capacitance  $C_f$ , but with opposite sign. The final stage combines the output  $V_2$  with the input reference signal such that the two cancel exactly when  $C(t) = C_f$ .

The magnitude of the sum is detected by a lock-in amplifier. Knowing  $C_f$ , the time-averaged magnitude can then be converted to provide a measurement of the DC capacitance. The instantaneous magnitude as it appears at the output of the lock-in amplifier, however still contains the modulation at the strain frequency; a second demodulation stage of this signal provides direct access to the magnitude of the AC capacitance variation.

We have calibrated our bridge circuit against a commercial capacitance bridge for quasi-static strain, as shown in Fig. 4.10(b) and (c), and found that the behavior is well within the linear regime. The capacitance-to-voltage conversion factor is approximately 0.448 mV/fF, and the noise floor is approximately 43 aF. By simulating the strain-modulated capacitance sensor with an amplitude-modulated current source, we have also confirmed that the circuit described here maintains its accuracy to within 2% for strain frequencies up to 1 kHz.

Typical changes in capacitance for a 5 V<sub>rms</sub> oscillating voltage on the outer pair of piezoelectric stacks range between 0.75 fF at 20 K to approximately 2.5 fF<sub>rms</sub> at room temperature. Further details regarding the design and analysis of this AC capacitance measurement circuit can be found in Appendix A

## 4.B Frequency dependence of ECE measurements

As described in detail in ref. [134], the criteria for quasi-adiabatic behavior in ECE measurements depend on the thermal properties of the sample, as well as the properties of the materials used to mount the sample and to adhere the thermocouple. At low strain frequencies, the sample tends to thermalize with the mounting plates, decreasing the observed temperature oscillation magnitude. At high strain frequencies, the thermocouple can no longer follow the changes in temperature. The maximum signal is observed at intermediate frequencies. Formally, the low frequency cutoff for quasi-adiabatic behavior  $\omega_{qa}$  depends on the thermal conductivity  $\kappa$ , the volumetric specific heat  $\rho c_p$ , and the sample length  $L$  as

$$\omega_{qa} \propto \frac{\kappa}{\rho c_p L^2}. \quad (4.10)$$

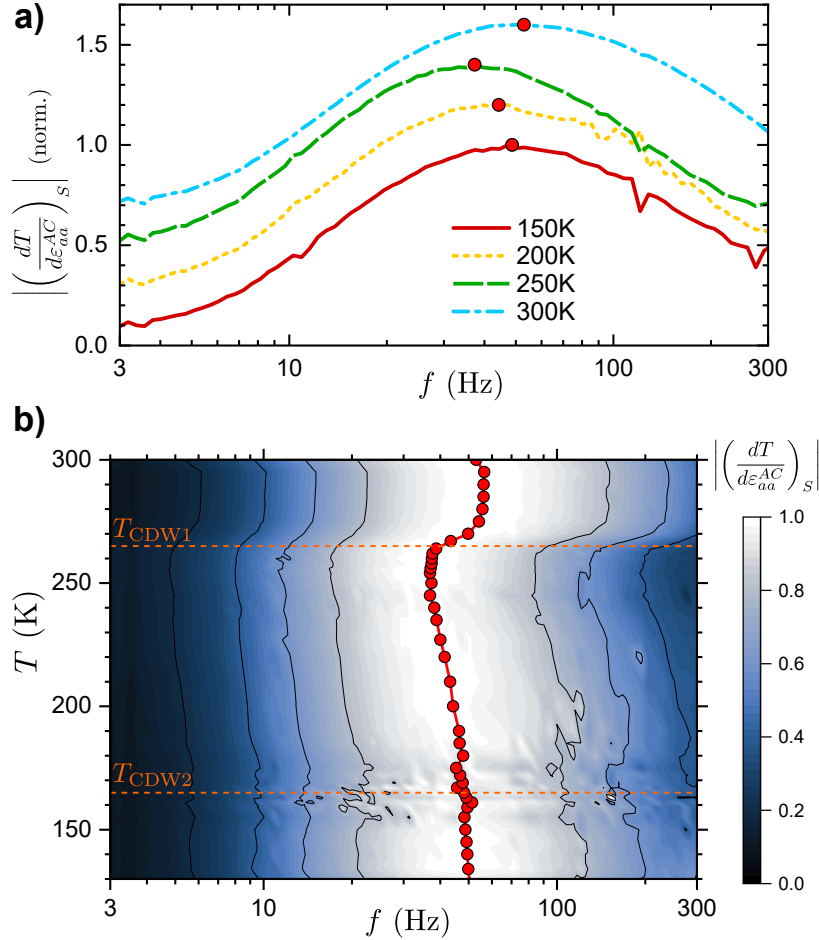


Figure 4.11: Frequency dependence of elastocaloric effect measurements on  $\text{ErTe}_3$  under  $a$ -axis stress. (a) Magnitude of the ECE signal as a function of strain frequency for several representative temperatures. Each curve is normalized to the maximum signal observed at that temperature, and the curves are vertically offset for clarity. The peak is notated with a red circle. Panel (b) shows similar data for a dense set of temperatures, presented as a contour plot. As the sample cools below  $T_{CDW1}$ , the peak frequency decreases from approximately 55 Hz to approximately 35 Hz. This shift in the peak frequency reflects a sudden decrease in thermal conductivity. This is consistent with the Wiedemann-Franz law: this measurement is most sensitive to the thermal conductivity along the  $a$ -axis, and the electrical resistivity  $\rho_{aa}$  also shows the highest increase when cooling through  $T_{CDW1}$ . Data presented in the main text was acquired for a constant frequency in the range of 20 – 40 Hz. Shifts in the frequency dependence with temperature will affect the absolute magnitudes of the ECE signals in Figs. 4.3 and 4.4, but would alter neither qualitative behavior nor the conclusions stemming from this data.

As a consequence, any changes in the thermal conductivity or specific heat will result in a change of the observed elastocaloric signal.

Upon cooling, as one passes through the CDW transition temperature  $T_{CDW1}$ , the electrical resistivity is shown in Fig. 4.6 to change significantly, especially  $\rho_{aa}$ . The Wiedemann-Franz law suggests that a similar change would be observed in the thermal conductivity. The temperature dependence data presented in Figs. 4.3 and 4.4 was taken using a single frequency for the entire temperature and strain range; the temperature dependence of the thermal conductivity should be expected to alter the signal.

Figure 4.11 shows the frequency dependence of magnitude of the elastocaloric effect for  $a$ -axis stress on  $\text{ErTe}_3$  as a function of temperature. The frequency  $f_p$  at which the ECE reaches its peak is denoted by the filled symbols. As the sample is cooled through  $T_{CDW1}$ , the location of the maximum moves to lower frequencies, corresponding to a change in the ratio  $\kappa/c_p$ . The heat capacity, which is dominated by the phonon background (the Debye temperature  $\Theta_D \approx 180$  K[83, 70]) is known to be approximately constant through  $T_{CDW1}$ [104]. Therefore the change in the frequency dependence must arise from changes in the thermal conductivity.

Two different contributions to the ECE anomaly at  $T_{CDW1}$  were discussed in the main text: critical fluctuations near a strain-tuned phase transition, and changes in the thermal expansion tensor. For an ECE measurement at a constant frequency  $f_0$ , however, a sharp change in the frequency dependence can also contribute to this anomaly. If  $f_0 < f_p$ , the frequency dependence would cause the ECE magnitude to rise upon cooling through  $T_{CDW1}$ . The ECE measurements in Figs. 4.3 and 4.4 were made with strain frequencies of 37 Hz and 51 Hz, respectively. The ECE anomaly in the near-freestanding case does indeed increase the ECE magnitude on cooling through  $T_{CDW1}$ , implying that a frequency dependence could indeed be contributing to the behavior. However, both the  $\mathbf{q}_c$  and strain-induced  $\mathbf{q}_a$  states should correspond to a decrease in thermal conductivity due to the opening of a CDW gap. Therefore we conclude that changes in the frequency dependence can decrease the size of the ECE anomaly, but such changes cannot explain the change in sign of the anomaly. Frequency dependent effects can at most alter the absolute magnitude, but the effects discussed in the main text must still be the primary contributions to the ECE.



## Chapter 5

# Disorder suppression of CDW order in Pd-intercalated $\text{ErTe}_3$

*This chapter reports the results of a systematic study of tuning the properties of  $\text{ErTe}_3$  with chemical disorder. Disorder is generically anticipated to suppress long range charge density wave (CDW) order. Transport, thermodynamic, and scattering experiments on  $\text{Pd}_x\text{ErTe}_3$ , a model CDW system with disorder induced by intercalation, are presented. The pristine parent compound ( $x = 0$ ) shows two separate, mutually perpendicular, incommensurate unidirectional CDW phases setting in at 270 K and 165 K. track the suppression of signatures corresponding to these two parent transitions as the Pd concentration increases. At the largest values of  $x$ , one observes complete suppression of long range CDW order in favor of superconductivity. Evidence is also presented from electron and x-ray diffraction measurements, which suggest a tendency toward short-range ordering along both wavevectors which persists even well above the crossover temperature.  $\text{Pd}_x\text{ErTe}_3$  provides a promising model system for the study of the interrelation of charge order and superconductivity in the presence of quenched disorder. This chapter has been taken nearly verbatim from J.A.W. Straquadine, F. Weber, S. Rosenkranz, A.H. Said & I.R. Fisher. “Suppression of charge density wave order by disorder in Pd-intercalated  $\text{ErTe}_3$ ”. *Physical Review B* **99**, 235138 (2019). This work was supported by AFOSR Grant No. FA9550-09-1-0583. Part of this work was performed at the Stanford Nano Shared Facilities (SNSF) supported by the National Science Foundation under award ECCS-1542152.*

### 5.1 Introduction

Charge order is a ubiquitous feature in the phase diagrams of many strongly correlated materials. In the cuprate family of high- $T_c$  superconductors, for instance, evidence of unidirectional charge-ordered states has been observed both in scattering[184, 185, 16, 9, 186, 187, 15, 11] and via local probes

[188, 7, 8]. In these materials, however, charge order always forms in the presence of significant disorder due to the large concentration of dopant ions or intentionally induced oxygen non-stoichiometry that are required to suppress the parent Mott-insulating state. Such disorder tends to frustrate the charge-ordered state, resulting in the formation of short-range-correlated domains. In order to fully understand what role(s) charge order and/or its fluctuations play in enhancing or suppressing superconductivity, the effects of disorder must be taken into account. This motivates the study of model systems which capture the essential physics of charge order without the complications of strong magnetic interactions. In particular, a model system which mimics the square plane symmetry of all known high- $T_c$  superconductors (cuprates and Fe-pnictides), and which hosts a unidirectional CDW state which can be affected by disorder, would be the most relevant point of comparison. Here, we examine the phase diagram of Pd-intercalated  $\text{ErTe}_3$ , a candidate system which, as we will show, fits this description.

CDWs in the presence of disorder have been studied in many systems, perhaps most intensely in the transition metal dichalcogenides (TMDCs).[189, 59, 190, 191, 61] While the physical manifestation of disorder and its effects on collective behavior all depend on microscopic details, several general statements can be drawn from this literature. First, disorder acts to suppress and smear CDW transitions. As a point of principle, even arbitrarily weak disorder prevents a long-range-ordered incommensurate CDW state [50]. The most important consequence of this statement is that while signatures resembling the CDW phase transitions of the pristine material may still appear in the presence of disorder (likely broadened in temperature), they are, strictly speaking, only crossovers. Furthermore, in a system with 4-fold symmetry, a unidirectional density wave must also break a rotational symmetry by ordering along only one in-plane direction. Even if long-range phase coherence is precluded by disorder, a sharp phase transition which breaks this discrete symmetry ( $C_4 \rightarrow C_2$ , Ising-like) is still allowed to occur in the presence of weak disorder.[50] That is to say that the orientational order of the CDW may be preserved even without long-range phase coherence.

Second, localized defects tend to induce Friedel oscillations in the electron density, even at temperatures far above the crossover temperature.[189] This quenched disorder strongly affects the growth of phase correlations of the CDW[191], and thereby can alter the macroscopic properties of the material.

Finally, disorder can tune the interplay between CDWs and superconductivity in subtle ways. For example, in the case of isoelectronic substitution in  $2\text{H-Ta}(\text{Se,S})_2$ , the CDW state is sensitive to disorder, while superconductivity is enhanced due to the increased density of available states — in effect, superconductivity is “protected” from disorder according to Anderson’s theorem, whereas the competing CDW state is not.[59] For electron-irradiated  $2\text{H-NbSe}_2$ [190] a similar trend of phase competition is seen until the CDW is suppressed completely.

The rare-earth tritellurides  $\text{RTe}_3$  ( $\text{R}=\text{Y}, \text{La-Nd}, \text{Sm}, \text{Gd-Tm}$ ) form a family of quasi-2D metals which exhibit unidirectional incommensurate CDW states. [91, 83, 85, 82] The crystal structure is

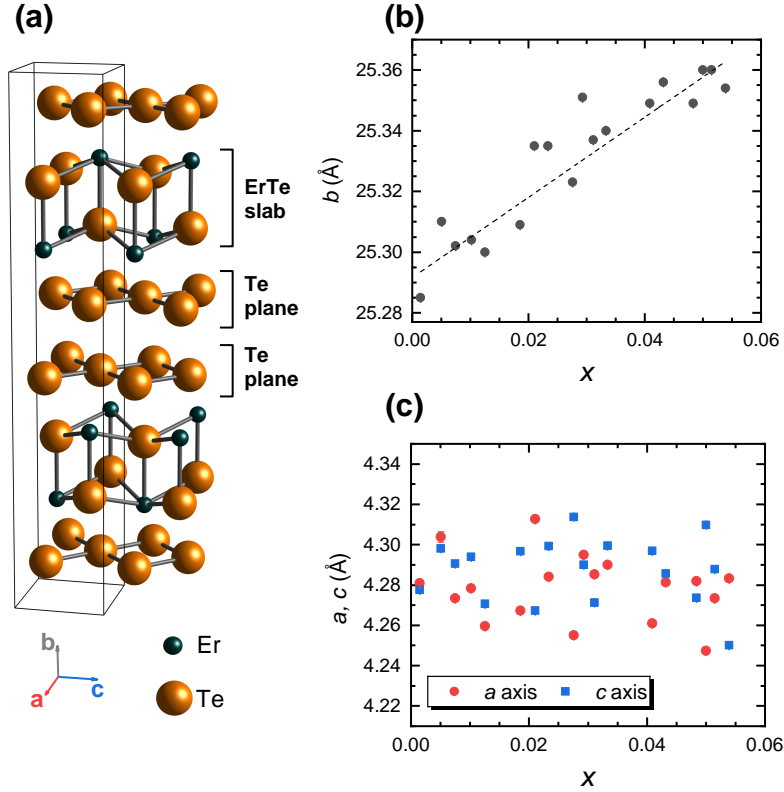


Figure 5.1: (a) Crystal structure of the  $x = 0$  parent compound  $\text{ErTe}_3$ , which consists of alternating ErTe slabs with bilayers of square Te nets. Unit cell is shown by black lines. (b) The out-of-plane lattice parameter  $b$  determined by single-crystal x-ray measurements, as a function of Pd content  $x$  (determined by microprobe analysis). Error bars are calculated as the variance in a simultaneous fit to the Cu  $K\alpha_1$  and  $K\alpha_2$  peaks at the  $(0,8,0)$  position. The lattice expands perpendicular to the planes as  $x$  increases, which is consistent with incorporation of Pd atoms between the planes. (c) The two in-plane lattice parameters  $a$  and  $c$  on the same set of crystals, extracted from the  $(1,9,0)$  and  $(1,7,1)$  peaks. There is no significant trend in  $a$  or  $c$  with increasing  $x$ . Reproduced from Straquadine, et. al. “Suppression of charge density wave order by disorder in Pd-intercalated  $\text{ErTe}_3$ ”. *Phys. Rev. B* **99**, 235138 (2019) with permission of the American Physical Society.

formed of alternating puckered RTe slabs with bilayers of approximately square nets of Te atoms, illustrated in Fig. 5.1(a). The presence of a glide plane in the stacking of these layers creates a 0.05% [69] difference between the in-plane  $a$ - and  $c$ -axis lattice parameters at room temperature, and biases the primary CDW transition to order along the  $c$ -axis. Strictly speaking, the space group of RTe<sub>3</sub> is orthorhombic [72] ( $Cmcm$ , with the  $b$ -axis out of plane), but the electronic properties above the CDW phase transition, as witnessed for example via density functional theory calculations [80], ARPES [81] and transport measurements [69, 107], are effectively 4-fold symmetric. The Fermi surface of these materials is well described by a tight-binding model using only the Te in-plane  $p_x$  and  $p_z$  orbitals. For heavier  $R$  elements ( $R$ =Tb, Dy, Ho, Er, and Tm), the material also exhibits a separate, lower-temperature phase transition [69, 192, 70, 193] characterized by a second unidirectional CDW perpendicular to the first. These two CDW ordering vectors appear to compete for density of states at the Fermi surface, such that suppressing one CDW by chemical [70] or hydrostatic pressure [98, 194, 100] enhances the other. High-resolution x-ray diffraction measurements on tritellurides provide a lower bound on the CDW correlation length of several microns, indicating minimal disorder effects for pristine crystals. [69]

At temperatures above the CDW transition, calculations of the electronic susceptibility  $\chi_q$  exhibit peaks very close to both of the orthogonal CDW wavevectors [40]. Similarly, measurements of the phonon dispersion [102] also shows a Kohn anomaly where the phonons at both wavevectors soften considerably when approaching the transition with decreasing temperature. However, the slight anisotropy induced by the glide plane causes the phonons to soften completely along the  $c$ -axis before the  $a$ -axis, instigating the CDW transition. Despite the proximity of  $q_{CDW}$  to the peak in the calculated  $\chi_q$ , inelastic x-ray scattering measurements indicate that the CDW wavevector is determined by a strongly  $q$ -dependent electron-phonon coupling.

This well-understood material family of incommensurate charge density waves may also provide a model system for exploring the evolution of unidirectional CDW correlations in the presence of disorder, which is intentionally introduced here by Pd intercalation. Pd atoms assume a stable, filled shell  $4d^{10}$  configuration, and therefore should not affect the carrier concentration as the Pd content is increased. Consequently, it can be anticipated that the dominant effect of Pd intercalation is the introduction of disorder to the adjacent Te planes via local lattice strains and/or variation in the local potential. As we will show below, the phase diagram and physical properties of Pd<sub>x</sub>ErTe<sub>3</sub> is consistent with this intuition.

While many of the disorder-induced features seen in the TMDCs may be expected in the case of Pd<sub>x</sub>ErTe<sub>3</sub>, a systematic study is required to determine the magnitude of the effect each will have on the collective behavior of the system. The near-tetragonal structure and unidirectional charge ordering in RTe<sub>3</sub> set it apart from the TMDCs, which exhibit three- or sixfold crystal symmetry and often show a CDW state with three simultaneous ordering vectors oriented 120° from each other. Also, it is worth noting that all measurements point to a truly incommensurate CDW in all members

of the  $\text{RTe}_3$  family, with no observation of a lock-in transition to a commensurate wavevector at low temperatures. [92, 95]

Polycrystalline samples of  $\text{Pd}_x\text{RTe}_3$  ( $\text{R}=\text{Y, La, Pr, Sm, Gd, Tb, Dy, Ho, Er, Tm}$ ) have been reported previously [113], and it was established that for high enough  $x$ , the material superconducts with  $T_c \approx 2\text{-}3$  K regardless of the chosen rare earth. Single crystal measurements have only previously been reported in  $\text{Pd}_x\text{HoTe}_3$  [114], and only the remnant of the first CDW transition was observed. From this it was assumed that the two CDWs merge together and appear simultaneously at a single crossover. In this work, we show transport, magnetometry, x-ray, and electron diffraction studies on samples of  $\text{Pd}_x\text{ErTe}_3$ , and observe that the vestigial signatures of both of the phase transitions are suppressed independently, and that significant CDW correlations appear in both directions, even once the resistivity signature of the second CDW has been suppressed to 0 K. We also demonstrate the appearance of a short-range-ordered structural distortion, evidenced by diffuse streaks in electron diffraction patterns. The short range correlations persist up to temperatures far above the ordering crossover, suggesting that the Pd intercalants nucleate small regions of static CDW order along both in-plane directions. This work establishes  $\text{Pd}_x\text{ErTe}_3$  as a model system for studying the interplay of CDW formation and disorder close to the onset of superconductivity. Recent theoretical work has pointed out the potential complexities of this interplay with the expected appearance of “fragile” states stemming from topological defects in the CDW and vortices in the superconductor[63]. This work sets the stage for further studies of this interplay.

## 5.2 Experimental Methods

Samples were grown using a Te self-flux as described elsewhere for pure  $\text{RTe}_3$  compounds [83], with the addition of small amounts of Pd to the melt. Crystals of  $\text{Pd}_x\text{ErTe}_3$  with  $0 \leq x \leq 0.055$  were produced with this method, though for  $x > 0.03$  crystals of  $\text{PdTe}_2$  also formed. Increasing the Er concentration in the melt and raising the temperature at which the melt is decanted minimized the formation of  $\text{PdTe}_2$  in favor of  $\text{Pd}_x\text{ErTe}_3$ . Microprobe analysis showed that  $\approx 12\%$  of the Pd present in the melt incorporated into the crystals during growth, and that crystal composition is uniform to within experimental error at different spots on a crystal surface and between crystals grown in the same batch. Plate-shaped crystals ( $b$ -axis normal to the plane) 1-3 mm across were routinely produced. Crystal plate area remained fairly constant for all but the largest  $x$  values, but the resulting thicknesses decreased as Pd concentration increased, from several hundred microns for  $x = 0$  to approximately 50 microns for  $x = 0.05$ . This offers indirect evidence that Pd atoms act as intercalants between the Te planes, in that their presence tends to disrupt and slow the rate of growth in this direction. The resulting crystals are orange in color, shiny, soft, and micaceous metals.

Chemical analysis was performed in a JEOL JXA-8230 “SuperProbe” electron microprobe system, calibrated to  $\text{ErTe}_3$  and  $\text{PdTe}_2$  secondary standards.

Measurements of resistance versus temperature were performed in a Janis Supertran-VP continuous flow cryostat. The resistivity in the  $ac$ -plane was measured on thin rectangular crystals which had been cut with a scalpel and cleaved to expose a clean surface immediately before contacting. Crystals were cut such that current flows along the  $[101]$  axis, and contacts were attached to the surface in the transverse geometry described elsewhere. [107] In this geometry, the sum of the resistivity components along the crystal axes  $\rho_a + \rho_c$  and the in-plane resistivity anisotropy  $\rho_a - \rho_c$  are measured simultaneously within the same crystal.

Selected area electron diffraction patterns (SADPs) were taken using an FEI Tecnai G2 F20 X-TWIN transmission electron microscope. Samples were mounted using a liquid  $N_2$  cryogenic holder with a base temperature of 95 K. Samples were prepared by exfoliating thin crystals, which produced large (hundreds of square microns) regions of electron transparent material free of cracks, dislocations, and significant curvature. While  $ErTe_3$  crystals have been observed to grow with small angle twin domains as well as  $90^\circ$  stacking faults, defects such as grain boundaries and dislocations can be observed directly in TEM imaging, and are therefore avoided. SADPs were collected with the beam along the  $[010]$  zone axis, normal to the plane.

Lattice parameter measurements were made from single-crystal x-ray diffraction in a PANalytical X'Pert PRO diffractometer using  $Cu K_\alpha$  radiation. Comparison of superlattice peak intensity along the orthogonal directions was done on the HERIX beamline 30-ID at the Advanced Photon Source.[195] Samples were also screened for twinning and stacking faults in all x-ray measurements by comparing the intensity of the allowed  $(0,6,1)$  peak to the forbidden  $(1,6,0)$  peak prior to collecting data.

Magnetic moment and susceptibility measurements were performed using a Magnetic Property Measurement System 3 from Quantum Design. Samples were cut into rectangular prisms, and measurements were made with field both parallel to and perpendicular to the Te planes.

### 5.3 Results and Discussion

Figure 5.1(b) and (c) show the extracted values of the lattice parameter from single-crystal x-ray diffraction measurements. The out-of-plane  $b$ -axis is observed to expand linearly with  $x$ , which is consistent with the Pd atoms intercalating between the square nets of the Te bilayer. We propose this as the most likely position for the Pd atoms, as the bilayers are only bonded by van der Waals forces. This observation is also consistent with the results of DFT calculations[113] for  $Pd_{0.25}YTe_3$ . The in-plane lattice parameters are unchanged within experimental error. This argues against chemical substitution of Pd on the Er site, as the smaller radius of Pd ions would be expected to compress the lattice in-plane.

Results from microprobe analysis shown in Fig. 5.2 show that Pd atoms are indeed incorporated into the material, at a rate of roughly 12% of the initial concentration in the melt. This data also

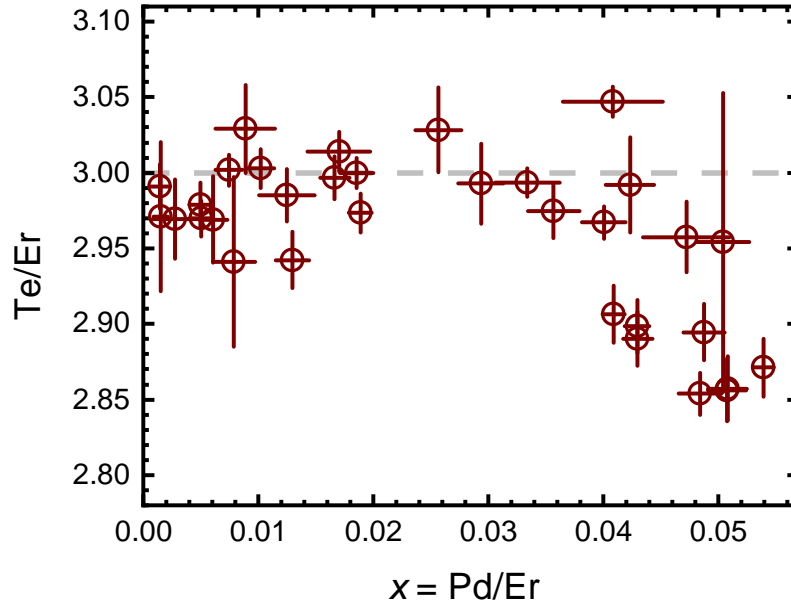


Figure 5.2: Stoichiometric ratios determined from electron microprobe measurements. The  $x$ -axis value is used throughout this work to quantify the concentration of Pd atoms per formula unit. We found no crystals with Pd concentrations above  $x = 0.055$  with this growth method. For growths of the highest Pd concentrations, the formation of  $\text{Pd}_x\text{ErTe}_3$  competes with the formation of  $\text{PdTe}_2$ . For  $x > 0.035$ , a significant deviation from the ideal ratio of 3 Te per Er is observed. This decrease is believed to be due to an increased population of Te vacancies within the bilayers. Reproduced from Straquadine, et. al. “Suppression of charge density wave order by disorder in Pd-intercalated  $\text{ErTe}_3$ ”. *Phys. Rev. B* **99**, 235138 (2019) with permission of the American Physical Society.

shows that the Te:Er ratio falls for  $x > 0.035$ , suggesting that for large concentrations the Pd atoms displace Te atoms from the planes and generate vacancies. This would also be consistent with intergrowth of the  $\text{RTe}_3$  structure with the related polytype  $\text{R}_2\text{Te}_5$ , in which Te bilayers alternate with single Te layers. However, as no extra peaks with the proper periodicity for  $\text{R}_2\text{Te}_5$  were observed in the x-ray diffraction measurements in Fig. 5.1, this effect is negligible if it is present at all.

Figure 5.3 shows the in-plane components of the resistivity tensor of  $\text{Pd}_x\text{ErTe}_3$ , normalized to the room temperature value. For the parent compound, the resistivity is fourfold symmetric in the plane at room temperature, with anisotropy setting in sharply below the first CDW transition.[107] Below the second CDW transition, the anisotropy decreases again. The two CDW transitions can be identified by the clear dips observed in the derivative of the  $c$ -axis resistivity. For  $x \neq 0$ , while the dips no longer signal true phase transitions, we can still use the evolution of the corresponding feature as  $x$  increases to map out the crossover. Tracking these features across the composition series clearly shows that both CDW crossovers are suppressed by the inclusion of Pd in the crystals. The residual resistivity ratio also quickly drops with the introduction of Pd, as should be expected with increasing impurity scattering.

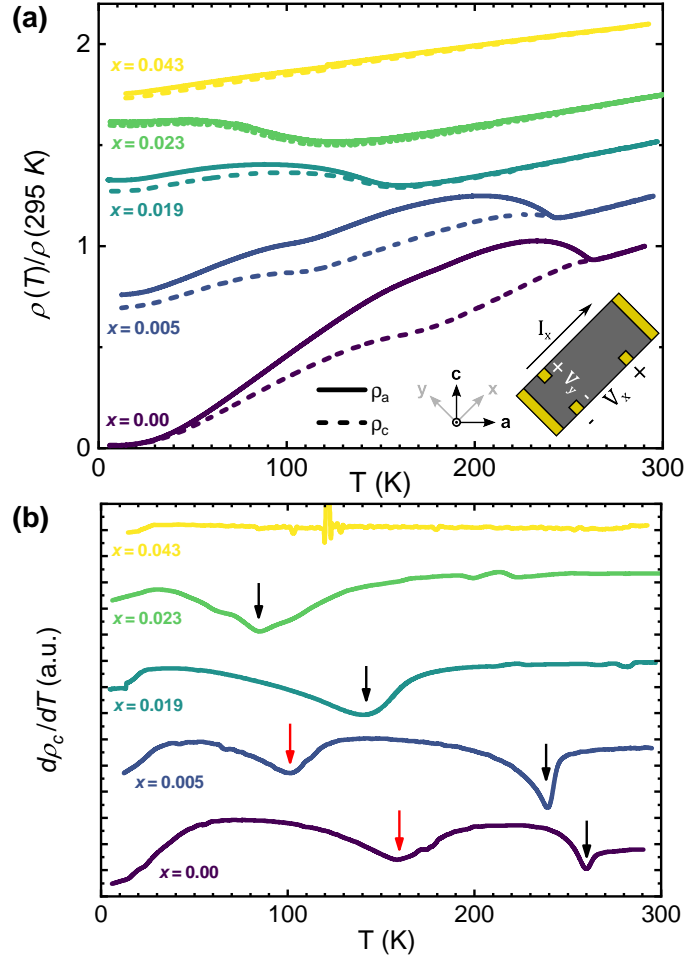


Figure 5.3: (a) Temperature-dependence of the in-plane resistivity between 4 K and 300 K, resolved into the two in-plane directions, normalized to the value at room temperature, and offset for clarity. Data is shown for representative compositions only. Solid and dashed lines correspond to the resistivity along the  $a$  and  $c$  axes, respectively. The inset describes the measurement geometry, in which a rectangular bar is cut with a scalpel at a  $45^\circ$  angle to the crystal axes. In a coordinate frame rotated by the same amount (denoted here by  $x$  and  $y$ ) current passing in the  $x$  direction generates a longitudinal voltage  $V_x$  proportional to  $\rho_a + \rho_c$ , and a transverse voltage  $V_y$  proportional to  $\rho_c - \rho_a$ . Simultaneous measurement of these voltages allows for both components of the resistivity to be measured simultaneously [107]. (b) Temperature derivative of  $\rho_c$  for each composition shown in (a). The dips marked by arrows correspond to the first (black) and second (red) CDW transitions in the parent compound, which are shown here to be suppressed towards zero as  $x$  increases. We define the crossover temperature  $T_{CDW}$  as the temperature at which the derivative reaches a local minimum. Curves were smoothed using a Loess filter prior to taking the numerical derivative. Reproduced from Straquadine, et. al. “Suppression of charge density wave order by disorder in Pd-intercalated  $\text{ErTe}_3$ ”. *Phys. Rev. B* **99**, 235138 (2019) with permission of the American Physical Society.

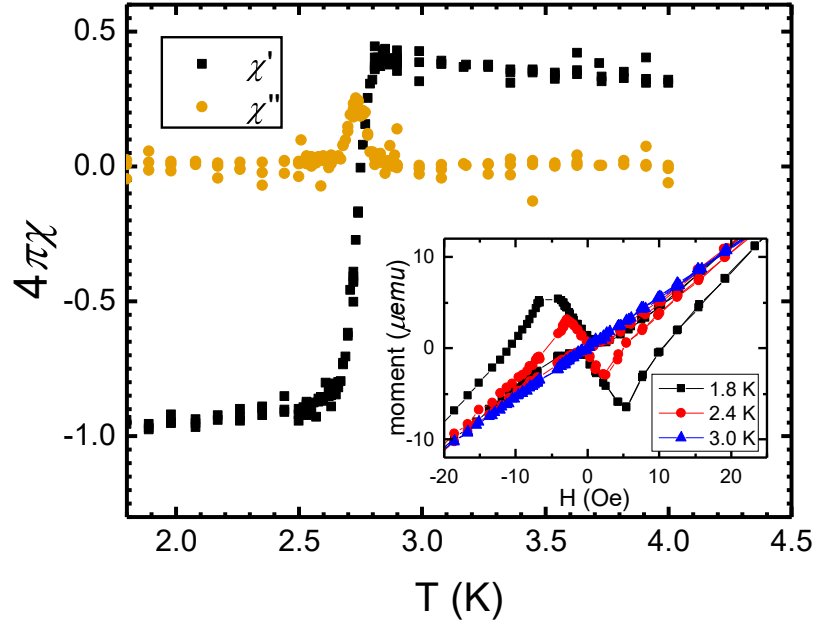


Figure 5.4: Representative AC magnetic susceptibility measurement for an  $x = 0.043$  sample. Field was applied parallel to the plane of the sample in this measurement. The sample shows near-perfect diamagnetism below  $T_c = 2.7$  K, suggesting that the superconducting state is bulk, rather than filamentary.  $T_c$  is extracted as the peak in the imaginary part of the susceptibility. Inset:  $M(H)$  curves above and below  $T_c$ , showing the small  $H_{c1} \approx 5$  Oe. The normal state just above  $T_c$  also shows significant paramagnetism, a consequence of the proximity to antiferromagnetic ordering of the rare earth moments. Reproduced from Straquadine, et. al. “Suppression of charge density wave order by disorder in Pd-intercalated  $\text{ErTe}_3$ ”. *Phys. Rev. B* **99**, 235138 (2019) with permission of the American Physical Society.

The presence of a superconducting state at low temperatures is clearly detected by SQUID magnetometry, as shown in Fig. 5.4. Superconductivity first appears abruptly above our base temperature of 1.8 K when  $x \approx 0.02$ , where the higher CDW crossover has been suppressed to  $\approx 100$  K, and remains near 2.5 K for all samples with  $x > 0.02$ . Analysis of the superconducting volume fraction from zero-field cooled  $M(T)$  curves shows that this is a bulk effect. The resistivity also drops to zero at the same temperature as the onset of the Meissner effect, within slight differences in thermometry in different cryostats.  $H_{c1}$  determined from  $M(H)$  hysteresis curves are on the order of 10-20 G. The area within these hysteresis loops is quite small, suggesting that vortex pinning is weak in this material, even at the largest  $x$  values. However, it should be noticed that this signal is complicated by the presence of antiferromagnetic order of the localized rare-earth moments[85, 86] which produces a large background in the susceptibility measurement.

Resistivity and magnetometry measurements across the composition series are combined in Fig. 5.5. The resistivity signatures of both CDW crossovers disappear quickly, and the lower CDW is

undetectable in resistivity above  $x = 0.01$ . The upper CDW becomes undetectable above  $x = 0.035$ . Unlike other perturbations such as chemical or hydrostatic pressure, under which one CDW is stabilized at the expense of the other[69, 100], we see that both CDWs are suppressed monotonically as  $x$  increases. This is further evidence that the primary effect of the Pd intercalation is to introduce disorder rather than electronic doping. This demonstrates that  $\text{Pd}_x\text{ErTe}_3$  is a promising model system for studying the interplay of incommensurate CDWs and disorder.

While the phase diagram presented here appears at first glance to fit the paradigm of a superconducting dome around a quantum critical point, we emphasize that no true phase transition is being suppressed to zero temperature. Also, unlike other systems with putative quantum critical points,  $T_c$  is never observed to decrease back to zero for larger  $x$ . A superconducting state with similar behavior is also observed for  $\text{RTe}_3$  ( $\text{R}=\text{Gd},\text{Tb},\text{Dy}$ ) under hydrostatic pressure[100, 101]. However, there are a few notable differences between the responses of superconductivity in  $\text{ErTe}_3$  to disorder and to pressure. First, the critical temperature achieved by disorder is universally lower than that achieved by the application of pressure. Ref. [101] reported a trend of  $T_c$  which closely matched that of elemental Te under pressure, and which reached approx. 4 K for pressures greater than 6 GPa, and tends to increase with pressure up to 14 GPa. In the presence of disorder, by contrast,  $T_c$  is always below 3 K, and decreases slightly as  $x$  increases. Both cases, however, exhibit a sharp increase in  $T_c$  above a critical value of the tuning parameter. This is consistent with the interpretation that superconductivity and charge density waves compete over regions of the Fermi surface; as the CDW is suppressed, regardless of the tuning parameter, more electrons are available to condense into a superconducting state, which enhances  $T_c$ .

In order to get a clearer picture of the structure of the CDW, we also conducted electron and x-ray diffraction measurements. In Fig. 5.6 we show selected area electron diffraction patterns (SADPs) taken on  $\approx 100$  nm thick samples with varying concentrations. As  $x$  increases, two different trends develop in the SADPs. First, peaks appear at the expected CDW wavevector  $q_{CDW,1} \approx 0.29c^*$ , but also along orthogonal directions far beyond the Pd concentrations where the second, CDW has been completely suppressed in resistivity. The  $q$ -vectors of peaks along the  $a^*$  and  $c^*$  axes are indistinguishable within the resolution of the images. Measurements of the diffraction pattern shows that the position of the CDW vector decreases by about 1.1% of a reciprocal lattice unit (r.l.u.) between  $x = 0$  and  $x = 0.33$ .

As the intensity of the CDW peaks decreases with increasing  $x$ , the SADPs also begin to exhibit significant diffuse scattering indicative of short-range correlations, primarily along lines spanning between the two orthogonal CDW satellite peaks [dashed lines in Fig. 5.6(d)]. While these patterns do become slightly brighter as the temperature decreases, the pattern was also observed at room temperature in both the  $x = 0.03$  and  $x = 0.04$  samples. This is indicative of a static structural distortion nucleated by the Pd impurities, which in heavily disordered samples persists even above the CDW transition temperature of the pristine samples, which is 270 K.

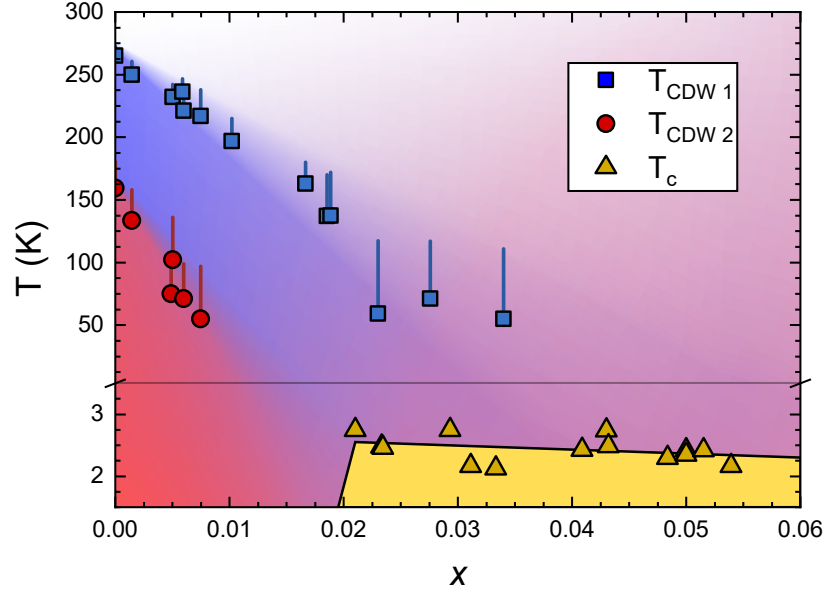


Figure 5.5: Phase diagram constructed from transport and magnetometry measurements. The temperature axis is rescaled below 3.5 K to better display the trend in superconducting transition temperatures. The second CDW is suppressed quickly as  $x$  increases, and extrapolates to zero around  $x = 0.01$ . A superconducting ground state emerges abruptly from below our base temperature of 1.8 K at  $x = 0.02$ , and continues with an approximately constant transition temperature out to the solubility limit of Pd. The first CDW extrapolates to zero around  $x = 0.035$ . It should be noted that both CDW features decrease in magnitude and become harder to distinguish as  $x$  increases. Lines extend upward from each data point to the first onset of the CDW signature in resistivity, illustrating how disorder smears the crossover. Background shading approximates the magnitude of CDW correlations along the two in-plane axes: blue signifies the primary  $c$ -axis CDW, and red signifies the  $a$ -axis. As disorder increases, the material begins to exhibit short range correlations along both directions (indicated by purple shading). True long-range-ordered CDW phases exist only on the  $x = 0$  axis. Reproduced from Straquadine, et. al. “Suppression of charge density wave order by disorder in Pd-intercalated  $\text{ErTe}_3$ ”. *Phys. Rev. B* **99**, 235138 (2019) with permission of the American Physical Society.

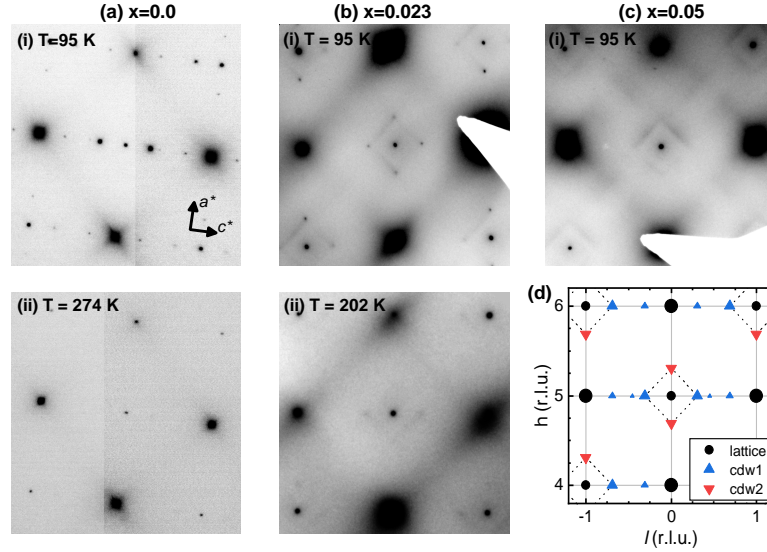


Figure 5.6: Representative selected area diffraction patterns (SADPs) at various Pd concentrations and temperatures. (a) Parent compound ( $\text{ErTe}_3$ ) at 95 K (i) and 274 K  $\sim T_{CDW,1}$  (ii), showing the disappearance of the satellite peaks on either side of the center peak at high temperatures. (b) SADP for an  $x = 0.023$  sample ( $T_{CDW,1} \approx 97\text{ K}$ ) at 95 K (i), clearly showing satellite peaks forming along *both* the  $c^*$  and  $a^*$  axes, despite the fact that the transport signature of the second CDW has been completely suppressed for this composition. This suggests that the introduction of disorder elicits a nearly 4-fold symmetric response from the material, reflective of the underlying electronic susceptibility and phonon dispersion. A small square of diffuse streaks also begins to appear between these peaks, suggestive of short-range ordering. It should be noted, however, that the width of the satellite peaks sets a lower bound on the correlation length of 40 nm, or about 94 unit cells. In (ii) remnants of the CDW peaks and the diffuse squares can be seen on this same sample even at 202 K, more than double the CDW crossover temperature. (c) Finally for a  $x = 0.05$ , which shows no signatures of CDW in resistivity, no sharp satellite peaks are observed to the lowest temperature attainable, but the diffuse square remains visible at all temperatures. This is suggestive of a structural distortion with a similar  $q$ -vector, likely stemming from nucleation of CDW correlations by individual Pd atoms. Panel (d) shows a schematic describing the origin of the various peaks for the parent compound. The small upward triangles correspond to higher order CDW peaks which are only observable in (a). Reproduced from Straquadine, et. al. “Suppression of charge density wave order by disorder in Pd-intercalated  $\text{ErTe}_3$ ”. *Phys. Rev. B* **99**, 235138 (2019) with permission of the American Physical Society.

The observed full-width at half maximum of the CDW satellite peaks in electron diffraction patterns is resolution limited, and corresponds to a minimum correlation length of approximately 40 nm. In the  $x = 0.03$  samples (the highest concentration for which peaks can be seen within the temperature range of the cryogenic holder), the CDW peaks are not detectably broader than in the clean limit. It should be noted that assuming the Pd atoms lie only between the Te bilayers, the average distance between Pd atoms is approximately 2 nm, much shorter than this lower bound on the correlation length. This seems to imply that the CDW is in the weak-pinning limit, where the potential of a single impurity is insufficient to locally lock the CDW phase.

The apparent four-fold symmetry of the CDW peaks which appear in the electron diffraction patterns for the largest values of  $x$  studied are consistent with the Friedel oscillations and associated lattice distortions that should be expected to arise from the calculated electronic susceptibility[40]. The diffuse streaks, which are present at all temperatures, qualitatively match the Lindhard susceptibility calculated in ref. [40], which exhibits peaks at both orthogonal CDW wavevectors, but also a ridge of local maxima along a line between them. In general, the distortion in the neighborhood of a delta-function impurity should be expected to produce the largest effect at the  $q$ -vectors for which the susceptibility is largest (and hence the lattice is softest), and these observations support this interpretation. A similar structure has also been observed in calculations of the energy-integrated phonon linewidth[102], which suggests that phonons couple strongly to the electrons at the wavevectors of these diffuse streaks. This coupling does not, however, appear for the phonons responsible for the CDW order, which implies that the strong electron-phonon coupling at the streak wavevectors, and therefore the static distortions in the presence of impurities, involves phonons of different symmetries.

In order to characterize the satellite peak intensities down to lower temperatures, we also present energy-resolved x-ray scattering measurements on a sample with  $x = 0.023$ . We focus on two superlattice peak positions,  $(3, 7, 0.29)$ , and  $(0.29, 7, 3)$ , corresponding to the two CDW ordering vectors along the  $c$ - and  $a$ -axis, respectively. This composition only shows evidence of one CDW crossover in resistivity. Figure 5.7 shows the intensity of elastic scattering (zero energy transfer within resolution of 1.5 meV) at each of the two CDW wavevectors. Approaching the crossover temperature from above, both peaks grow in intensity at the same rate, while below the crossover (approx. 95 K for this composition) the two intensities differ. The peak corresponding to the primary CDW wavevector in the parent compound continues to become both stronger and sharper as temperature decreases, until the observed width levels off at the resolution limit of 0.0112 r.l.u. at 30 K. The intensity of the peak at the secondary CDW wavevector grows more slowly and the temperature dependence of the width levels off at approximately 90 K. Similar conclusions have recently been reached by STM measurements of  $\text{Pd}_x\text{ErTe}_3$ . [44]

Previous measurements on pristine  $\text{ErTe}_3$ [69] have demonstrated that the integrated intensity of the peak below  $T_{CDW,1}$  follows a BCS temperature dependence with a sharp increase at the transition. The gradual increase of the intensity of both peaks for the intercalated sample is consistent with

the CDW transition being smeared into a crossover in the presence of disorder. Consistent with the weak-pinning picture described above, the full width at half maximum (FWHM) of both peaks becomes sharper as the temperature decreases. While the  $c$  axis correlations reach the resolution limit, for the CDW correlations along the  $a$  axis we deduce a maximum possible correlation length of approx. 108 nm ( $\approx 25$  unit cells). This difference in correlation lengths confirms that the single crossover observed in resistivity for this composition still reflects the  $c$ -axis character of the first CDW transition in pristine  $\text{ErTe}_3$ , despite the slight enhancement of CDW correlations along the orthogonal direction.

One possible explanation of the appearance of CDW correlations along both in-plane directions in TEM is that the Pd atoms nucleate stacking faults, disrupting the glide plane symmetry in the parent compound. To test this theory, the relative intensity of the symmetry allowed (0,6,1) peak and its forbidden counterpart (1,6,0) were compared in single-crystal x-ray diffraction. In the limit of a high density of stacking faults, one would expect that peaks of comparable magnitudes would be observed in both locations. In all crystals studied, only one peak was observed above the instrument noise floor, which gives confidence that the average distance between stacking faults is greater than the x-ray penetration depth (approx. 2  $\mu\text{m}$ ). Further, crystals were then repeatedly exfoliated *in situ* using adhesive tape, removing between 4  $\mu\text{m}$  and 30  $\mu\text{m}$  of material each time. The newly exposed surfaces always exhibited the same orientation in further scans. This sets a lower bound on the average distance between stacking faults which compares favorably to the thicknesses of samples used in TEM (of order 100 nm) and transport (tens of microns). With this result, corroborated by the observed asymmetry in Fig. 5.7 of the two CDW orientations, we are confident that the effects reported here accurately represent the bulk behavior of the material.

The appearance and evolution with temperature of superlattice peaks along both in-plane directions implies that the response of the material to disorder reflects the intrinsically pseudo-tetragonal nature of the electronic susceptibility and the phonon spectrum, as mentioned in the introduction. This raises the intriguing possibility that in-plane antisymmetric strain could be used to tune the system to an effectively tetragonal state, in which a vestigial nematic phase transition could be observed. (It should be noted that while the glide plane, being a nonsymmorphic symmetry operation, is fundamentally different from an in-plane strain, they both break the same point group symmetries as the vestigial nematic state.) Secondly, the mechanism of the relatively sharp increase of the superconducting transition temperature from below 1.8 K to 2.5 K remains in question. It may be that the Pd atoms increase the density of topological defects in the CDW order parameter, or that the magnitude of the CDW gap itself decreases as a consequence of disorder. Either mechanism would increase the density of states available at the Fermi level for superconducting pairing. Further studies are underway to clarify these details.

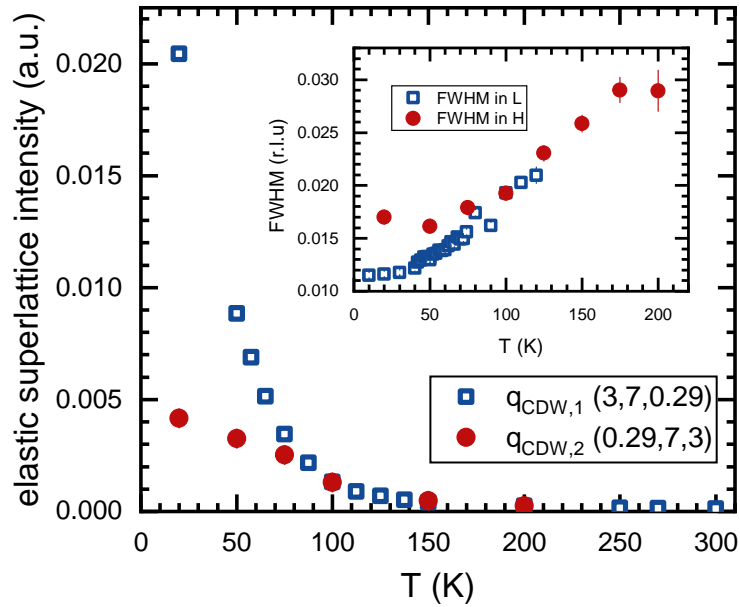


Figure 5.7: Measurement of the elastic CDW superlattice peak intensity observed in x-ray diffraction at zero energy transfer as a function of temperature for a sample with  $x = 0.023$ . Data was taken at the HERIX beamline 30-ID at the Advanced Photon Source, with photon energy 23.72 keV and energy resolution of 1.5 meV. Above the transition temperature (95 K from resistivity) the amplitude of CDW correlations begin to grow identically, but the intensity of the primary CDW grows further at lower temperatures. Inset: FWHM measurements of longitudinal scans through  $q_{CDW,1}$  and  $q_{CDW,2}$  also show similar behavior above the crossover. Below the crossover, the correlation length of the secondary CDW along  $a$  reaches a maximum around 90 K, while the correlation length of the primary continues to grow at least to the resolution limit. We estimate a reciprocal-space resolution for this beamline of 0.0112 r.l.u. Reproduced from Straquadine, et. al. “Suppression of charge density wave order by disorder in Pd-intercalated  $\text{ErTe}_3$ ”. *Phys. Rev. B* **99**, 235138 (2019) with permission of the American Physical Society.

## 5.4 Conclusions

We have presented the results of transport, magnetization, and scattering measurements on the model CDW system  $\text{ErTe}_3$  intercalated with Pd. We have demonstrated that the primary effect of Pd intercalation is to provide a weak, random potential, which serves to suppress and smear the two CDW transitions into crossovers, and eventually elicit superconductivity. Our data also provides evidence for localized distortions of the crystal structure, which is strongest at the CDW wavevectors along both directions, as a consequence of the nearly 4-fold symmetric nature of the material. This work establishes  $\text{Pd}_x\text{ErTe}_3$  as an easily tunable and weakly-coupled model system for the study of incommensurate, unidirectional CDWs in the presence of disorder. Study of this model system is a promising avenue for understanding the role of charge order within the complicated phase diagrams of strongly correlated systems such as the cuprate superconductors.

## Chapter 6

# Concluding Remarks

*As the previous two chapters have emphasized, the rare-earth tritellurides provide a promising sandbox for the study of charge density wave states under several perturbations. Both of the tuning parameters applied here, uniaxial stress and disorder, produce significant and qualitative changes to the CDW states under modest and easily accessible conditions, placing large regions of phase space within the experimentalist's reach. Furthermore, the objective of this thesis is to provide a roadmap of this space to enable the future application of other measurement techniques to disordered or uniaxially stressed samples. This final chapter summarizes the current state of affairs regarding measurement techniques under uniaxial stress (focusing on the AC-elastocaloric technique) and research into the rare-earth tritellurides themselves, and concludes with a discussion of a few of the most promising avenues for research in the near future.*

### 6.1 Current status of uniaxial stress techniques

While the idea of measuring materials under uniaxial stress is in no way new, the past decade has seen a blossoming of innovations and improvements in the techniques and tools. At the same time, the versatility of stress and strain in elucidating a wide range of physical effects and materials has become clear, driving widespread adoption of the measurement techniques.

The introduction of oscillating stress and strain in the AC elastoresistivity[127] and AC elastocaloric effect[134] has expanded capabilities even further. In itself, the AC-elastocaloric technique fills an important need of the physics community by providing a high-resolution, low-background probe of thermodynamic quantities under strain. The numerical studies in this work represent a further important step in the application of the AC elastocaloric technique. First, by calculating the realistic shapes of the magnitude and phase of the sensitivity function, we provide a baseline against which the quality of future measurements can be compared. The variability of the sensitivity underscores the practical importance of verifying the sensitivity at all temperatures as the thermal

parameters of the sample vary with temperature. Additionally, the calculation of the sensitivity function for a wide range of parameters places limits on the expected behavior; experimental results with qualitatively different frequency dependence must arise from a nontrivial effect not considered here. Finally, by providing a simple empirical prescription for estimating the peak sensitivity, it is now possible to achieve quantitative estimates of the magnitude of the elastocaloric tensor.

Both AC-ER and AC-ECE techniques also require reliable measurements of the strain oscillations as well, but measurements of high-frequency capacitance modulations are not possible with existing commercial equipment. The design, construction, and calibration of an auto-balancing bridge circuit in Section 4.A and Appendix A addresses this problem directly, and provides the experimentalist with unprecedented accuracy. Having a direct probe of the oscillating strain removes the uncertainties inherent in extrapolations of the behavior of piezoelectric actuators. Together, these technical advances help to pave the way for the continued adoption and application of the AC-elastocaloric technique throughout the condensed matter community

## 6.2 Future outlook for research in the tritellurides

The work presented in this thesis has established a roadmap for tuning the properties of single crystals of  $R\text{Te}_3$  with both strain and disorder, opening the door for a wide range of follow-up experiments. Nearly any experimental probe of the tritellurides, when combined with uniaxial stress or disorder, could provide new insights into the behavior of this model system. The most promising future experiments, considering both the expected advancement in knowledge as well as practical feasibility for state-of-the-art techniques, are listed below.

### 6.2.1 X-ray diffraction under stress

The immediate follow-up on the work of Chapter 4 is to perform standard synchrotron x-ray diffraction measurements of an  $R\text{Te}_3$  sample under strain. A reciprocal space probe would provide direct evidence of the wavevector realignment transition with a quantitative measure of the amplitudes of either wavevector. Measurement of the widths of the superlattice peaks will also provide insight into the evolution of the correlation lengths. Additionally, diffraction measurements will provide a precise measure of the exact sample strain required (the value of  $\varepsilon_{aa}^0$ , as defined in Section 4.3) to drive the sample into the strain-induced  $\mathbf{q}_a$  state. The implementation of piezoelectric-driven uniaxial stress cells has already begun at several synchrotrons around the world[196], so this experiment requires no new technique development.

### 6.2.2 Uniaxial stress combined with disorder

If the vestigial nematic picture[50] (as discussed in Section 1.2.2.1) is correct for  $R\text{Te}_3$ , then there should be two different observable signatures. First, on cooling toward a nematic transition the nematic susceptibility should diverge similar to what is seen in the iron-pnictide superconductors.[123, 125, 130] In spatially uniform electron nematic materials such the pnictides, the in-plane resistivity anisotropy  $\rho_{aa} - \rho_{bb}$  is directly proportional to the nematic order parameter, and a properly isolated component of the elastoresistivity tensor  $m_{ijkl}$  can therefore be used as a proxy for the nematic susceptibility. Despite the different microscopic behavior, the order parameter of the vestigial nematic state,  $\overline{|\psi_c|^2} - \overline{|\psi_a|^2}$  breaks the same symmetries and would also couple linearly to antisymmetric strain.

A freestanding crystal of  $R\text{Te}_3$  cannot exhibit a nematic phase transition on account of the orthorhombic distortion; the symmetry has already been broken. However, at the critical point defined by  $T = T_{c0}$  and  $\tilde{\varepsilon}_A = 0$ , the two CDW order parameters will become degenerate and a nematic transition can occur. Deforming away from  $\tilde{\varepsilon}_A = 0$  to either side, the transition becomes a crossover and would be smeared out as the antisymmetric strain increases. For a given temperature just above the transition, the prevalence of nematic fluctuations, and therefore the nematic susceptibility, would be strongest at  $\tilde{\varepsilon}_A = 0$ , weakening quickly on either side. Careful study of the offset-strain dependent elastoresistivity for temperatures slightly above the crossover temperature  $T_{CDW1}$  for lightly-disordered  $\text{Pd}_x\text{ErTe}_3$  would be able to detect the precursor fluctuations related to a nearby vestigial nematic state if one exists in  $\text{Pd}_x\text{ErTe}_3$ . A recent STM study of  $\text{Pd}_x\text{ErTe}_3$ [44] suggests that for small  $x$  the autocorrelation function of CDW correlations in the  $\mathbf{q}_c$  direction maintains a finite value over the widest dimensions measured, which is indeed consistent with a Bragg glass phase. The existence of at least quasi-long-range order despite the presence of impurities may already be evidence for a vestigial nematic phase, although the responses of this phase to a conjugate strain field will be required to demonstrate this definitively. Since the thermodynamic signatures of the transition will broaden on either side of  $\tilde{\varepsilon}_A = 0$ , the anomaly observed in the AC-ECE signal may become sharper as one approaches the critical strain.

The existence of a phase transition, or even a relatively sharp crossover, into a vestigial nematic state in  $\text{Pd}_x\text{ErTe}_3$  requires that the non-symmorphic glide-plane element of the crystal structure is irrelevant at the critical temperature. The anisotropy in the softening of phonons at  $\mathbf{q}_a$  and  $\mathbf{q}_c$  at  $T_{CDW1}$  suggests an energy scale of approximately 20 K, which is an order of magnitude lower than the transition temperature. However, it is unclear what effects this may have on the existence and characteristics of a vestigial nematic state, and any measurement will undoubtedly provide new understanding into the behavior of this state. Even a negative result, in which nematic fluctuations are shown to play little to no role in this system, would produce valuable new information about factors which prevent the appearance of vestigial nematic order.

### 6.2.3 Phonon and electron spectroscopies under stress

Inelastic x-ray spectroscopy (IXS) in  $R\text{Te}_3$  have already shown clear evidence of the Kohn anomaly in the phonon spectrum at  $\mathbf{q}_c$  upon cooling through  $T_{CDW1}$ , with a similar yet incomplete softening of the phonon mode at  $\mathbf{q}_a$  at the same temperature.[102] Naively, the strain-induced  $\mathbf{q}_a$  state would exhibit the opposite behavior, softening at  $\mathbf{q}_a$  before  $\mathbf{q}_c$ . Additionally, while no softening has been observed at  $T_{CDW2}$  in freestanding crystals, it is possible that observing the strain dependence of the phonons near  $T_{CDW2}$  may provide new insights into the driving force behind this state.

Additionally, comparisons of the observed phonon energies and linewidths against density functional perturbation theory [46] has already provided strong evidence of the momentum-dependent electron-phonon coupling which seems to instigate the formation of the CDW. Similar studies in and near the strain-induced  $\mathbf{q}_a$  state would be crucial to observing what, if anything, differs in the physics of the CDW of the two stripe states.

Complementary to the IXS study of the phonons would be angle resolved photoemission spectroscopy (ARPES) studies of the electronic structure. The thermodynamic and transport evidence presented in Chapter 4 establishes that the CDW wavevector changes direction within the plane for sufficient tensile strain along the  $a$ -axis. However, much remains to be discovered regarding the character of this strain-induced  $\mathbf{q}_a$  state. For example, in a freestanding sample, the magnitudes of two wavevectors differ by a small but consistent amount. It is possible that the two simply exchange magnitudes upon crossing the strain-induced transition, or the magnitudes could arise solely from the non-symmorphic crystal structure.

The clearly defined electron bands in  $R\text{Te}_3$ , combined with the tendency of  $R\text{Te}_3$  to cleave, make this system ideal for detailed ARPES studies[67, 81, 197, 198], and the relatively large CDW gaps[94] and the expected sharp inversion of the gap anisotropy will appear quite clearly in the spectrum. ARPES would also provide a much clearer picture of the behavior of the second, lower temperature CDW transition, to which elastoresistivity and elastocaloric effects are only minimally sensitive. Importantly, the necessary technology for performing ARPES measurements under strain using a similar uniaxial stress cell has been demonstrated.[199]

### 6.2.4 CDW depinning under strain

The observation of nonlinear current-voltage characteristics in  $R\text{Te}_3$  for large electric fields[200, 201, 202] parallel to either of the CDW wavevectors in  $\text{ErTe}_3$ , coupled with the observation of narrow-band noise and Shapiro steps[203] suggests the presence of a Fröhlich-type conduction mechanism related to the cooperative translational motion of the CDW condensate, commonly referred to as a “sliding” CDW.[204] From measurements of the depinning transition as well as the sliding CDW state, one can access a few of the characteristics of the CDW itself and its interactions with the lattice. First, the magnitude of the excess conductivity and the fundamental frequency of the narrow-band noise provide an estimate of the density of the CDW condensate, and the threshold

field and contains information about the CDW-lattice and CDW-impurity potentials[205]. X-ray scattering measurements of the sliding CDW in  $R\text{Te}_3$ [206] have demonstrated a motional narrowing effect in which the CDW wavevector changes under large threshold fields and that the density wave acts like an elastic medium deforming to accommodate impurity and externally applied electric potentials. Additionally, the temperature-, time-, and voltage history of a given sample appears to strongly affect the value of the threshold field[207], which not only supports the conception of the CDW as an elastically deformable medium, but also implies that the normal metal-incommensurate CDW phase transition does not in general produce an equilibrium density wave configuration. Falling out of equilibrium in  $R\text{Te}_3$  has previously been observed in pump-probe measurements[208, 197], and has been ascribed to the slow recombination of topological defects of the CDW.

Based on the evidence provided in Chapter 4 for a strain-induced  $\mathbf{q}_a$  CDW state, one should also expect that sufficiently large electric fields parallel to  $\mathbf{q}_a$  will drive this CDW to slide as well. Comparing the depinning characteristics along the two axes, as well as comparison for different strain values, will provide direct insight into the relationship between the two states. Additionally, it is natural to assume that the first-order strain-induced CDW transition will also exhibit non-ergodic behavior. Uniaxial stress should couple well to the elastic nature of the CDW phase, and observing the long-time relaxation dynamics for various values of strain would shed light on the interactions, pinning forces, and non-equilibrium behavior of the CDW.

### 6.3 Final remarks

As mentioned in Section 1.1.3, this thesis set out to determine the extent to which the rare-earth tritellurides can be considered a model system for more general questions of charge density wave order in a quasi-tetragonal system. It was shown in Chapter 4 that modest uniaxial stresses—which are easily accessible in the laboratory—can instigate a strain-induced realignment of the wavevector despite the presence of an orthorhombic crystal structure. In Chapter 5, it was demonstrated that chemical disorder created Pd concentrations well below the solubility limit—which enables the reproducible synthesis of single crystals—suffice to completely suppress all signatures of a CDW crossover and to elicit a superconducting ground state. Together, these results indicate that a wide range of conditions which are relevant for strongly-correlated materials such as the high- $T_c$  cuprate superconductors can all be easily achieved within the rare-earth tritellurides. In conclusion, this work establishes a detailed map of new regions of phase space and clears the way for an abundance of further studies in the near future.



# Appendix A

## AC Capacitance Measurements

*Accurate measurement of the sample strain is crucial to understanding the results of elasto-resistivity and elastocaloric measurements. The use of a capacitive transducer, like the displacement sensor intrinsic to the CS-100 stress cell used here, to quantify the time-varying component of the strain, however, has not been developed. Existing techniques fail for frequencies above a few Hz. The piezoelectric actuators which drive these oscillating strains, however, are highly nonlinear, and the AC strain magnitude depends strongly on temperature, DC offset voltage, and frequency. This appendix provides an in-depth discussion of the auto-balancing bridge circuit I designed to solve this problem, the general theory of detecting oscillating capacitances, and the calibration procedures establishing estimates of both the precision and accuracy.*

### A.1 Introduction

The CS-100 strain cell from *Razorbill Instruments*, used throughout Chapter 4 of this work and growing in prominence throughout the condensed matter physics community, incorporates an air-gap capacitive displacement sensor in order to reproducibly quantify the strain generated by the piezoelectric (PZT) stacks. The capacitance  $C$  of this sensor follows the basic formula

$$C = \frac{\epsilon_0 A}{\Delta L + d_0} + C_p \tag{A.1}$$

where  $A$  is the area of the sensor plates,  $\epsilon_0$  is the permittivity of free space,  $d_0$  is the neutral spacing with no applied voltage,  $\Delta L$  is the displacement, and  $C_p$  is the parasitic background capacitance between the plates and the sensor's housing. The values of  $A$ ,  $d_0$ , and  $C_p$  are calibrated by *Razorbill* when the cell is purchased. For a sample of known length  $L$ , one can then calculate the resulting

strain  $\varepsilon = \Delta L/L$ .<sup>1</sup>

High resolution capacitance bridges (such as the *Andeen-Hagerling* AH2700A, which boasts a 0.8 aF detection limit[137]) already exist on the market. However, these are generically designed with the intention of measuring stable or slowly varying capacitance values, and do not have the capability to report the amplitude of a modulation of the capacitance at a given frequency, nor to sample fast enough to extract a meaningful time-dependent trace for oscillations above just a few hertz. For example, the minimum time between readings for the AH2700A is 40 ms, corresponding to a Nyquist limit of approximately 10 Hz for sinusoidal modulations. Additionally, extrapolations based on low-frequency behavior are known to fail—the PZT stacks themselves are highly nonlinear, temperature dependent, and hysteretic, so the magnitude of the AC strain oscillation is very difficult to estimate. For the AC elastoresistivity and elastocalorimetry techniques employed in this work, a more elegant solution is required.

The primary challenge in sensitive capacitance measurements at any frequency, however, is avoiding parasitic effects. The CS-100 capacitance sensor, for example, is about one picofarad at its neutral position. Standard laboratory coaxial cables, both inside and outside of the cryostat, will realistically reach several hundred picofarads. The small signal would be difficult to isolate from such a background. To this end, I have created and characterized a simple circuit system based on an auto-balancing bridge topology, which produces a modulated signal proportional to the sensor capacitance. This circuit has been lovingly dubbed the “Capacitizer”. This signal can then be read out by a pair of lock-in amplifiers, and allowing for the precise calculation of both the AC oscillation as well as the DC offset strain. This circuit topology also rejects parasitic capacitances such as the coaxial cables between the circuit and the sensor.

## A.2 Autobalancing bridge circuit for capacitance measurements

Figure A.1 shows a basic schematic of the circuit. A sinusoidal voltage (approximately 19 kHz,  $0.5 V_{\text{rms}}$  for this implementation) is applied to the input terminal at the left. This passed through a unity-gain buffer to minimize the output impedance, and is then passed into the cryostat to one of the terminals of the capacitance sensor. Minimizing the impedance is critical: this decreases the RC charging time of the parasitic cable capacitance, and allows  $C_{p1}$  to be ignored for frequencies below approximately 100 kHz. The other terminal of the capacitance sensor is connected to an inverting integrator circuit, which incorporates a reference capacitor and a large resistor for stability. The

---

<sup>1</sup>This measure of the linear strain contains the underlying assumption that the cell assembly, including all of the various mounting plates and epoxies, are infinitely stiff, such that 100% of the strain is transferred into the sample. This is of course an oversimplification, and work by the original designers of the cell[116] as well as our own simulations[134] have demonstrated that the actual sample strain is closer to 70% of the measured value for real samples and epoxies. While this may limit the absolute accuracy of the strain measurement, the problem of measuring the relative changes in both the AC and DC strain remains, and this is the problem which the circuit described in this appendix solves.

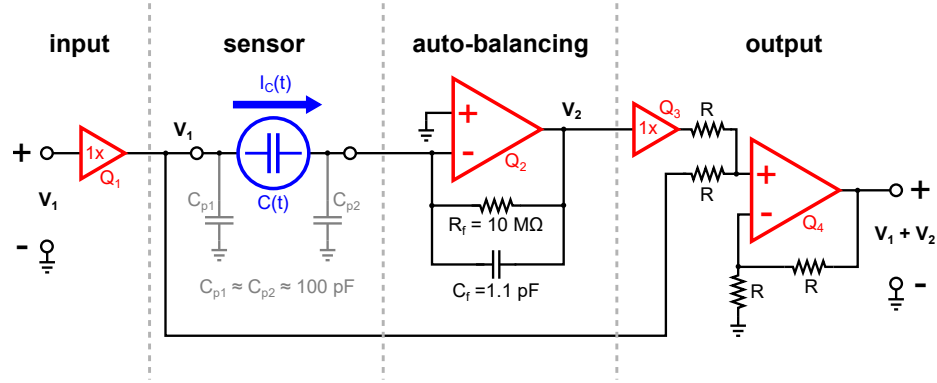


Figure A.1: Simplified schematic of the capacitance bridge described in this appendix. The circuit consists of four operational amplifiers  $Q_1$ - $Q_4$ .  $Q_1$  and  $Q_3$  are set up as unity-gain buffers,  $Q_4$  is a non-inverting summing amplifier, and  $Q_2$  is the integrator at the heart of the auto-balancing bridge. The two capacitors  $C_{p1}$  and  $C_{p2}$  represent the parasitic capacitances of the cables between this circuit and the sensor in the cryostat. The low-output impedance of  $Q_1$  pushes the charging time of  $C_{p1}$  to frequencies above the operating regime, while the virtual ground enforced by  $Q_2$  prevents  $C_{p2}$  from charging. In this configuration, the current  $I_C(t)$  is controlled primarily by the sensor capacitance  $C(t)$ . The summing amplifier  $Q_4$  removes a background signal and ensures that the output voltage is directly proportional to the imbalance between  $C(t)$  and the reference capacitor  $C_f$ .

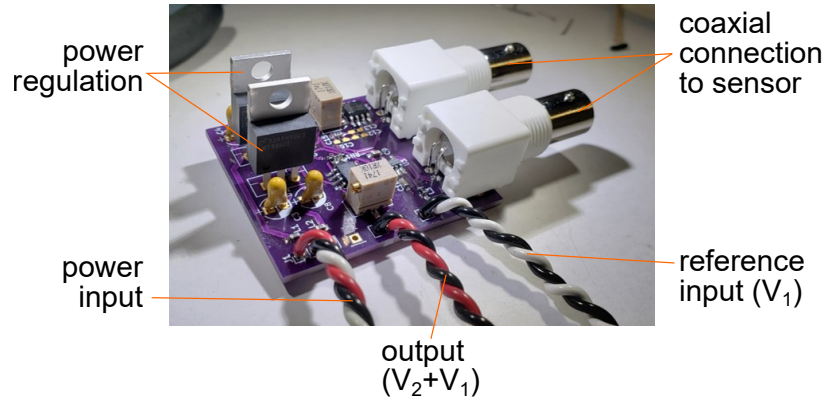


Figure A.2: Photograph of the assembled AC-capacitance bridge circuit board, identifying several of the components. The power regulation circuitry consists of two linear regulators producing stable supplies at  $\pm 5$  V. The input and output signals are buffered using LT1797 op-amps, and the auto-balancing and summing amplifiers are use OP27 op-amps. The entire circuit is nested inside of an aluminum box for shielding.

op-amp  $Q_2$  is connected such that the input terminal acts like a virtual ground: the output sources and sinks whatever current is necessary to ensure that the second terminal of the capacitance sensor remains at a potential of 0 V. In so doing, the cable capacitance  $C_{p2}$  does not charge (both sides are held at the same voltage) and can therefore  $C_{p2}$  can also be neglected for the operating frequency range. This virtual ground connection is the primary advantage of using an auto-balancing bridge circuit. If one knows the component values of the feedback network ( $R_f$  and  $C_f$ ), then the amplitude of the output voltage of  $Q_2$  (here denoted  $V_2$ ) can be used to extract the capacitance. However, to improve dynamic range, we here use the fact that when  $C = C_f$ , the output voltage and the input voltage are equal in magnitude and  $180^\circ$  shifted in phase. The two op-amps on the right simply buffer and then add these signals together, resulting in a final output voltage proportional to the change  $\Delta C = C - C_f$ . Up to this point, no reference to the time-dependence of  $C$  has been made. In principle, this produces some nontrivial terms in the spectrum of the resulting signal. It will be shown that these effects are avoided in the relevant frequency limits for this implementation, and that the naïve case predominates. However, the analysis is included here for completeness.

### A.3 Theory of operation for modulated capacitance

We begin by describing the oscillating capacitance <sup>2</sup> as

$$C(t) = C_0 + \frac{C_\Delta}{2}(e^{i\omega_s t} + e^{-i\omega_s t}) \quad (\text{A.2})$$

The voltage across the capacitor, assuming an ideal virtual ground at the second terminal, is simply the input signal

$$V(t) = V_1(t) = V_0 e^{i\omega t} \quad (\text{A.3})$$

Then the time-dependent current through the sensor capacitor will be given by the time derivative of the instantaneous charge  $Q(t) = V(t)C(t)$ :

$$\begin{aligned} I_C(t) &= \frac{dQ(t)}{dt} \\ &= \frac{d}{dt}(V(t)C(t)) \\ &= i\omega C_0 V_0 e^{i\omega t} + iC_\Delta V_0 (\omega - \omega_s)/2 e^{i(\omega - \omega_s)t} + iC_\Delta V_0 (\omega + \omega_s)/2 e^{i(\omega + \omega_s)t} \end{aligned} \quad (\text{A.4})$$

---

<sup>2</sup>Two linearizing assumptions must be made in applying this equation to the relevant case. Generally, it is the voltage applied to the piezoelectric stacks which is a pure sine wave. The PZT stacks are inherently nonlinear, such that the strain in the cell will contain higher harmonics of the driving frequency. Additionally, the capacitance depends on the cell displacement as  $(\Delta L)^{-1}$ , which again will generate higher harmonics. We assume that small enough voltages and displacements are used that both of these effects are negligible. In any case, the phase-sensitive detection method at the first harmonic will discard these higher order terms.

And the output voltage  $V_2$  is calculated by passing this current through the feedback network of  $Q_2$ :

$$V_2(t) = -V_0 \left[ \frac{i\omega R_f C_0}{1 + i\omega R_f C_f} e^{i\omega t} + \frac{iR_f C_\Delta (\omega - \omega_s)}{2(1 + i(\omega - \omega_s)R_f C_f)} e^{i(\omega - \omega_s)t} + \frac{iR_f C_\Delta (\omega + \omega_s)}{2(1 + i(\omega + \omega_s)R_f C_f)} e^{i(\omega + \omega_s)t} \right] \quad (\text{A.5})$$

This signal can be described as an amplitude modulated sine wave, but with a slight asymmetry in the two sidebands. The carrier signal can be detected trivially using a lock-in amplifier, which provides a measurement of the time-averaged value,  $C_0$ . The modulated component, however, is not so trivial, as is illustrated in Fig. A.1. We factor out the carrier oscillation by converting to a co-rotating phasor frame and observe the signal's evolution. In a symmetrically modulated sine wave signal, such as that observed in standard AM radio or AC elasto-resistivity experiments, the signal in phasor plot moves back and forth along a line parallel with the carrier signal. Any extra phase shift generated by parasitic wiring capacitance will affect the carrier and sideband equally. In this case, the detected ratio between the carrier signal and the sideband will be identical regardless of the detection quadrature:  $\Delta X/X = \Delta R/R$ .

The introduction of sideband asymmetry, however, results in a signal which traces out an ellipse in phasor space. The eccentricity and orientation of this ellipse will depend on the relative magnitudes of the three frequency scales in the problem:  $f = \omega/2\pi$ ,  $f_s = \omega_s/2\pi$ , and the pole frequency of the feedback network,  $f_p = 1/2\pi R_f C_f$ . The orientation  $\theta$  and principal axes  $D_\pm$  of this ellipse in phasor space, as defined in Fig. A.3a, are straightforward to calculate from Eq. (A.5).

In the case of asymmetric sidebands, the detected signal will depend on the detection method. Modern lock-in amplifiers are capable of detecting directly at a sideband frequency. For instance, the *Stanford Research Systems* 860 can natively isolate the lower sideband in a dual demodulation mode. Simultaneous measurement of the lower sideband and the carrier signals produces enough information to extract the AC and DC capacitance. If this is not possible, the modulation can be extracted using a dual-demodulation technique similar to that described in Chapter 4, either using two lock-in amplifiers[127] or fast digitization and post-processing[130]. Practical implementations of these techniques may report only one quadrature: the detected signal is then the projection of the phasor-space ellipse on that quadrature axis, which requires careful analysis.

As shown in panels (b), (c), and (d) of Fig. A.3, the characteristics of the ellipse in phasor space depend strongly on frequency. The semimajor axis, which sets the maximum possible sensitivity, becomes largest and least sensitive to strain frequency  $f_s$  for the highest input frequencies  $f$ . However, nonideal effects of the operational amplifiers (not captured by Eq. (A.5)) will decrease the signal in the high-frequency limit, which sets a practical limit on practicable choices of  $f$ . Secondly, the angle of misalignment between the carrier signal and the semi-major axis,  $\theta - \phi$  will depend on both  $f_s$  and  $f$ . The phase  $\phi$  of the carrier signal is set by the feedback pole frequency  $f_p$ , and the misalignment angle only becomes significant when  $f_s \approx f_p$ . The relevant strain frequencies for strain in the CS-100 strain cell are  $f_s \leq 1$  kHz, for which the misalignment angle is always a small fraction

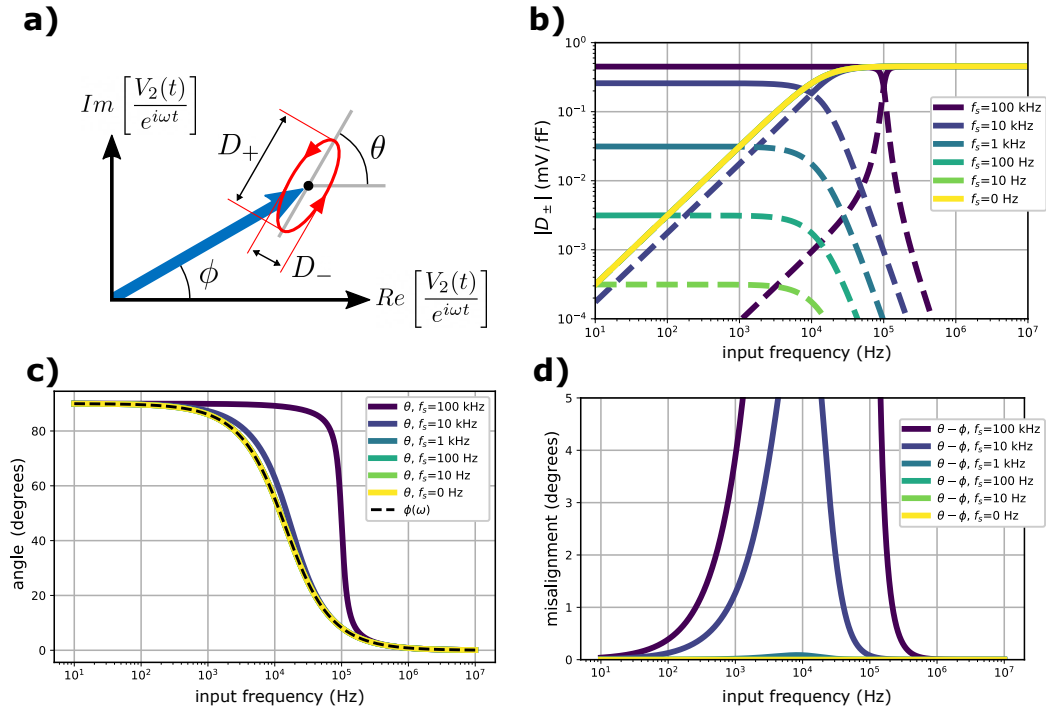


Figure A.3: Theoretical characteristics of the output signal from an autobalancing bridge measuring a sinusoidally modulated capacitance. Panel (a) defines the geometry of the ellipse traced out in a phasor space co-rotating at the input signal radial frequency  $\omega$ . The magnitude of the large blue arrow corresponds to the time-averaged capacitance signal. Panel (b) displays the magnitudes of the semi-major axis (solid lines) and semi-minor axis (dashed lines) as a function of input frequency for selected strain frequencies. In panel (c), the phases of the carrier signal ( $\phi$ ) and the orientation angle of the signal ellipse ( $\theta$ ). The misalignment between the ellipse orientation and carrier signal phase as a function of input and strain frequencies is shown in panel (d). For the relevant strain frequencies ( $f_s \leq 1$  kHz) the misalignment is always smaller than a fraction of a degree. This justifies the use of a single quadrature for detection of the amplitude of modulation.

of a degree. This justifies the use of the X quadrature alone in measuring both the carrier signal and the modulation, which can be corrected by dividing both by known factor of  $\cos \phi$ .

## A.4 Calibration

Before exploring the possibility of measuring AC modulated capacitances, I'll begin by understanding the DC response. The experimental setup for this is shown in Fig. A.4a. The capacitance sensor of a CS-100 cell (no sample mounted) is alternatively connected to an AH2500 capacitance bridge and the Capacitizer, and the PZT voltage is cycled through several polarization/depolarization loops. The resulting raw signals from both of these measurements are shown in Fig. A.4b as a function of PZT voltage. Plotting one against the other Fig. A.4c clearly shows the linear relationship between

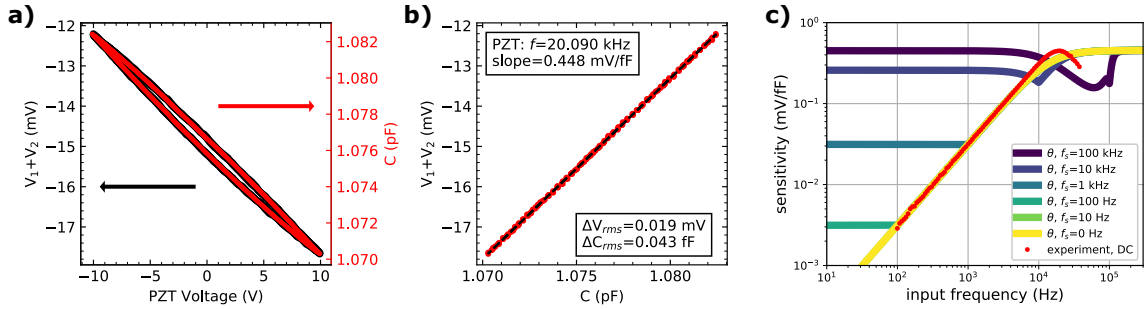


Figure A.4: Calibration of the AC capacitance bridge for quasi-static changes in sensor capacitance. Panel (a) shows the measured output voltage from the bridge (left axis) and the capacitance on the same cell measured by an AH2500 capacitance bridge from *Andeen-Hagerling* (right axis). These measurements were made one after another using the same cycle of voltage steps to the outer PZT stacks in the cell, and run through three full loops. The input signal is a sine wave of  $500 \text{ mV}_{\text{rms}}$  at  $20.090 \text{ kHz}$ . Panel (b) plots the two signals against each other, showing a remarkably linear relationship. The slope of this line sets the calibration factor of the AC capacitance bridge, which is measured to be  $0.448 \text{ mV/fF}$ . The theoretical value for ideal components and exact component values would be  $0.454 \text{ mV/fF}$ . Panel (c) shows the sensitivity as a function of input frequency (horizontal axis). Theoretical responses for single-quadrature in-phase detection at various strain frequencies  $f_s$  based on Eq. (A.5) are shown as solid lines. The measured sensitivity for quasi-static capacitance changes is shown as points.

the two circuits, corresponding to a slope of  $0.448 \text{ mV/fF}$ . The theoretical sensitivity for the given component values is  $0.454 \text{ mV/fF}$ . The theory and data presented in Fig. A.4c includes zero free parameters. The downturn in the sensitivity in the high frequency limit is likely due to non-ideal effects in the operational amplifiers in the circuit.

To my knowledge, there is no truly calibrated time-dependent capacitance which can be used to prove that the measured frequency dependence of the strain arises only from the cell itself and not as an unintended artifact from the bridge circuit. I can, however, simulate such a standard by injecting an amplitude modulated current. The setup for this test is shown in Fig. A.5a]. An amplitude-modulated voltage signal is produced by mixing a carrier wave at  $19 \text{ kHz}$  against the sum of a DC offset and another sine wave at the simulated strain frequency. The mixer was a custom-built circuit based on an AD835 analog multiplier integrated circuit. This voltage is converted into a current using a CS580 converter from *Stanford Research Systems*, and injected into the virtual ground terminal of the auto-balancing bridge.

In order to accurately mimic the behavior of a capacitive load, the carrier wave of the simulated current must lead the voltage drive input by a  $90^\circ$  phase. This was achieved by making use of the phase shifters inside of a lock-in amplifier: by applying a DC voltage to the input terminals of an SR860 lock-in and minimizing the strength of the low-pass filter, the X- and Y-quadrature outputs can be made to produce  $90^\circ$  phase-shifted sine waves at the reference frequency. These sine waves

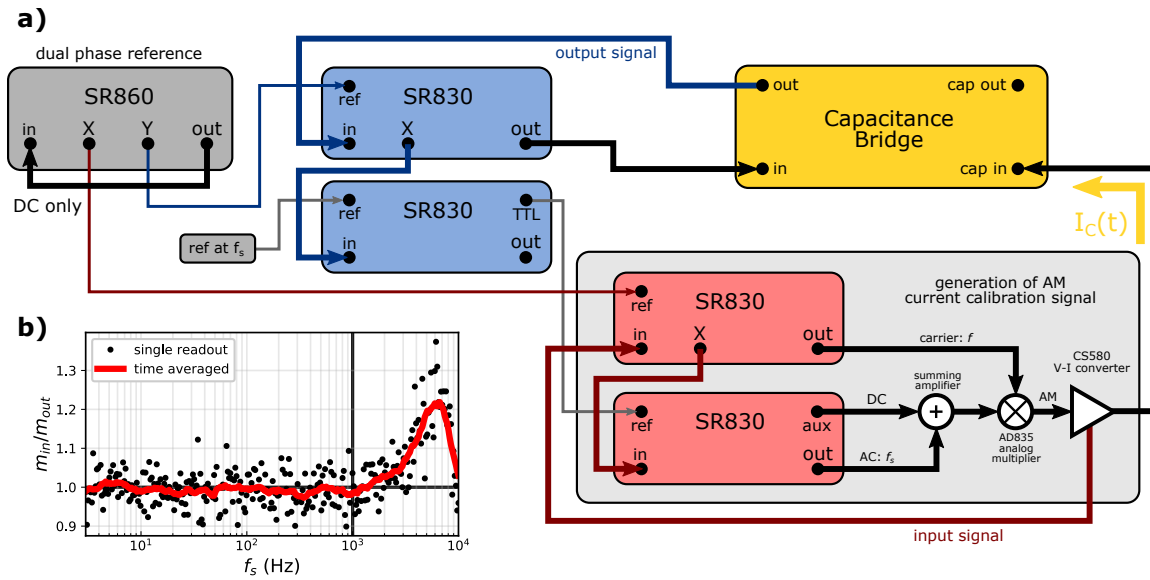


Figure A.5: Measurement of the dependence of AC capacitance bridge signals on the frequency of modulation. The output quadratures from a single lock-in amplifier are used as  $90^\circ$  phase-shifted frequency references for two pairs of lock-ins, which are arranged to detect both a carrier amplitude and a sideband. The lower (red) pair generates an amplitude modulated waveform using an external summing amplifier (to create the envelope function) and an analog multiplier (to perform the modulation). This signal is converted to a current and passed into the AC capacitance bridge to simulate the current generated by a modulated capacitance. The upper (blue) pair of lock-ins then detects the carrier and sideband of the output signal. The inset panel (b) shows the ratio of the modulation depths of the input and output signal, which confirms that the bridge sensitivity is independent of strain frequency when  $f_s \lesssim 1$  kHz.

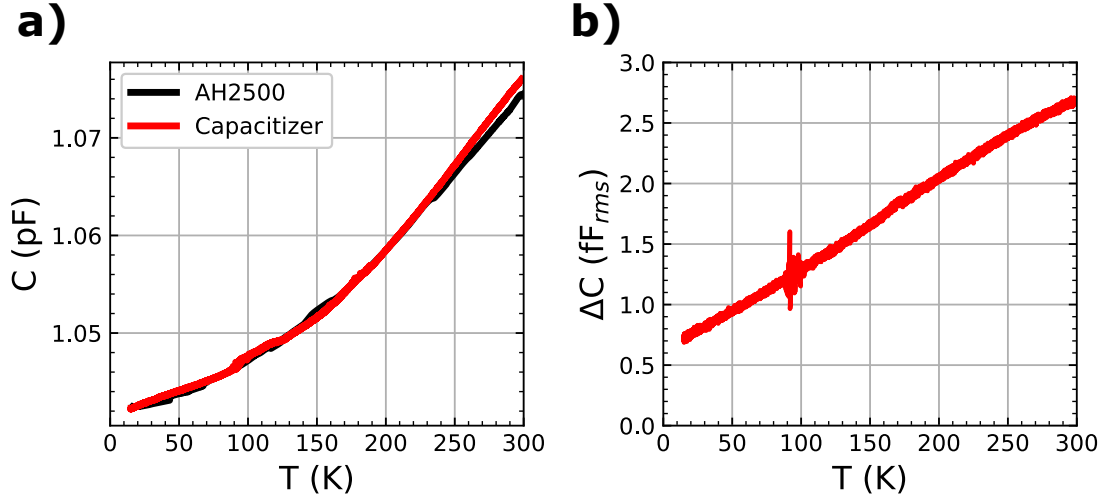


Figure A.6: Temperature dependence of the observed DC and AC capacitance. Panel (a) shows the time-averaged capacitance measured by both the commercial AH2500 bridge and the Capacitizer. The two match quantitatively with no free parameters. Panel (b) shows the direct measurement of the root-mean-square amplitude of the capacitance modulation enabled by this circuit. This measurement provides new and essential information for the accurate detection of the AC displacement, and achieving this measurement is the main result of this appendix. The modulation frequency for this measurement is 23.73 Hz, and the amplitude of the PZT drive voltage is 5 V<sub>rms</sub>. These two results can be converted to displacements, and then sample strains, through Eq. (A.1).

were then passed as reference signals to the lock-in amplifiers which provide the voltage input and current simulation inputs. By comparing the depth of the measured input and output modulation as a function of sideband frequency, we observe that there is no significant frequency dependence of the detected signal up to 1 kHz. The Capacitizer therefore covers the entire relevant range of strain frequencies in the CS-100 without need for any frequency correction or calibration.

Finally, Fig. A.6 shows the results of a representative temperature dependence of the strain cell sensor capacitance and modulation. The extracted DC capacitance from the Capacitizer is compared to the results of a measurement using the AH2500 commercial capacitance bridge, and the two match quantitatively with no free parameters. The slight variation between the two is an artifact of nonideal effects within the cell itself, and the fact that the two measurements necessarily must be performed during separate temperature sweeps. The temperature dependence of the time-averaged sensor capacitance reflects the thermal expansion and contraction of the cell, while the decreasing modulation at low temperatures reflects the decreasing piezoelectricity of the PZT.

In conclusion, the direct measurement of the AC capacitance modulation removes the need to extrapolate the strain from quasi-static measurements. Additionally, this measurement makes it possible to explore frequency and offset-voltage dependence of the AC displacement amplitude, an important step forward in reporting accurate elastoresistivity and elastocalorimetry results.



## Appendix B

# Details of the $R\text{Te}_3$ Landau Expansion

*This appendix serves to describe in detail how the Landau free energy expansion concepts described in Section 1.2.4 have been applied to the specific case of the rare-earth tritellurides under stress. Section B.1 defines the nomenclature, establishes the list of symmetry-allowed terms up through eighth order, and describes the thermodynamic conditions and the Legendre transformation in the symmetrized basis. Section B.2 assembles the simplest model to lowest order and discusses the constraints and results, and Section B.3 extends the theory to the sixth order. Finally, Section B.4 applies the theory to quantify the values of the coefficients for  $\text{ErTe}_3$ , which were the coefficients used in the creation of Fig. 4.1.*

### B.1 Setup and definitions

For the simplest phenomenological model of  $R\text{Te}_3$ , we constrain ourselves to a mean-field treatment of the disorder-free case, and we neglect the gradient terms defined in Eq. (1.21). The quasi-2D nature of the material suggests that the phase transitions may not be mean-field-like, and experimental evidence does support the existence of a significant region of critical fluctuations. However, as will be seen in later sections of this appendix, this simple model does appear to reproduce the phase diagram well, justifying mean-field as a jumping-off point for exploring the strain-CDW interaction. The CDW wavevector is assumed to be fully incommensurate with the lattice, such that Umklapp energy terms leading to commensurability transitions are negligible as well. Finally, order parameters describing the two in-plane wavevectors  $\mathbf{q}_a$  and  $\mathbf{q}_c$  are independent and orthogonal in space, which implies that there are no nontrivial “phasing” effects due to quartic cross terms.[65] The free energy, then has no dependence whatsoever on the phases of the complex CDW order parameters, and only

depends on the magnitudes.

The formal space group of the high-temperature normal metal,  $Cmcm$ [92] reduces to the  $D_{2h}$  point group upon removing the translation symmetry breaking effects. Examination of the character table of the  $D_{2h}$  point group shows that all of the irreducible representations (irreps) are one dimensional and Abelian[209]. However, treating the orthorhombic distortion as a small perturbation, we will work in a two-dimensional system with  $C_4$  symmetry in the absence of external stress. We will therefore use the language of irreps for the  $D_{4h}$  point group instead. The relevant irreps for the study of strain CDW coupling are

- $A_{1g}$ : which breaks no symmetries
- $B_{1g}$ : a shear term which breaks mirror plane symmetries diagonal to the principal axes (the orthorhombic distortion which restores the realistic  $R\text{Te}_3$  structure has  $B_{1g}$  character)
- $B_{2g}$ : a shear term rotated by  $45^\circ$  in the plane which breaks the mirror planes normal to the in-plane axes.

We begin by defining the physical quantities involved in a phenomenological free-energy expansion:

- $\psi_{\mathbf{x}}$  or  $\mathbf{x}$  for short: amplitude of the CDW order parameter with wavevector along the  $x$ -axis
- $\psi_{\mathbf{y}}$  or  $\mathbf{y}$  for short: amplitude of the CDW order parameter with wavevector along the  $y$ -axis
- $\varepsilon$ : strain tensor, which we assume to be given by

$$\varepsilon = \begin{pmatrix} \varepsilon_{xx} & 0 \\ 0 & \varepsilon_{yy} \end{pmatrix} \quad (\text{B.1})$$

- $\sigma$ : stress tensor, given by

$$\sigma = \begin{pmatrix} \sigma_{xx} & 0 \\ 0 & \sigma_{yy} \end{pmatrix} \quad (\text{B.2})$$

- $\varepsilon_{\mathbf{A}}$ : antisymmetric strain component, equal to  $(\varepsilon_{xx} - \varepsilon_{yy})/2$
- $\varepsilon_{\mathbf{S}}$ : symmetric strain component, equal to  $(\varepsilon_{xx} + \varepsilon_{yy})/2$
- $\sigma_{\mathbf{A}}$ : antisymmetric stress component, equal to  $(\sigma_{xx} - \sigma_{yy})/2$
- $\sigma_{\mathbf{S}}$ : symmetric stress component, equal to  $(\sigma_{xx} + \sigma_{yy})/2$
- $\mathbf{C}_{ij}$ : elastic constant tensor, in Voigt notation. Relevant terms here are given by  $i, j \in (1 = xx, 2 = yy)$  (ignoring shears) and working in tetragonal materials and only in 2D:

$$C_{ij} = \begin{pmatrix} C_{11} & C_{12} \\ C_{12} & C_{11} \end{pmatrix} \quad (\text{B.3})$$

### B.1.1 Terms allowed in the Landau expansion

From the assumptions made regarding the CDWs, we can tabulate all possible coupling terms between the order parameters and strains of different symmetries which can be included in the free energy expansion. We begin with a general categorization of linear combinations of powers of the order parameters into the irreps in the  $D_{4h}$  point group. Consider a linear combination of all relevant powers of the order parameter, which we will call  $Z$ :

$$Z \equiv \sum_{i,j} z_{ij} x^{2i} y^{2j} \quad (\text{B.4})$$

where  $i, j \in \mathbb{Z}$ . The goal is to determine all possible sets  $\{z_{ij}\}$  such that  $Z$  belongs to one of the irreducible representations of  $D_{4h}$ , as this defines which terms couple to what types of strains. The powers of  $x$  and  $y$  in Eq. (B.4) must all be even even as a consequence of the incommensurability of the wavevector; translational symmetry implies independence of the free energy on the phase.

Now, consider the behavior of  $Z$  under various symmetry operations. In order for  $Z$  to belong to one of the 1D irreps, the only possible actions of  $C_4$  on  $Z$  can be  $Z \rightarrow \pm Z$ . Consider first the action of a  $C_4$  rotation on  $Z$ :  $x \rightarrow -y, y \rightarrow x$

$$\sum_{i,j} z_{ij} x^{2i} y^{2j} = \pm \sum_{i,j} z_{ij} (-y)^{2i} (x)^{2j} \quad (\text{B.5})$$

$$= \sum_{i,j} \pm z_{ji} x^{2i} y^{2j} \quad (\text{B.6})$$

Where in the last step the indices have been relabeled. Exploiting the orthogonality of functions of differing powers, we make the general claim that

$$z_{ij} = \pm z_{ji} \quad (\text{B.7})$$

Any  $Z$  for which  $z_{ij}$  forms a symmetric matrix will respect  $C_4$  symmetry: all  $A_{1g}$  combinations of the order parameters will require  $z_{ij} = z_{ji}$ . In contrast, for  $Z$  to belong to either one of the  $B$  irreps,  $z_{ij}$  must be antisymmetric.

There are also four mirror planes to consider: reflections about the planes  $x = 0, y = 0, x = y,$  and  $x = -y$ . These operations can also, at most, change the sign of  $Z$  if  $Z$  belongs to any of the relevant irreps. We can work through the same process as Eq. (B.5) to find that for each mirror

plane:

$$x = 0 : y \rightarrow -y \qquad z_{ij} = \pm z_{ij} \qquad (\text{B.8})$$

$$y = 0 : x \rightarrow -x \qquad z_{ij} = \pm z_{ij} \qquad (\text{B.9})$$

$$x = y : x \rightarrow y, y \rightarrow x \qquad z_{ij} = \pm z_{ji} \qquad (\text{B.10})$$

$$x = -y : x \rightarrow -y, y \rightarrow -x \qquad z_{ij} = \pm z_{ji} \qquad (\text{B.11})$$

The first two of these, reflections about the  $x = 0$  and  $y = 0$  planes, imply the trivial result that *any* choice of  $z_{ij}$  terms will still preserve the mirror planes. Only the trivial  $z_{ij} = 0$  satisfies these equations with negative signs: no nontrivial  $Z$  will ever break these two mirror symmetries. The consequence is that no linear combination of any powers of the order parameters will never transform like the  $B_{2g}$  irrep. This formally prevents the inclusion of CDW-strain coupling terms which contain odd powers of  $B_{2g}$  strains.

The second two provide exactly the same condition as the  $C_4$  rotation shown in Eq. (B.7). This discussion therefore collapses into the simple rules for generating allowed terms:

- If we choose  $z_{ij}$  as symmetric, the resulting  $Z$  will transform like the  $A_{1g}$  representation.
- If we choose  $z_{ij}$  as antisymmetric, the resulting  $Z$  will transform like the  $B_{1g}$  representation.
- Those are the *only* two options for  $Z$ , and any arbitrary choice of  $z_{ij}$  can be written as a linear combination of  $B_{1g}$  and  $A_{1g}$  terms.

We can now establish an exhaustive list of invariants which may contribute to a free-energy expansion. These rules permit numerous combinations of terms, but many of them are not independent. In the list below, only the first few terms in each segment (presented in boldface) span the entirety of allowed terms. The rest can all be written as linear combinations of the boldface terms.

Quadratic terms:

- $(\mathbf{x}^2 + \mathbf{y}^2)$ : lowest order  $A_{1g}$  invariant

Quartic terms:

- $(\mathbf{x}^2 + \mathbf{y}^2)^2 = x^4 + 2x^2y^2 + y^4$ :  $A_{1g}$  term squared
- $(\mathbf{x}^2 - \mathbf{y}^2)^2 = x^4 - 2x^2y^2 + y^4$ : even powers of the  $B_{1g}$  component
- $(xy)^2$ : not independent, but arises from linear combinations of the first two

Sixth order terms:

- $(\mathbf{x}^2 + \mathbf{y}^2)^3 = x^6 + 3x^4y^2 + 3x^2y^4 + y^6$ :  $A_{1g}$  term cubed
- $(\mathbf{x}^2 + \mathbf{y}^2)(\mathbf{x}^2 - \mathbf{y}^2)^2 = x^6 - x^4y^2 - x^2y^4 + y^6$ :  $A_{1g}$  times  $B_{1g}$  squared

- $x^4y^2 + x^2y^4$ , not independent

Eighth order terms:

- $(\mathbf{x}^2 + \mathbf{y}^2)^4 = x^8 + 4x^6y^2 + 6x^4y^4 + 4x^2y^6 + y^8$ :  $A_{1g}$  term to the fourth
- $(\mathbf{x}^2 - \mathbf{y}^2)^4 = x^8 - 4x^6y^2 + 6x^4y^4 - 4x^2y^6 + y^8$ :  $B_{1g}$  term to the fourth
- $(\mathbf{x}^2 + \mathbf{y}^2)^2(\mathbf{x}^2 - \mathbf{y}^2)^2 = x^8 + 2x^4y^4 + y^8$ :  $A_{1g}/B_{1g}$  cross term
- $x^8 + y^8$ : not independent
- $x^4y^4$ : not independent
- $x^6y^2 + x^2y^6$ : not independent

We now consider invariants formed from combinations of the order parameter with the strain components. Symmetric ( $S$ ) strains belong to  $A_{1g}$ , while the antisymmetric strains under consideration ( $A$ ) belong to  $B_{1g}$ . Shear strains relative to the CDW wavevector ( $\varepsilon_D = \varepsilon_{xy}$ ) belong to  $B_{2g}$ .

Linear in strain, quadratic in order parameter:

- $\varepsilon_S(\mathbf{x}^2 + \mathbf{y}^2)$ :  $A_{1g}$  strain times  $A_{1g}$  invariant
- $\varepsilon_A(\mathbf{x}^2 - \mathbf{y}^2)$ :  $B_{1g}$  strain times  $B_{1g}$  invariant

Linear in strain, quartic in order parameter:

- $\varepsilon_S(\mathbf{x}^2 + \mathbf{y}^2)^2$ :  $A_{1g}$  strain times  $A_{1g}$  invariant squared
- $\varepsilon_S(\mathbf{x}^2 - \mathbf{y}^2)^2$ :  $A_{1g}$  strain times  $B_{1g}$  invariant squared
- $\varepsilon_A(\mathbf{x}^2 - \mathbf{y}^2)(\mathbf{x}^2 + \mathbf{y}^2) = \varepsilon_A(x^4 - y^4)$ :  $B_{1g}$  strain times  $B_{1g}$  and  $A_{1g}$
- $\varepsilon_S x^2 y^2$ : not independent

Quadratic in strain, quadratic in order parameter:

- $\varepsilon_S^2(\mathbf{x}^2 + \mathbf{y}^2)$ :  $A_{1g}$  strain squared times  $A_{1g}$  invariant
- $\varepsilon_A^2(\mathbf{x}^2 + \mathbf{y}^2)$ :  $B_{1g}$  strain squared times  $A_{1g}$  invariant
- $\varepsilon_A \varepsilon_S(\mathbf{x}^2 - \mathbf{y}^2)$ :  $A_{1g}$  and  $B_{1g}$  strains,  $B_{1g}$  order parameter
- $\varepsilon_D^2(\mathbf{x}^2 + \mathbf{y}^2)$ :  $B_{2g}$  strain squared times  $A_{1g}$  order parameter

### B.1.2 Legendre transform to Gibbs ensemble

The thermodynamic conditions of the experiments presented in Chapter 4 are, in an ideal case, that one component of strain (say,  $\varepsilon_{xx}$ ) is fixed, while the other two are allowed to relax. However, finite stiffness in the mounting epoxy and the stress cell itself means that even  $\varepsilon_{xx}$  will also vary. We therefore make the Legendre transformation to the Gibbs ensemble where stress is assumed to be held constant. Working in the symmetrized basis of  $\varepsilon_S$  and  $\varepsilon_A$ , however, requires a few factors of two to be added into the standard formulae.

The standard elastic energy term is given by

$$F_\varepsilon = \frac{C_{ij}}{2} \varepsilon_i \varepsilon_j \quad (\text{B.12})$$

where  $i, j \in (1, 2)$  as in Voigt notation for normal strains relative to the principle axes. Varying  $F$ :

$$dF_\varepsilon = \frac{C_{ij}}{2} (d\varepsilon_i \varepsilon_j + \varepsilon_i d\varepsilon_j) = C_{ij} \varepsilon_i d\varepsilon_j \quad (\text{B.13})$$

where in the last step I have rearranged terms in the sum and made use of the symmetric nature of  $C_{ij}$ . The standard Legendre transformation is given in Voigt notation by

$$G_\varepsilon = F_\varepsilon - \sigma_i \varepsilon_i. \quad (\text{B.14})$$

Changing from Voigt notation to the  $S/A$  basis for stress and strain follows from the definitions

$$\varepsilon_S = \frac{\varepsilon_{xx} + \varepsilon_{yy}}{2} \quad (\text{B.15})$$

$$\varepsilon_A = \frac{\varepsilon_{xx} - \varepsilon_{yy}}{2} \quad (\text{B.16})$$

$$\varepsilon_{xx} = \varepsilon_S + \varepsilon_A \quad (\text{B.17})$$

$$\varepsilon_{yy} = \varepsilon_S - \varepsilon_A \quad (\text{B.18})$$

$$\sigma_S = \frac{\sigma_{xx} + \sigma_{yy}}{2} \quad (\text{B.19})$$

$$\sigma_A = \frac{\sigma_{xx} - \sigma_{yy}}{2} \quad (\text{B.20})$$

$$\sigma_{xx} = \sigma_S + \sigma_A \quad (\text{B.21})$$

$$\sigma_{yy} = \sigma_S - \sigma_A \quad (\text{B.22})$$

$$(\text{B.23})$$

Simply substituting these terms into Eq. (B.14), we get

$$G_\varepsilon = F_\varepsilon - \sigma_{xx}\varepsilon_{xx} - \sigma_{yy}\varepsilon_{yy} \quad (\text{B.24})$$

$$= F_\varepsilon - (\sigma_S + \sigma_A)(\varepsilon_S + \varepsilon_A) - (\sigma_S - \sigma_A)(\varepsilon_S - \varepsilon_A) \quad (\text{B.25})$$

Which results in the equivalent definition of the Legendre transformation in the new basis:

$$G_\varepsilon = F_\varepsilon - 2(\sigma_A\varepsilon_A + \sigma_S\varepsilon_S). \quad (\text{B.26})$$

One step still remains, and that is to convert the elastic constants into the  $S/A$  basis as well.

$$\frac{C_{ij}}{2}\varepsilon_i\varepsilon_j = \frac{C_{11}}{2}(\varepsilon_{xx}^2 + \varepsilon_{yy}^2) + C_{12}\varepsilon_{xx}\varepsilon_{yy} \quad (\text{B.27})$$

$$= \frac{C_{11}}{2}((\varepsilon_S + \varepsilon_A)^2 + (\varepsilon_S - \varepsilon_A)^2) + C_{12}(\varepsilon_S + \varepsilon_A)(\varepsilon_S - \varepsilon_A) \quad (\text{B.28})$$

$$= \frac{C_{11}}{2}(2\varepsilon_S^2 + 2\varepsilon_A^2) + C_{12}(\varepsilon_S^2 - \varepsilon_A^2) \quad (\text{B.29})$$

$$= (C_{11} + C_{12})\varepsilon_S^2 + (C_{11} - C_{12})\varepsilon_A^2 \quad (\text{B.30})$$

$$\equiv \frac{C_S}{2}\varepsilon_S^2 + \frac{C_A}{2}\varepsilon_A^2 \quad (\text{B.31})$$

where we have defined

$$C_S = 2(C_{11} + C_{12}) \quad (\text{B.32})$$

$$C_A = 2(C_{11} - C_{12}) \quad (\text{B.33})$$

In this basis, then, the elastic component of the Gibbs free energy should be written as

$$G_\varepsilon = \frac{C_S}{2}\varepsilon_S^2 + \frac{C_A}{2}\varepsilon_A^2 - 2(\sigma_A\varepsilon_A + \sigma_S\varepsilon_S) \quad (\text{B.34})$$

Finally, it's worth noting that since the elastic constant matrix has to be positive definite in order for the material to be stable:

$$C_{11} > 0 \quad (\text{B.35})$$

$$C_{11}^2 - C_{12}^2 > 0 \quad (\text{B.36})$$

$$\implies |C_{11}| > |C_{12}| \quad (\text{B.37})$$

such that  $C_S$  and  $C_A$  are always positive, even if  $C_{12}$  is not.

## B.2 Assembling a model

We begin with the simplest expansion which exhibits CDW phase transitions, which requires only terms to fourth order. (It will be shown later that the strain varies like the order parameter squared.)

$$G = G_\psi + G_\varepsilon + G_i \quad (\text{B.38})$$

$$G_\psi = \frac{a_0(T - T_c^0)}{2T_c^0}(x^2 + y^2) + \frac{b}{4}(x^2 + y^2)^2 + \frac{g}{2}x^2y^2 \quad (\text{B.39})$$

$$G_\varepsilon = \frac{C_S}{2}\varepsilon_S^2 + \frac{C_A}{2}\varepsilon_A^2 - 2(\sigma_A\varepsilon_A + \sigma_S\varepsilon_S) \quad (\text{B.40})$$

$$G_i = \eta\varepsilon_S(x^2 + y^2) + \lambda\varepsilon_A(x^2 - y^2) \quad (\text{B.41})$$

Where the quartic terms are presented in a slightly different basis from the symmetry basis described in Appendix B.1.1—this choice makes it such that different signs of the  $g$  parameter correspond to different ground states, which would not be the case in other bases.

We begin by solving for the equilibrium values of the strain

$$0 = \frac{\partial G}{\partial \varepsilon_A} = C_A\varepsilon_A - 2\sigma_A + \lambda(x^2 - y^2) \quad (\text{B.42})$$

$$0 = \frac{\partial G}{\partial \varepsilon_S} = C_S\varepsilon_S - 2\sigma_S + \eta(x^2 + y^2) \quad (\text{B.43})$$

resulting in

$$\varepsilon_A = \frac{2\sigma_A - \lambda(x^2 - y^2)}{C_A} \quad (\text{B.44})$$

$$\varepsilon_S = \frac{2\sigma_S - \eta(x^2 + y^2)}{C_S} \quad (\text{B.45})$$

Reinsert these expressions into the original free energy to eliminate the strain variables gives

$$G_\varepsilon = \frac{C_A}{2} \left( \frac{2\sigma_A - \lambda(x^2 - y^2)}{C_A} \right)^2 + \frac{C_S}{2} \left( \frac{2\sigma_S - \eta(x^2 + y^2)}{C_S} \right)^2 - 2\sigma_A \left( \frac{2\sigma_A - \lambda(x^2 - y^2)}{C_A} \right) - 2\sigma_S \left( \frac{2\sigma_S - \eta(x^2 + y^2)}{C_S} \right) \quad (\text{B.46})$$

$$= \frac{-4\sigma_A^2 + \lambda^2(x^2 - y^2)^2}{2C_A} + \frac{-4\sigma_S^2 + \eta^2(x^2 + y^2)^2}{2C_S} \quad (\text{B.47})$$

$$G_i = \eta \left( \frac{2\sigma_S - \eta(x^2 + y^2)}{C_S} \right) (x^2 + y^2) + \lambda \left( \frac{2\sigma_A - \lambda(x^2 - y^2)}{C_A} \right) (x^2 - y^2) \quad (\text{B.48})$$

$$= \frac{4\eta\sigma_S(x^2 + y^2) - 2\eta^2(x^2 + y^2)^2}{2C_S} + \frac{4\lambda\sigma_A(x^2 - y^2) - 2\lambda^2(x^2 - y^2)^2}{2C_A} \quad (\text{B.49})$$

$$\begin{aligned}
G &= \frac{a_0(T - T_c^0)}{2T_c^0}(x^2 + y^2) + \frac{b}{4}(x^2 + y^2)^2 + \frac{g}{2}x^2y^2 - \frac{\lambda^2(x^2 - y^2)^2}{2C_A} \\
&\quad - \frac{\eta^2(x^2 + y^2)^2}{2C_S} + \frac{2\sigma_A[\lambda(x^2 - y^2) - \sigma_A]}{C_A} + \frac{2\sigma_S[\eta(x^2 + y^2) - \sigma_S]}{C_S} \\
&= -2 \left( \frac{\sigma_A^2}{C_A} + \frac{\sigma_S^2}{C_S} \right) \\
&\quad + \left[ \frac{a_0(T - T_c^0)}{2T_c^0} + \frac{2\sigma_A\lambda}{C_A} + \frac{2\sigma_S\eta}{C_S} \right] x^2 \\
&\quad + \left[ \frac{a_0(T - T_c^0)}{2T_c^0} - \frac{2\sigma_A\lambda}{C_A} + \frac{2\sigma_S\eta}{C_S} \right] y^2 \\
&\quad + \left[ \frac{b}{4} - \frac{\lambda^2}{2C_A} - \frac{\eta^2}{2C_S} \right] x^4 \\
&\quad + \left[ \frac{b}{4} - \frac{\lambda^2}{2C_A} - \frac{\eta^2}{2C_S} \right] y^4 \\
&\quad + \left[ \frac{b+g}{2} + \frac{\lambda^2}{C_A} - \frac{\eta^2}{C_S} \right] x^2y^2
\end{aligned} \tag{B.50}$$

$$\tag{B.51}$$

The character of this model then unfolds directly. First, we calculate the effective critical temperatures under stress:

$$\frac{a_0(T - T_x^*)}{2T_c^0} = \left[ \frac{a_0(T - T_c^0)}{2T_c^0} + \frac{2\sigma_A\lambda}{C_A} + \frac{2\sigma_S\eta}{C_S} \right] \tag{B.52}$$

$$T_x^* = -\frac{2T_c^0}{a_0} \left[ \frac{a_0(T - T_c^0)}{2T_c^0} + \frac{2\sigma_A\lambda}{C_A} + \frac{2\sigma_S\eta}{C_S} \right] + T \tag{B.53}$$

$$T_x^* = T_c^0 \left( 1 - \frac{4}{a_0} \left[ \frac{\sigma_A\lambda}{C_A} + \frac{\sigma_S\eta}{C_S} \right] \right) \tag{B.54}$$

$$\frac{a_0(T - T_y^*)}{2T_c^0} = \left[ \frac{a_0(T - T_c^0)}{2T_c^0} - \frac{2\sigma_A\lambda}{C_A} + \frac{2\sigma_S\eta}{C_S} \right] \tag{B.55}$$

$$T_y^* = -\frac{2T_c^0}{a_0} \left[ \frac{a_0(T - T_c^0)}{2T_c^0} - \frac{2\sigma_A\lambda}{C_A} + \frac{2\sigma_S\eta}{C_S} \right] + T \tag{B.56}$$

$$T_y^* = T_c^0 \left( 1 - \frac{4}{a_0} \left[ -\frac{\sigma_A\lambda}{C_A} + \frac{\sigma_S\eta}{C_S} \right] \right) \tag{B.57}$$

Next, we address the question of a second CDW transition for  $T < T_c^0$ . Formally, a Landau expansion loses validity far from the critical temperature, and the assumptions which led to its creation may not hold at a hypothetical  $T_{CDW2}$ ; quantitative predictions at low temperatures should be taken with a grain of salt. Forging ahead with this caveat in mind, however, we can assume that the first transition produced  $x \neq 0$ , then expand in  $y$  and do a similar analysis to find a critical

temperature.

$$\begin{aligned}
G &= G_0(x) \\
&+ \left[ \frac{a_0(T - T_c^0)}{2T_c^0} - \frac{2\sigma_A\lambda}{C_A} + \frac{2\sigma_S\eta}{C_S} + \left( \frac{b+g}{2} + \frac{\lambda^2}{C_A} - \frac{\eta^2}{C_S} \right) x^2 \right] y^2 \\
&+ \left[ \frac{b}{4} - \frac{\lambda^2}{2C_A} - \frac{\eta^2}{2C_S} \right] y^4
\end{aligned} \tag{B.58}$$

$$G = G_0(x) + \left[ \frac{a_0(T - T_y^*)}{2T_c^0} + g^* x^2 \right] y^2 + b^* y^4 \tag{B.59}$$

where the effective coefficients  $g^*$  and  $b^*$  are defined as

$$b^* = \frac{b}{4} - \frac{\lambda^2}{2C_A} - \frac{\eta^2}{2C_S} \tag{B.60}$$

$$g^* = \frac{b+g}{2} + \frac{\lambda^2}{C_A} - \frac{\eta^2}{C_S} \tag{B.61}$$

We need to know the temperature dependence of  $x$  above the second CDW transition but below the first, which is given by:

$$\frac{\partial G}{\partial x} = 0 = \left[ \frac{a_0(T - T_x^*)}{2T_c^0} \right] x + 2b^* x^3 \tag{B.62}$$

$$\implies x^2 = \frac{a_0(T_x^* - T)}{4b^* T_c^0} \tag{B.63}$$

Which then leads to a definition for the second CDW transition,  $T_{2y}^*$  (distinct from the transition for the first CDW along the  $y$  direction,  $T_y^*$ )

$$0 = \frac{a_0(T_{2y}^* - T_y^*)}{2T_c^0} + \frac{a_0 g^* (T_x^* - T_{2y}^*)}{4b^* T_c^0} \tag{B.64}$$

$$= \frac{(2b^* T_{2y}^* - 2b^* T_y^*) + (g^* T_x^* - g^* T_{2y}^*)}{2b^*} \tag{B.65}$$

$$= (2b^* - g^*) T_{2y}^* - 2b^* T_y^* + g^* T_x^* \tag{B.66}$$

$$T_{2y}^* = \frac{2b^* T_y^* - g^* T_x^*}{b} \tag{B.67}$$

Physical solutions for this second CDW transition only include those in the range  $0 < T_{2y}^* < T_x^*$ , and it can be shown that solutions for this second CDW exist only if  $g < 0$ .

Up until this point, the stability of the the expansion has been implicitly assumed. To check this, we convert from the  $x$  and  $y$  order parameter space to polar coordinates  $(r, \theta)$  and explore the

quartic terms only:

$$G_4 = r^4 (b^* (\cos^4(\theta) + \sin^4(\theta)) + g^* \cos^2(\theta) \sin^2(\theta)) \quad (\text{B.68})$$

$$= r^4 \left( b^* \left[ \left( \frac{1 + \cos(2\theta)}{2} \right)^2 + \left( \frac{1 - \cos(2\theta)}{2} \right)^2 \right] + g^* \frac{1 + \cos(2\theta)}{2} \frac{1 - \cos(2\theta)}{2} \right) \quad (\text{B.69})$$

$$= \frac{r^4}{4} \left\{ b^* \left[ (1 + \cos(2\theta))^2 + (1 - \cos(2\theta))^2 \right] + g^* (1 + \cos(2\theta))(1 - \cos(2\theta)) \right\} \quad (\text{B.70})$$

$$= \frac{r^4}{4} \left\{ b^* [2 + 2 \cos^2(2\theta)] + g^* [1 - \cos^2(2\theta)] \right\} \quad (\text{B.71})$$

In order for this Landau model to be unconditionally stable, we require that  $G_4 \rightarrow \infty$  for all  $\theta$  as  $r \rightarrow$  infinity, or, renaming  $\cos^2(2\theta) \equiv z$ :

$$2b^* + g^* + (2b^* - g^*)z > 0 \quad \forall z \in [0, 1] \quad (\text{B.72})$$

$$2b^* + g^* + 2b^* - g^* > 0 \quad (z = 1) \quad (\text{B.73})$$

$$\implies b^* > 0 \quad (\text{B.74})$$

$$2b^* + g^* > 0 \quad (z = 0) \quad (\text{B.75})$$

$$\implies g^* > -2b^* \quad (\text{B.76})$$

Expanding the  $g^*$  and  $b^*$  terms:

$$\left[ \frac{b}{4} - \frac{\lambda^2}{2C_A} - \frac{\eta^2}{2C_S} \right] > 0 \quad (\text{B.77})$$

$$b > \frac{2\lambda^2}{C_A} + \frac{2\eta^2}{C_S} \quad (\text{B.78})$$

which both states that  $b$  must be greater than zero (as the right hand side is strictly non-negative) and also places a limit on how strong the elastic-CDW coupling terms  $\eta$  and  $\lambda$  can be relative to  $b$ . The other condition gives:

$$\frac{b+g}{2} + \frac{\lambda^2}{C_A} - \frac{\eta^2}{C_S} > \frac{\lambda^2}{C_A} + \frac{\eta^2}{C_S} - \frac{b}{2} \quad (\text{B.79})$$

$$g > \frac{4\eta^2}{C_S} - 2b \quad (\text{B.80})$$

which, in combination with the Eq. (B.78) states that the free energy may be stable for both positive and negative  $g$ , provided that  $g$  is not too large and negative. In general, for given values of the  $g$  and  $b$  coefficients, we see that increasing the elastic coupling terms always pushes the free energy toward instability, and would eventually cause the phase transitions to become first order if higher order bounding terms were included.

If the above conditions are met, then this fourth order expansion will host a second order CDW

transition to an incommensurate unidirectional state. Antisymmetric strain selects one or the other of the two in-plane directions. If  $g$  is positive, then the two regions will meet up at a first order transition running down the  $\sigma_A = 0$  axis from  $T_c^0$ . If  $g$  is negative, then there will be a triangular region of coexistence with its peak at  $T = T_c^0$ ,  $\sigma_A = 0$  and its base at  $T = 0$ .

Technically, every possible situation in this model is described as two competing orders. The competition is not always completely binary, and there can be a region of coexistence when  $g < 0$ , but the second CDW transition is always suppressed by the first. In order to see cooperative effects, one would have to include higher order coupling terms.

From a comparison to experiments in the tritellurides, we can bound a few other terms as well. Aside from  $a_0$ ,  $b$ ,  $C_A$ ,  $C_S$  being positive, as discussed above, we also know that  $\lambda$  must be negative. This can be seen from the fact that the CDW tends to align itself with the long axis: positive strain (tension) in the  $x$  direction lowers the energy of the  $x \neq 0$  ordered state. Additionally,  $\eta$  must also be negative: for hydrostatic pressure ( $\sigma_S < 0$ ) we know that the critical temperature drops.[100, 93, 101]

### B.3 Higher order terms: reintroducing the second CDW

As evidenced by DC elastoresistivity experiments in Chapter 4, the two CDW states are separated by a first order transition. However, a second CDW transition is also observed. These two features cannot coexist within a fourth-order Landau model, and we therefore require terms of the next highest order.

Consider, then, an expansion containing terms up to the sixth order. This is slightly subtle due to the coupling between strain and the order parameter. Adding a term which is linear in strain but quartic in the order parameters actually changes the behavior of the strain. Instead of remaining quadratic in the order parameter, it gains a component which is quartic in order parameters, such that the original coupling term now is 8th order. Therefore we would require that we have an 8th or higher order bounding term. A biquadratic CDW-strain term would produce slightly more complicated behavior, but again for large order parameters the strain will always become quartic in  $x$ . For moderate  $x$ , though, the strain may be much more tame given a proper choice of coefficients. In order to have a model which is unconditionally stable, however, we are unable to add any more terms involving strain if we want to constrain ourselves to sixth order.

There are therefore only two more terms which can be added:

$$G = G_\psi + G_\varepsilon + G_i + \frac{r}{6}(x^2 + y^2)^3 + \frac{\gamma}{6}(x^4 y^2 + x^2 y^4) \quad (\text{B.81})$$

Now we can relax some of the constraints for the quartic terms by enforcing positivity in the sixth

order term:

$$r + \gamma(\cos^4(\theta) \sin^2(\theta) + \cos^2(\theta) \sin^4(\theta)) > 0 \quad \forall \theta \quad (\text{B.82})$$

$$r + \frac{\gamma z}{4} > 0 \quad \forall z \in [0, 1] \quad (\text{B.83})$$

$$\implies r > 0 \quad (\text{B.84})$$

$$\implies \gamma > -4r \quad (\text{B.85})$$

As long as Eq. (B.85) is met, we now have a stable free energy landscape even if we drop the conditions in Eq. (B.78) and Eq. (B.80). However, this is likely to cause the first CDW transition temperature to increase and become first order at least for some regions of phase space, which, as far as has been determined experimentally, is not the case.

Considering  $g < 0$ , we find (through numerically minimizing the free energy across the phase diagram) that the  $r$  term adds some downward curvature to the second CDW transition, decreasing the range of strain over which the coexistence region appears at low temperatures. The  $\gamma$  term can either widen (for  $\gamma < 0$ ) or shrink the coexistence region as well. For a region where  $\gamma \approx 3r$  and with  $g < 0$ , one can find a phase diagram topology where the coexistence region is localized near the pentacritical point at  $\sigma_A = 0$ ,  $T = T_c^0$ . As temperature decreases, the transition between the two checkerboard states gives way to a first order transition between the two stripes. This is the opposite of what is observed in experiments.

On the other hand, for  $g > 0$  and  $\gamma \approx -3r$ , we achieve the lowest order expansion which *does* properly describe the phase transitions seen in strain measurements. More specifically, we see the emergence of two critical points: one at the first CDW transition  $T_c^0$ , and another at a lower temperature  $T_{c2}^0$ , with both lying on the  $\sigma_A = 0$  axis. This second one occurs when there is a ring of degenerate states which also happen to be a global minimum in  $xy$  space. Convert to polar coordinates, and solve one of the conditions for the radius  $\rho_c(\theta)$  of this ring as a function of angle:

$$\frac{\partial G}{\partial \theta} = 0 = \rho_c^4 \left( g^* + \frac{\gamma \rho_c^2}{6} \right) \frac{\partial}{\partial \theta} \cos^2(\theta) \sin^2(\theta) \quad (\text{B.86})$$

$$\rho_c^2 = \frac{-6g^*}{\gamma} = \frac{-6}{\gamma} \left[ \frac{b+g}{2} + \frac{\lambda^2}{C_A} - \frac{\eta^2}{C_S} \right] \quad (\text{B.87})$$

where I have, on symmetry grounds, neglected the terms involving stress. This says that all states where  $x^2 + y^2 = \rho_c^2$  have the same energy—stripes and checkerboards of all sorts can coexist. If the coefficients, including the temperature, conspire to cause the order parameters to grow beyond this level, then what was a stripe state will convert (continuously!) into a checkerboard.

Having included these higher order terms, the order parameter no longer follows the same simple temperature dependence. The critical exponent  $\beta$  in  $x \propto (1 - T/T_c^0)^\beta$  is still 0.5 just below the transition, but this no longer holds far from the transition. (It should be noted that the real material

is NOT mean field, with the upper transition exhibiting  $\beta = 0.3$ [210] and the lower transition exhibiting  $\beta = 0.7$ [70].) However, keeping  $\beta = 0.5$  as a simple estimator and taking the order parameter temperature dependence from Eq. (B.63), we can get a sensible approximation for the temperature at which we cross this lower critical point:

$$\frac{-6g^*}{\gamma} \approx \frac{a_0(T_x^* - T_{2c}^0)}{4b^*T_c^0} \quad (\text{B.88})$$

$$T_{2c}^0 \approx \frac{24b^*T_c^0g^*}{\gamma a_0} + T_x^* \quad (\text{B.89})$$

$$T_{2c}^0 \approx T_c^0 \left[ 1 + \frac{24b^*g^*}{\gamma a_0} \right] \quad (\text{B.90})$$

Where  $T_x^* = T_c^0$  when  $\sigma_A = \sigma_S = 0$

## B.4 Quantifying the tritellurides

We now attempt to estimate realistic values for which this free energy expansion approximates the observed phase diagram of the tritellurides. We provide sensible estimates for the parameters  $a_0$ ,  $b$ ,  $\lambda$ ,  $\eta$ ,  $C_A$ , and  $C_S$ . The remaining coefficients  $g$ ,  $\gamma$ , and  $r$ , which set the behavior of the second transition, are more difficult to calculate. Attempts at using the estimate in Eq. (B.90) of the second critical point set a relation between  $\gamma$  and  $g$ , but the value of  $r$  is poorly constrained and strongly affects the resulting phase diagram. This likely indicates a breakdown of the linear-in- $T$  behavior which is assumed for the quadratic coefficient.

First, we establish an estimate for the elastic constants. The reported value of  $C_{11}$  from ultrasound measurements[181]. is approximately 50 GPa, and  $C_{13}$  (returning now to the crystallographic convention of the  $b$ -axis perpendicular to plane) has not been measured. In principle one can calculate  $C_{13}$  by comparison with x-ray scattering measurements under pressure[93]. However, existing literature values produce thermodynamically incompatible values of  $C_{13}$ . In the absence of other data, the next approximation would be to consider only in-plane elasticity in an appeal to the layered structure of  $R\text{Te}_3$ . In this case, the in-plane Poisson ratio is just the ratio between  $C_{11}$  and  $C_{12}$ , and we can assume a fairly standard Poisson ratio of  $\nu = 0.2$ . [211]. Combining this with the estimate from ultrasound, we get  $C_S=60$  GPa and  $C_A=40$  GPa.

The critical temperatures are also well established: for  $\text{ErTe}_3$ ,  $T_c^0=265$  K, and  $T_{2c}^0=165$  K= $0.62T_c^0$ . For  $\text{TmTe}_3$ ,  $T_c^0=245$  K and  $T_{2c}^0=180$  K= $0.73T_c^0$ .

The effective critical temperature  $T_x^*$  is given by Eq. (B.54), and the strain (and, using the elastic constants, stress) dependence of this can be measured. Experiments in Chapter 4 were performed

under uniaxial stress  $\sigma_x x = 2\sigma_A = 2\sigma_S$ , so we get the constraint

$$\frac{dT_x^*}{d\sigma_{xx}} = 86 \text{ K GPa}^{-1} = \frac{-4T_c^0}{a_0} \frac{d}{d\sigma_{xx}} \left[ \frac{\sigma_S \eta}{C_S} + \frac{\sigma_A \lambda}{C_a} \right] \quad (\text{B.91})$$

$$-0.16 \text{ GPa}^{-1} = \frac{1}{a_0} \left[ \frac{\eta}{C_S} + \frac{\lambda}{C_a} \right] \quad (\text{B.92})$$

The other coefficients require a scale of the order parameter—the CDW gap magnitude has been measured extensively. In ErTe<sub>3</sub>, the maximum gaps are 175 meV and 50 meV along the  $c$  and  $a$  axes, respectively.[81] With this, and again making the approximation that the order parameter grows like  $(1 - T/T_c)^{1/2}$  below the phase transition:

$$x^2 = (175 \text{ meV})^2 = \frac{a_0}{4b^*} \quad (\text{B.93})$$

$$= \frac{a_0}{b - \frac{2\lambda^2}{C_A} - \frac{2\eta^2}{C_S}} \quad (\text{B.94})$$

The thermal expansion has also been measured from x-ray measurements under pressure[69] in TbTe<sub>3</sub> just below the critical temperature. This quantity inevitably includes some extra background component stemming from anharmonic phonons, so I will subtract the value in the uniform state. From this, in the  $x$  stripe state, we can extract

$$\alpha_A = -5.93 \times 10^{-5} \text{ K}^{-1} \quad (\text{B.95})$$

$$\alpha_S = -7.5 \times 10^{-6} \text{ K}^{-1} \quad (\text{B.96})$$

Combining Eqs. (B.44), (B.45) and (B.63), we get

$$\alpha_A = \frac{d\varepsilon_A}{dT} = \frac{d}{dT} \left[ \frac{2\sigma_A - \lambda \left( \frac{a_0(T_x^* - T)}{4b^*T_c^0} \right)}{C_A} \right] \quad (\text{B.97})$$

$$= \frac{\lambda a_0}{4b^*T_c^0 C_A} \quad (\text{B.98})$$

$$-0.157 \text{ GPa}^{-1} = \frac{\lambda a_0}{b^*} \quad (\text{B.99})$$

$$\alpha_S = \frac{d\varepsilon_S}{dT} = \frac{d}{dT} \left[ \frac{2\sigma_S - \eta \left( \frac{a_0(T_x^* - T)}{4b^*T_c^0} \right)}{C_S} \right] \quad (\text{B.100})$$

$$= \frac{\eta a_0}{4b^*T_c^0 C_S} \quad (\text{B.101})$$

$$-0.0298 \text{ GPa}^{-1} = \frac{\eta a_0}{b^*} \quad (\text{B.102})$$

Equations (B.92), (B.94), (B.99) and (B.102) form four constraints for the four unknowns  $a_0$ ,  $b$ ,

$\lambda$ , and  $\eta$ . Solving for these, we get

$$a_0 = 0.226 \text{ eV}^{-2} \quad (\text{B.103})$$

$$b = 7.45 \text{ eV}^{-4} \quad (\text{B.104})$$

$$\lambda = -1.282 \text{ GPa}^{-1} \text{ eV}^{-2} \quad (\text{B.105})$$

$$\eta = -0.243 \text{ GPa}^{-1} \text{ eV}^{-2} \quad (\text{B.106})$$

These values accurately describe the behavior of the phase diagram above, at, and slightly below the first transition.

# Bibliography

- [1] P. W. Anderson, “More is different”, *Science* **177** (1972), no. 4047, 393–396.
- [2] J. G. Bednorz and K. A. Müller, “Possible high  $T_c$  superconductivity in the Ba–La–Cu–O system”, *Zeitschrift für Phys. B Condens. Matter* **64** (1986), no. 2, 189–193.
- [3] J. M. Tranquada, B. J. Sternlieb, J. D. Axe, Y. Nakamura, and S. Uchida, “Evidence for stripe correlations of spins and holes in copper oxide superconductors”, *Nature* **375** (1995), no. 6532, 561–563.
- [4] V. J. Emery, S. A. Kivelson, and J. M. Tranquada, “Stripe phases in high-temperature superconductors”, *Proc. Natl. Acad. Sci. U. S. A.* **96** (1999), no. 16, 8814–8817.
- [5] S. A. Kivelson, I. P. Bindloss, E. Fradkin, V. Oganesyan, J. M. Tranquada, A. Kapitulnik, and C. Howald, “How to detect fluctuating stripes in the high-temperature superconductors”, *Rev. Mod. Phys.* **75** (2003), no. 4, 1201–1241.
- [6] J. E. Hoffman, E. W. Hudson, K. M. Lang, V. Madhavan, H. Eisaki, S. Uchida, and J. C. Davis, “A four unit cell periodic pattern of quasi-particle states surrounding vortex cores in  $\text{Bi}_2\text{Sr}_2\text{CaCu}_2\text{O}_{8+\delta}$ ”, *Science* **295** (2002), no. 5554, 466–469.
- [7] C. Howald, H. Eisaki, N. Kaneko, M. Greven, and A. Kapitulnik, “Periodic density-of-states modulations in superconducting  $\text{Bi}_2\text{Sr}_2\text{CaCu}_2\text{O}_{8+\delta}$ ”, *Phys. Rev. B* **67** (2003), no. 1, 014533.
- [8] T. Wu, H. Mayaffre, S. Krämer, M. Horvatić, C. Berthier, W. Hardy, R. Liang, D. Bonn, and M. Julien, “Incipient charge order observed by NMR in the normal state of  $\text{YBa}_2\text{Cu}_3\text{O}_y$ ”, *Nat. Commun.* **6** (2015), no. 1, 6438.
- [9] G. Ghiringhelli, M. Le Tacon, M. Minola, S. Blanco-Canosa, C. Mazzoli, N. B. Brookes, G. M. De Luca, A. Frano, D. G. Hawthorn, F. He, T. Loew, M. M. Sala, D. C. Peets, M. Salluzzo, E. Schierle, R. Sutarto, G. A. Sawatzky, E. Weschke, B. Keimer, and L. Braicovich, “Long-Range incommensurate charge fluctuations in  $(\text{Y,Nd})\text{Ba}_2\text{Cu}_3\text{O}_{6+x}$ ”, *Science* **337** (2012), no. 6096, 821–825.

- [10] T. P. Croft, C. Lester, M. S. Senn, A. Bombardi, and S. M. Hayden, “Charge density wave fluctuations in  $\text{La}_{2-x}\text{Sr}_x\text{CuO}_4$  and their competition with superconductivity”, *Phys. Rev. B* **89** (2014), no. 22, 224513.
- [11] W. Tabis, B. Yu, I. Bialo, M. Bluschke, T. Kolodziej, A. Kozłowski, E. Blackburn, K. Sen, E. M. Forgan, M. V. Zimmermann, Y. Tang, E. Weschke, B. Vignolle, M. Hepting, H. Gretarsson, R. Sutarto, F. He, M. Le Tacon, N. Barišić, G. Yu, and M. Greven, “Synchrotron x-ray scattering study of charge-density-wave order in  $\text{HgBa}_2\text{CuO}_{4+\delta}$ ”, *Phys. Rev. B* **96** (2017), no. 13, 134510.
- [12] S. E. Sebastian, N. Harrison, F. F. Balakirev, M. M. Altarawneh, P. A. Goddard, R. Liang, D. A. Bonn, W. N. Hardy, and G. G. Lonzarich, “Normal-state nodal electronic structure in underdoped high- $T_c$  copper oxides”, *Nature* **511** (2014), no. 7507, 61–64.
- [13] S. E. Sebastian and C. Proust, “Quantum oscillations in hole-doped cuprates”, *Annu. Rev. Condens. Matter Phys.* **6** (2015), no. 1, 411–430.
- [14] S. Gerber, H. Jang, H. Nojiri, S. Matsuzawa, H. Yasumura, D. A. Bonn, R. Liang, W. N. Hardy, Z. Islam, A. Mehta, S. Song, M. Sikorski, D. Stefanescu, Y. Feng, S. A. Kivelson, T. P. Devereaux, Z. X. Shen, C. C. Kao, W. S. Lee, D. Zhu, and J. S. Lee, “Three-dimensional charge density wave order in  $\text{YBa}_2\text{Cu}_3\text{O}_{6.67}$  at high magnetic fields”, *Science* **350** (2015), no. 6263, 949–952.
- [15] H. Jang, W. Lee, H. Nojiri, S. Matsuzawa, H. Yasumura, L. Nie, A. V. Maharaj, S. Gerber, Y. Liu, A. Mehta, D. A. Bonn, R. Liang, W. N. Hardy, C. A. Burns, Z. Islam, S. Song, J. Hastings, T. P. Devereaux, Z. Shen, S. A. Kivelson, C. Kao, D. Zhu, and J. Lee, “Ideal charge-density-wave order in the high-field state of superconducting YBCO”, *Proc. Natl. Acad. Sci. U. S. A.* **113** (2016), no. 51, 14645–14650.
- [16] J. Chang, E. Blackburn, A. T. Holmes, N. B. Christensen, J. Larsen, J. Mesot, R. Liang, D. A. Bonn, W. N. Hardy, A. Watenphul, M. V. Zimmermann, E. M. Forgan, and S. M. Hayden, “Direct observation of competition between superconductivity and charge density wave order in  $\text{YBa}_2\text{Cu}_3\text{O}_{6.67}$ ”, *Nat. Phys.* **8** (2012), no. 12, 871–876.
- [17] F. Laliberté, M. Frachet, S. Benhabib, B. Borgnic, T. Loew, J. Porras, M. Le Tacon, B. Keimer, S. Wiedmann, C. Proust, and D. Leboeuf, “High field charge order across the phase diagram of  $\text{YBa}_2\text{Cu}_3\text{O}_y$ ”, *npj Quantum Mater.* **3** (2018), no. 1, 1–7.
- [18] H. Kim, S. M. Souliou, M. E. Barber, E. Lefrançois, M. Minola, M. Tortora, R. Heid, N. Nandi, R. A. Borzi, G. Garbarino, A. Bosak, J. Porras, T. Loew, M. König, P. J. W. Moll, A. P. Mackenzie, B. Keimer, C. W. Hicks, and M. Le Tacon, “Uniaxial pressure control of competing orders in a high-temperature superconductor”, *Science* **362** (2018), no. 6418, 1040–1044.

- [19] C. M. Varma, “Non-Fermi-liquid states and pairing instability of a general model of copper oxide metals”, *Phys. Rev. B* **55** (1997), no. 21, 14554.
- [20] J. Wu, A. T. Bollinger, X. He, and I. Božović, “Spontaneous breaking of rotational symmetry in copper oxide superconductors”, *Nature* **547** (2017), no. 7664, 432–435.
- [21] Y. Sato, S. Kasahara, H. Murayama, Y. Kasahara, E. G. . Moon, T. Nishizaki, T. Loew, J. Porras, B. Keimer, T. Shibauchi, and Y. Matsuda, “Thermodynamic evidence for a nematic phase transition at the onset of the pseudogap in  $\text{YBa}_2\text{Cu}_3\text{O}_y$ ”, *Nat. Phys.* **13** (2017), no. 11, 1074–1078.
- [22] H. Murayama, Y. Sato, R. Kurihara, S. Kasahara, Y. Mizukami, Y. Kasahara, H. Uchiyama, A. Yamamoto, E. . Moon, J. Cai, J. Freyermuth, M. Greven, T. Shibauchi, and Y. Matsuda, “Diagonal nematicity in the pseudogap phase of  $\text{HgBa}_2\text{CuO}_{4+\delta}$ ”, *Nat. Commun.* **10** (2019), no. 1, 3282.
- [23] S. Sachdev and D. Chowdhury, “The novel metallic states of the cuprates: Topological Fermi liquids and strange metals”, *Prog. Theor. Exp. Phys.* **2016** (2016), no. 12, 1–26.
- [24] S. A. Kivelson and V. J. Emery, “Stripe liquid, crystal, and glass phases of doped antiferromagnets”, in “Stripes and Related Phenomena”, pp. 91–100. Kluwer Academic Publishers, Boston, 2006.
- [25] J. A. Robertson, S. A. Kivelson, E. Fradkin, A. C. Fang, and A. Kapitulnik, “Distinguishing patterns of charge order: Stripes or checkerboards”, *Phys. Rev. B* **74** (2006), no. 13, 1–10.
- [26] P. Monçeau, N. P. Ong, A. M. Portis, A. Meerschaut, and J. Rouxel, “Electric field breakdown of charge-density-wave-induced anomalies in  $\text{NbSe}_3$ ”, *Phys. Rev. Lett.* **37** (1976), no. 10, 602–606.
- [27] C. Schlenker, ed., “Low-Dimensional electronic properties of molybdenum bronzes and oxides”, Springer Netherlands, Dordrecht, 1989.
- [28] J. Dumas and C. Schlenker, “Charge density wave properties of molybdenum bronzes”, *Int. J. Mod. Phys. B* **07** (1993), no. 23,24, 4045–4108.
- [29] J. A. Wilson, F. J. Di Salvo, and S. Mahajan, “Charge-density waves in metallic, layered, transition-metal dichalcogenides”, *Phys. Rev. Lett.* **32** (1974), no. 16, 882–885.
- [30] P. Williams, C. B. Scruby, W. B. Clark, and G. S. Parry, “Charge density waves in the layered transition metal dichalcogenides”, *Le J. Phys. Colloq.* **37** (1976), no. C4, C4–139–C4–150.
- [31] R. E. Peierls, “Quantum theory of solids”, Oxford University Press, New York, 1955.

- [32] B. Renker, H. Rietschel, L. Pintschovius, W. Gläser, P. Brüesch, D. Kuse, and M. J. Rice, “Observation of giant kohn anomaly in the one-dimensional conductor  $\text{K}_2\text{Pt}(\text{CN})_4\text{Br}_{0.3}\cdot 3\text{H}_2\text{O}$ ”, *Phys. Rev. Lett.* **30** (1973), no. 22, 1144–1147.
- [33] R. Peierls, “Zur Theorie der elektrischen und thermischen Leitfähigkeit von Metallen”, *Ann. Phys.* **396** (1930), no. 2, 121–148.
- [34] G. Grüner, “Density waves in solids”, Addison Wesley, Reading, MA, 1994.
- [35] J. Lindhard, “On the properties of a gas of charged particles”, *Dan. Mat. Fys. Medd.* **28** (1954), no. 8, 1–57.
- [36] W. Kohn, “Image of the Fermi surface in the vibration spectrum of a metal”, *Phys. Rev. Lett.* **2** (1959), no. 9, 393–394.
- [37] H. Smith, “The Lindhard function and the teaching of solid state physics”, *Phys. Scr.* **28** (1983), no. 3, 287–293.
- [38] W. E. Pickett and P. B. Allen, “Superconductivity and phonon softening. III. relation between electron bands and phonons in Nb, Mo, and their alloys”, *Phys. Rev. B* **16** (1977), no. 7, 3127–3132.
- [39] M. D. Johannes, I. I. Mazin, and C. A. Howells, “Fermi-surface nesting and the origin of the charge-density wave in  $\text{NbSe}_2$ ”, *Phys. Rev. B* **73** (2006), no. 20, 1–8.
- [40] M. D. Johannes and I. I. Mazin, “Fermi surface nesting and the origin of charge density waves in metals”, *Phys. Rev. B* **77** (2008), no. 16, 165135.
- [41] J. Pouget, “The Peierls instability and charge density wave in one-dimensional electronic conductors”, *Comptes Rendus Phys.* **17** (2016), no. 3-4, 332–356.
- [42] C. M. Varma and A. L. Simons, “Strong-coupling theory of charge-density-wave transitions”, *Phys. Rev. Lett.* **51** (1983), no. 2, 138–141.
- [43] W. L. McMillan, “Microscopic model of charge-density waves in  $2H\text{-TaSe}_2$ ”, *Phys. Rev. B* **16** (1977), no. 2, 643–650.
- [44] A. Fang, J. A. W. Straquadine, I. R. Fisher, S. A. Kivelson, and A. Kapitulnik, “Disorder-induced suppression of charge density wave order: STM study of Pd-intercalated  $\text{ErTe}_3$ ”, *Phys. Rev. B* **100** (2019), no. 23, 235446.
- [45] F. Weber, S. Rosenkranz, J. Castellán, R. Osborn, R. Hott, R. Heid, K. Bohnen, T. Egami, A. H. Said, and D. Reznik, “Extended phonon collapse and the origin of the charge-density wave in  $2H\text{-NbSe}_2$ ”, *Phys. Rev. Lett.* **107** (2011), no. 10, 107403.

- [46] M. Maschek, S. Rosenkranz, R. Heid, A. H. Said, P. Giraldo-Gallo, I. R. Fisher, and F. Weber, “Wave-vector-dependent electron-phonon coupling and the charge-density-wave transition in  $\text{TbTe}_3$ ”, *Phys. Rev. B* **91** (2015), no. 23, 235146.
- [47] I. Tüttő and A. Zawadowski, “Quantum theory of local perturbation of the charge-density wave by an impurity: Friedel oscillations”, *Phys. Rev. B* **32** (1985), no. 4, 2449–2470.
- [48] H. Fukuyama and P. A. Lee, “Dynamics of the charge-density wave. I. Impurity pinning in a single chain”, *Phys. Rev. B* **17** (1978), no. 2, 535–541.
- [49] P. A. Lee and H. Fukuyama, “Dynamics of the charge-density wave. II. Long-range Coulomb effects in an array of chains”, *Phys. Rev. B* **17** (1978), no. 2, 542–548.
- [50] L. Nie, G. Tarjus, and S. A. Kivelson, “Quenched disorder and vestigial nematicity in the pseudogap regime of the cuprates”, *Proc. Natl. Acad. Sci. U. S. A.* **111** (2014), no. 22, 7980–7985.
- [51] L. Nie, A. V. Maharaj, E. Fradkin, and S. A. Kivelson, “Vestigial nematicity from spin and/or charge order in the cuprates”, *Phys. Rev. B* **96** (2017), no. 8, 085142.
- [52] R. M. Fernandes, P. P. Orth, and J. Schmalian, “Intertwined vestigial order in quantum materials: nematicity and beyond”, *Annu. Rev. Condens. Matter Phys.* **10** (2019), no. 1, 133–154.
- [53] Y. Imry and S. K. Ma, “Random-field instability of the ordered state of continuous symmetry”, *Phys. Rev. Lett.* **35** (1975), no. 21, 1399–1401.
- [54] A. M. Ferrenberg and D. P. Landau, “Critical behavior of the three-dimensional Ising model: A high-resolution monte Carlo study”, *Phys. Rev. B* **44** (1991), no. 10, 5081–5091.
- [55] A. B. Harris, “Effect of random defects on the critical behaviour of Ising models”, *J. Phys. C Solid State Phys.* **7** (1974), no. 9, 1671–1692.
- [56] T. Vojta and R. Sknepnek, “Critical points and quenched disorder: From Harris criterion to rare regions and smearing”, *Phys. Status Solidi* **241** (2004), no. 9, 2118–2127.
- [57] T. Giamarchi and P. Le Doussal, “Elastic theory of flux lattices in the presence of weak disorder”, *Phys. Rev. B* **52** (1995), no. 2, 1242–1270.
- [58] J. Bardeen, L. N. Cooper, and J. R. Schrieffer, “Microscopic theory of superconductivity”, *Phys. Rev.* **106** (1957), no. 1, 162–164.
- [59] L. Li, X. Deng, Z. Wang, Y. Liu, M. Abeykoon, E. Dooryhee, A. Tomic, Y. Huang, J. B. Warren, E. S. Bozin, S. J. L. Billinge, Y. Sun, Y. Zhu, G. Kotliar, and C. Petrovic,

- “Superconducting order from disorder in  $2\text{H-TaS}_{2-x}\text{S}_x$ ”, *npj Quantum Mater.* **2** (2017), no. 1, 11.
- [60] P. Anderson, “Theory of dirty superconductors”, *J. Phys. Chem. Solids* **11** (1959), no. 1-2, 26–30.
- [61] E. Morosan, H. W. Zandbergen, B. S. Dennis, J. W. G. Bos, Y. Onose, T. Klimczuk, A. P. Ramirez, N. P. Ong, and R. J. Cava, “Superconductivity in  $\text{Cu}_x\text{TiSe}_2$ ”, *Nat. Phys.* **2** (2006), no. 8, 544–550.
- [62] A. Kogar, G. A. de la Pena, S. Lee, Y. Fang, S. X. Sun, D. B. Lioi, G. Karapetrov, K. D. Finkelstein, J. P. C. Ruff, P. Abbamonte, and S. Rosenkranz, “Observation of a charge density wave incommensuration near the superconducting dome in  $\text{Cu}_x\text{TiSe}_2$ ”, *Phys. Rev. Lett.* **118** (2017), no. 2, 027002.
- [63] Y. Yu and S. A. Kivelson, “Fragile superconductivity in the presence of weakly disordered charge density waves”, *Phys. Rev. B* **99** (2018), no. 14, 144513.
- [64] J. Chang, E. Blackburn, O. Ivashko, A. T. Holmes, N. B. Christensen, M. Hücker, R. Liang, D. A. Bonn, W. N. Hardy, U. Rütt, M. V. Zimmermann, E. M. Forgan, and S. M. Hayden, “Magnetic field controlled charge density wave coupling in underdoped  $\text{YBa}_2\text{Cu}_3\text{O}_{6+x}$ ”, *Nat. Commun.* **7** (2016), no. 1, 11494.
- [65] W. L. McMillan, “Landau theory of charge-density waves in transition-metal dichalcogenides”, *Phys. Rev. B* **12** (1975), no. 4, 1187–1196.
- [66] A. Kikuchi and S. Tsuneyuki, “Electronic structure and charge density wave state in polytypes of  $\text{NbSe}_2$ ”, *Surf. Sci.* **409** (1998), no. 3, 458–464.
- [67] V. Brouet, W. L. Yang, X. J. Zhou, Z. Hussain, R. G. Moore, R. He, D. H. Lu, Z. X. Shen, J. Laverock, S. B. Dugdale, N. Ru, and I. R. Fisher, “Angle-resolved photoemission study of the evolution of band structure and charge density wave properties in  $R\text{Te}_3$  ( $R=\text{Y, La, Ce, Sm, Gd, Tb, and Dy}$ )”, *Phys. Rev. B* **77** (2008), no. 23, 1–16.
- [68] P. A. Vorobyev, P. D. Grigoriev, K. K. Kesharpu, and V. V. Khovaylo, “The evolution of electron dispersion in the series of rare-earth tritelluride compounds obtained from their charge-density-wave properties and susceptibility calculations”, *Materials (Basel)*. **12** (2019), no. 14, 2–9.
- [69] N. Ru, C. L. Condon, G. Y. Margulis, K. Y. Shin, J. Laverock, S. B. Dugdale, M. F. Toney, and I. R. Fisher, “Effect of chemical pressure on the charge density wave transition in rare-earth tritellurides  $R\text{Te}_3$ ”, *Phys. Rev. B* **77** (2008), no. 3, 035114.

- [70] A. Banerjee, Y. Feng, D. M. Silevitch, J. Wang, J. C. Lang, H. H. Kuo, I. R. Fisher, and T. F. Rosenbaum, “Charge transfer and multiple density waves in the rare earth tellurides”, *Phys. Rev. B* **87** (2013), no. 15, 155131.
- [71] N. Ru, “Charge density wave formation in rare-earth tellurides”, PhD thesis, Leland Stanford Jr. University, 2008.
- [72] B. K. Norling and H. Steinfink, “The crystal structure of neodymium tritelluride”, *Inorg. Chem.* **5** (1966), no. 9, 1488–1491.
- [73] E. DiMasi, B. Foran, M. C. Aronson, and S. Lee, “Quasi-two-dimensional metallic character of  $\text{Sm}_2\text{Te}_5$  and  $\text{SmTe}_3$ ”, *Chem. Mater.* **6** (1994), no. 10, 1867–1874.
- [74] R. Patschke and M. G. Kanatzidis, “Polytelluride compounds containing distorted nets of tellurium”, *Phys. Chem. Chem. Phys.* **4** (2002), no. 14, 3266–3281.
- [75] W. Tremel and R. Hoffmann, “Square nets of main group elements in solid-state materials”, *J. Am. Chem. Soc.* **109** (1987), no. 1, 124–140.
- [76] H. Jahn and E. Teller, “Stability of polyatomic molecules in degenerate electronic states: I—Orbital degeneracy”, *Proc. R. Soc. London. Ser. A - Math. Phys. Sci.* **161** (1937), no. 905, 220–235.
- [77] C. Adenis, V. Langer, and O. Lindqvist, “Reinvestigation of the structure of tellurium”, *Acta Crystallogr. Sect. C Cryst. Struct. Commun.* **45** (1989), no. 6, 941–942.
- [78] C. Malliakas, S. J. Billinge, J. K. Hyun, and M. G. Kanatzidis, “Square nets of tellurium: Rare-earth dependent variation in the charge-density wave of  $\text{RETe}_3$  (RE = Rare-Earth element)”, *J. Am. Chem. Soc.* **127** (2005), no. 18, 6510–6511.
- [79] S. Lei, J. Lin, Y. Jia, M. Gray, A. Topp, G. Farahi, S. Klemenz, T. Gao, F. Rodolakis, J. L. McChesney, C. R. Ast, A. Yazdani, K. S. Burch, S. Wu, N. P. Ong, and L. M. Schoop, “High mobility in a van der waals layered antiferromagnetic metal”, *Sci. Adv.* **6** (2020), no. 6, eaay6407.
- [80] J. Laverock, S. B. Dugdale, Z. Major, M. A. Alam, N. Ru, I. R. Fisher, G. Santi, and E. Bruno, “Fermi surface nesting and charge-density wave formation in rare-earth tritellurides”, *Phys. Rev. B* **71** (2005), no. 8, 085114.
- [81] R. G. Moore, V. Brouet, R. He, D. H. Lu, N. Ru, J. Chu, I. R. Fisher, and Z. Shen, “Fermi surface evolution across multiple charge density wave transitions in  $\text{ErTe}_3$ ”, *Phys. Rev. B* **81** (2010), no. 7, 073102.

- [82] N. Ru, R. A. Borzi, A. Rost, A. P. Mackenzie, J. Laverock, S. B. Dugdale, and I. R. Fisher, “De Haas-van Alphen oscillations in the charge density wave compound lanthanum tritelluride  $\text{LaTe}_3$ ”, *Phys. Rev. B* **78** (2008), no. 4, 045123.
- [83] N. Ru and I. R. Fisher, “Thermodynamic and transport properties of  $\text{YTe}_3$ ,  $\text{LaTe}_3$ , and  $\text{CeTe}_3$ ”, *Phys. Rev. B* **73** (2006), no. 3, 033101.
- [84] Y. Iyeiri, T. Okumura, C. Michioka, and K. Suzuki, “Magnetic properties of rare-earth metal tritellurides  $R\text{Te}_3$  ( $R=\text{Ce}$ , Pr, Nd, Gd, Dy)”, *Phys. Rev. B* **67** (2003), no. 14, 1–7.
- [85] N. Ru, J. Chu, and I. R. Fisher, “Magnetic properties of the charge density wave compounds  $R\text{Te}_3$  ( $R = \text{Y}$ , La, Ce, Pr, Nd, Sm, Gd, Tb, Dy, Ho, Er, and Tm)”, *Phys. Rev. B* **78** (2008), no. 1, 012410.
- [86] K. Deguchi, T. Okada, G. F. Chen, S. Ban, N. Aso, and N. K. Sato, “Magnetic order of rare-earth tritelluride  $\text{CeTe}_3$  at low temperature”, *J. Phys. Conf. Ser.* **150** (2009), no. 4, 042023.
- [87] Z. Yang, A. J. Drew, S. van Smaalen, N. van Well, F. L. Pratt, G. B. G. Stenning, A. Karim, and K. Rabia, “Multiple magnetic-phase transitions and critical behavior of charge-density wave compound  $\text{TbTe}_3$ ”, *J. Phys. Condens. Matter* **32** (2020), no. 30, 305801.
- [88] H. Yao, J. A. Robertson, E. A. Kim, and S. A. Kivelson, “Theory of stripes in quasi-two-dimensional rare-earth tellurides”, *Phys. Rev. B* **74** (2006), no. 24, 1–7.
- [89] G. Gweon, J. D. Denlinger, J. A. Clack, J. W. Allen, C. G. Olson, E. DiMasi, M. C. Aronson, B. Foran, and S. Lee, “Direct observation of complete Fermi surface, imperfect nesting, and gap anisotropy in the high-temperature incommensurate charge-density-wave compound  $\text{SmTe}_3$ ”, *Phys. Rev. Lett.* **81** (1998), no. 4, 886–889.
- [90] E. DiMasi, B. Foran, M. C. Aronson, and S. Lee, “Stability of charge-density waves under continuous variation of band filling in  $\text{LaTe}_{2-x}\text{Sb}_x$  ( $0 \leq x \leq 1$ )”, *Phys. Rev. B* **54** (1996), no. 19, 13587–13596.
- [91] E. DiMasi, M. C. Aronson, J. F. Mansfield, B. Foran, and S. Lee, “Chemical pressure and charge-density waves in rare-earth tritellurides”, *Phys. Rev. B* **52** (1995), no. 20, 14516–14525.
- [92] C. D. Malliakas and M. G. Kanatzidis, “Divergence in the behavior of the charge density wave in  $\text{RETe}_3$  ( $\text{RE} = \text{rare-earth element}$ ) with temperature and RE element”, *J. Am. Chem. Soc.* **128** (2006), no. 39, 12612–12613.
- [93] A. Sacchetti, C. L. Condon, S. N. Gvasaliya, F. Pfuner, M. Lavagnini, M. Baldini, M. F. Toney, M. Merlini, M. Hanfland, J. Mesot, J. H. Chu, I. R. Fisher, P. Postorino, and

- L. Degiorgi, “Pressure-induced quenching of the charge-density-wave state in rare-earth tritellurides observed by x-ray diffraction”, *Phys. Rev. B* **79** (2009), no. 20, 4–7.
- [94] V. Brouet, W. L. Yang, X. J. Zhou, Z. Hussain, N. Ru, K. Y. Shin, I. R. Fisher, and Z. X. Shen, “Fermi surface reconstruction in the CDW state of CeTe<sub>3</sub> observed by photoemission”, *Phys. Rev. Lett.* **93** (2004), no. 12, 126405.
- [95] A. Fang, N. Ru, I. R. Fisher, and A. Kapitulnik, “STM studies of TbTe<sub>3</sub>: evidence for a fully incommensurate charge density wave”, *Phys. Rev. Lett.* **99** (2007), no. 4, 046401.
- [96] U. Ralević, N. Lazarević, A. Baum, H. M. Eiter, R. Hackl, P. Giraldo-Gallo, I. R. Fisher, C. Petrovic, R. Gajić, and Z. V. Popović, “Charge density wave modulation and gap measurements in CeTe<sub>3</sub>”, *Phys. Rev. B* **94** (2016), no. 16, 1–8.
- [97] L. Fu, A. M. Kraft, B. Sharma, M. Singh, P. Walmsley, I. R. Fisher, and M. C. Boyer, “Multiple charge density wave states at the surface of TbTe<sub>3</sub>”, *Phys. Rev. B* **94** (2016), no. 20, 205101.
- [98] A. Sacchetti, E. Arcangeletti, A. Perucchi, L. Baldassarre, P. Postorino, S. Lupi, N. Ru, I. R. Fisher, and L. Degiorgi, “Pressure dependence of the charge-density-wave gap in rare-earth tritellurides”, *Phys. Rev. Lett.* **98** (2007), no. 2, 026401.
- [99] F. Pfuner, P. Lerch, J. H. Chu, H. H. Kuo, I. R. Fisher, and L. Degiorgi, “Temperature dependence of the excitation spectrum in the charge-density-wave ErTe<sub>3</sub> and HoTe<sub>3</sub> systems”, *Phys. Rev. B* **81** (2010), no. 19, 1–7.
- [100] J. J. Hamlin, D. A. Zocco, T. A. Sayles, M. B. Maple, J. H. Chu, and I. R. Fisher, “Pressure-induced superconducting phase in the charge-density-wave compound terbium tritelluride”, *Phys. Rev. Lett.* **102** (2009), no. 17, 177002.
- [101] D. A. Zocco, J. J. Hamlin, K. Grube, J. Chu, H. Kuo, I. R. Fisher, and M. B. Maple, “Pressure dependence of the charge-density-wave and superconducting states in GdTe<sub>3</sub>, TbTe<sub>3</sub>, and DyTe<sub>3</sub>”, *Phys. Rev. B* **91** (2015), no. 20, 205114.
- [102] M. Maschek, D. A. Zocco, S. Rosenkranz, R. Heid, A. H. Said, A. Alatas, P. Walmsley, I. R. Fisher, and F. Weber, “Competing soft phonon modes at the charge-density-wave transitions in DyTe<sub>3</sub>”, *Phys. Rev. B* **98** (2018), no. 9, 094304.
- [103] M. Saint-Paul, C. Guttin, P. Lejay, G. Remenyi, O. Leynaud, and P. Monceau, “Elastic anomalies at the charge density wave transition in TbTe<sub>3</sub>”, *Solid State Commun.* **233** (2016) 24–29.

- [104] M. Saint-Paul, G. Remenyi, C. Guttin, P. Lejay, and P. Monceau, “Thermodynamic and critical properties of the charge density wave system  $\text{ErTe}_3$ ”, *Phys. B Condens. Matter* **504** (2017), no. September 2016, 39–46.
- [105] M. Saint-Paul, C. Guttin, P. Lejay, O. Leynaud, and P. Monceau, “Elastic properties of the charge density wave system  $\text{HoTe}_3$ ”, *Int. J. Mod. Phys. B* **32** (2018), no. 23, 1–12.
- [106] A. A. Sinchenko, P. D. Grigoriev, P. Lejay, and P. Monceau, “Spontaneous breaking of isotropy observed in the electronic transport of rare-earth tritellurides”, *Phys. Rev. Lett.* **112** (2014), no. 3, 036601.
- [107] P. Walmsley and I. R. Fisher, “Determination of the resistivity anisotropy of orthorhombic materials via transverse resistivity measurements”, *Rev. Sci. Instrum.* **88** (2017), no. 4, 043901.
- [108] M. E. Fisher and J. S. Langer, “Resistive anomalies at magnetic critical points”, *Phys. Rev. Lett.* **20** (1968), no. 13, 665–668.
- [109] P. D. Grigoriev, A. A. Sinchenko, P. A. Vorobyev, A. Hadj-Azzem, P. Lejay, A. Bosak, and P. Monceau, “Interplay between band crossing and charge density wave instabilities”, *Phys. Rev. B* **100** (2019), no. 8, 081109.
- [110] P. Walmsley, S. Aeschlimann, J. A. W. Straquadine, P. Giraldo-Gallo, S. C. Riggs, M. K. Chan, R. D. McDonald, and I. R. Fisher, “Magnetic breakdown and charge density wave formation: a quantum oscillation study of the rare-earth tritellurides”, *arXiv*, 2020 [arXiv:2003.09657](https://arxiv.org/abs/2003.09657).
- [111] C. B. Carter and P. M. Williams, “An electron microscopy study of intercalation in transition metal dichalcogenides”, *Philos. Mag.* **26** (1972), no. 2, 393–398.
- [112] R. Friend and A. Yoffe, “Electronic properties of intercalation complexes of the transition metal dichalcogenides”, *Adv. Phys.* **36** (1987), no. 1, 1–94.
- [113] J. B. He, P. P. Wang, H. X. Yang, Y. J. Long, L. X. Zhao, C. Ma, M. Yang, D. M. Wang, X. C. Shangguan, M. Q. Xue, P. Zhang, Z. A. Ren, J. Q. Li, W. M. Liu, and G. F. Chen, “Superconductivity in pd-intercalated charge-density-wave rare earth poly-tellurides  $\text{RETe}_n$ ”, *Supercond. Sci. Technol.* **29** (2016), no. 6, 065018.
- [114] R. Lou, Y. Cai, Z. Liu, T. Qian, L. Zhao, Y. Li, K. Liu, Z. Han, D. Zhang, J. He, G. Chen, H. Ding, and S. Wang, “Interplay between multiple charge-density waves and the relationship with superconductivity in  $\text{Pd}_x\text{HoTe}_3$ ”, *Phys. Rev. B* **93** (2016), no. 11, 115133.
- [115] I. Fisher, M. Shapiro, and J. Analytis, “Principles of crystal growth of intermetallic and oxide compounds from molten solutions”, *Philos. Mag.* **92** (2012), no. 19-21, 2401–2435.

- [116] C. W. Hicks, M. E. Barber, S. D. Edkins, D. O. Brodsky, and A. P. Mackenzie, “Piezoelectric-based apparatus for strain tuning”, *Rev. Sci. Instrum.* **85** (2014), no. 6,.
- [117] <https://razorbillinstruments.com/>, “Razorbill instruments Ltd.”, 2020.
- [118] R. J. Corruccini and J. J. Gniewek, “Thermal expansion of technical solids at low temperatures; a compilation from the literature”, tech. rep., National Bureau of Standards, Gaithersburg, MD, 1961.
- [119] M. C. Shapiro, P. Hlobil, A. T. Hristov, A. V. Maharaj, and I. R. Fisher, “Symmetry constraints on the elastoresistivity tensor”, *Phys. Rev. B* **92** (2015), no. 23, 235147.
- [120] Y. Sun, S. E. Thompson, and T. Nishida, “Strain effect in semiconductors”, Springer US, Boston, MA, 2010.
- [121] J. Chu, J. G. Analytis, C. Kucharczyk, and I. R. Fisher, “Determination of the phase diagram of the electron-doped superconductor  $\text{Ba}(\text{Fe}_{1-x}\text{Co}_x)_2\text{As}_2$ ”, *Phys. Rev. B* **79** (2009), no. 1, 014506.
- [122] M. A. Tanatar, A. Kreyssig, S. Nandi, N. Ni, S. L. Bud’ko, P. C. Canfield, A. I. Goldman, and R. Prozorov, “Direct imaging of the structural domains in the iron pnictides  $A\text{Fe}_2\text{As}_2$  ( $A=\text{Ca}, \text{sr}, \text{ba}$ )”, *Phys. Rev. B* **79** (2009), no. 18, 180508.
- [123] J. Chu, H. Kuo, J. G. Analytis, and I. R. Fisher, “Divergent nematic susceptibility in an iron arsenide superconductor”, *Science* **337** (2012), no. 6095, 710–712.
- [124] S. Kasahara, H. J. Shi, K. Hashimoto, S. Tonegawa, Y. Mizukami, T. Shibauchi, K. Sugimoto, T. Fukuda, T. Terashima, A. H. Nevidomskyy, and Y. Matsuda, “Electronic nematicity above the structural and superconducting transition in  $\text{BaFe}_2(\text{As}_{1-x}\text{P}_x)_2$ ”, *Nature* **486** (2012), no. 7403, 382–385.
- [125] H. Kuo, J. Chu, J. C. Palmstrom, S. A. Kivelson, and I. R. Fisher, “Ubiquitous signatures of nematic quantum criticality in optimally doped fe-based superconductors”, *Science* **352** (2016), no. 6288, 958–962.
- [126] J. C. Palmstrom, A. T. Hristov, S. A. Kivelson, J. Chu, and I. R. Fisher, “Critical divergence of the symmetric ( $A_{1g}$ ) nonlinear elastoresistance near the nematic transition in an iron-based superconductor”, *Phys. Rev. B* **96** (2017), no. 20, 205133.
- [127] A. T. Hristov, J. C. Palmstrom, J. A. W. Straquadine, T. A. Merz, H. Y. Hwang, and I. R. Fisher, “Measurement of elastoresistivity at finite frequency by amplitude demodulation”, *Rev. Sci. Instrum.* **89** (2018), no. 10, 103901.

- [128] A. T. Hristov, M. S. Ikeda, J. C. Palmstrom, P. Walmsley, and I. R. Fisher, “Elastoresistive and elastocaloric anomalies at magnetic and electronic-nematic critical points”, *Phys. Rev. B* **99** (2019), no. 10, 100101.
- [129] A. T. Hristov, M. S. Ikeda, J. C. Palmstrom, and I. R. Fisher, “Signatures of anelastic domain relaxation in  $\text{Ba}(\text{Fe}_{1-x}\text{Co}_x)_2\text{As}_2$  investigated by mechanical modulation of resistivity”, *arXiv*, 2019 [arXiv:1903.04732](https://arxiv.org/abs/1903.04732).
- [130] J. A. W. Straquadine, J. C. Palmstrom, P. Walmsley, A. T. Hristov, F. Weickert, F. F. Balakirev, M. Jaime, R. McDonald, and I. R. Fisher, “Growth of nematic susceptibility in the field-induced normal state of an iron-based superconductor revealed by elastoresistivity measurements in a 65 T pulsed magnet”, *Phys. Rev. B* **100** (2019), no. 12, 125147.
- [131] M. Jaime, C. Corvalán Moya, F. Weickert, V. Zapf, F. Balakirev, M. Wartenbe, P. Rosa, J. Betts, G. Rodriguez, S. Crooker, and R. Daou, “Fiber bragg grating dilatometry in extreme magnetic field and cryogenic conditions”, *Sensors* **17** (2017), no. 11, 2572.
- [132] J. A. W. Straquadine, M. S. Ikeda, and I. R. Fisher, “Evidence for realignment of the charge density wave state in  $\text{ErTe}_3$  and  $\text{TmTe}_3$  under uniaxial stress via elastocaloric and elastoresistivity measurements”, *arXiv*, 2020 [arXiv:2005.10461](https://arxiv.org/abs/2005.10461).
- [133] A. Kobayashi, “Elastocaloric effect in Many-Valley semiconductors”, *J. Phys. Soc. Japan* **17** (1962), no. 9, 1518–1518.
- [134] M. S. Ikeda, J. A. W. Straquadine, A. T. Hristov, T. Worasaran, J. C. Palmstrom, M. Sorensen, P. Walmsley, and I. R. Fisher, “AC elastocaloric effect as a probe for thermodynamic signatures of continuous phase transitions”, *Rev. Sci. Instrum.* **90** (2019), no. 8, 083902.
- [135] M. C. Croarkin and W. F. Guthrie, “Temperature-electromotive force reference functions and tables for the letter-designated thermocouple types based on the ITS-90”, tech. rep., National Institute of Standards and Technology, Gaithersburg, MD, 1993.
- [136] M. S. Ikeda, T. Worasaran, J. C. Palmstrom, J. A. W. Straquadine, P. Walmsley, and I. R. Fisher, “Symmetric and antisymmetric strain as continuous tuning parameters for electronic nematic order”, *Phys. Rev. B* **98** (2018), no. 24, 245133.
- [137] “AH2700A product brochure”, tech. rep., Andeen-Hagerling, 2010.
- [138] J. A. W. Straquadine, M. S. Ikeda, and I. R. Fisher, “Frequency-dependent sensitivity of AC elastocaloric effect measurements explored through analytical and numerical models”, *arXiv*, 2020 [arXiv:2006.01291](https://arxiv.org/abs/2006.01291).
- [139] A. Ziótkowski, “Theoretical analysis of efficiency of shape memory alloy heat engines (based on constitutive models of pseudoelasticity)”, *Mech. Mater.* **16** (1993), no. 4, 365–377.

- [140] J. Cui, Y. Wu, J. Muehlbauer, Y. Hwang, R. Radermacher, S. Fackler, M. Wuttig, and I. Takeuchi, “Demonstration of high efficiency elastocaloric cooling with large  $\Delta T$  using NiTi wires”, *Appl. Phys. Lett.* **101** (2012), no. 7, 2–6.
- [141] S. Qian, Y. Geng, Y. Wang, J. Ling, Y. Hwang, R. Radermacher, I. Takeuchi, and J. Cui, “A review of elastocaloric cooling: Materials, cycles and system integrations”, *Int. J. Refrig.* **64** (2016) 1–19.
- [142] S. Qian, D. Nasuta, A. Rhoads, Y. Wang, Y. Geng, Y. Hwang, R. Radermacher, and I. Takeuchi, “Not-in-kind cooling technologies: A quantitative comparison of refrigerants and system performance”, *Int. J. Refrig.* **62** (2016) 177–192.
- [143] D. Luo, Y. Feng, and P. Verma, “Modeling and analysis of an integrated solid state elastocaloric heat pumping system”, *Energy* **130** (2017) 500–514.
- [144] C. W. Hicks, D. O. Brodsky, E. A. Yelland, A. S. Gibbs, J. A. N. Bruin, M. E. Barber, S. D. Edkins, K. Nishimura, S. Yonezawa, Y. Maeno, and A. P. Mackenzie, “Strong increase of  $T_c$  of  $\text{Sr}_2\text{RuO}_4$  under both tensile and compressive strain”, *Science* **344** (2014), no. 6181, 283–285.
- [145] M. D. Bachmann, G. M. Ferguson, F. Theuss, T. Meng, C. Putzke, T. Helm, K. R. Shirer, Y. S. Li, K. A. Modic, M. Nicklas, M. König, D. Low, S. Ghosh, A. P. Mackenzie, F. Arnold, E. Hassinger, R. D. McDonald, L. E. Winter, E. D. Bauer, F. Ronning, B. J. Ramshaw, K. C. Nowack, and P. J. Moll, “Spatial control of heavy-fermion superconductivity in  $\text{CeIrIn}_5$ ”, *Science* **366** (2019), no. 6462, 221–226.
- [146] E. W. Rosenberg, J. Chu, J. P. C. Ruff, A. T. Hristov, and I. R. Fisher, “Divergence of the quadrupole-strain susceptibility of the electronic nematic system  $\text{YbRu}_2\text{Ge}_2$ ”, *Proc. Natl. Acad. Sci. U. S. A.* **116** (2019), no. 15, 7232–7237.
- [147] O. Riou, J. Durastanti, and Y. Sfaxi, “Determination of proper frequency range for accurate heat capacity measurement by AC microcalorimeter”, *Superlattices Microstruct.* **35** (2004), no. 3-6, 353–361.
- [148] R. B. Hetnarski, “Thermal stresses – advanced theory and applications”, Springer Netherlands, Dordrecht, 2009.
- [149] M. A. Biot, “Thermoelasticity and irreversible thermodynamics”, *J. Appl. Phys.* **27** (1956), no. 3, 240–253.
- [150] H. Lord and Y. Shulman, “A generalized dynamical theory of thermoelasticity”, *J. Mech. Phys. Solids* **15** (1967), no. 5, 299–309.
- [151] A. E. Green and K. A. Lindsay, “Thermoelasticity”, *J. Elast.* **2** (1972), no. 1, 1–7.

- [152] P. F. Sullivan and G. Seidel, “Steady-state, ac-temperature calorimetry”, *Phys. Rev.* **173** (1968), no. 3, 679–685.
- [153] I. Velichkov, “On the problem of thermal link resistances in a.c. calorimetry”, *Cryogenics* **32** (1992), no. 3, 285–290.
- [154] M. S. Alnæs, J. Blechta, J. Hake, A. Johansson, B. Kehlet, A. Logg, C. Richardson, J. Ring, M. E. Rognes, and G. N. Wells, “The FEniCS project version 1.5”, *Arch. Numer. Softw.* **3** (2015), no. 100, 9–23.
- [155] A. Logg and G. N. Wells, “DOLFIN: automated finite element computing”, *ACM Trans. Math. Softw.* **37** (2010), no. 2, 1–28.
- [156] C. Geuzaine and J. Remacle, “Gmsh: A 3-D finite element mesh generator with built-in pre- and post-processing facilities”, *Int. J. Numer. Methods Eng.* **79** (2009), no. 11, 1309–1331.
- [157] Y. Machida, K. Tomokuni, T. Isono, K. Izawa, Y. Nakajima, and T. Tamegai, “Possible sign-reversing  $s$ -wave superconductivity in Co-doped  $\text{BaFe}_2\text{As}_2$  proved by thermal transport measurements”, *J. Phys. Soc. Japan* **78** (2009), no. 7, 5–8.
- [158] M. Meinero, F. Caglieris, I. Pallecchi, G. Lamura, S. Ishida, H. Eisaki, A. Continenza, and M. Putti, “In-plane and out-of-plane properties of a  $\text{BaFe}_2\text{As}_2$  single crystal”, *J. Phys. Condens. Matter* **31** (2019), no. 21, 214003.
- [159] R. J. Corruccini and J. J. Gniewek, “Specific heats and enthalpies of technical solids at low temperatures: a compilation from the literature”, tech. rep., National Bureau of Standards, Gaithersburg, MD, 1960.
- [160] F. R. Schwartzberg, “Cryogenic materials data handbook”, National Technical Information Service, Springfield, VA, 1970.
- [161] B. Sundqvist, “Thermal diffusivity and thermal conductivity of chromel, alumel, and constantan in the range 100-450 K”, *J. Appl. Phys.* **72** (1992), no. 2, 539–545.
- [162] S. Nakamura, T. Fujii, S. Matsukawa, M. Katagiri, and H. Fukuyama, “Specific heat, thermal conductivity, and magnetic susceptibility of cyanate ester resins – an alternative to commonly used epoxy resins”, *Cryogenics* **95** (2018), no. September, 76–81.
- [163] H. P. Langtangen and A. Logg, “Solving PDEs in Python”, Springer International Publishing, Cham, 2016.
- [164] J. Kopp and G. Slack, “Thermal contact problems in low temperature thermocouple thermometry”, *Cryogenics* **11** (1971), no. 1, 22–25.

- [165] D. Rittel, “Transient temperature measurement using embedded thermocouples”, *Exp. Mech.* **38** (1998), no. 2, 73–78.
- [166] C. D. Henning and R. Parker, “Transient response of an intrinsic thermocouple”, *J. Heat Transfer* **89** (1967), no. 2, 146–152.
- [167] W. Tabis, Y. Li, M. L. Tacon, L. Braicovich, A. Kreyssig, M. Minola, G. Dellea, E. Weschke, M. J. Veit, M. Ramazanoglu, A. I. Goldman, T. Schmitt, G. Ghiringhelli, N. Barišić, M. K. Chan, C. J. Dorow, G. Yu, X. Zhao, B. Keimer, and M. Greven, “Charge order and its connection with fermi-liquid charge transport in a pristine high- $T_c$  cuprate”, *Nat. Commun.* **5** (2014), no. 1, 5875.
- [168] R. Comin, R. Sutarto, F. He, E. H. da Silva Neto, L. Chauviere, A. Fraño, R. Liang, W. N. Hardy, D. A. Bonn, Y. Yoshida, H. Eisaki, A. J. Achkar, D. G. Hawthorn, B. Keimer, G. A. Sawatzky, and A. Damascelli, “Symmetry of charge order in cuprates”, *Nat. Mater.* **14** (2015), no. 8, 796–800.
- [169] J. Wen, H. Huang, S. Lee, H. Jang, J. Knight, Y. S. Lee, M. Fujita, K. M. Suzuki, S. Asano, S. A. Kivelson, C. Kao, and J. Lee, “Observation of two types of charge-density-wave orders in superconducting  $\text{La}_{2-x}\text{Sr}_x\text{CuO}_4$ ”, *Nat. Commun.* **10** (2019), no. 1, 3269.
- [170] S. K. Chan and V. Heine, “Spin density wave and soft phonon mode from nesting Fermi surfaces”, *J. Phys. F Met. Phys.* **3** (1973), no. 4, 795–809.
- [171] H. Requardt, J. E. Lorenzo, P. Monceau, R. Currat, and M. Krisch, “Dynamics in the charge-density-wave system  $\text{NbSe}_3$  using inelastic x-ray scattering with meV energy resolution”, *Phys. Rev. B* **66** (2002), no. 21, 214303.
- [172] M. Leroux, I. Errea, M. Le Tacon, S. Souliou, G. Garbarino, L. Cario, A. Bosak, F. Mauri, M. Calandra, and P. Rodière, “Strong anharmonicity induces quantum melting of charge density wave in  $\text{NbSe}_2$  under pressure”, *Phys. Rev. B* **92** (2015), no. 14, 140303.
- [173] M. Maschek, S. Rosenkranz, R. Hott, R. Heid, M. Merz, D. A. Zocco, A. H. Said, A. Alatas, G. Karapetrov, S. Zhu, J. Van Wezel, and F. Weber, “Superconductivity and hybrid soft modes in  $\text{TiSe}_2$ ”, *Phys. Rev. B* **94** (2016), no. 21, 1–10.
- [174] A. Soumyanarayanan, M. M. Yee, Y. He, J. V. Wezel, D. J. Rahn, K. Rossnagel, E. W. Hudson, M. R. Norman, and J. E. Hoffman, “Quantum phase transition from triangular to stripe charge order in  $\text{NbSe}_2$ ”, *Proc. Natl. Acad. Sci. U. S. A.* **110** (2013), no. 5, 1623–1627.
- [175] F. Flicker and J. Van Wezel, “Charge ordering geometries in uniaxially strained  $\text{NbSe}_2$ ”, *Phys. Rev. B* **92** (2015), no. 20, 1–5.

- [176] R. M. Fernandes, S. A. Kivelson, and E. Berg, “Vestigial chiral and charge orders from bidirectional spin-density waves: Application to the iron-based superconductors”, *Phys. Rev. B* **93** (2016), no. 1, 014511.
- [177] P. D. Grigoriev, A. A. Sinchenko, P. Lejay, A. Hadj-Azzem, J. Balay, O. Leynaud, V. N. Zverev, and P. Monceau, “Bilayer splitting versus fermi-surface warping as an origin of slow oscillations of in-plane magnetoresistance in rare-earth tritellurides”, *Eur. Phys. J. B* **89** (2016), no. 6, 151.
- [178] S. C. Riggs, M. Shapiro, A. V. Maharaj, S. Raghu, E. Bauer, R. Baumbach, P. Giraldo-Gallo, M. Wartenbe, and I. Fisher, “Evidence for a nematic component to the hidden-order parameter in URu<sub>2</sub>Si<sub>2</sub> from differential elastoresistance measurements”, *Nat. Commun.* **6** (2015), no. 1, 6425.
- [179] H. Eiter, M. Lavagnini, R. Hackl, E. A. Nowadnick, A. F. Kemper, T. P. Devereaux, J. Chu, J. G. Analytis, I. R. Fisher, and L. Degiorgi, “Alternative route to charge density wave formation in multiband systems”, *Proc. Natl. Acad. Sci. U. S. A.* **110** (2013), no. 1, 64–69.
- [180] A. Kogar, A. Zong, P. E. Dolgirev, X. Shen, J. Straquadine, Y. Bie, X. Wang, T. Rohwer, I. Tung, Y. Yang, R. Li, J. Yang, S. Weathersby, S. Park, M. E. Kozina, E. J. Sie, H. Wen, P. Jarillo-Herrero, I. R. Fisher, X. Wang, and N. Gedik, “Light-induced charge density wave in LaTe<sub>3</sub>”, *Nat. Phys.* **16** (2020), no. 2, 159–163.
- [181] M. Saint-Paul and P. Monceau, “Survey of the thermodynamic properties of the charge density wave systems”, *Adv. Condens. Matter Phys.* **2019** (2019) 1–14.
- [182] J. A. W. Straquadine, F. Weber, S. Rosenkranz, A. H. Said, and I. R. Fisher, “Suppression of charge density wave order by disorder in Pd-intercalated ErTe<sub>3</sub>”, *Phys. Rev. B* **99** (2019), no. 23, 235138.
- [183] “Impedance measurement handbook: A guide to measurement technology and techniques”, tech. rep., Keysight Instruments, 2016.
- [184] S. Wakimoto, R. J. Birgeneau, Y. Fujimaki, N. Ichikawa, T. Kasuga, Y. J. Kim, K. M. Kojima, S. H. Lee, H. Niko, J. M. Tranquada, S. Uchida, and M. V. Zimmermann, “Effect of a magnetic field on the spin- and charge-density-wave order in La<sub>1.45</sub>Nd<sub>0.4</sub>Sr<sub>0.15</sub>CuO<sub>4</sub>”, *Phys. Rev. B* **67** (2003), no. 18, 184419.
- [185] M. Hücker, M. v. Zimmermann, G. D. Gu, Z. J. Xu, J. S. Wen, G. Xu, H. J. Kang, A. Zheludev, and J. M. Tranquada, “Stripe order in superconducting La<sub>2-x</sub>Ba<sub>x</sub>CuO<sub>4</sub> (0.095 ≤ x ≤ 0.155)”, *Phys. Rev. B* **83** (2011), no. 10, 104506.

- [186] R. Comin, A. Frano, M. M. Yee, Y. Yoshida, H. Eisaki, E. Schierle, E. Weschke, R. Sutarto, F. He, A. Soumyanarayanan, Y. He, M. Le Tacon, I. S. Elfimov, J. E. Hoffman, G. A. Sawatzky, B. Keimer, and A. Damascelli, “Charge order driven by Fermi-arc instability in  $\text{Bi}_2\text{Sr}_{2-x}\text{La}_x\text{CuO}_{6+\delta}$ ”, *Science* **343** (2014), no. 6169, 390–392.
- [187] R. Comin, R. Sutarto, E. H. da Silva Neto, L. Chauviere, R. Liang, W. N. Hardy, D. a. Bonn, F. He, G. A. Sawatzky, and A. Damascelli, “Broken translational and rotational symmetry via charge stripe order in underdoped  $\text{YBa}_2\text{Cu}_3\text{O}_{6+y}$ ”, *Science* **347** (2015), no. 6228, 1335–1339.
- [188] J. E. Hoffman, K. McElroy, D. Lee, K. M. Lang, H. Eisaki, S. Uchida, and J. C. Davis, “Imaging quasiparticle interference in  $\text{Bi}_2\text{Sr}_2\text{CaCu}_2\text{O}_{8+\delta}$ ”, *Science* **297** (2002), no. 5584, 1148–1151.
- [189] C. J. Arguello, S. P. Chockalingam, E. P. Rosenthal, L. Zhao, C. Gutiérrez, J. H. Kang, W. C. Chung, R. M. Fernandes, S. Jia, A. J. Millis, R. J. Cava, and A. N. Pasupathy, “Visualizing the charge density wave transition in  $2H\text{-NbSe}_2$  in real space”, *Phys. Rev. B* **89** (2014), no. 23, 235115.
- [190] K. Cho, M. Kończykowski, S. Teknowijoyo, M. A. Tanatar, J. Guss, P. B. Gartin, J. M. Wilde, A. Kreyssig, R. J. McQueeney, A. I. Goldman, V. Mishra, P. J. Hirschfeld, and R. Prozorov, “Using controlled disorder to probe the interplay between charge order and superconductivity in  $\text{NbSe}_2$ ”, *Nat. Commun.* **9** (2018), no. 1, 2796.
- [191] U. Chatterjee, J. Zhao, M. Iavarone, R. Di Capua, J. P. Castellan, G. Karapetrov, C. D. Malliakas, M. G. Kanatzidis, H. Claus, J. P. C. Ruff, F. Weber, J. van Wezel, J. C. Campuzano, R. Osborn, M. Randeria, N. Trivedi, M. R. Norman, and S. Rosenkranz, “Emergence of coherence in the charge-density wave state of  $2H\text{-NbSe}_2$ ”, *Nat. Commun.* **6** (2015), no. 1, 6313.
- [192] B. F. Hu, B. Cheng, R. H. Yuan, T. Dong, A. F. Fang, W. T. Guo, Z. G. Chen, P. Zheng, Y. G. Shi, and N. L. Wang, “Optical study of the multiple charge-density-wave transitions in  $\text{ErTe}_3$ ”, *Phys. Rev. B* **84** (2011), no. 15, 155132.
- [193] B. F. Hu, B. Cheng, R. H. Yuan, T. Dong, and N. L. Wang, “Coexistence and competition of multiple charge-density-wave orders in rare-earth tritellurides”, *Phys. Rev. B* **90** (2014), no. 8, 085105.
- [194] M. Lavagnini, A. Sacchetti, C. Marini, M. Valentini, R. Sopracase, A. Perucchi, P. Postorino, S. Lupi, J. H. Chu, I. R. Fisher, and L. Degiorgi, “Pressure dependence of the single particle excitation in the charge-density-wave  $\text{CeTe}_3$  system”, *Phys. Rev. B* **79** (2009), no. 7, 075117.
- [195] A. H. Said, H. Sinn, and R. Divan, “New developments in fabrication of high-energy-resolution analyzers for inelastic x-ray spectroscopy”, *J. Synchrotron Radiat.* **18** (2011), no. 3, 492–496.

- [196] L. Gannon, A. Bosak, R. G. Burkovsky, G. Nisbet, A. P. Petrović, and M. Hoesch, “A device for the application of uniaxial strain to single crystal samples for use in synchrotron radiation experiments”, *Rev. Sci. Instrum.* **86** (2015), no. 10,.
- [197] A. Zong, A. Kogar, Y. Bie, T. Rohwer, C. Lee, E. Baldini, E. Ergeçen, M. B. Yilmaz, B. Freelon, E. J. Sie, H. Zhou, J. Straquadine, P. Walmsley, P. E. Dolgirev, A. V. Rozhkov, I. R. Fisher, P. Jarillo-Herrero, B. V. Fine, and N. Gedik, “Evidence for topological defects in a photoinduced phase transition”, *Nat. Phys.* **15** (2019), no. 1, 27–31.
- [198] C. Lee, T. Rohwer, E. J. Sie, A. Zong, E. Baldini, J. Straquadine, P. Walmsley, D. Gardner, Y. S. Lee, I. R. Fisher, and N. Gedik, “High resolution time- and angle-resolved photoemission spectroscopy with 11 eV laser pulses”, *Rev. Sci. Instrum.* **91** (2020), no. 4, 043102.
- [199] H. Pfau, S. D. Chen, M. Yi, M. Hashimoto, C. R. Rotundu, J. C. Palmstrom, T. Chen, P. Dai, J. Straquadine, A. Hristov, R. J. Birgeneau, I. R. Fisher, D. Lu, and Z. Shen, “Momentum dependence of the nematic order parameter in iron-based superconductors”, *Phys. Rev. Lett.* **123** (2019), no. 6, 066402.
- [200] A. A. Sinchenko, P. Lejay, and P. Monceau, “Sliding charge-density wave in two-dimensional rare-earth tellurides”, *Phys. Rev. B* **85** (2012), no. 24, 1–5.
- [201] A. Sinchenko, P. Lejay, O. Leynaud, and P. Monceau, “Unidirectional charge-density-wave sliding in two-dimensional rare-earth tritellurides”, *Solid State Commun.* **188** (2014) 67–70.
- [202] A. Sinchenko, P. D. Grigoriev, P. Lejay, O. Leynaud, and P. Monceau, “Anisotropy of conductivity in rare-earth tritellurides in the static and sliding states of the CDW”, *Phys. B Condens. Matter* **460** (2015) 21–25.
- [203] A. A. Sinchenko, P. Lejay, O. Leynaud, and P. Monceau, “Dynamical properties of bidirectional charge-density waves in  $\text{ErTe}_3$ ”, *Phys. Rev. B* **93** (2016), no. 23, 235141.
- [204] H. Fröhlich, “On the theory of superconductivity: the one-dimensional case”, *Proc. R. Soc. London. Ser. A. Math. Phys. Sci.* **223** (1954), no. 1154, 296–305.
- [205] G. Grüner, “The dynamics of charge-density waves”, *Rev. Mod. Phys.* **60** (1988), no. 4, 1129–1181.
- [206] D. Le Bolloc’h, A. A. Sinchenko, V. L. Jacques, L. Ortega, J. E. Lorenzo, G. A. Chahine, P. Lejay, and P. Monceau, “Effect of dimensionality on sliding charge density waves: The quasi-two-dimensional  $\text{TbTe}_3$  system probed by coherent x-ray diffraction”, *Phys. Rev. B* **93** (2016), no. 16, 1–5.

- [207] A. V. Frolov, A. P. Orlov, A. Hadj-Azzem, P. Lejay, A. A. Sinchenko, and P. Monceau, “Toward equilibrium ground state of charge density waves in rare-earth tritellurides”, *arXiv*, 2020 [arXiv:2004.04503](https://arxiv.org/abs/2004.04503).
- [208] T. Mertelj, P. Kusar, V. V. Kabanov, P. Giraldo-Gallo, I. R. Fisher, and D. Mihailovic, “Incoherent topological defect recombination dynamics in  $\text{TbTe}_3$ ”, *Phys. Rev. Lett.* **110** (2013), no. 15, 1–5.
- [209] C. Bradley and A. Cracknell, “The mathematical theory of symmetry in solids: Representation theory for point groups and space groups”, Oxford University Press, New York, revised ed., 2009.
- [210] N. Lazarević, Z. V. Popović, R. Hu, and C. Petrovic, “Evidence of coupling between phonons and charge-density waves in  $\text{ErTe}_3$ ”, *Phys. Rev. B* **83** (2011), no. 2, 2–6.
- [211] S. Woo, H. C. Park, and Y. W. Son, “Poisson’s ratio in layered two-dimensional crystals”, *Phys. Rev. B* **93** (2016), no. 7, 1–5.